Imperial College London

Functional Mechanical Metamaterials

Development of Programmable Mechanical Structures

Mohammad Usman Waheed

2021

Dyson School of Design Engineering

Imperial College London

Submitted in part fulfilment of the requirements for the degree of

Doctor of Philosophy of Imperial College London

and the Diploma of Imperial College London

Abstract

In recent years, and with the continual development of Additive Manufacturing (AM) technologies, Mechanical Metamaterials (MMs) are explored for their programmable and tunable nature. This has opened a new design space into mechanical devices that utilise the structure of a material to perform a function, otherwise known as Functional Mechanical Metamaterials (FMMs). Material Jetting is used to build programmable MMs by combining elastic flexure elements to rigid beams. The proposed metamaterial controls the buckling response of a biased Von-Mises Truss through the actuation of unit cells to perform Boolean logic. By developing an anisotropic 3D unit cell and a bistable system for signal propagation, AND and OR logic gates have successfully been demonstrated in three different configurations, zz, yy and zy-polarisation. Additionally, an SLA-printed compliant MM is successfully developed, combining anisotropic unit cells to coupled slender beams. The separation distance between the fixed ends of a slender beam can be used to tune the MM between monostable and bistable states. This behaves as a control system, allowing mechanical signals to pass only when the correct actuation pattern and force is applied. In both MM examples, *sense-decide-respond* logic sequences under mechanical actuation are demonstrated. These FMM implementations pose several advantages for use in larger combinatorial systems. Experimentation successfully demonstrates bistable wave propagation, allowing multiple mechanical signals to pass through larger structures in multiple planes. A compliant rod-logic FMM is developed, actuation of the structure engages a gating function that modulates mechanical signals through a plane. Finally, integrated multi-material FMM sensors are developed, highlighting the use of mechanical sensors in architected systems. The proposed FMMs have applications as nuclear safety devices, accelerometers in automobiles, and as a diagnostic tool in lattice-based crash helmets.

Declaration of Originality

I declare that this thesis was composed by myself, that the work contained here in is my own except where explicitly stated otherwise in the text, and that this work has not been submitted for any other degree or professional qualification except as specified. Due references have been provided on all supporting literature and resources.

Parts of this work have been published in the following articles:

- U. Waheed, C. Myant, S. Dobson, "Boolean AND/OR Mechanical Logic using Multi-Plane Mechanical Metamaterials", *Extreme Mechanics Letters*, vol. 40, p.100865, 2020. doi:https://doi.org/10.1016/j.eml.2020.100865.
- U. Waheed, C. Myant, "Passive Mechanical Metamaterial Sensor and Actuator", *44th Mechanisms and Robotics Conference, International Design Engineering Technical Conference and Computers and Information in Engineering Conference*, 2020.

Copyright Statement

The copyright of this thesis rests with the author. Unless otherwise indicated, its contents are licensed under a Creative Commons Attribution-Non Commercial 4.0 International Licence (CC BY-NC). Under this licence, you may copy and redistribute the material in any medium or format. You may also create and distribute modified versions of the work. This is on the condition that: you credit the author and do not use it, or any derivative works, for a commercial purpose. When reusing or sharing this work, ensure you make the licence terms clear to others by naming the licence and linking to the licence text. Where a work has been adapted, you should indicate that the work has been changed and describe those changes. Please seek permission from the copyright holder for uses of this work that are not included in this licence or permitted under UK Copyright Law.

Acknowledgements

In the name of Allah, the Most Gracious and the Most Merciful.

All praises to Allah and His blessing for the completion of this thesis. I thank God for all the opportunities, trials, and strength showered on me to finish writing the thesis. I experienced so much during this process, not only from the academic aspect but also personally. My humblest gratitude to the Holy Prophet Muhammad (Peace be upon him), whose way of life has been continuous guidance for me.

First and foremost, I would like to sincerely thank my supervisor, Connor Myant, for his continued support and guidance throughout this project. I will be forever grateful for his mentorship and encouragement throughout my time at Imperial to never doubt myself and my ideas.

Special thanks to the ICO CDT and all those involved in delivering such a great experience. Jon Tate for his never wavering patience and Claire for her continued efforts in improving the CDT experience. Huge thanks to the constantly shrinking Cohort 3, Ben, Jon, Stewart and Johannes, for enduring my music throughout the many long car journeys.

A special thanks to AWE for sponsoring my project and continuing to guide me throughout. To the Mechanisms Group for their valuable input and discussion. I would like to sincerely thank my industrial supervisor, Simon Dobson. I have thoroughly enjoyed our discussions over the years, and I am very grateful for his words of encouragement during difficult times over the past year.

Special thanks to the AM group, Livia, Borut, Freddy, Ali, Mohanad, for their continued support and motivation. To Shen and Mo for their continual help in the lab. To the special pie room, Jiwoo and Shiya, even in a pandemic, they find ways to keep me motivated; my PhD experience would not be the same without them.

Lastly, my deepest gratitude to all my family for their love, support, prayers and most of all, patience.

In memory of my late grandmother

Amma

Contents

1 Introduction **15**

1.1 Introduction . . . 15

1.2 Research Proposal . . . 16

1.3 Thesis Overview . . . 17

2 Literature Review **18**

2.1 Mechanical Metamaterials Overview . . . 19

2.2 Mechanical Metamaterials . . . 21

2.2.1 Auxetic . . . 22

2.2.2 Origami & Kirigami . . . 24

2.2.3 Multistable . . . 25

2.2.4 Topological . . . 28

2.2.5 Combinatorial . . . 29

2.3 Functional Metamaterials . . . 32

2.3.1 Non-Mechanical Stimuli . . . 32

2.3.2 Mechanical Metamaterials exhibiting Boolean Logic . . . 33

2.3.3 Industrial Applications . . . 36

2.4 Summary . . . 38

3 Manufacturing **40**

3.1 Manufacturing Overview . . . 41

3.2 Printing Technologies . . . 43

3.3 Material Jetting . . . 45

3.3.1 Materials Properties . . . 46

3.3.2 Printing Setup . . . 47

3.4 Vat Polymerisation . . . 50

3.4.1 Material Properties . . . 51

3.4.2 Printing Setup . . . 52

3.5 Fused Deposition Modelling . . . 55

4 Mechanical Metamaterial Logic **58**

4.1 Mechanical Boolean Logic Gates . . . 59

4.2 Bistable Systems for Mechanical Logic . . . 60

4.2.1 Euler Buckling Theory for a Fixed-Fixed Beam . . . 60

4.2.2 Asymmetric Bistable Systems . . . 61
4.3 Metamaterial Development . . . 65
4.3.1 Multi-Material Development . . . 66
4.4 Mechanical AND/OR Boolean Logic Gates . . . 73
4.4.1 X-Polarised Unit Cells . . . 81
4.5 Standard Logic Gates . . . 82
4.5.1 NOT Gate . . . 82
4.5.2 Connected Logic Gates . . . 84
4.6 Discussion . . . 86

5 Tunable Bistable Mechanical Metamaterial System 89
5.1 Mechanical Control System . . . 90
5.2 Proposed Tunable Bistable System . . . 93
5.3 Compliant Mechanism Design . . . 96
5.3.1 Beam Design . . . 97
5.3.2 Unit Cell Design . . . 98
5.3.3 MM Tunable System . . . 101
5.4 Analytical Model of a Compressed Coupled Bistable Buckled Beam . . . 102
5.5 Experimental Setup . . . 105
5.5.1 Buckling Experimental Setup . . . 105
5.5.2 Bistable Experimental Setup . . . 106
5.6 Results . . . 108
5.7 Discussion . . . 112

6 Combinatorial Functional Mechanisms 117
6.1 3D Mechanical Metamaterials . . . 118
6.2 Multi-Plane Bistable System . . . 120
6.3 Rod-Logic Mechanical Metamaterial . . . 122
6.4 Mechanical Metamaterial Safety System . . . 125
6.5 Discussion . . . 131

7 Case Study - Nuclear Safety Mechanism 135
7.1 Nuclear Safety Principles . . . 136
7.1.1 Isolation . . . 136
7.1.2 Incompatibility . . . 137
7.1.3 Inoperability . . . 138
7.1.4 Independence . . . 139
7.1.5 Unique Signals . . . 139
7.2 Discriminating Mechanisms . . . 141
7.2.1 Pin-in-Maze . . . 143
7.2.2 Counter Meshing Gears . . . 145
7.2.3 Discriminator Summary . . . 147
7.2.4 Recent Developments . . . 149

7.3 MM for Discriminating Mechanisms 153
7.4 Discussion 160

8 Conclusion and Future Work **164**
8.1 Conclusion 164
8.2 Future Work 168

List of Figures

2.1 MM Reentrant Example 20
2.2 MM Building Blocks 21
2.3 Auxetic Structures 22
2.4 Biholar Auxetic Examples 23
2.5 Origami Examples 24
2.6 Multistable Examples 26
2.7 Topological Metamaterial Examples 28
2.8 Frustration-Free Combinatorial Mechanical Metamaterials 30
2.9 Frustration in Combinatorial Mechanical Metamaterials 31
2.10 Stimuli Responsive Metamaterials 32
2.11 MM Logic Gate Examples - 2D 34
2.12 MM Logic Gate Examples - 3D 35
2.13 MM Industrial Application Examples 37

3.1 AM 2025 Global Projection 42
3.2 Overview of AM Technologies 43
3.3 Material Jetting Printing Process 45
3.4 PolyJet Printing Considerations 48
3.5 SLA Printing Process 50
3.6 SLA Printing Considerations 52
3.7 FDM Printing Process 55
3.8 Unit Cell FDM Anisotropy 56

4.1 Symmetric Fixed-Fixed Slender Beam 60
4.2 Fixed-Fixed Curved Slender Beam 61
4.3 Snap-Through Motion 62
4.4 Von-Mises Truss 63
4.5 2D Elastic MM Development 65
4.6 Unit Cell Development 67
4.7 Unit Cell Iteration 68
4.8 Unit Cell Technical Drawing 70
4.9 Bistable System Development 70
4.10 Bistable Testing 72
4.11 Bistable System Technical Drawing 73

4.12 2D Mechanical AND Gate . . . 74
4.13 Printed Component and Rig Design . . . 75
4.14 MM Logic Gates . . . 76
4.15 MM Logic Gates $S_d = 0.6$ . . . 78
4.16 MM Logic Gates $S_d = 0.8$ . . . 79
4.17 MM Logic Gates $S_d = 0.85$ . . . 79
4.18 MM Logic Gates $S_d = 0.98$ . . . 80
4.19 x-Polarised Unit Cell . . . 81
4.20 NOT Gate Example . . . 83
4.21 Connected AND Gate . . . 85
4.22 Four-Input AND Gate . . . 86

5.1 Common MEMS Sensors . . . 91
5.2 Bistale MEMS Examples . . . 92
5.3 Symmetric Fixed-Fixed Slender Beam with Changing Force . . . 94
5.4 Schematic of a Monostable and Bistable System . . . 95
5.5 Fixed-Fixed Slender Beam Design . . . 97
5.6 Common Flexure Designs . . . 99
5.7 Compliant Unit Cell Development . . . 100
5.8 Final Compliant MM Design . . . 101
5.9 Compressed Beam Schematic . . . 102
5.10 Buckling Experimental Setup . . . 106
5.11 Bistable Experimental Setup . . . 107
5.12 Buckling Results . . . 108
5.13 Bistable Results . . . 110
5.14 Tunable Bistable Comparison - 1^{st} & 2^{nd} Run . . . 111
5.15 Tunable Bistable Comparison - Excluding 1^{st} & 2^{nd} Run . . . 111
5.16 Microscope Images of Slender Beams . . . 113

6.1 MM Hierarchy . . . 119
6.2 Multi-Plane Bistable MM - Combinatorial Design . . . 120
6.3 Multi-Plane Bistable MM - Experimental Results . . . 122
6.4 Rod-Logic - Combinatorial Design . . . 123
6.5 Rod-Logic - Experimental Results . . . 124
6.6 Lattice-Based Design Industry Examples . . . 125
6.7 FMM Sensor Design - Propagating Signals . . . 126
6.8 FMM Propagating Signals - Experimental Validation . . . 127
6.9 FMM Integrated Sensor - Combinatorial Design . . . 128
6.10 FMM Integrated Sensor - Experimental Validation . . . 129

7.1 ENDS Principles . . . 137
7.2 Safety Response to a Worst Case Directional Fire . . . 138
7.3 UQS Dependencies Graph . . . 141
7.4 MC2935 Discriminator . . . 143

7.5 Benavides- Pin-in-Maze Discriminator - 1 144
7.6 Benavides- Pin-in-Maze Discriminator - 2 144
7.7 Polosky - Counter Meshing Gears Discriminator 146
7.8 Counter Meshing Gears SEM 147
7.9 SJU CMG Discriminator 150
7.10 SNL Wedge Discriminator 151
7.11 SNL Knot Discriminator 151
7.12 Compliant MM Actuation Sequence 154
7.13 Proposed MM Discriminator 154
7.14 Alternative MM Discriminators 156
7.15 MM Discriminator - Experimental Validation 157
7.16 MM Mechanical Safety 158

List of Tables

3.1 PolyJet Rigid Materials 46
3.2 DM-Agilus Material Properties 46
3.3 Tough1500 Materials Properties 51

4.1 Unit Cell Testing 69

5.1 Beam Dimensions 97
5.2 Bistable Experiment Results 110

7.1 UQS Pattern for Different Event Types 140
7.2 Anatomy of a Stronglink 142

List of Acronyms

AM Additive Manufacturing

CMG Counter Meshing Gear

DM Digital Material

DMLS Direct Metal Laser Sintering

FDM Fused Deposition Modelling

FMM Functional Mechanical Metamaterial

FRMM Field Responsive Mechanical Metamaterial

MC Morphological Computation

MEMS Micro-Electro Mechanical System

MM Mechanical Metamaterial

PIM Pin-in-Maze

PTD Pop Through Defect

SLA Stereolithography

SLS Selective Laser Sintering

UQS Unique Signal

VMT Von-Mises Truss

Chapter 1

Introduction

1.1 Introduction

The programmable nature of materials has been an area of research interest for several decades [1]. The ability to engineer materials that 'compute' by sensing and actuating in response to external stimuli is a disruptive technology for future systems [2, 3]. With recent developments in Additive Manufacturing (AM) technologies, the ability to rationally design materials to perform device-like functionality can be realised (metadevices). A particular avenue in constructing programmable and functional materials is through the investigation of mechanical metamaterials (MM). Metamaterials are architected materials designed to exhibit properties superior to their constituent material. MMs exploit structural deformations and mechanical energies to exhibit unique phenomena. An advantage of MM for functional materials is building devices that respond to external stimuli via material composition and material architecture.

Technological advancements in manufacturing have given rise to a new era of material science research on smart materials. Often inspired through biology, multifunctional materials are engineered, coupling the material and geometric properties with devices to build intelligent and functional systems. These materials sense and respond to stimuli in a programmable manner much like biological systems, for example, tactile sensing in human skin. Smart materials can couple sensing, actuation, computation and communication into an integrated material architecture. Comprehended as 'morphological computation' (MC), the *sense-decide-respond* control loop of smart materials is due to structural (bulk) deformations. MMs are smart structures presumed to exhibit morphological computation. It is proposed the development of MMs can be utilised to build functional mechanical devices.

1.2 Research Proposal

MMs are extensively studied for the unique phenomena they present. However, functional applications are seldom explored. The lack of functional mechanical metamaterials (FMMs) beyond energy harvesters and deployable structures lags behind the manufacturing advancements. This is because MM research is heavily focused on the material science of the architected structures. As a result, few MM devices are developed for engineering applications. The limited FMMs studied show structures often constrained to a single plane. There are a limited number of FMMs that are inherently 3D and function across multiple planes. For MMs to penetrate industries such as aerospace, automotive and biomedical, a design-based approach is necessary to build FMMs.

In line with morphological computation, can mechanical metamaterials' structural deformations be used to *sense, decide* & *respond* to a stimulus? This problem leads on to the research question to be investigated in this thesis: **Can functional devices be developed using 3D mechanical metamaterials that exhibit programmable and tunable behaviour in response to mechanical actuation?**

In investigating this research question, several aspects of mechanical metamaterials will be explored:

- *Can mechanical metamaterials compute Boolean logic?*
- *Can a mechanical metamaterial control system be developed?*
- *Can the mechanical metamaterial device form part of a larger morphological system?*
- *Can multi-plane programmable behaviour be exhibited?*

The development of FMMs could lead to several industrial applications where morphological computation could be advantageous, such as soft robotics, aerospace and automotive. Non-charged based logic devices can be used in harsh environments to perform functions where electronics are often unstable and unreliable [4]. MMs can be used as passive mechanical control systems and sensors/actuators in the automotive industry, and in structured lattice helmets. Finally, a long-term goal in the nuclear industry is to develop safety mechanisms that are non-charged based. This is to ensure predictable responses occur in harsh environments [5, 6].

1.3 Thesis Overview

Chapter 2 - The literature review provides an overview of MMs' programmable and tunable nature. Common MM structures are described, including auxetic, origami & kirigami, multistable, topological and combinatorial metamaterials. Functional applications of MM designs such as mechanical logic, aerofoils and meta-implants are reviewed.

Chapter 3 - The manufacturing chapter provides an overview of Additive Manufacturing (AM) technologies. The AM technologies used in this research are Material Jetting (PolyJet), Stereolithography (SLA) and Fused Deposition Modelling (FDM). The chapter highlights the printer settings, material properties and design considerations of manufacturing MMs using AM.

Chapter 4 - MM logic is developed. The chapter describes Euler buckling theory, the snap-through response of a bistable system and the design of a MM logic device using multi-material Polyjet printing. Boolean logic gates AND, OR & NOT are explored. In addition, combining multiple logic gates is studied.

Chapter 5 - Mechanical metamaterial control system is developed. Analogous to planar MEMS tunable bistable beam. A compliant MM design using SLA technology is manufactured and experimentally verified for its pattern-sensing and tunable capabilities. The dynamics of the snap-through response is mechanically tested and compared to an analytical model.

Chapter 6 - Combinatorial functional mechanisms are developed. Using the results from Chapters 4 & 5, MM designs are combined to build multi-plane systems. Bistable systems, accelerometers, passive mechanical fuses and rod-logic systems that function through multiple-planes are experimentally validated.

Chapter 7 - A case study on the use of MMs as safety devices. In particular, for use as discriminating mechanisms in the nuclear industry, mechanical safety devices are preferred over electronics. The pattern-sensing capabilities of MMs are developed to function as safety mechanisms.

Chapter 8 - A summary and discussion on the key findings from the thesis and suggested future work to develop the field of functional mechanical metamaterials further.

Chapter 2

Literature Review

Mechanical metamaterials (MM) are architected materials that exhibit properties superior to the constituent material. These materials are constructed from unit cells that deform in response to mechanical forces. A programmable and tunable bulk material response can be achieved by combining unit cells and harnessing the elastic instabilities present. This chapter explores common MM structures found throughout literature, including auxetic, chiral, origami & kirigami, multistable, topological and combinatorial structures. The functional capabilities of MM are also examined, including structures programmed to non-mechanical stimuli and structures that perform Boolean logic. In addition, the functional applications of MM in industry are examined, such as chiral aerofoils in aerospace and meta-implant designs for the biomedical industry. The review's focus is on the tunable and programmable nature of MM and the functional capabilities. The review highlights the planar limitations of FMMs, and the relatively unexplored mechanical 'metadevices'. This shows a need in the research field for further development of FMMs.

2.1 Mechanical Metamaterials Overview

With the advent of Additive Manufacturing (AM) technologies, there is growing research interest in architected materials to explore unique phenomena. Metamaterials are rationally designed architected materials that exhibit properties and functionalities often beyond those of their constituent materials. Mechanical Metamaterials (MM) exploit structural deformations and mechanical energies to exhibit unique phenomena. Metamaterials are well established in optics, acoustics and thermodynamics, and exhibit unique phenomena such as thermal cloaking [7], negative refraction [8] and acoustic steering [9]. Developments in negative refractive index materials have resulted in applications such as perfect lenses [8]. In particular, the use of metamaterials has become commonplace in engineering electromagnetic space. With advancements in manufacturing capabilities, research is shifting towards achieving tunable, switchable, nonlinear and sensing functionalities by hybridising functional matter with metamaterials. As such, the emerging field of metadevices has been an area of research interest, particularly in photonics, due to the ability to guide light via the engineered electromagnetic space using metamaterials with spatially variable parameters [8]. In contrast to the research shift towards metadevices in photonics, there currently lacks development of mechanical counterparts. This research focuses on developing mechanical metadevices, otherwise known as functional mechanical materials (FMMs), exhibiting tunable, switchable, nonlinear and sensing functionalities. This is accomplished by investigating programmable and tunable MMs, building devices that respond to external stimuli via material composition and material architecture.

The manufacturing capabilities of AM technologies has been a catalyst in the rapid expansion of MMs studied. There is, however, no prescribed design strategy for the development of MMs. Typically, MM structures are designed from unit cells arranged in a periodic arrangement that elastically deform in response to mechanical forces. By investigating how the response from a unit cell influences its adjacent neighbours, the collective bulk material behaviour of the MM is engineered. The architected structures of MM mean the global response to deformation differs from the localised formations of the unit cells. One of the earliest analysis on metamaterial structures was conducted by Lakes [10] on foam structures. Through conventional low-density open-cell polymer foams, reentrant structures were developed. The typical unit cell, a 24-sided polyhedron with cubic symmetry, is shown in Figure 2.1.a. This structure highlighted the capabilities of reentrant foams to exhibit negative Poisson's ratios. As stated in Bertoldi *et al.* [12], a fundamental reason why

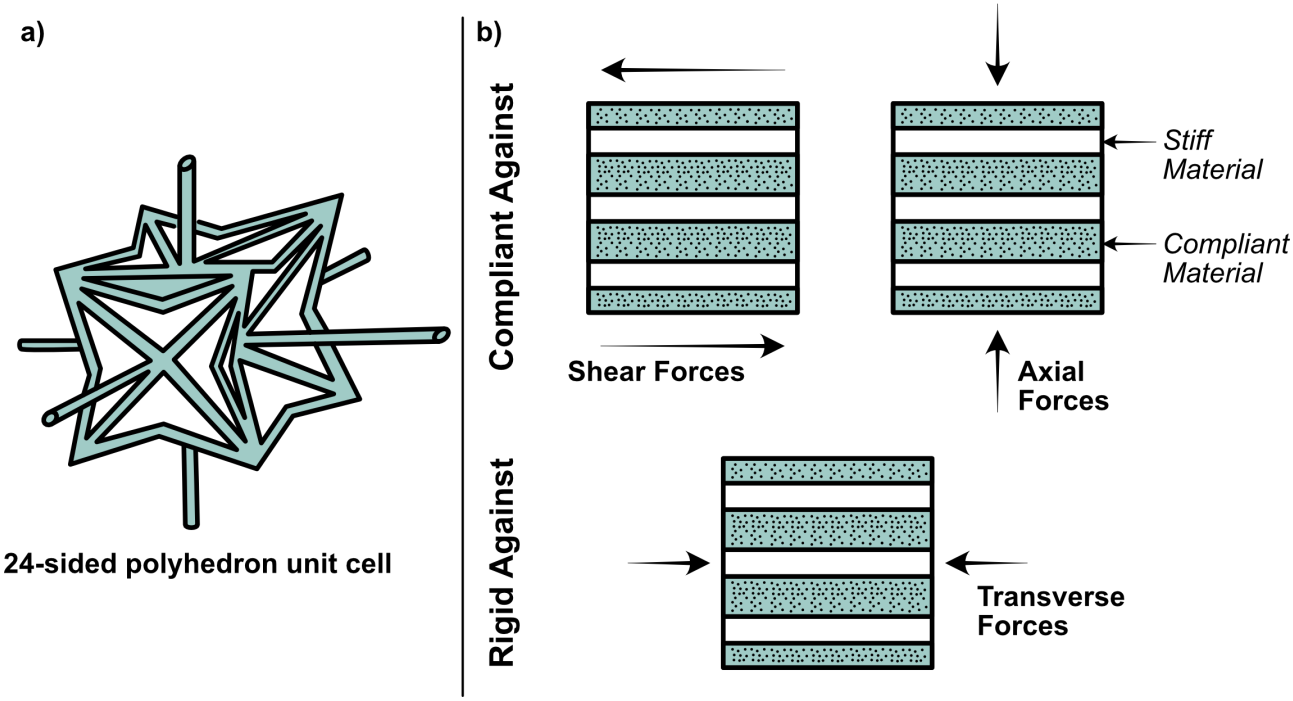


Figure 2.1: *a) Reentrant unit cell design - 24-sided polyhedron with cubic symmetry [10]. b) Extremal materials example - layering of stiff and compliant materials as proposed by Milton and Cherkaev lead to anisotropic behaviour [11]. Schematics adapted from: (a) Lakes [10] and (b) Milton and Cherkaev [11].*

architected materials lead to new properties is the resulting heterogeneity of stresses and deformations. The affine assumption states that locally, particles follow the globally applied deformation field [13]. However, in disordered, non-uniform systems such as a reentrant foam, there is a breakdown of the affine assumption leading to novel properties, such as a negative Poisson's ratio. Milton and Cherkaev [11] explore heterogeneous structures by combining stiff and compliant materials to form a bulk material response. The proposed extremal material showed in Figure 2.1.b exhibits extremely stiff modes to transverse forces and compliant soft modes to shear and axial forces. Anisotropy of the bulk material through the combination of stiff and compliant material lead to tunable elasticity. For example, pentamode structures with a very large bulk modulus and a low shear modulus can be achieved. Alternatively, extremal materials with a low bulk modulus and high shear modulus can be achieved, exhibiting a negative Poisson's ratio.

2.2 Mechanical Metamaterials

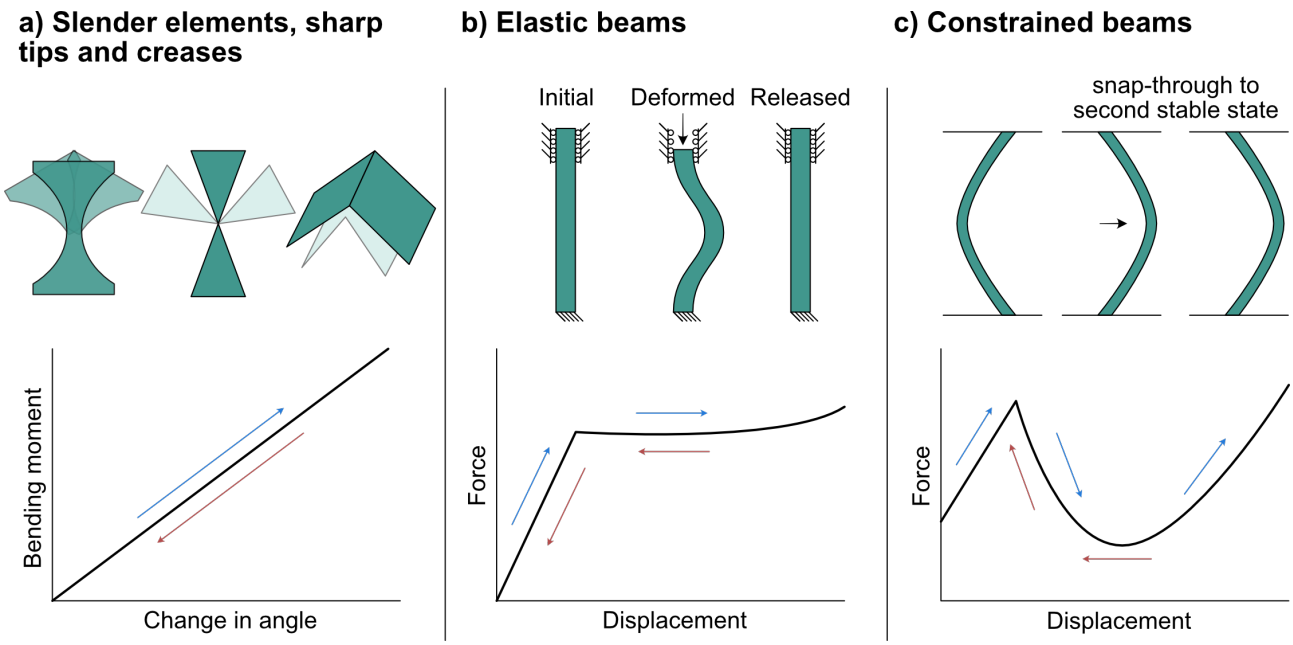


Figure 2.2: *a) Unit cells can respond to shear forces and bending moments through a change in angle, these are introduced through material structures such as free slender beams, top joints and creases such as in Origami. b) Slender beams when constrained to one axis buckle under loading forces. Elastic materials allow the buckled beam to return to its original shape. c) When a slender beam is compressed and fixed from both ends, a bistable system is formed. A snap-through response occurs when a force overcoming the potential energy barrier is applied. Schematic adapted from Bertoldi et al. [12].*

In defining the hierarchy of cellular materials, a lattice receives the lowest order n = 0 of hierarchy [14]. The unit cell follows n = 1, and the structural elements that make up the unit cell have n = 2. At a fundamental level, the element deformations (n = 2) are categorised into three types. (1) elements that utilise localised bending, (2) elastic beams deformed to buckle, and (3) constrained beams exhibiting bistability. As described by Bertoldi *et al.* [12] and shown in Figure 2.2, these are the common building blocks of MMs. Sharp tips and creases in rigid elements allow for zero energy-free motion. The structuring of these building blocks leads to free hinging motion, exhibited in auxetic and origami-based metamaterials. Instability based metamaterials that constitute buckling and bistable elements lead to novel properties such as multistable and switchable deformation behaviour. For a comprehensive review of MMs, Bertoldi's review on 'Flexible Mechanical Metamaterials' [12], Kadic's review on '3D Metamaterials' [15], and Surjadis review on 'Mechanical Metamaterials and their Engineering Applications' [16] are recommended for further reading.

2.2.1 Auxetic

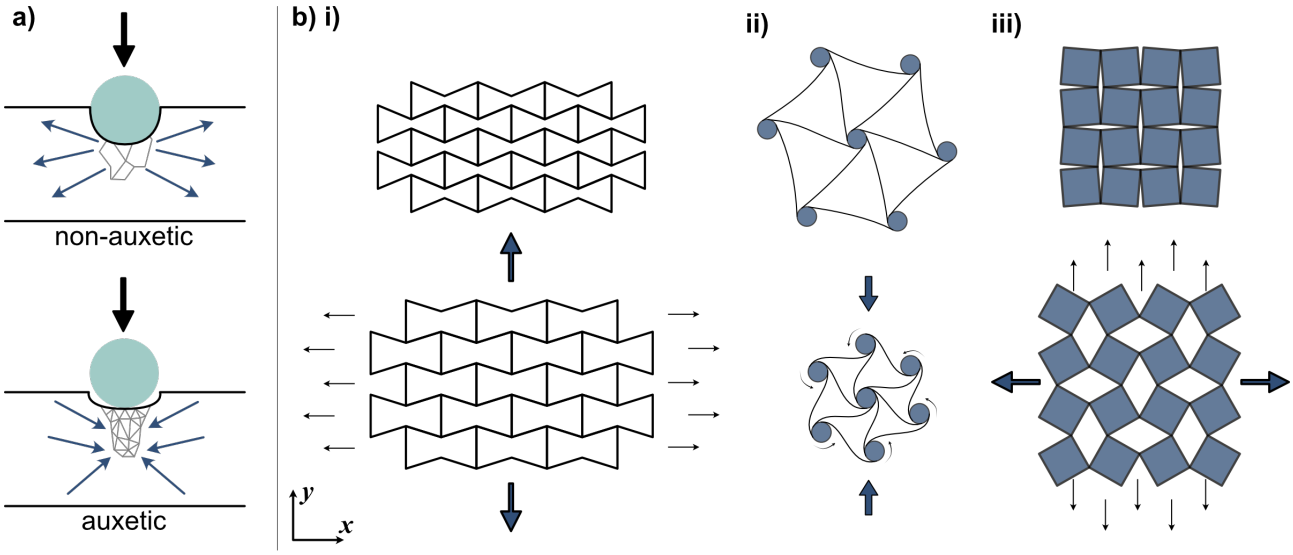


Figure 2.3: *a) Difference in response to deformation and fracture resistance for non-auxetic and auxetic materials. b) Typical 2D auxetic structures i) reentrant honeycomb (bow-tie), ii) chiral structure, iii) semi-rigid rotating squares. Schematics adapted from Kolken and Zadpoor [17].*

Auxetic structures such as reentrant foams are early examples of how the rational structuring of materials leads to unique properties [10]. Auxetic structures [18, 19, 20, 17] are MM's that expand or contract perpendicular to an applied force, resulting in a negative Poisson's ratio. The development of auxetic structures has been rapid due to their broad applicability as shock absorbers and the control over material properties, such as hardness and fracture toughness [21]. This is highlighted in Figure 2.3.a, showing the difference in deformation between non-auxetic and auxetic materials. The superior properties of auxetics allow for contraction in loading conditions, resisting deformation and improving fracture toughness [22]. Typical auxetic structures include reentrant foams [10], honeycomb structures [22], chiral structures [23, 24] and semi-rigid structures [25, 26]. Figure 2.3.b highlights typical auxetic structures in rest and under loading conditions. Figure 2.3.b.i shows a reentrant bow-tie honeycomb structure; the deformation is dominated by the hinging of the bow-tie unit cell [26]. Tensile forces cause an extension from the hinges and a resulting expansion along the x and y axis. Chiral MM's are architected materials that exhibit reflective symmetry [27]. This leads to the rotation on nodes and a resulting contraction in the 2D-plane in response to compressive forces, as shown in Figure 2.3.b.ii [17]. In the two examples, the auxetic properties are from the elastic response to deformation, causing hinging at the bow-tie centre and folding ligaments in chiral materials. Auxetic properties are also shown in semi-rigid structures, such as rigid squares connected through simple hinges shown in Figure 2.3.b.iii [25, 26]. Complex MM designs utilising semi-rigid connected unit cells exhibit shape reconfigurability, and multistable material responses [28].

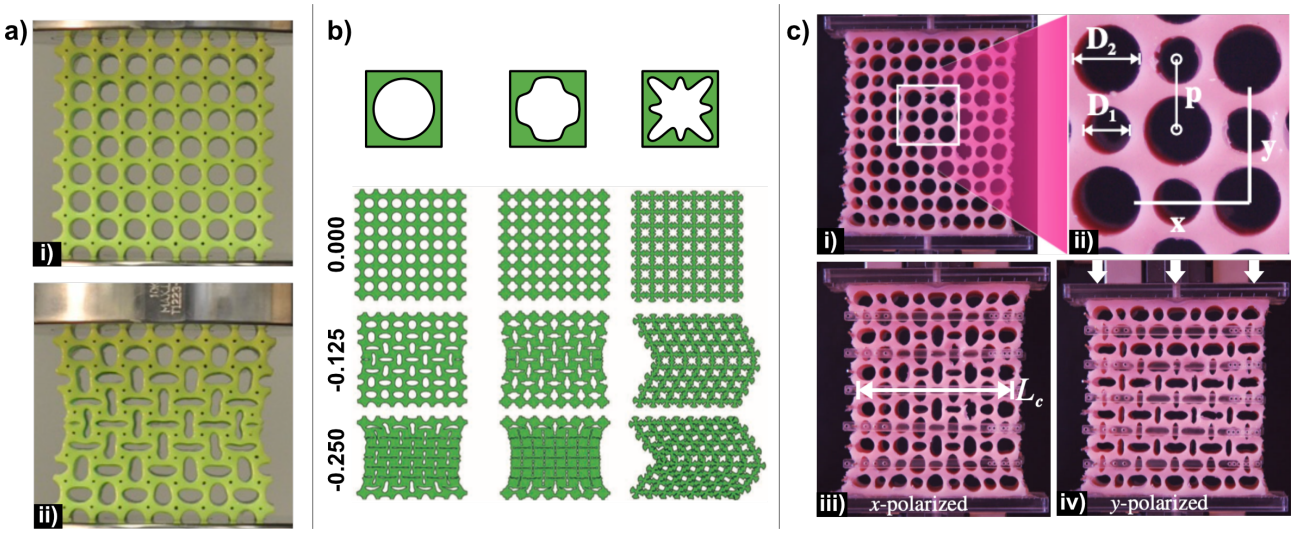


Figure 2.4: *Biholar auxetic examples - perforated elastic 2D slabs. a) Biholar slab with circular holes in i) zero compression and ii) uniaxial compression [29]. b) Comparison of material response to uniaxial compression for different perforation shapes: circular, plus-shaped and star-shaped [30]. c) Slab with alternating large and small holes exhibits switchable polarisation under different loading conditions when constrained along the x-axis [31]. Images adapted from: (a) Bar-Sinai et al. [29], (b) Overvelde and Bertoldi [30], and (c) Florijn et al. [31].*

More recently, research has shown by leveraging geometric nonlinearities and instabilities in auxetic structures, tunable and programmable responses to actuation can be achieved [32]. The biholar elastic slab, as shown in Figure 2.4 has been an auxetic metamaterial extensively studied for the pattern transformations that occur due to snapping based instabilities [20, 29, 30, 31, 33, 34, 35]. This MM consists of an elastomeric sheet with perforated circular holes in a square array. The mechanics of the biholar sheet under low deformation energies are comparable to semi-rigid structures connected by hinges as shown in Figure 2.3. Studies by T. Mullin *et al.* [20] and Bertoldi *et al.* [34, 35] highlight the reversible pattern transformation of a typical biholar pattern when under uniaxial compression. As the system's stress increases, the circular-shaped holes' present during compression in the linear elastic regime are replaced by a sudden shape transformation to alternating orthogonal ellipses as shown in Figure 2.4.a.ii. The proposed auxetic structure is nonlinear; thus, small changes to the material's bulk strain result in a sudden transformation in the pattern. Unlike many other auxetic structures, the negative Poisson's behaviour is only found under compression and above a critical value of an applied strain due to the elastic instability. These transformative structures have particular uses in photonics, where the sudden change in shape can be used as optical switches to direct light in a controlled manner.

A study by Overvalde [33, 30] examines the role of perforation shape on the transformative response of biholar structures. The research shows perforation shape to have a strong effect on mechanical instabilities as shown in Figure 2.4.b. Circular hole shapes result in microstructure instabilities; in

comparison, star-shaped holes result in bulk material buckling. In contrast, plus-shaped holes exhibit the most substantial auxetic response to actuation, highlighting the role perforation shape has on the nonlinear response of a material and how it can tune the mechanical response. The biholar MM examples examined are highly planar, restricting their use in FMMs. Babaee [18] investigates this further, using an array of patterned elastomeric spherical shells (Bucklicrystals). It is shown, the use of spherical unit cells of octahedral or icosahedral symmetry results in 3D auxetic behaviour over a wide range of applied strains.

The programmable nature of auxetic structures is highlighted in quasi-2D elastic slabs under confinement constraints [31]. The elastic slab perforated with alternating large and small circular holes in a square array is shown in Figure 2.4.c. Under conditions of uniaxial compression and lateral confinement, the auxetic structure exhibits monotonic, non-monotonic and hysteretic behaviour. For example, hysteretic switching from x to y polarisation (shape of circular holes) is observed in large systems. Furthermore, multistable states are present through inhomogeneities in the structure. This study highlights the tunable and repeatable functionality attainable in auxetic structures through mechanical instabilities and how they are exploited to form programmable materials.

2.2.2 Origami & Kirigami

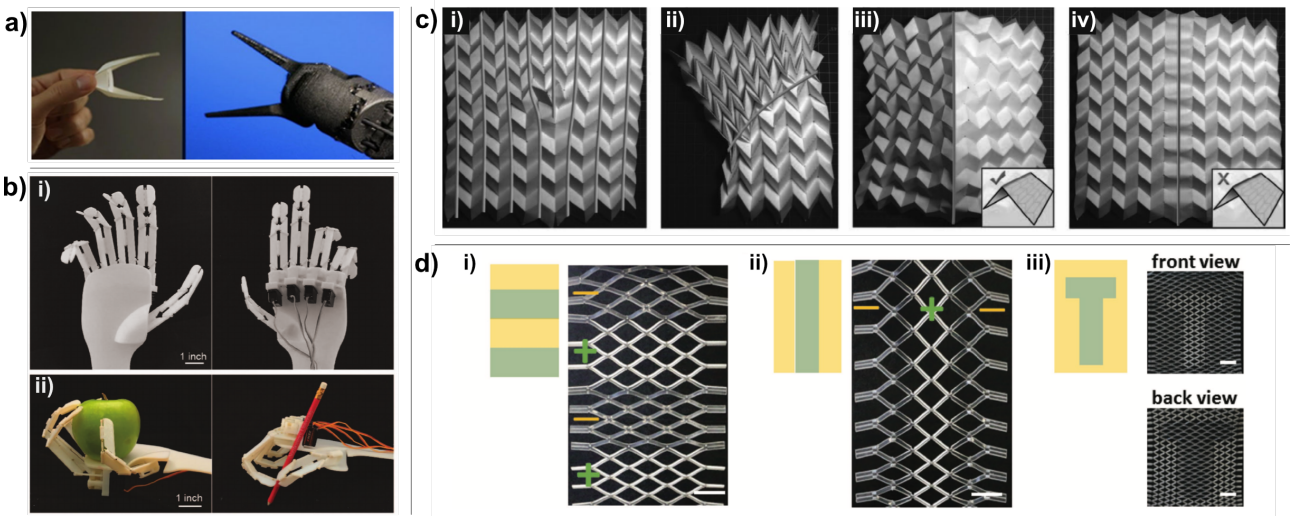


Figure 2.5: *Uses of Origami and Kirigami in compliant mechanisms and MMs. a) Compliant micro-gripper for surgery [36]. b) Foldable robotic hand [37]. c) PTD in Miura-ori sheet can create edge dislocations (i), structural grain boundaries (ii), bulk hinge structures (iii) and rigid corrugated structures (iv) exhibiting tunable mechanical properties [38, 39]. d) Kirigami sheet with patterned bistable notches. Patterned outputs in response to tensile forces [40]. Images adapted from: (a) Johnson et al. [36], (b) Kamrava et al. [37], (c) Silverberg et al. [39], and (d) Tang et al. [40].*

Origami & Kirigami have been of great interest in robotics and the aerospace industry due to their versatility in creating FMMs. Origami is a traditional Japanese paper folding technique; by systematically folding flat paper along creases, complex 3D structures can be achieved. Kirigami is a

variation of an Origami technique, cutting paper and folding along creases to build structures. Mechanisms utilising Origami techniques have become increasingly important due to their industry applications. For example, Miura-ori origami patterns are used as deployable structures for satellites in aerospace [41]. In the biomedical industry, origami-inspired stent-grafts and micro-grippers (Figure 2.5.a) [36] are developed. Furthermore, origami-inspired structures are used in soft robotics for foldable robotic hands [37] (Figure 2.5.b) and biomimetic load-bearing wings [42]. The bulk material properties in an origami structure are defined by the geometry and pattern of the constituent folds. The Miura-ori tessellation [41] is observed to be mechanically bistable at every crease, allowing a structure to switch between multiple states. Stacked-origami based on the Miura-ori architecture exhibits stiffness and effective modulus tunability, considered for soft robotic systems [43]. Recent studies by Silverberg [39, 38] have shown through the use of pop through defects (PTD) on a Miura-ori tessellation, programmable mechanical responses are exhibited. By altering PTD locations and interactions with other defects, different modulus values for the material can be determined, displaying tunable behaviour. As shown in Figure 2.5.c, PTD locations can be designed to create edge dislocations (i), structural grain boundaries (ii), bulk hinge structures (iii) and rigid corrugated structures (iv). This highlights the programmable response of metamaterials due to geometric frustration mechanisms created through defects in the structure.

The uses of Kirigami have also been highlighted for their programmable capabilities. Research by Y. Tang [40] introduces a new structure called Kiri-kirigami, obtained by creating patterned notches to kirigami sheets. These sheets are designed to be highly responsive to their environment under different stretching conditions. The position of the notches determines the buckling direction of the kirigami sheets. These are used to build responsive MMs that buckle in/out of the plane in response to uniaxial forces. Figure 2.5.c shows through the control over in-plane and out of plane buckling, a patterned output can be programmed into the Kirigami sheet in response to stretching. As shown, the versatility in constructing adaptable, functional structures through Origami & Kirigami techniques plays an increasing role in developing FMMs.

2.2.3 Multistable

Multistable mechanical metamaterials are architected materials that exhibit multiple stable equilibria that are fully recoverable. They are often defined as shape-reconfigurable materials (SRM). SRM's are architected materials with structurally derived nonlinearity, exhibiting multifunctional capabilities. Of particular interest is developing multistable MMs for energy

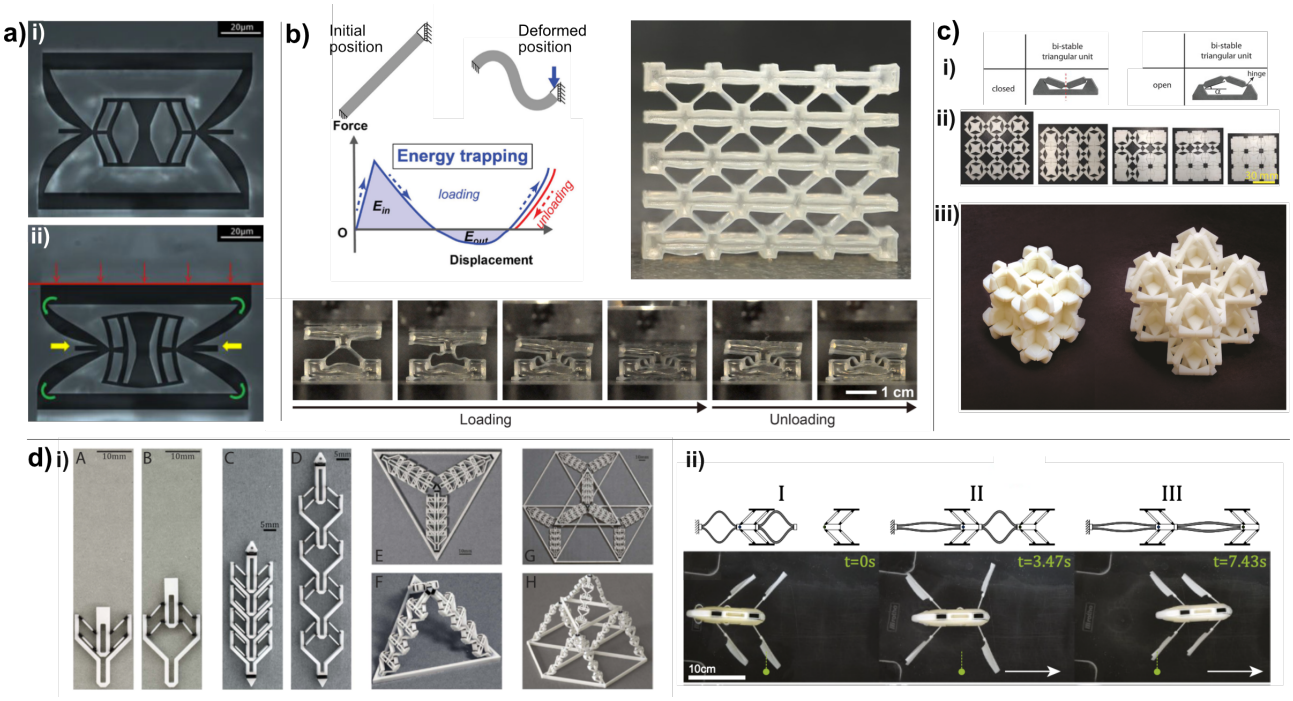


Figure 2.6: *Multistable metamaterial examples. a) Metastable unit cell design connecting a bow-tie structure to a coupled bistable system [14]. b) Bistable unit cell using tilted slender beams shown in loaded and unloaded condition. When combined, structure exhibits sequential multiple stable states for effective energy trapping [44]. c) Multistable structure using rigid elements and living hinge design. i) living hinge design in open and close states. ii) 2D multistable structure in different collapsed states. iii) 3D multistable structure in fully collapsed state [28]. d) Bistable unit cell modelled on a VMT design. i) Combining unit cells to build hierarchical 3D structures. ii) Combining unit cell with SMP beams to propel soft robot [45, 46]. Images adapted from: (a) Berwind et al. [14], (b) Shan et al. [44], (c) Haghpanah et al. [28], and (d) Chen et al. (i) [45], (ii) [46].*

absorption [47] and tunable behaviour. Studies have shown multistability for impact energy trapping, shape morphing, and sensing capabilities. In comparison to foams and auxetic structures examined in Section 2.2.1, the deformation often (not exclusively) occurred in the linear elastic regime. Multistable materials exhibit a negative stiffness at defined loads, resulting in geometric changes to a stable equilibrium. These result from bistable elements in the unit cell design (hierarchy n = 2), causing a snap-through transition between stable equilibria.

Berwind *et al.* [14] presents a hierarchical structure developed from the traditional bow-tie auxetic unit cell. The unit cell exhibits programmable and tunable behaviour of a metastable state through bistable elements. The proposed unit cell under compression is shown in Figure 2.6.a.ii. The bow-tie structure under compression forces the bistable system to transition to a second stable state. Once the load is released, the unit cell remains in a metastable compressed state until the bistable beams snap-through to their original position (i) due to the bow tie's outward transverse force. It is shown this time-dependent recovery between states is highly tunable and programmable, analogous to shape-memory materials. However, in this design, the phase changes result from the non-linear buckling of structural elements instead of crystal structure transformations. The unit cells time-dependent shape

recovery is a function of its negative Poisson's ratio and has been proposed as a building block for mechanical Boolean logic. For example, building a matrix of the unit cells [14] with local variations allows decision trees with nested functions to be realised.

Shan *et al.* [44] and Haghpanah *et al.* [28] highlight the uses of multistable architectures for energy absorption capabilities. Shan [44] proposes a unit cell design of bistable tilted slender beams fabricated from Polydimethylsiloxane (PDMS) as shown in Figure 2.6.b. The trapping of elastic energy is a direct result of buckling slender beams; the energy trapping mechanism is material and loading rate independent. The proposed structure is shown to reduce peak acceleration during impact, and the mechanical response can be tuned by controlling the unit cells' geometric parameters, such as the beams tilt angle. Figure 2.6.b shows the loading/unloading response of a single unit cell and how they can be combined into a multistable lattice structure, as each row of bistable unit cells buckles sequentially. Haghpanah [28] proposes a multistable structure of constrained living hinges to implement bistability. As shown in Figure 2.6.c, living hinges (i) can be used to construct 2D (ii) and 3D (iii) architected materials – with complex shape morphing multistable patterns. Evident in Figure 2.6.c.ii, the proposed structure allows multi-axial deformation with large volumetric and morphological changes that are reconfigurable. The 2D structure from its fully expanded to contracted state shows several different stable configurations during compression. Due to the use of living hinges, the structures can be realised in a broad range of constituent materials: polymer, metal, ceramic and composite.

Chen *et al.* [45] highlights a bistable unit cell based on a Von-Mises Truss (VMT) to construct deployable structures using multi-material 3D printing, as shown in Figure 2.6.d.i. Similar to origami structures that fold to create 3D functional structures, the VMT unit cells can be connected to construct multiple hierarchical structures. Multi-state mechanisms utilising VMT unit cells have also been utilised in soft robotic systems. Chen develops on the deployable structures further by tethering the bistable unit cell to shape memory polymers. This creates a change of state when responding to stimuli and a consequent movement of a fin to propel a soft robot [46] as shown in Figure 2.6.d.ii. The multistable MMs described exhibit programmable and highly tunable deformation behaviour. In most cases, through harnessing buckling instabilities and non-linear bistable elements, metamaterials can be designed that perform Boolean logic, tune material stiffness and function to release energy and drive soft robotic systems.

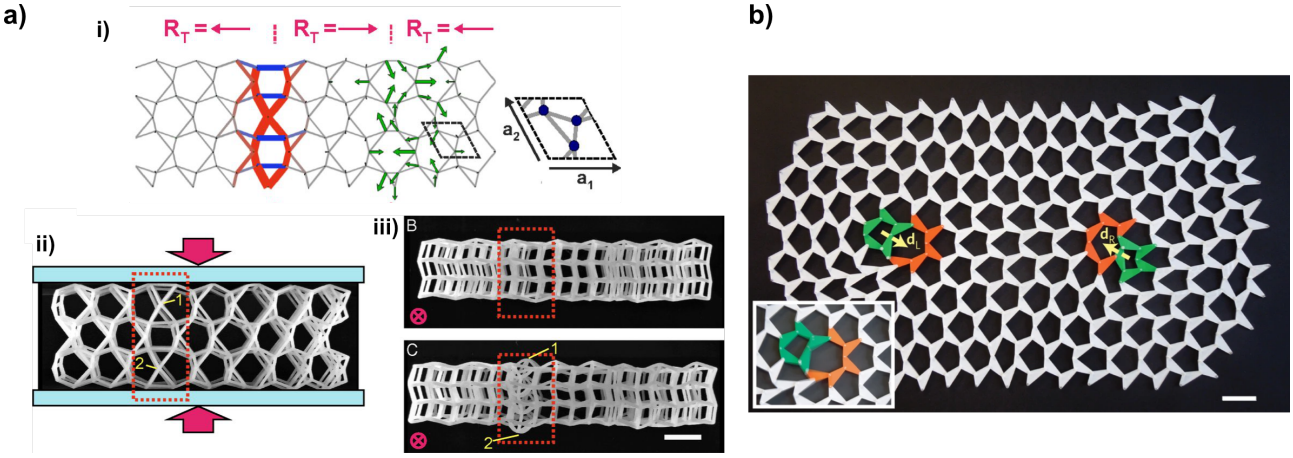


Figure 2.7: *Topological metamaterial examples. a) i) Localised states of self stress in a Kagome lattice. ii) Compression of a 3D topological cellular material. iii) Response to 0% and 20% compression respectively, red box shows self stress region buckling, whereas surrounding lattice structure deforms as expected [48]. b) Deformed Kagome network with two interior dislocations, left dislocation has a topologically protected soft-mode [49]. Images adapted from: Paulose et al. (a) [48], (b) [49].*

2.2.4 Topological

The topological characteristics of a system are of increasing interest to MM development. A topologically protected MM is designed to remain resilient against disorder and noise, maintaining the classical state of the system [50]. This robustness in maintaining the state of a system, such as load-bearing states in the presence of local perturbations, make topological materials exciting for us in programmable and tunable matter. An early example of a topological MM was discovered by studying zero-frequency modes (floppy modes) in a finite Maxwell lattice [51, 52]. Topologically protected states such as floppy modes are concentrated on one side of the lattice and insensitive to local perturbations. Of particular interest to this body of work is the tunable mechanical properties that can be programmed. Research by Paulose [49] shows selective buckling states are designed into an MM by engineering states of self-stress (combinations to tensions and compressions on a beam that result in zero net forces on hinges) within the structure. The study shows by concentrating areas of self-stress in the cellular material, compression of the bulk material results in localised beam buckling in the self-stress sites as shown in Figure 2.7.a. Self-stress topological states are a result of lattice defects and domain wall polarisation, and this drives the localised buckling of the material. In comparison to states of self stress, Paulose also shows for 2D Kagome lattices; topological soft modes can be realised [48]. As shown in Figure 2.7.b, the Kagome lattice has two topological defects (green and orange cells), the leftmost defect is a soft-mode, and the rightmost defect is a self-stress region. The defect sites are equivalent to edge modes placed within the structure of the Kagome lattice. The bulk structure is rigid against deformation; this is also the case in and around the rightmost defect.

However, the structure exhibits zero-energy modes (soft modes), allowing free movement in and around the leftmost defect. Through the positioning of defects and subsequent frustration designed into the structure – topological metamaterials exhibit notably tunable and programmable behaviour.

2.2.5 Combinatorial

Geometric frustration plays a significant role in the functionality of 3D MMs. As shown in previous sections, deliberate frustration between unit cells can lead to novel properties. In section 2.2.4, defects in topological metamaterials allow for states of self stress and zero energy modes [48]. In section 2.2.3, the metastable response of the coupled bow-tie and bistable system leads to frustration caused by opposing forces. This results in a tunable 'springback' response of the auxetic structure [14]. By developing an understanding of the interplay of frustration in architected materials, greater control over the macroscopic mechanical properties is achieved. For example, research by Sung Hoon Kang [53] shows how complex ordered patterns are tunable through geometrically frustrated triangular cellular structures. Square frames can buckle into an energetically favourable configuration through antiferromagnetic ordering. Conversely, triangular frame unit cells display parity conflicts, leading to lattice sites with opposing forces. Through placing a lattice structure of triangular frames under equibiaxial compression, ordered symmetric and chiral patterns are exhibited. These patterns are highly dependent on the porosity of the system and the interplay between geometry and deformation. This shows the tunable behaviour of lattice structures that can be achieved by utilising frustrated states.

The role of frustration in designing MMs is explored in several research papers [54, 55, 56, 57, 58, 59]. Through programming the orientation of individual unit cells that exhibit anisotropic behaviour and frustration-free deformation, complex aperiodic structures are realised. This leads to soft deformation modes with advanced machine-like functionalities, such as textured responses to actuation [58] and multistep shape-changing [60]. MMs' rational design for identifying and generating frustration-free systems is through the Ising model in cooperative phenomena [61, 62]. The model associates two-valued variables often denoted as spins and associates this with every node on a lattice. Through the configurations of all spins, the system interactions can be modelled. For example, an early example of material frustration was identified in crystalline ice, a disordered system. The four protons bonded to an Oxygen ion are in a 'two in, two out' configuration, known to follow the 'ice rule'. In this case, the proton disorder leads to a mismatch in crystal symmetry and subsequently a frustrated system. Ising spin systems and antiferromagnetic ordering are observed in

several MM examples, including the mountain and valley folds in Origami systems and horizontal and vertical ellipses in elastic systems. This design strategy has been employed in several combinatorial MMs to build frustration-free structures or structures with localised stress.

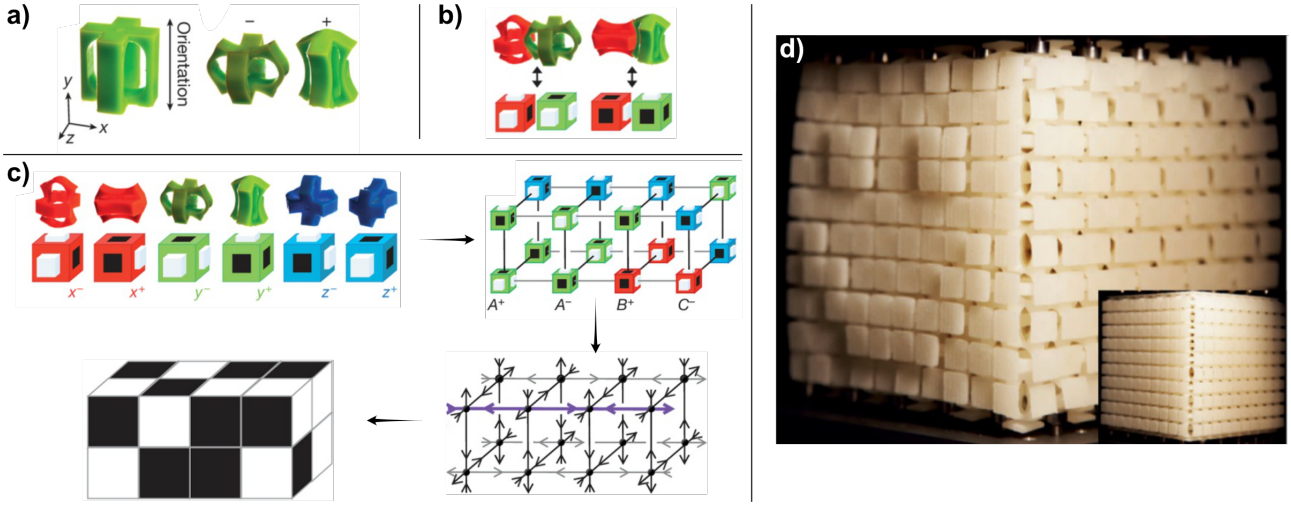


Figure 2.8: *Combinatorial design of textured mechanical metamaterials [58]. a) Unit cell design in negative y^- and positive y^+ spin. b) Combining unit cells through spin parity i.e. (x^-, y^-) & (x^+, y^+). c) Creating textured MM - voxels combine aperidocally, the associated spins ensure parity between connecting pairs, which results in a unique outward surface texture (black and white squares). d) 10×10 metacube showing outward texture of smiley face in response to a textured axial deformation. Images adapted from Coulais et al. [58].*

Voxelated mechanical metamaterials are a 3D design strategy of 'tiling' with the ice rule to construct aperiodic frustration-free structures such as the 'Metacube' proposed by Coulais *et al.* [58]. As shown in Figure 2.8, the asymmetric unit cell has a positive and negative spin resulting in an expansion and contraction along the y-axis, respectively. Because of the 3D nature of asymmetric unit cells, the central axis can be orientated in three different polarisations, x, y, & z. Mapping spin configurations to satisfy the ice rule is implemented through a voxel (cube) approach. Polarisation and spin configurations are related to the voxel colour and protrusions (in and out of plane) in response to actuation. The protrusions in and out of plane relate to negative and positive spins, respectively. By mapping using the ice rule, six bonds of each vertex should correspond to a brick configuration. The six bricks, x^-, x^+, y^-, y^+, z^- & z^+ as shown in Figure 2.8.c, correspond to the spin configurations $(\sigma_x, \sigma_y, \sigma_z) = (- + +), (+ - -), (+ - +), (- + -), (+ + -)$ & $(- - +)$, respectively. Through maintaining parity (spin-flip) symmetry between neighbouring voxels, the bricks can be compatibly stacked to build frustration-free systems. The requirement of spin parity results in long-range holographic order, which relates the boundary to the bulk structure. The outward spin configurations can be designed to programme surface texture in response to frustration-free actuation, as shown in Figure 2.8.d in the 'smiley face' Metacube example. As shown, the rational design of 3D aperiodic structures results in significant control over the bulk

material response to mechanical actuation.

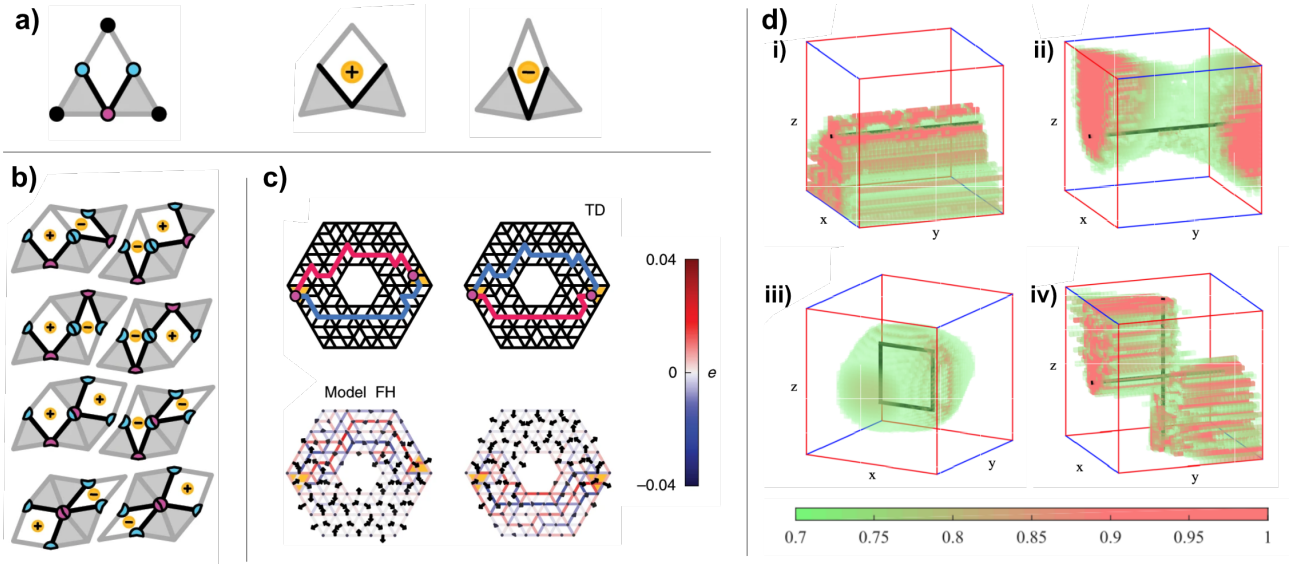


Figure 2.9: *Stress-steering in combinatorial mechanical metamaterials. a) Anisotropic triangular building blocks in positive and negative polarisation. b) Antiferromagnetic and ferromagnetic coupling of unit cells. c) Combinatorial architecture with a topological defect in the excised centre. Blue/red lines indicate ferromagnetic and antiferromagnetic pathways. i) Actuation produces deformation in blue strip and stress in red. ii) Change in actuation position flips stress to upper half (blue) and deformation to lower half (red) [55]. d) Stress concentration along different defect lines produced through frustration in 3D metacube example [56]. Images adapted from: (a-c) Meeussen et al. [55] and (d) Pisanty et al. [56].*

The metacube example shows the programmable nature of frustration-free deformation in MMs. Increasingly, the role of frustration through defects in combinatorial structures is investigated for the ability to steer stress. Meeussen [55] explores the role of topological defects in a combinatorial system. The structure combines 2D anisotropic triangular unit cells (Figure 2.9.a) to build a frustration-free system (Figure 2.9.b). A topological defect is formed by rotating consecutive unit cells up to the edge of the bulk material. The topological defect created results in long-range stress-strain conflicts in the material that cannot be resolved through local design changes. Figure 2.9.c shows the topological defect in the hexagonal MM leads to stiffness steering. Depending on the position of actuation, frustration-free deformation occurs in the upper half (blue line), and large stresses form in the bottom half (red line). As the actuation position is changed, the stiff region and frustration-free regions are flipped. Pisantry [56] explores similar concepts of stress steering and the effects of topological defects on the 3D metacube. Point defects in 2D systems are line defects in 3D structures. This leads to significant stress concentration via the line defects in the metacube design, as shown in Figure 2.9.d. In (i) & (ii), the actuation direction controls where the stress is concentrated in respect to the line defect. In (iii), stress is concentrated within a defect loop, and in (iv), it is concentrated within two quadrants. The examples show significant control and tunability over the material response to actuation because of the rational placement of defects.

2.3 Functional Metamaterials

The research question explored in this thesis is if MM structures can be developed into functional devices. In the previous section 2.2, MMs exhibiting programmable and tunable responses were examined. Although the library of architected materials that exhibit unique properties continues to expand, the development of functional metamaterials lags. This section explores the device-based approach taken to MM design.

2.3.1 Non-Mechanical Stimuli

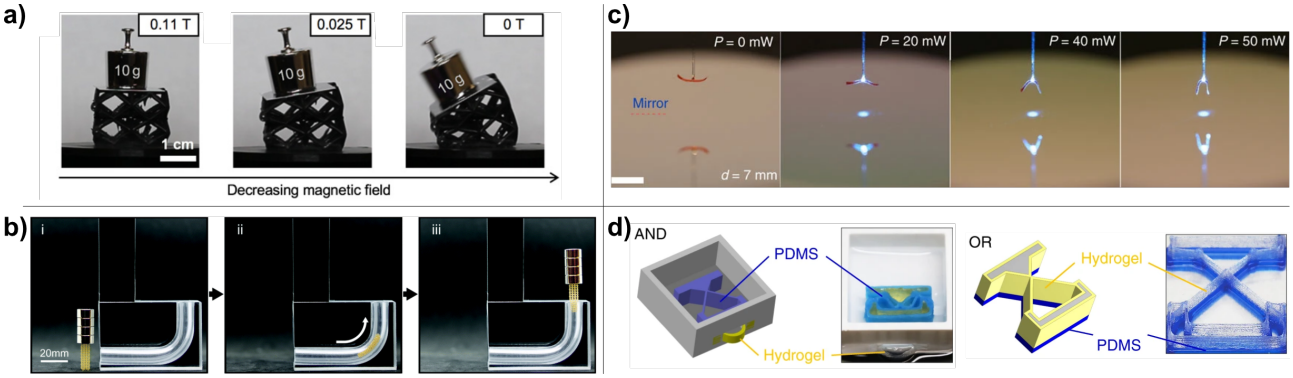


Figure 2.10: *Stimuli responsive materials. a) FRMM - structure consists of polymeric tubes infilled with magnetorheological fluid suspensions. Modulating magnetic field changes the effective stiffness of the structure [63]. b) SMP lattice structure created using digital micro 3D printing. Shape can be programmed through thermal energy. i) Lattice in original shape bearing load. ii) Lattice programmed with a small diameter to fit through channel. iii) Lattice expands to original shape to bear load [64]. c) Micro-gripper modelled on the Venus-fly trap. Laser power inhibits material bending which is used as a gripper [65]. d) Bifurcation based logic - AND gate requires water to open the hydrogel valve, allowing Toluene to enter chamber and cause the unit cell to snap-through. OR gate made of PDMS base layer and hydrogel top layer. Snap-through of unit cell occurs if either Water, Toluene or both solutions are added [66]. Images adapted from: (a) Jackson et al. [63], (b) Yang et al. [64], (c) Wani et al. [65], and (d) Jiang et al. [66].*

In section 2.2, the MMs were designed to respond to mechanical stimuli. Although the research question focuses on mechanical actuation, many MM structures utilise alternative forms of stimuli in addition to material architecture to achieve novel properties. Structures that respond to non-mechanical stimuli exhibit tunable and programmable behaviour [67]. With advancements in material engineering and AM technologies, stimuli-responsive materials, otherwise known as 4D printed materials, has rapidly expanded. 4D printed materials relate to the shape change of an object over time in response to a stimulus. For example, shape memory polymers (SMPs) [68, 69] and shape memory alloys (SMAs) [70] are programmed to transform in response to temperature changes. Although multi-configurable MMs are investigated [60], in most cases, once a MM is manufactured, its properties in response to stimuli remain fixed. Stimuli-responsive materials coupled with material architecture opens the avenue for reprogrammable and tunable material

properties. For example, Field Response Mechanical Metamaterials (FRMMs) [63] as shown in Figure 2.10.a, use a magnetic field to tune the stiffness of the material and subsequently the load-carrying capabilities. Yang [64] develops a similar structure using shape memory polymers, creating micro-4D MM structures whose effective stiffness can be varied over 100 times. The structure has been proposed for use in implantable biomedical microdevices due to the versatility in utilising its 'soft' properties to move through tiny channels and its subsequent increased stiffness in response to thermal stimuli to carry loads (Figure 2.10.b).

Light stimuli can inhibit a snap-through response of bistable arches [71], creating functional devices such as a light-driven Venus flytrap [65]. As shown in Figure 2.10.c, the increasing laser power causes light-induced bending of the SMP, causing the microgripper to close. Hydrogels swell when exposed to water; this response is programmed to build complex three-dimensional morphologies [72, 73, 74]. The microgripper and hydrogel examples achieve their responsiveness via the specific polymer matrix, i.e. fibre alignment, to yield the shape-changing response. By including geometric arrangement in addition to the material response, novel functional materials can be designed. For example, structures created from Polydimethylsiloxane (PDMS)-based materials swell when exposed to non-polar solvents such as Toluene [66]. By designing a structure with slender beams near geometric bifurcation points, a snap-through response to actuation was programmed to perform AND, OR and NAND Boolean logic. As shown in Figure 2.10.d, the OR gate is made of a PDMS base layer and hydrogel top layer. As the materials swell in response to Toluene and water, either of the solutions or both solutions applied to the unit cell will cause a snap-through event. Active materials that respond to non-mechanical forms of energy have many applications as sensors and actuators in soft robotic systems [75, 76, 77]. However, materials that respond to mechanical stimuli are still preferred for use in harsh environments due to their resistance to actuation from all other forms of stimuli.

2.3.2 Mechanical Metamaterials exhibiting Boolean Logic

FMMs are programmable structures that sense a mechanical force and respond per the programmed rules to perform a given function. Many researchers have proposed an avenue into metadevices through the development of Boolean logic gates. Analogous to electronic systems, it is stipulated [78] mechanical Boolean AND, OR & NOT gates can be combined to form complex logic systems. Mechanical logic is an active field of research for 'beyond CMOS' technologies. As Moore's law predicts the scaling of transistor technology to reach its physical limitations, alternative methods of

logic are being explored [79]. Although mechanical logic cannot compete against CMOS on speed and efficiency, the versatility of mechanical logic for use in harsh environments, soft robotics and integrated material systems shows MM logic a relevant consideration for future design.

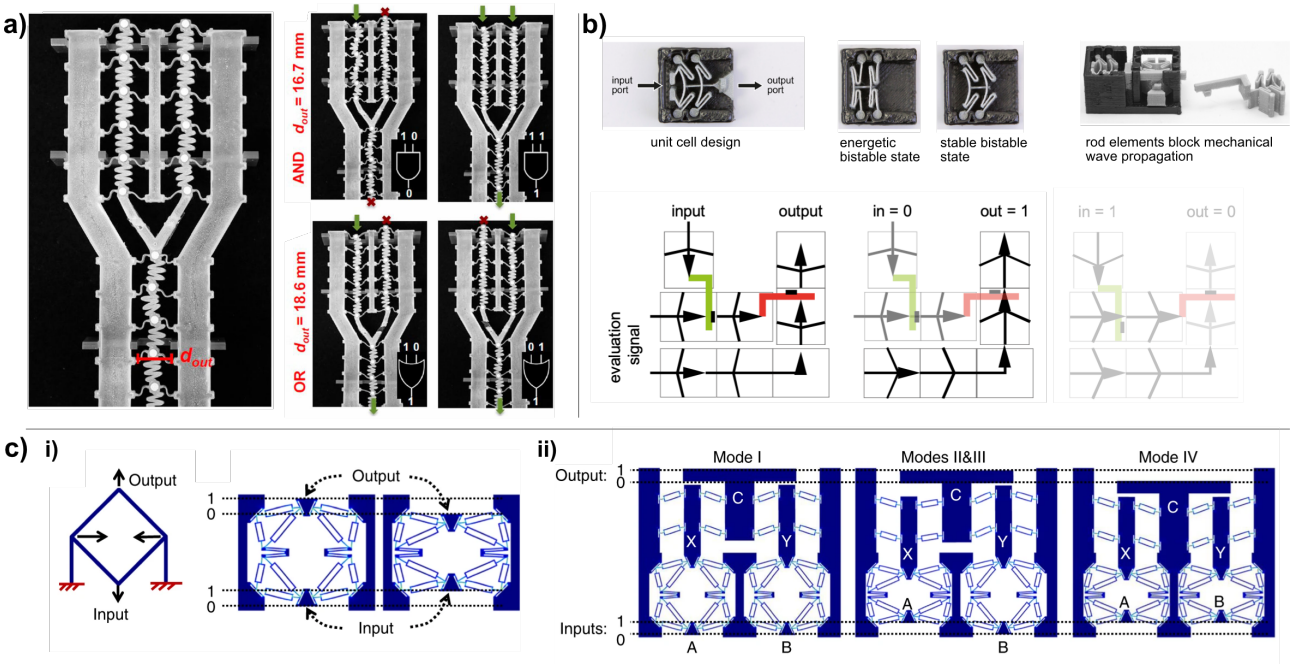


Figure 2.11: *Mechanical logic examples. a) Soft mechanical system exhibiting AND & OR logic. AND gate - bifuricated chains combine, require two inputs to force propagation of mechanical signal. OR gate - kink in bifurcation chain, only one input results in propagation of mechanical signal [80]. Mechanical rod-logic, using leaf-spring bistable unit cells to propagate mechanical signals and rod elements to block signals. System input positions rod elements to block or allow evaluation signals, AND, OR & NOT logic gates are demonstrated [81]. Bistable flexure design, connected inverter (NOT gate) used as system inputs. Mechanical NAND gate shown, state of connected bistable elements determines the position of the central shuttle and the output state [82]. Images adapted from: (a) Raney et al. [80], (b) Ion et al. [81], and (c) Song et al. [82].*

Fundamental to all mechanical logic systems is the control of mechanical instabilities and nonlinear responses of buckled systems to define a logical state [83]. Implementations of mechanical logic include origami mechanologic, pneumatic soft devices, propagating bistable elements, rod logic implementation and shuttle displacement. Figure 2.11 shows three logic systems where a bistable element defines the logic state. Raney *et al.* [80] explores the propagation of mechanical signals in soft media. By connecting tilted beams to a central shuttle of variable stiffness, a bistable element made of elastomeric material is developed. Boolean AND & OR logic are achieved through a bifurcation chain, as shown in Figure 2.11.a. Cascading logic can be achieved, as the output from one logic sequence can drive subsequent gates. However, the proposed OR gate does not fulfil all logic conditions, highlighting the proposed system's restrictions. Ion [81] explores mechanical logic using a rod-logic system. Using FDM printed leaf-spring bistable mechanisms with connecting rods, AND, OR & NOT logic gates are

demonstrated. The input signals position blocking elements (rods) to interfere or allow mechanical signals to pass. An evaluation signal (mechanical wave) comprising of connected bistable elements probes the system; the output is dependent on the position of the blocking rod elements as shown in Figure 2.11.b. The logic implementation is versatile and can theoretically be designed for any functional logic sequence. However, the interfering rod elements and the need for an evaluation signal are akin to moving mechanical components. Frustration results from individual units pushing against one another, not from states of stress in an architected system. Song [82] combines bistable elements with a central shuttle to perform AND, OR & NOT logic as shown in Figure 2.11.c. The mechanical inverter connected to the beam system controls the logic inputs; the central shuttle's position determines the logic state. Using two-photon stereolithography, they successfully demonstrate mechanical logic gates at the micrometre scale. The designs explored are highly planar (actuation and system response occur in the same plane) and do not utilise MMs' added multi-plane capabilities.

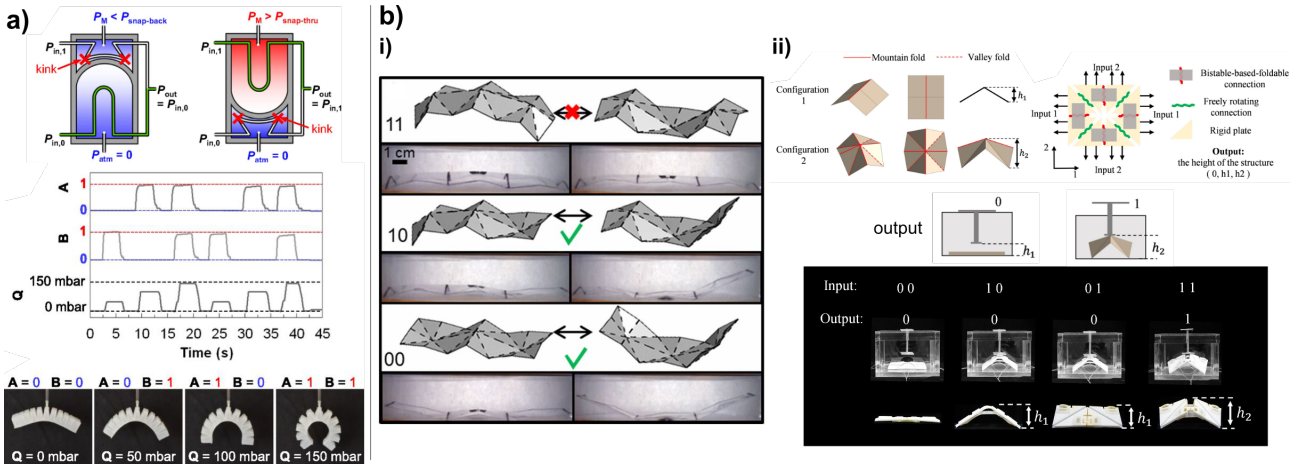


Figure 2.12: *MM logic examples. a) Soft pneumatic digital logic gates using binary high/low input and output pressures and bistable valve to perform logic. Two-bit DAC used to control the degree of closure of a pneu-net gripper [84]. b) Origami logic examples. i) Connected waterbomb origami units. Changes in humidity (input signal) can be used to change the state of the central waterbomb unit. Example shows structure used as a NAND gate [85]. ii) Folding pattern of a waterbomb origami unit determines the output height. Example shows structure used as an AND gate [86]. Images adapted from: (a) Preston et al. [84], (b.i) Treml et al. [85], and (b.ii) Meng et al. [86].*

Morphological computation (MC) describes the material architecture's deformation to perform logic, synonymous with MM systems. The metadevices explored in Figure 2.11 seldom showed full use of this concept. The logic examples showed interconnected mechanical parts instead of a single coherent piece of architected material. Recent studies have shown mechanical logic systems that better embody the design ideas of MC [84, 85, 86]. Preston *et al.* [84] proposes a soft pneumatic logic gate that controls airflow through the structure using bistable valves. The pressure differential between chambers in the membrane defines the valve position and the resulting airflow, AND, OR & NOT

gates are successfully demonstrated. Also, multiple soft logic gates can be arranged synergistically for different applications. For example, Figure 2.12.a shows a digital to analogue converter (DAC) used to control a robotic gripper's motion. The soft structure results in conformal logic gates in soft robots, and the bistable section is directly connected to the outer membrane, making this example suitable for MMs. Figure 2.12.b shows mechanical logic using Origami structures. Treml *et al.* and Meng *et al.* show mechanical logic based on an origami waterbomb design. Meng [86] shows mechanical logic can be achieved from the folding sequence of origami waterbomb structures. The resulting height change is defined as a change of logic state (Figure 2.12.b.ii). Treml [85] proposes an origami structure that connects bistable folds to a central waterbomb structure. The structure has a layer of material that responds to changes in humidity to inhibit buckling. As shown in Figure 2.12.b.i, the snap-through response of the adjacent bistable units (input) affects the end state of the waterbomb (output). This can be used to develop larger logic systems such as a 4-input Boolean device. The mechanisms explored are synonymous with the architected materials in Section 2.2; thus, the implemented logic is easily integrated into the bulk structure of the metamaterial. The literature on the development of MM logic mechanisms is still limited and continues to be an area of future focus in functional material development.

2.3.3 Industrial Applications

An objective highlighted in several review papers is the need to shift MMs' development to an applications based approach. These reviewers argue that the focus until now has been on the novel properties and tunable functionalities afforded through architected materials (Section 2.2). However, these structures have yet to disrupt traditional engineering fields such as aerospace and automotive. This is because of the limitations in AM printed structures' metallurgic properties and the lack of technical considerations of MMs, such as in field fatigue behaviour and fracture toughness in external environments. Although this view is rapidly changing, many industries still view AM manufacturing as a prototyping and modelling tool, seldom used for functional end-use parts. The adoption of MMs ties closely to the continued adoption of AM technologies for functional engineering materials.

There are, however, several examples of MMs finding their way into industry, often through the use of traditional manufacturing instead of AM. For example, Origami based MMs have been used in the aerospace industry as deployable solar cells for many years [41]; this field continues to flourish through novel Origami & Kirigami architectures [87]. More recently, the footwear industry has increased the exposure of 3D printing in retail with architected midsoles trainers [88], and explored novel midsoles

such as Origami-inspired no-lace trainers to help individuals with dexterity impairment [89]. Although MMs are beginning to find breakthroughs in particular fields, it has seldom shown complete adoption in engineering applications.

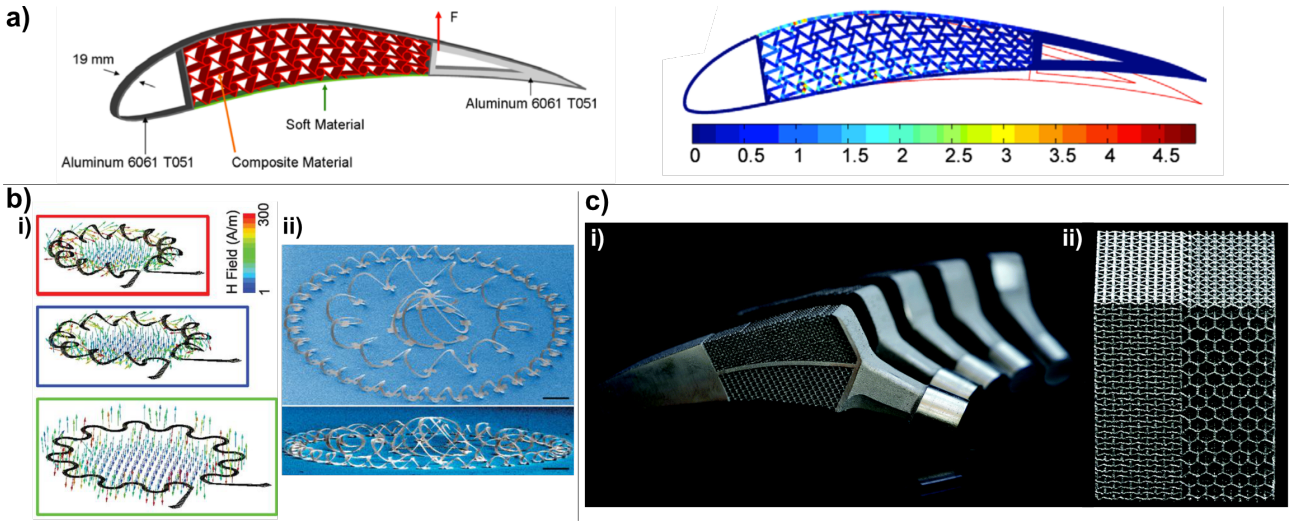


Figure 2.13: *Mechanical metamaterial industrial applications. a) Aerofoil design with a composite auxetic chiral core. Structure can undergo large deformations with limited straining [90]. b) 3D architectures of device-grade silicon by compressive buckling. i) Tunable 3D toroidal inductor under no compression (2D structure - green), 54% pre-strain release (blue) and complete release of pre-strain (red). ii) SEM image of 3D mesostructure - closed-loop circular filamentary serpentines and radially oriented ribbons [91]. c) Meta-implant design, combining negative and positive Poisson ratio materials for improved implant-bone contact. ii) Structure consists of bow-tie auxetic structure (left) and conventional hexagonal honeycomb lattice (right). Meta-implant made of Ti-6Al-4V alloy using SLM manufacturing process [92]. Images adapted from: (a) Bettini et al. [90], (b) Xu et al. [91], and (c) Kolken et al. [92].*

Several proposed MM applications are found in literature; however, they have yet to be utilised in industry. In soft robotics [42], the deformable nature of MMs has particular uses as a locomotion mechanism. For example, using auxetic [93] and Kirigami [94] MMs for motion. Additionally, artificial muscles using 'textuators' [95], fabricated through knitting and weaving of electroactive polymers, show the application of novel materials and structures to develop flexible actuators. In the aerospace industry, composite chiral structures by assembling thin carbon/epoxy or glass/epoxy composite laminates are proposed for use as morphing aerofoils [27, 90]. The chiral core aerofoil structure, shown in Figure 2.13.a, allows for large deformations with relatively small strains. The continuous deformations offered by morphing aerofoils is anticipated to eliminate the need for flap-type mechanisms. MM structures are expected to play an increasing role in electronics. Chen *et al.* proposes a tileable MM with stable memory at the unit cell level through switching bistable states using magnetic actuation [96]. The MM is reprogrammable and analogous to read and write hard disk drives. 3D functional electronics through Origami and Kirigami inspired structures have been demonstrated [97]. The assembly of micro/nanomaterials into complex functional structures

through compressive buckling has been proposed for several applications. For example, near field communication devices (NFC), stretchable soft electronics, mechanical resonators and in bioMEMSs sensors [98]. Figure 2.13.b shows a mechanically tunable conductor based on a 3D toroidal structure [91]. The frequency dependence of the inductance can be tuned through the pre-strain release of the mesostructure architectures. Finally, MMs have been explored for several uses in the biomedical industry (meta-biomaterials). Maggi *et al.* [99] proposes a 3D nano-architected cellular structure with tunable stiffness made of OrmoCorp, a UV curable and biocompatible hybrid polymer. When the scaffold stiffness is similar to that of bone cartilage, optimal cell growth occurs for new synthetic bone graft materials. Gatt *et al.* [100] propose a hierarchical auxetic structure based on rotating rigid units as first described in Section 2.2.1 for use as stents and skin grafts. Finally, Kolken *et al.* [92] proposes hybrid implants (meta-implants) with distributed values of negative and positive Poissons rations to create compression on either side of the meta-implant. As a result, the meta-biomaterials are proposed for use as hip stems (Figure 2.13.c) in total hip replacement surgery for improved implant-bone contact.

2.4 Summary

In Summary, the literature review covers MMs' main design principles and highlights the programmable and tunable nature. The main constituents of MMs are elements (n=2) that utilise (1) localised bending, (2) buckling and (3) bistability. The rational design of MMs lead to programmable and tunable; auxetic, Origami & Kirigami, multistable, topologically protected and combinatorial materials. Section 2.3 covered the research on functional materials focusing on MM development. Structures that are programmed to non-mechanical stimuli to exhibit shape changes are reviewed. Mechanical Boolean logic using MMs for MC are investigated. Finally, current industrial applications such as chiral aerofoils in aerospace and meta-implant designs for the biomedical industry are examined. Although these novel structures offer unique capabilities, a device based approach to mechanical metamaterial design has seldom been explored.

MMs' functional capabilities and the subsequent development of mechanical 'metadevices' were limited throughout the literature. In Section 2.3.2, MMs exhibiting Boolean logic were investigated. The designs examined had input-output signals in the same plane, limiting the computation capabilities of morphable structures. Studies that did show MC exhibited limited combinatorial capabilities, which is viewed as necessary to construct complex logic systems. Furthermore, Section

2.3.3 explored MMs use in industry. In particular, auxetic structures are shown in several examples due to their novel mechanical properties under deformation. However, there remains a disparity between these systems and materials that *sense-decide-respond* to actuation logically.

Although programmable and tunable MMs have been explored throughout the review, the limitations as functional 3D structures that *sense-decide-respond* have yet to be fully explored. Regarding the research problem, the current limitations on 3D FMMs will be addressed by exploring combinatorial MMs. This is because of the greater design capabilities in aperiodic structures and the ease in implementing the 'metadevice' in larger deformable structures such as the chiral aerofoils and meta-implant designs. This research hopes to shift the paradigm of metamaterial development from fundamental research to application-based design. The design approach is hoped to yield multi-plane FMMs that exhibit programmable and tunable behaviour that easily implement into lattice-based materials for industrial applications.

Chapter 3

Manufacturing

The manufacturing chapter provides a brief overview of the different types of AM technologies. Material Jetting, Vat Polymerisation (SLA) and Fused Deposition Modelling (FDM) are evaluated in greater detail. These printing technologies are used throughout this project to manufacture the proposed MM. Material Jetting is evaluated for its multi-material printing capabilities and digital materials, offering control over the material properties. SLA and FDM are evaluated for their use in compliant mechanisms. FDM printed compliant mechanisms provide a predictable flexural response and fatigue resistance. However, designs are limited to planar configurations due to their anisotropic nature. When printing 3D unit cells, FDM parts had little resistance to brittle fracture in one of the three-axis. In comparison, SLA printed components provided predictable flexural response and fracture resistance in all three axes. The development of Polypropylene-like materials and homogenous printed parts make SLA a suitable AM technology for compliant mechanisms. The chapter describes the entire MM manufacturing workflow, the chosen AM technology, the materials used, design limitations and post-processing.

3.1 Manufacturing Overview

Conventional manufacturing techniques can be categorised into three main groups, formative, subtractive and additive. A formative manufacturing process such as casting or stamping, and forging utilise heat and pressure to mould (cast) or press and pull (stamp and forge) material into the desired shape. This process offers superior control over the material properties, as grain structure can be controlled in the heating and forging process to tune material behaviour, such as fracture resistance. Subtractive processes such as CNC-milling employ rotating multipoint cutting tools to remove material from a solid block to form the desired shape. The subtractive manufacturing process enables tight tolerances on traditionally challenging materials, such as hard metals. More recently, manufacturing processes such as Mirco-EDM (Electrical Discharge Machining) subtract material by creating a highly localised plasma channel, melting and evaporating material due to electrical discharge from an electrode. Micro-EDM can create microelectrode array structures with minimum feature sizes of $10\mu m$ [101]. In contrast to subtractive processes, Additive Manufacturing (AM) builds the desired shape through a layer by layer additive process. Although this technique limits control over the material properties at the microstructure level, the additive process allows for geometrical control. AM provides the geometric freedom limited in subtractive and formative manufacturing techniques.

The complex geometries attainable through AM has been a driving force in the research and development of MMs over the past decade. As shown in Chapter 2, the unique phenomena exhibited in MMs due to novel structuring is made possible only through the enabling technology of AM. AM is viewed as a disruptive technology in many industries as shown in Figure 3.1 [102]. As the precision in manufacturing components and control of material properties improve, the global market of AM is predicted to increase substantially in the next decade. AM is anticipated to play a significant role in the automotive and aerospace industry, in addition to previous uses such as prototyping and education. The novel structures attainable through different AM processes allows 3D printed products to gain significant advantages over traditional manufacturing techniques. Topology optimisation is often utilised to reduce material consumption of AM parts whilst maintaining mechanical strength. This is evident in the additively manufactured titanium brackets for the Airbus AW350 XWB [103]. The printed brackets were 30% lighter and reduced manufacturing time by ∼75%. The novel geometry and light-weighting were utilised in NASA's Mars Perseverance Rover, which carries 11 metal printed parts [104]. AM is also finding uses in footwear, utilising Digital Light Synthesis to manufacture lattice

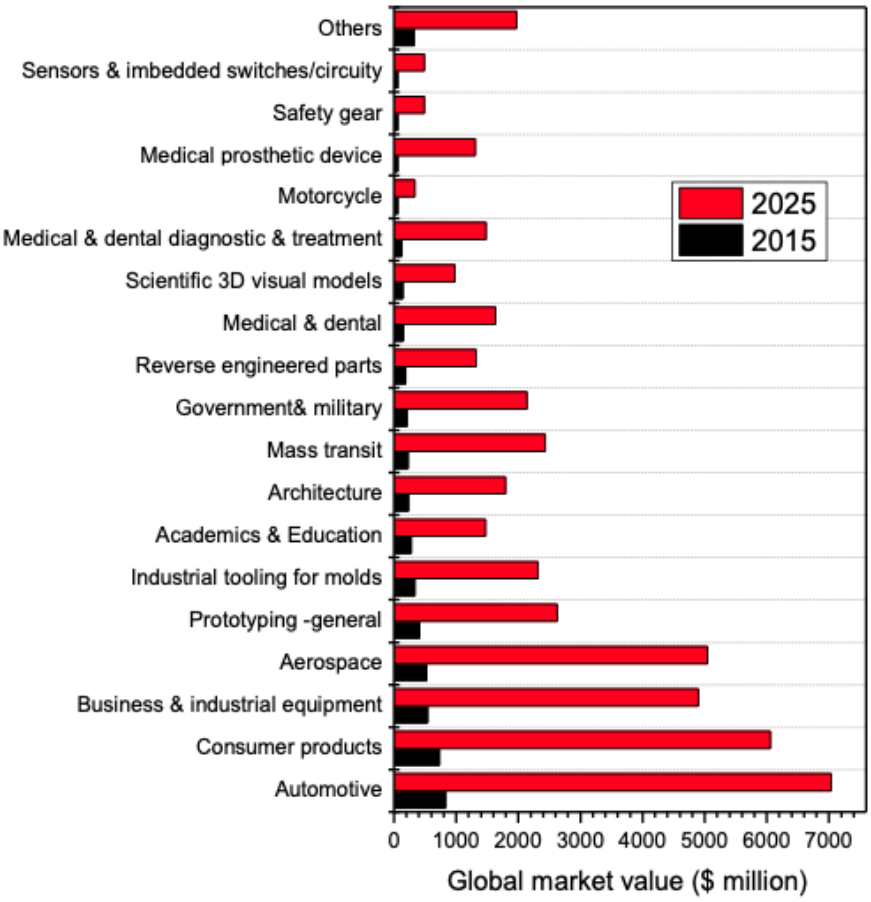


Figure 3.1: *Projected global industrial AM market by application from 2015 to 2025. Graph adapted from Myant and Wu [102].*

midsoles at improved speeds. 3D printing allows for functionally graded materials and structures, paving the way for mass customisation of shoes. AM is increasingly being developed and considered in the medical field. In addition to the developing uses in pharmaceuticals, stimuli-responsive printed structures are being considered for surgery and MM structures for prosthetic implants. For example, a hybrid meta implant structure comprising auxetic and conventional architectures manufactured using Selective Laser Melting (SLM) [92]. The printed structures exhibit desirable loading properties, finding applications as hip stems for improved implant-bone contact and longevity.

3.2 Printing Technologies

Driven by the continual advancements in AM technologies and materials for engineering use, functional materials and programmable structures are anticipated to play an increasing role in the automotive, aerospace, and medical field. Novel functionality gained from MM structures results in part consolidation, light-weighting, improved sensor capabilities and ease of tuning designs for specific uses and environments. The need to develop functional capabilities of AM printed mechanisms for a rapidly expanding manufacturing market is a driving force in investigating the research proposal. As a result, the novel 3D structures explored in forthcoming chapters utilise AM techniques over subtractive and formative manufacturing methods.

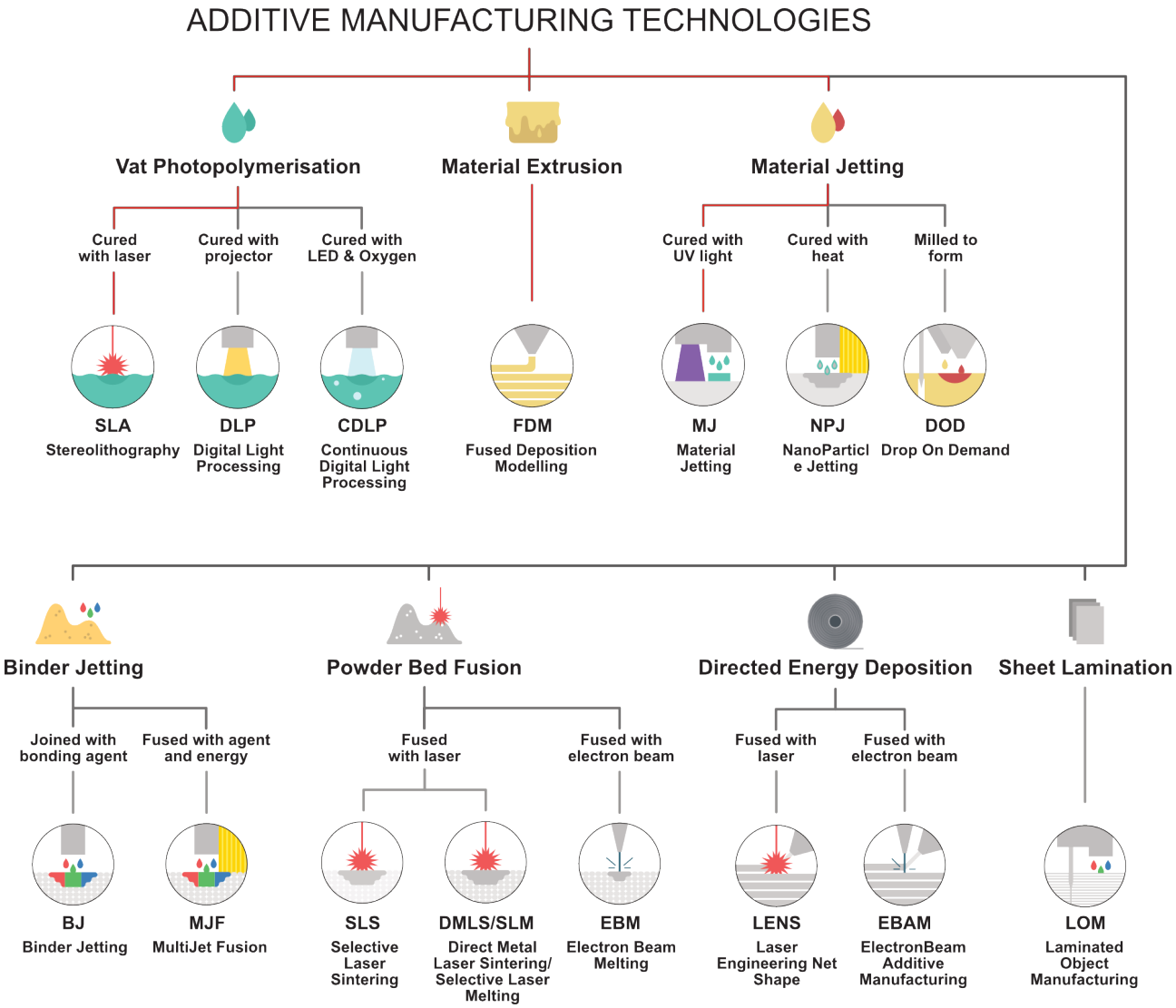


Figure 3.2: *Overview of Additive Manufacturing technologies. Red line indicates technologies used in the research. Schematic is adapted from Hubs [105, 106].*

The schematic in Figure 3.2 highlights the different AM technologies and categorises each under a specific additive process. These processes are classified under the ISO/ASTM-52900 standard. The red connecting lines indicate the specific technologies used for this research. A detailed description of Vat Polymerisation, Material Extrusion and Material Jetting is followed in later sections. The remaining processes: Binder Jetting, Powder Bed Fusion, Directed Energy Deposition and Sheet Lamination, are not used due to their limitations as functional components [106]. Sheet lamination is an additive process using paper sheets cut and bonded using adhesive in a cross-hatched configuration to build objects for visual models instead of structural use. Binder jetting is a process using liquid bonding agents deposited on a powder bed to bind powder particles together into a solid part. After each printed layer, a new layer of powder is coated over the print bed. The material options for Binder Jetting are limited to sand and metal. Though complex geometries are achieved, in the case of metal-bound parts, the mechanical properties are limited for functional applications compared to alternative processes. Directed Energy Deposition (DED) is similar to a material extrusion technique, where the material is deposited from a nozzle onto an existing surface. The material is often in wire or powder form and melted using a: laser, electron beam or plasma arc upon deposition. This technique is used with metals to create or repair features on an existing object. However, it is still limited in constructing architected structures.

Powder Bed Fusion is a versatile printing process that can create functional industry-standard parts as a polymer or metal [106]. Selective Laser Sintering (SLS) is the technology used for polymers, fusing polymer powders using a CO_2 laser. The laser heats the powder to just below the melting point, allowing the particles to fuse mechanically and create a solid part. Direct Metal Laser Sintering (DMLS) works by heating to a point the powders fuse on a molecular level. Selective Laser Melting (SLM), on the other hand, melts the metal powder forming a melt pool; this allows for a homogeneous final part. In the SLS process, the powder in the printing chamber acts as support, allowing greater geometric freedom. DMLS and SLM are fused onto a printing bed and require additional support material during the printing process. The range of materials and dimensional accuracy make Powder Bed Fusion a favourable option for industry-standard functional parts. DMLS/SLM parts are widely used for dental, medical, aerospace and automotive applications where weight reduction and complex geometries are realised in high-performance metals such as Titanium. Functional materials from MM are a result of the elastic and flexural properties gained from the material properties and unit cell design. Although SLS can build Polypropylene (PP) like structures with similar flexural responses to function as living hinges, material jetting and SLA offer greater design flexibility and material options.

3.3 Material Jetting

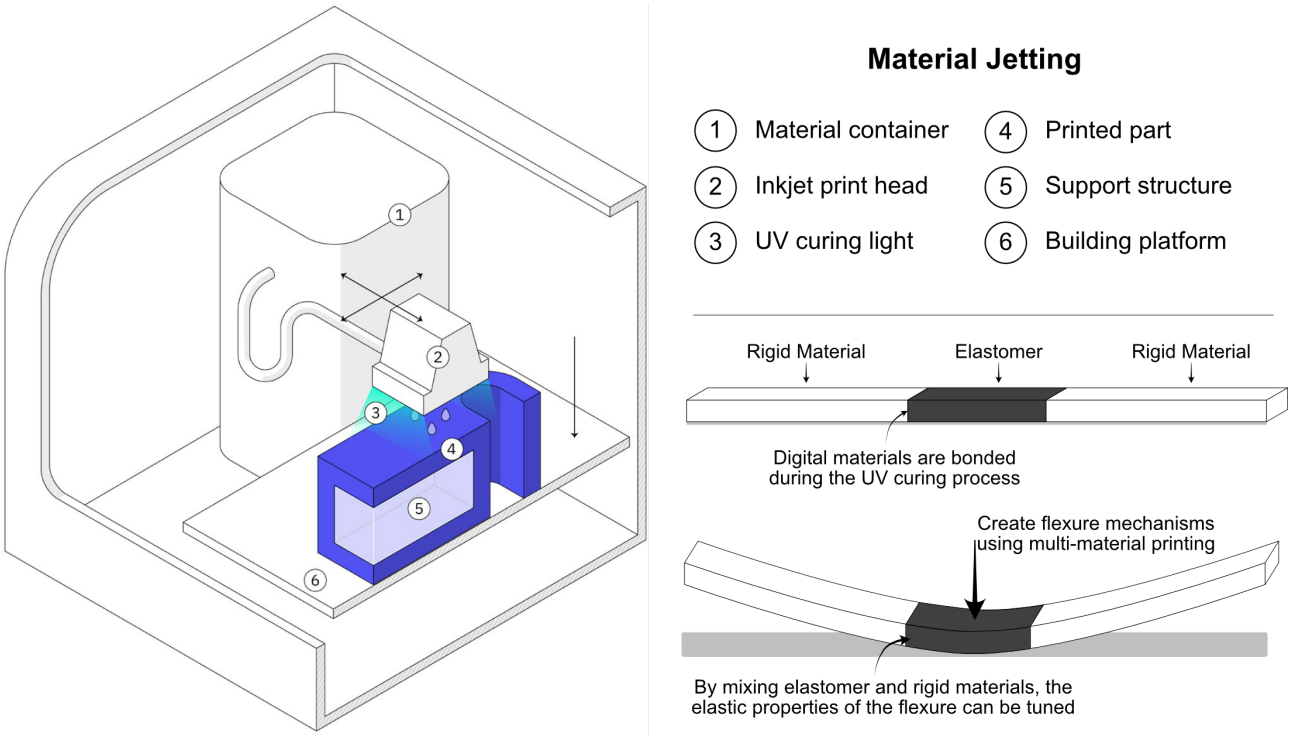


Figure 3.3: *Schematic of Material Jetting AM technology adapted from Hubs [105]. Photopolymer is cured using UV light. Dark purple (4) indicates build materials, light purple (5) indicates support. Beam schematic shows the multi-material capabilities of Material Jetting for flexure design.*

The process of Material Jetting (PolyJet) for AM is very similar to inkjet printing technology. Whereas inkjet printers deposit droplets of ink onto a paper substrate, the AM process jets photopolymer droplets in a continuous line deposition pattern onto a printing bed. The photopolymer is cured via UV light, solidifying the layer. This process is repeated layer by layer to build the final part. A schematic of the AM process is shown in Figure 3.3.a. In all Material Jetting technologies, support material is required throughout the printing process, deposited simultaneously with the build materials. Unlike Vat Polymerisation and Material Extrusion technologies that require support material in overhanging areas, Material Jetting requires the use of support material on any section with a gradient from the vertical axis. Although this allows for complete geometric freedom of the printed part, a significant amount of support material is used, requiring removal of support in hard to reach areas.

PolyJet offers superior surface finish, dimensional accuracy and geometric freedom to alternative AM technologies. Moreover, multi-material printing capabilities make this process suitable for manufacturing functional materials. PolyJet uses thermoset photopolymer resins to print parts. The resin is heated during the printing process to lower the viscosity and allow jetting in droplet form.

Multiple nozzles are utilised to precisely deposit resin. Different photopolymers can be used during the printing process, creating multi-material components with well-bonded sections. As shown in the schematic in Figure 3.3.b, the printed beam has an elastic middle region functioning as a pivot joint. More recently, PolyJet printers utilise the jetting technique to blend resin concentrations when deposited to control the material properties. Known as Digital Materials (DM), materials can be composed that blend flexible and rigid photopolymers. This creates the ability to tune the elastic properties in specific areas. The additional control offered by DMs improve the programmable capabilities of MMs and the functional uses.

3.3.1 Materials Properties

Table 3.1: *Mechanical properties of Stratasys VeroWhite [107], VeroClear [108] and PMMA (V826 Acrylic) [109].*

Property	ASTM	Units	VeroWhite	VeroClear	PMMA
Tensile Strength	D-638-03	MPa	50-65	50-65	70.3
Modulus of Elasticity	D-638-04	GPa	2.0-3.0	2.0-3.0	3.1
Elongation at break	D-638-05	%	10-25	10-25	6

Table 3.2: *Mechanical properties of Stratasys Agilus30 [110], DM-FLX9950 [111], DM-FLX9960 [111] and Natural Rubber (NRQX50) [112].*

Property	ASTM	Units	Agilus30	FLX9950	FLX9960	Natural Rubber (NR)
Tensile Strength	D-412	MPa	2.4-3.1	1.9-3.0	2.5-4.0	12.8-15.0
Elongation at break	D-412	%	220-270	95-110	75-85	425-500
Shore hardness (A)	D-2240	Scale A	30-35	45-50	57-63	50-54
Tensile tear resistance	D-624	Kg/cm	4.0-7.0	7.5-9.5	11.0-13.0	N/A

MM test specimens were manufactured on the Stratasys Connex 3 Objet500 PolyJet printer. The printer was selected because of the large print bed area ($490mm$ x $390mm$) and the ability to have three different materials loaded into the machine. The Objet500 has an $x/y/z$ build resolution of 600/600/1600 dpi, respectively. This equates to a minimum feature size of $40\mu m$ in the xy plane and a layer height of $30\mu m$. Although $40\mu m$ is the quoted minimum feature size, the minimum free-standing wall thickness whilst ensuring dimensional accuracy is $400\mu m$ [113]. This is because of the jetting process, where the photopolymer droplets impact the build platform. The loss of control during impact causes the droplets to spread out, resulting in loss of accuracy when printing thin

features. The printer is loaded with Stratasys VeroWhite (opaque-rigid), VeroClear (transparent-rigid) and Agilus30 (elastic), mechanical properties of these materials can be found in Tables 3.1 & 3.2 respectively. VeroWhite and VeroClear are rigid polymers similar in properties to PMMA. The multi-material flexure design for the MM focuses on the pivot movement from the elastic elements. As a result, the stresses on the rigid beams (VeroWhite) are kept low compared to the yield strength of the Vero plastics. Agilus30 is a viscoelastic photopolymer designed to exhibit rubber-like mechanical properties. It is designed to be durable and tear-resistant to repeated flexing and bending with a Shore A hardness of 30. The proposed MM test specimens utilise two DMs, FLX9950 and FLX9960, with a Shore A hardness of 50 and 60, respectively. The base resin of Agilus30 is mixed with VeroClear to increase the rigidity of the printed material. The material properties of Agilus30 and the corresponding DMs are shown in Table 3.2. The challenge of AM technologies to obtain similar material properties to their natural counterparts is evident in the significant differences between Agilus30 and Natural Rubber.

3.3.2 Printing Setup

The schematic in Figure 3.4 shows the manufacturing setup for the MM. Due to the change in unit cell (yellow region) orientation between different designs, maintaining the same print direction between prints is not feasible. Although the literature on the isotropy of PolyJet printed parts is limited, research points towards materials being transversely isotropic [114, 115]. The mechanical properties do not vary when printed along the x-y plane (isotropic) but vary significantly when printed along the z-axis (anisotropic). As the central bistable system (blue region) requires slender beams, orientating the bistable system along the y-axis ensures consistency between prints, as shown in Figure 3.4.a. Additionally, printing the beams in the x-y plane ensures dimensional accuracy, superior surface finish, and reduced support material. As shown in Figure 3.4.b, when the bistable system is printed in a z-axis orientation, stepping along the edge of the beam occurs. The part is printed in an assembly of four separate STL files and printed with two different finishing settings for the unit cells and the bistable system. The STLs are imported as an assembly into the Objet Studio slicing software (Version 9.2.11.6825). The unit cells are printed in matte to ensure consistency between prints because printing in glossy results in different finishes depending on unit cell orientation. The central bistable system is printed in glossy as the orientation between prints remains unchanged. Moreover, glossy finishes are recommended for slender beams due to their smooth surface, as matte finishes on thin-walled structures result in weakness due to increased stress risers.

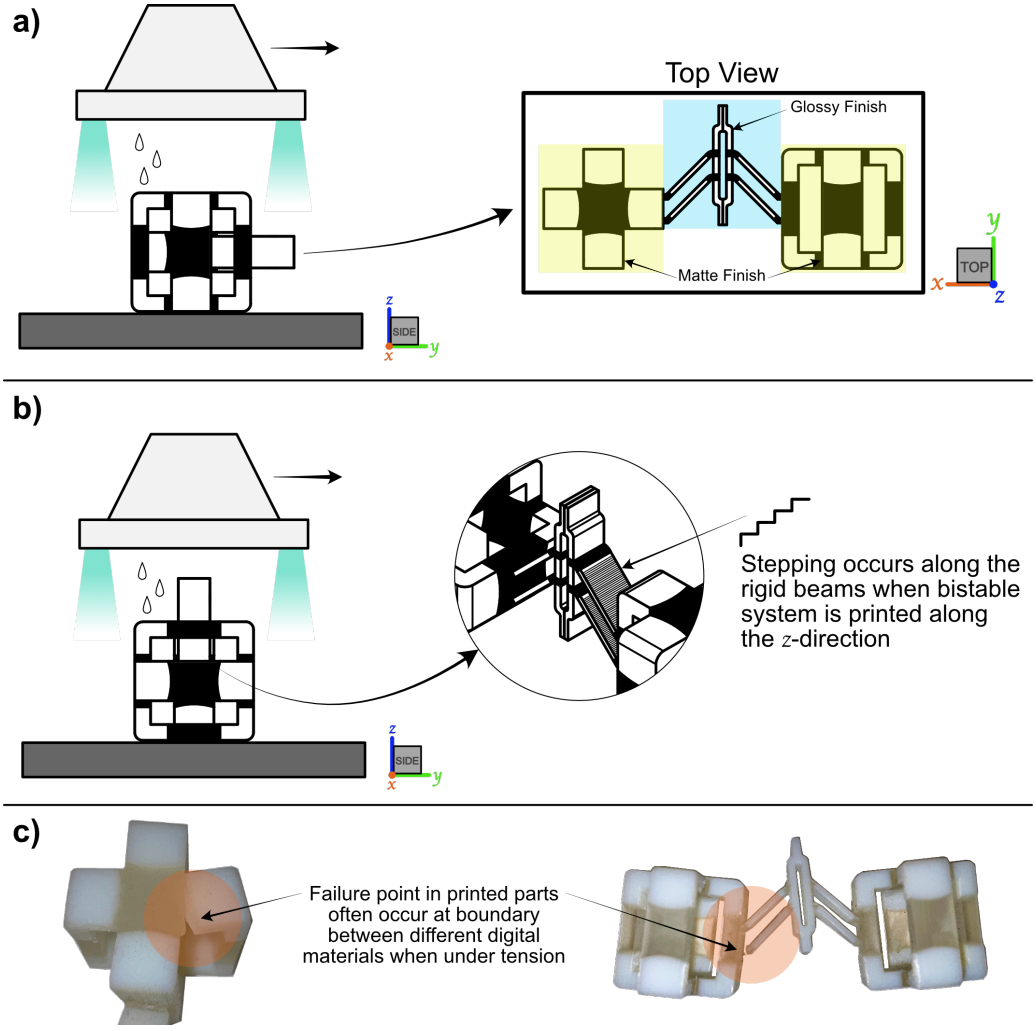


Figure 3.4: *a) Correct orientation of MM when PolyJet printed. The bistable system is along the y-axis. Insert shows a top view of the MM, yellow sections show areas with a matte finish. Blue section shows areas with a glossy finish. b) Incorrect printing orientation of MM when PolyJet printed. The bistable system is along the z-axis. Insert shows stepping along the rigid section of the beam. c) Failure points of the MM during testing, fracture often occurred at the boundaries between different DMs.*

Multiple post-processing techniques are utilised to remove support material from the printed part. Stratasys SUP706 dissolvable support is used for the printed part. Once the part is taken off the print bed, the support material is first manually removed from the larger supported sections using a spatula. Due to the 3D unit cell design and thin-walled bistable system, not all support can be manually removed. A water jet-wash (Balco UK - Powerblast (20-120 bar)) removes the remaining support from inside the unit cells. Care must be taken in ensuring the high-pressure jet does not come into contact with the delicate thin beams. The part is then dissolved in a 2L ultrasonic bath (EMAG AG-Germany - Emmi 30) with a caustic solution of Sodium Hydroxide (2%) (WaterWorks - P400SC) and Sodium Metasilicate (1%) (Aldrich - 307815) to dissolve the remaining support around the beams. Due to the thin-walled features, the printed part is limited to ∼15 minutes in the caustic solution to ensure no adverse effects on the stiffness of the beam. Finally, the part is gently washed

and left to dry before testing.

The images in Figure 3.4.c show some of the main issues when using Material Jetting for functional materials. Although PolyJet printing offers improved accuracy and multi-material capabilities, the printed materials are brittle and prone to fracture. Furthermore, as shown in the images, the main failure point during testing was a material fracture at the joints between different DMs. This is likely due to reduced cross-linking between polymer chains of different DMs during the curing process. The unit cell often failed from repeated actuation along the z-axis, causing a fracture between the connecting VeroWhite and FLX9950 sections. A more common failure point of the MM occurred at the connecting interfaces with the thin-walled elastic elements. During a snap-through event which will be discussed further in Chapter 4, the thin elastic elements (FLX9960) break from the connecting unit cell (FLX9950) or the centre shuttle (VeroWhite). Although suitable for prototyping and proof of concept, PolyJet printed parts are limited in their capabilities as functional materials due to fatigue limitations in repeated use.

3.4 Vat Polymerisation

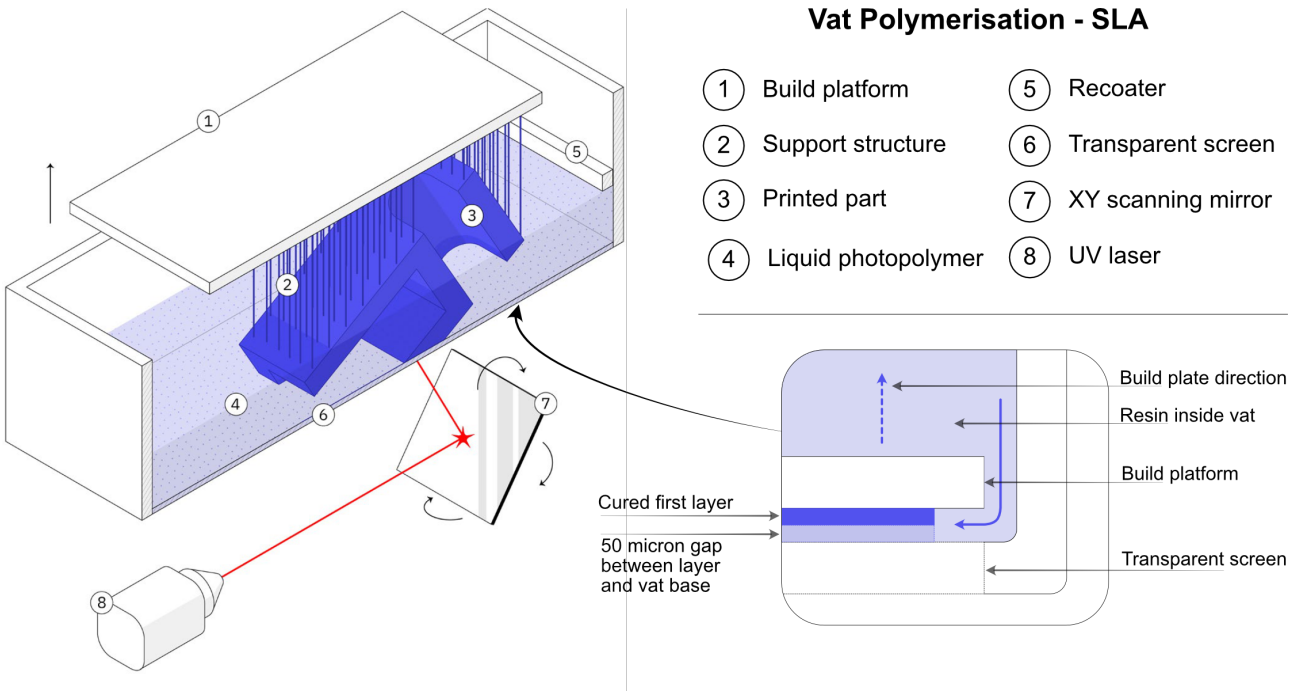


Figure 3.5: *Schematic of Stereolithography (SLA) AM technology adapted from Hubs [105]. Photopolymer is cured using UV laser. Dark purple (2 & 3) indicates solid cured layers, light purple (4) indicates uncured liquid photopolymer. Insert shows in detail printing process closer to the transparent vat screen.*

Stereolithography (SLA) is a Vat Polymerisation process and the earliest developed 3D printing technique. It uses UV solid-state lasers to polymerise viscous light-reactive thermoset resins. The UV wavelength ($405nm$) joins together short molecular chains, polymerising monomers and oligomers to create solid geometries [116]. Galvanometers are used to reflect the UV laser, as shown in Figure 3.5. They map out the desired printing shape by tilting a mirror in the xyz direction. The example in Figure 3.5 shows a bottom-up SLA approach; the light source points up from below a transparent window at the base of the resin vat. The build plate is lowered to leave a gap of uncured resin between the vat base and build platform; this gap defines the layer height of the print. The laser cures the resin between this gap, causing the thin printed layer to stick to the build platform. A coated soft PDMS layer stops the printed layer from sticking to the vat window. Once the layer is cured, a separation step occurs, lifting the build platform. The build platform is lowered for the next layer, maintaining the defined layer height between the previously printed layer and the platform base.

SLA printing offers smooth surface finishes, high accuracy and can print fine details, limited only by the laser spot size ($140\mu m$). It is often considered a technology suitable for visual prototyping, with limited mechanical properties to replicate industry grade materials. Recently, there have been

significant developments in engineering resins suitable for functional applications, a previous limitation in Vat Polymerisation. These include flexible, tough, durable and high-temperature materials. As a result, SLA printing is considered a suitable AM technology to manufacture MMs.

3.4.1 Material Properties

Table 3.3: *Mechanical properties of Formlabs Durable [117] and Tough1500 resin post cured [118], and Natural Polypropoylene (PP) [119].*

Property	ASTM	Units	Durable	Tough1500	PP
Tensile Strength	D-638	MPa	28	33	33.1
Tensile Modulus	D-638	GPa	1.0	1.5	1.31
Elongation at break	D-638	%	55	51	400
Flexural Strength	D-790	MPa	24	39	33.1
Flexural Modulus	D-790	GPa	0.66	1.4	1.34

A Formlabs Form2 desktop SLA printer was used to manufacture the proposed compliant MM test specimen. The Form2 has a print bed area of $145mm$ x $145mm$ and uses a $405nm$ wavelength with a spot size of $140\mu m$ and an XY printing resolution $\sim 25\mu m$. The mechanism is printed at a layer thickness of $0.05mm$ for an improved flexural response. The Formlabs printer was selected due to the range of tough and durable resins suitable for compliant mechanisms. Tough1500 is used in developing compliant MMs due to its flexibility and resistance to brittle fracture. A common polymer material for compliant mechanisms and living hinge designs in consumer packaging products is Polypropylene (PP) due to its fatigue resistance. Tough1500 is designed to simulate PP in strength and stiffness, as PP is considered a tough material with a range of elasticity. Tough1500, as shown in Table 3.3, has similar properties; its modulus of elasticity allows the material to be pliable and suitable for compliant mechanism design. Furthermore, 51% elongation and 1.4GPa flexural modulus allow for fatigue resistance. Although durable materials such as Polyethylene (PE) (Formlabs Durable resin) exhibit similar properties, Tough1500 is a stiff material with greater spring-back.

Unlike Material Extrusion AM techniques that exhibit significant anisotropy, SLA printed components are broadly isotropic, with minimal difference in Young's modulus and maximum tensile stress along different axes. Although conclusions in literature differ, SLA-printed parts are either completely isotropic [120, 121] or transversely isotropic [122, 123]. This is because of the multi-layer curing process, resulting in crosslinking between bonds. As the laser passes over a previously printed area, covalent bonds are formed along the x-y plane and between the current and previously printed

layers. The different conclusions appear due to testing conditions and the broad range of resins examined that are currently less understood. In particular, literature on Polypropylene-like photopolymers such as Tough1500 is limited. Although the mechanical properties do not significantly differ due to orientation, printing 3D anisotropic unit cells and slender beams pose several design challenges.

3.4.2 Printing Setup

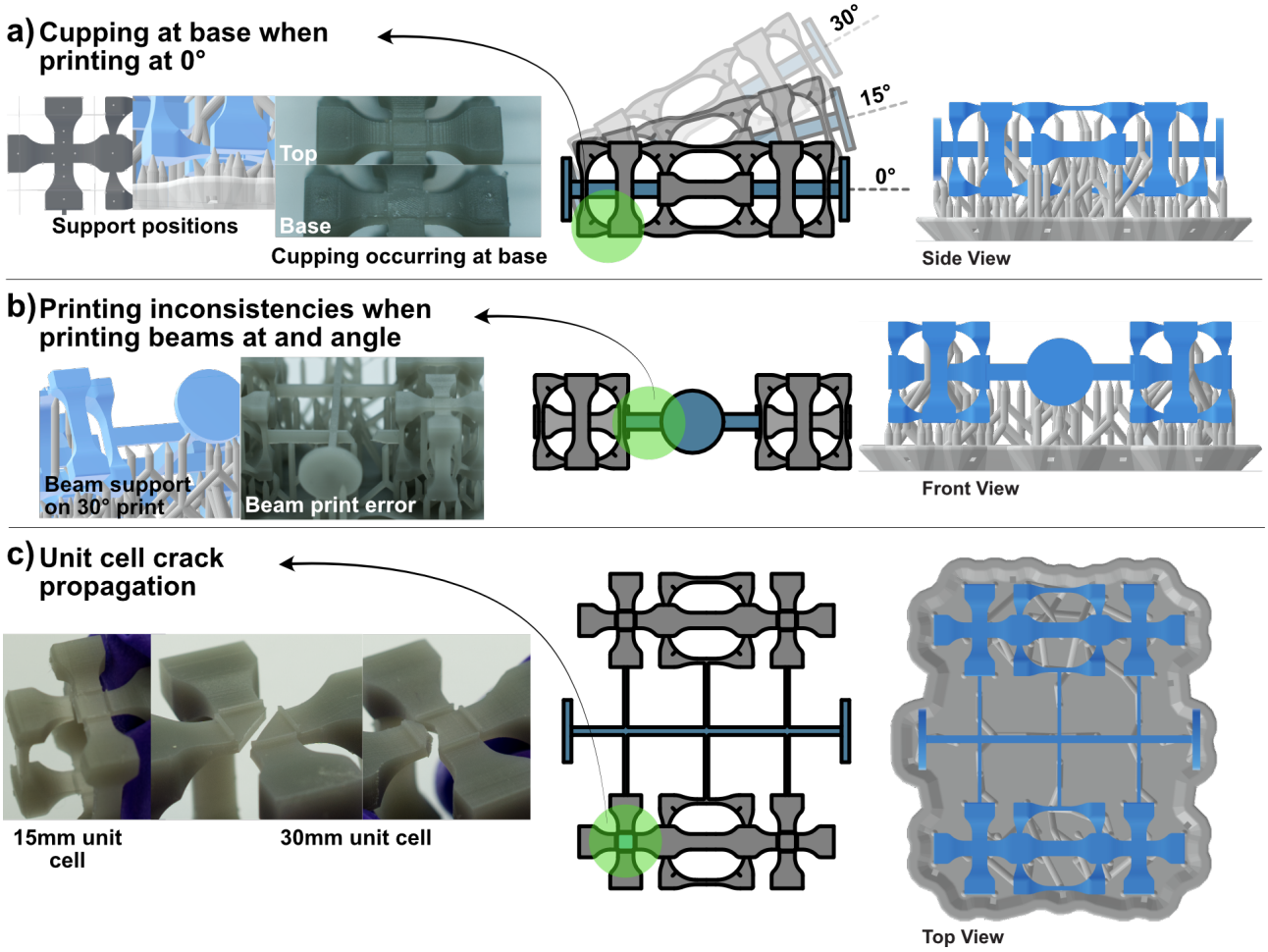


Figure 3.6: *a) Centre - Schematic showing the side view of the compliant MM at 0°, 15° and 30°. Right - Supports generated through Formlabs PreForm software. Left - Curling at base of unit cell. b) Centre - Schematic showing the front view of the compliant MM at 0°. Left - Errors in printing slender beam when printing at 30°. c) Centre - Schematic showing the top view of the compliant MM at 0°. Left - Crack propagation of unit cells due to repeated actuation.*

The proposed MM was designed and exported in STL format using Autodesk Fusion360. The STL file was imported into Formlabs-Preform (Version 3.14.0) slicing software to create the laser toolpath. A layer height of $50\mu m$ and Tough1500 material is selected. A full raft is used, with a support density of 0.9 and touchpoint size of $0.3mm$. The height above the raft is increased to $5mm$, and raft thickness is reduced to $1.8mm$. On average, each sample uses ~11mL of resin. Once the printing is complete,

the model is removed from the build plate using a spatula. The model is then agitated in a pre and post rinse tub filled with Isapropanol for 2.5 minutes in each tub. It is then rigorously washed in Isapropanol for 20 minutes using the Formlabs-Wash. The model is left to dry for half an hour to ensure the Isapropanol has evaporated. Finally, the model is cured at 70°C for 60 minutes under a $405nm$ LED (Formlabs-Cure). Once cured, a combination of side cutters (C.K - Sensoplus - 3766D) and tweezers are used to remove the support material. Due to the complex geometry and challenging to reach areas, no surfaces are sanded down.

Figure 3.6.a shows the proposed MM design in three printing orientations; horizontal, 15° and 30°. Sections of the MM have been highlighted due to separate printing considerations and particular failure points in testing. The MM has an unsupported slender beam of thickness $0.6mm$ and an anisotropic unit cell design with a minimum thickness of $0.725mm$. Typically to avoid warping, SLA printed unsupported walls should be no thinner than 1.0mm. As a result, printing orientation, support location and size, and post-processing are considered to ensure the functionality of the mechanism is not compromised during printing.

The bistable system comprises a long slender beam with unsupported walls. Consequently, during the separation step in SLA printing, there is an increased likelihood of warping and surface defects. Support structures with a $0.25mm$ tip size are manually placed along the base of the beams to reduce the likelihood of warping. These structures replace the automatically created Preform supports ($0.3mm$) on the beam. The supports are positioned at the base to reduce surface defects, as nibs from support remnants are difficult to sand down. Furthermore, as the beam buckles along the transverse direction, defects along the surface affect the buckling properties. Moreover, printing orientation affects the print quality of the slender beams. Figure 3.6.b shows the possible defects when printing at 15° and 30°. Due to the unsupported walls, the likelihood of warping increases when an extended thin surface area is printed. Although this can be mitigated by rotating the mechanism along the x and y axes to reduce the printing surface area, the introduction of diagonal layers along the slender beam introduces anisotropy and affects the buckling characteristics of the beam. To ensure consistency in printing quality, the MM is printed in a horizontal (0°) orientation.

Printing in a horizontal orientation for bottom-up SLA printers is not recommended, as the MM cross-section is not minimised. This increases the likelihood of print failure due to the separation forces when removing the printed layer from the vat base. Although the proposed MM has an overall size of $50.6mm$ x $46mm$, due to the nature of the unit cells, the surface area difference between a horizontal print vs 15/30° is minimal, resulting in very few print failures. Although print failure is

unlikely, there are defects introduced when printing horizontally. As shown in Figure 3.6.a, curling occurs at the base of the print (first layer of the unit cell). This is due to internal stresses between the first printed layers of the flat surface resulting in shrinkage along the edges. Although this affects the accuracy of the printed part, due to curling occurring in the unit cell corners where no bending occurs, the effect is negligible on the functionality of the MM. The pros of ensuring the slender beams print consistently outweigh the cons of curling occurring at the unit cell base.

SLA technology is well suited for use in compliant mechanisms due to the low anisotropic nature of the printed parts. This leads to specimens with no specific point of failure. In testing the printed components, failure often occurred along the square region where the hinge flexures connect, as highlighted by the coloured region in Figure 3.6.c. Due to the nature of the anisotropic unit cell, residual stresses during printing occur in the connecting region. Furthermore, during actuation, stress is concentrated along the connecting hinge region and where the unit cell and slender beam connect. As a result, crack propagation is likely under specific loading conditions. For a $30mm$ unit cell under compression along the z-axis of the unit cell, the crack propagated diagonally across the flexures. In a $15mm$ unit cell, the crack propagation is less defined, either cracking diagonally or along the square edge, likely due to the build-up of stress in the area during printing and the layer direction.

3.5 Fused Deposition Modelling

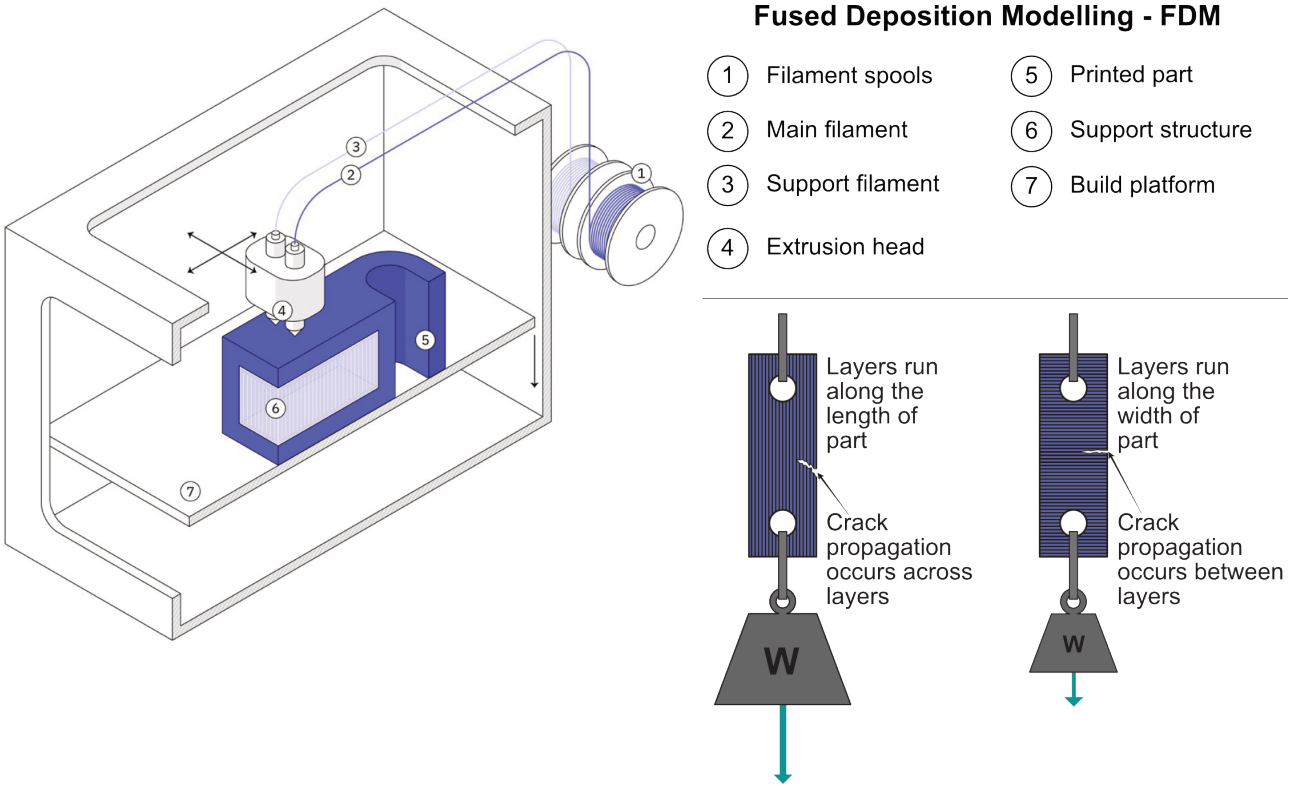


Figure 3.7: *Schematic of Fused Deposition Modelling (FDM) AM technology adapted from Hubs [105]. Extrusion head (4) heats filament (2,3) and deposits the melted thermoplastics onto a heated build platform (7) to construct printed components. Schematic showing anisotropic nature of FDM printed parts.*

Fused Deposition Modelling (FDM) is a material extrusion technology and the most widely used AM technology by user base due to low-cost material use and desktop machine availability. The schematic in Figure 3.7 describes the FDM printing process, a spool of thermoplastic filament (1,2) passes through a heated extrusion head (4). At the filament melting temperature, a motor drives the filament through the heated nozzle. As the nozzle moves, the melted filament is deposited onto a heated print bed (7). The filament cools and solidifies to form a printed layer (5). To form a cohesive solid part, bonding between printed layers results from the heated filament pressing against previous layers. The extruded material heats and re-melts previously printed layers. The coupling of the partially melted layer and the additional force from the extruded filament enables bonding between layers. An advantage of FDM printing is the use of infill. Due to the extrusion and deposition process, components can be manufactured with hollowed-out sections reinforced with an infill lattice, reducing material consumption and making the part lightweight. The use of thermoplastic filament offers a variety of materials for FDM. High-performance materials such as PEEK (Polyetheretherketone) and PEI (Polyetherimide) can be printed with excellent mechanical properties.

A limitation in FDM printing is the anisotropic mechanical properties. The mechanical strength of FDM printed parts is highly dependent on the printing orientation and the direction of forces applied to the material. As shown in Figure 3.7, the schematic shows two equally sized FDM printed parts with different printing orientations. As a result, the component with the printed layers running along its length can withhold stress without fracture compared to a printed part with layers orientated along the width. This is because of the added pressure when depositing extruded filament onto a previous layer. The extruded shape of the filament is oval instead of circular. This leads to small valleys between printed layers, which become areas of stress concentration. As a result, forces perpendicular to the layer direction results in cracks forming between layers and brittle fracture. In comparison, forces parallel to the layer direction have superior mechanical properties, as failure results from layer slippage or cracks propagating through multiple layers.

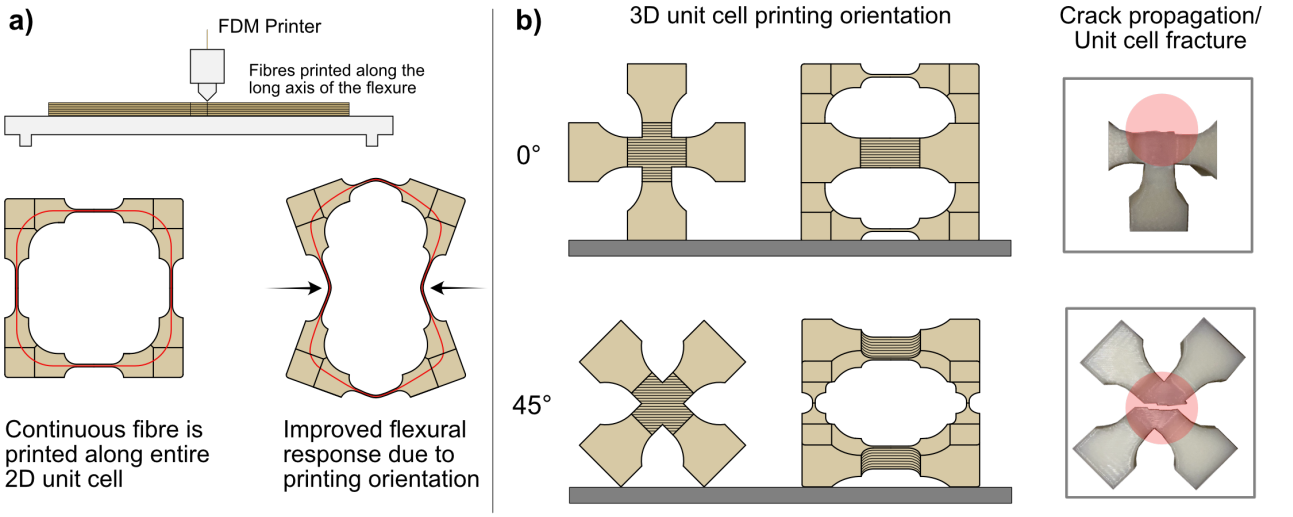


Figure 3.8: *a) Schematic showing FDM printed fibre direction for improved flexural response of rectangular unit cell. b) Schematic showing the layer pattern at flexure points for an anisotropic unit cell orientated along horizontally (0°) and at 45°. Images show fracture position after actuation as a result of layer pattern. Unit cells were compressed along the z-axis in both printed examples.*

The printed unit cells in Figure 3.8.b are printed in ABS (M30i) (Supplier - Stratasys) using the Stratasys FORTUS 400MC FDM printer. The 400MC is a dual nozzle industrial-size printer; the second nozzle is used to deposit soluble support material (SR-100). Specimens are printed using a T12 nozzle with a layer thickness of $0.18mm$ and toolpath width of $0.36mm$. STL files exported from Autodesk Fusion360 are imported into the GrabCAD-Print slicing software (version 1.50). All specimens are printed using 100% infill. The soluble support material can be dissolved in a caustic solution (2.3% Sodium Hydroxide (WaterWorks - P400SC)) using a washing and finishing system (Gemini Cleaning Systems Ltd - EFT-500), allowing parts with several overhangs such as the unit cell

to be printed. Once the support material is removed, the printed specimens are rinsed in water and left to dry before testing.

The anisotropic mechanical properties pose several problems for the use of FDM printed compliant mechanisms. A printing orientation that maximises the flexural response in the x and y directions consequently restricts movement in the z-axis. This is because of the anisotropy of the 3D unit cell and the resultant layer direction. The hinge flexures for the FDM unit cell have a minimum thickness of $0.45mm$. As shown in Figure 3.8.a, the unit cell is printed in an orientation to allow the printed fibres to build orthogonal along the long axis flexure direction. This enables the printed part to deform with minimal strain and to maximise the flexural response. The flexure is composed of two extruded fibres printed in a single loop in the unit cell. The flexures can deform with minimal crack propagation and repeated bending with no plasticity. As a result, FDM printing for 2D structures is suitable for compliant mechanism living hinge designs.

However, the anisotropic limitations pose design constraints for the 3D unit cell designs. As shown in Figure 3.8.b, when the unit cells are in an orientation where the z-axis is parallel to the print bed, stress is concentrated in the highlighted area where the flexures join. This is due to the unit cell design and the printed fibre direction. During actuation, the centre of the cross is pulled in four separate directions. The anisotropy of FDM printed parts results in a favourable flexure response in 2 directions and an unfavourable response in the other, as the tensile/compressive forces are perpendicular to the fibre orientation. As shown, this results in the brittle fracture between printed layers and part failure. Changing the printing orientation by 45° as shown in Figure 3.8.b reduces the anisotropy along the z-direction. However, this results in fracture along the centre of the z-axis or fracture of the flexure elements in the x and y-axis. As a result, FDM printing is not considered further for the complaint MM. The FORTUS 400MC is continually used throughout for initial flexure prototyping and building testing rigs.

Chapter 4

Mechanical Metamaterial Logic

In this chapter, Material Jetting is used to build programmable MMs by combining elastic flexure elements to rigid beams. The proposed metamaterial controls the buckling response of a biased Von-Mises Truss through the actuation of unit cells to perform Boolean logic. By developing an anisotropic 3D unit cell and a bistable system for signal propagation, AND and OR logic gates have successfully been demonstrated in three different configurations, zz, yy and zy-polarisation. The actuation of the unit cell changes the effective beam length of the bistable system, allowing a snap-through response to occur. This is achieved by controlling the separation distance between unit cells, affecting the strain energy within the bistable system. The multi-plane approach provided a further layer of tunability to the proposed MM design, as the direction and order of input are both factors of consideration in the logic sequence. For a mechanical AND gate, both unit cells must be simultaneously actuated for the shuttle to propagate from a LOW to HIGH position. With a zy MM, propagation occurs when one input is along the z-axis and one along the y-axis. Although the complete set of universal mechanical logic gates are yet to be achieved, it is evident that the introduction of multi-plane mechanical logic gates offers clear advantages over single plane mechanical logic.

Sections of this chapter have been previously published under the following citation;
U. Waheed, C. Myant, S. Dobson, "Boolean AND/OR Mechanical Logic using Multi-Plane Mechanical Metamaterials", *Extreme Mechanics Letters*, vol. 40, 2020. doi:10.1016/j.eml.2020.100865.

4.1 Mechanical Boolean Logic Gates

An objective of this work is to develop FMMs. One particular avenue to develop programmable systems is to achieve a complete set of universal logic gates. Theoretically, if a system can perform Boolean logic and gates can be cascaded, i.e. the output from one gate drives the input for subsequent gates, a 'computing' system can be achieved.

The concept of performing logic operations using mechanical components has previously been explored. Pioneering work by Charles Babbage on the Analytical Engine was one of the earliest known examples of mechanical computing. The proposed Analytical Engine was a general-purpose mechanical computer, utilising logic structures similar to modern computation design [124]. Despite being ground-breaking for its time, mechanisms such as gears and cogs for computing seldom showed advantages over electronic systems. The continual development of transistor technology in the electronics industry has also stifled any resurgence of mechanical logic, from becoming a plausible alternative for computing going beyond Moore's law [79]. Mechanical logic systems are limited in processing speeds and architecture; presently, they cannot compete with alternative beyond Moore's systems. Mechanical logic at the molecular level currently remains a theoretical study.

However, there are several advantages to mechanical logic systems for use in devices that require a simple logic architecture, i.e. for the independence from electronic systems. As mechanical forms of energy are required, these devices generate no electromagnetic signature and are insensitive to radiation damage, making them ideal for use in harsh environments such as in space or nuclear systems. Merkle [78, 125] provides a compelling argument on the potential merits of mechanical logic devices at the molecular level, exploring several configurations: rod logic [78], bistability [78] and a link and rotary system [125]. Merkle also explored the idea of using the deformations of an elastic bulk material with a complex shape (lattice) for computation [78] i.e. morphological computation (MC). This is similar to the use of MM to perform Boolean logic.

In Section 2.3.2, several examples of MMs that exhibited Boolean logic were examined. A common theme between designs was the unidirectional response to the system, where the input and output occur in the same plane of motion. In this chapter, the MC notion is investigated further; if by developing 3D structures, can Boolean logic be exhibited? The anisotropic unit cell design proposed by Coulais [58] is adapted for multi-material printing and combined with a bistable system. Due to the 3D unit cell design, the direction of actuation is essential to the logic sequence. This is a different approach from previous metamaterial designs [126, 80, 81, 82], in which logic was performed in a single

plane and material buckling occurred by overcoming the potential energy barrier. In this study, it is through the actuation of unit cells from different directions that control the buckling behaviour.

4.2 Bistable Systems for Mechanical Logic

In the mechanical logic systems explored in Section 2.3.2, harnessing elastic instabilities in bistable systems [127] was shown to be well suited to perform mechanical logic. This is because of the frictionless transitions between states and the clear distinction between two stable states, synonymous to Boolean algebra statements *True* and *False*, or *HIGH* and *LOW* voltage levels in digital circuits. A *HIGH* and *LOW* voltage is represented in computing by 1 and 0-bit units, respectively. In this section, we explore how bistable mechanisms are used as logic devices, how the dynamics of a snap-through transition occurs and a corresponding bistable system that will be used to define the state of the MM logic device.

4.2.1 Euler Buckling Theory for a Fixed-Fixed Beam

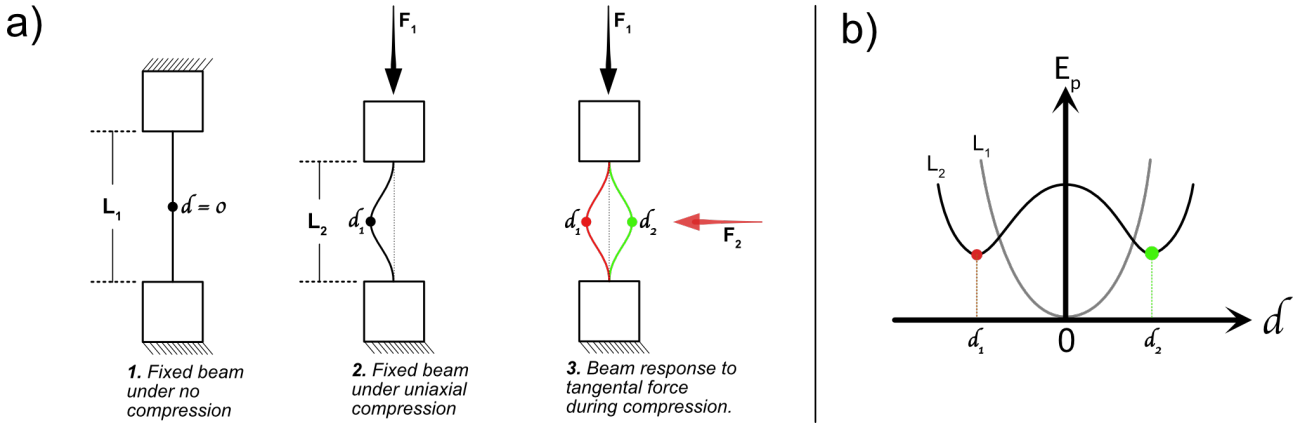


Figure 4.1: *a) Schematic of a fixed-fixed slender beam 1) under no compression, 2) under uniaxial compression and 3) in response to a tangential force when under compression (beam transitions between stable states d_1 and d_2). b) Potential energy (E_p) vs displacement (d) graph for L_1) a thin rigid beam under no compression and L_2) a rigid beam under uniaxial compression.*

In Euler buckling theory, a double clamped slender beam in its first buckled mode has a critical load defined by [128, 129, 130],

$$P_{cr} = \frac{4\pi^2 EI}{L^2} \tag{4.1}$$

where P_{cr} is the critical load, E is the modulus of elasticity, I is the moment of inertia, and L is the effective beam length. At the critical load, thin, slender beams buckle into a stable cosine shape. If the buckling load is maintained (F_1), the slender beam changes from a monostable system to a

bistable system, shown by the symmetric bistable diagram in Figure 4.1.a. The two stable states are synonymous with Boolean logic states of 0 (red) and 1 (green), shown as two symmetric local minima in the energy displacement diagram (Figure 4.1.b). To transition between stable states, force must be applied against the curvature of the beam (F_2), creating a snap-through event. The energy required for a snap-through to occur depends on the separation distance between the clamped ends of a beam. By decreasing the separation distance, the effective length L of the beam is shortened, resulting in a higher threshold force (F_2). This also increases the potential energy barrier between the two stable states of the beam (Figure 4.1.b).

4.2.2 Asymmetric Bistable Systems

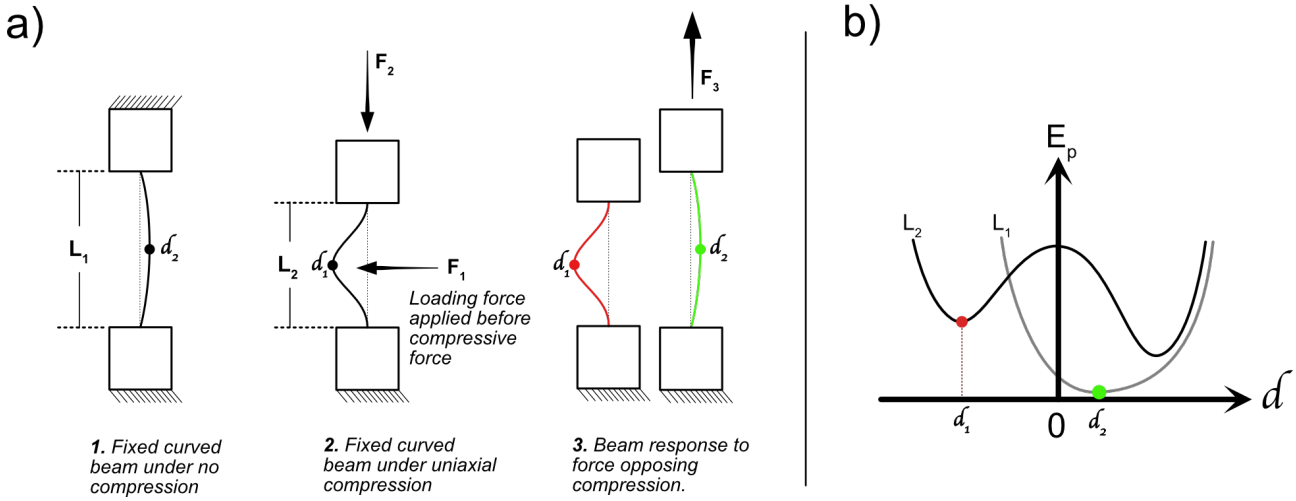


Figure 4.2: *a) Schematic of a fixed-fixed curved beam 1) under no compression, 2) under uniaxial compression and 3) in response to a force opposing the compression (beam transitions from d_1 to d_2). b) Potential energy (E_p) vs displacement (d) graph for L_1) A curved beam under no compression, L_2) A curved beam under compression exhibiting asymmetric nonlinear behaviour.*

There are several methods a slender bistable beam can be controlled to perform mechanical logic. As shown in Figure 4.1, energy must be supplied to the system to overcome the symmetric energy barrier. The MM logic mechanisms explored in Section 2.3.2 required actuation in the same direction as the beam's motion [80, 81, 82, 126]. There are limitations to such designs, as the energy required to enable a snap-through response can be significant and highly dependent on the uniaxial compression.

An alternative approach is shown in Figure 4.2, the response of a curved beam under uniaxial compression is explored [131, 132]. A curved beam adds implicit bias, trapping energy in the system — there is a favourable buckling response in the direction of the curved beam. The asymmetric potential energy diagram for a pre-curved beam is shown in Figure 4.2.b. The schematic in Figure 4.2.a shows an initial loading force F_1 before the compressive force F_2 places the slender beam in its

logical 0 (red) state. If an opposing force increases the effective length of the beam, elastic potential energy is released, and the system returns to its initial curved state. The same logic states are exhibited in Figures 4.1 & 4.2, although the transformation in the curved beam example occurs because of a perpendicular force rather than a force parallel to the motion of the beam. By combining unit cells to slender beams with implicit bias, mechanical logic devices with tunable responses can be realised.

When designing an asymmetric bistable system, there must be implicit bias in the system to program the initial beam response to lateral compression. This often requires geometric imperfections to ensure a programmed response. In Figure 4.2, the pre-curved beam has a geometric imperfection due to the pre-stressed initial state during the manufacturing process. Zhang *et al.* [132] shows how a similar response to a pre-curved beam can be obtained through imperfections in the slender beam design, such as notches positioned in the centre of the beam. Topological metamaterials such as the design by Paulose *et al.* [49] have also shown, through geometric imperfections, that the buckling response is programmable.

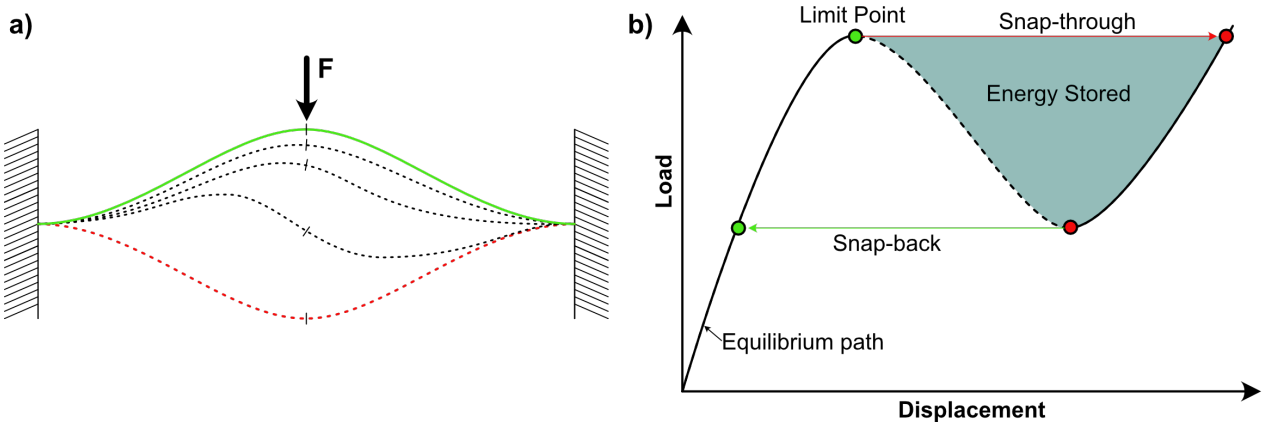


Figure 4.3: *a) Schematic of double clamped curved slender beam. Dotted lines indicate the motion of the beam as the incident force F on the centre of the beam is increased. b) Load Displacement diagram for a typical curved bistable system. [130, 131, 133]*

The schematic in Figure 4.3 explores the snap-through response of a curved beam when fixed from both ends. In Figure 4.3.a, the motion of the beam is shown as the loading force (F) on the centre of the beam increases until the limit point is reached and a snap-through occurs, causing the sudden change in beam displacement. This is shown in Figure 4.3.b, where the equilibrium path of a bistable system is modelled as the centre line load is increased. A sudden change in displacement occurs at the limit point, highlighting the non-linear nature of bistable systems. The length, thickness and rise of the curved beam are factors to consider when forming a bistable system to have implicit bias. As shown by Qiu *et al.* [131], when a shallow curved beam is clamped from both ends (when the beam rise is small), the beam exhibits monostable behaviour and bounces back in response to a centre line

load. The paper by Qui *et al.* [131] also shows that a thickness modulated curved beam can be used to form an asymmetric bistable system.

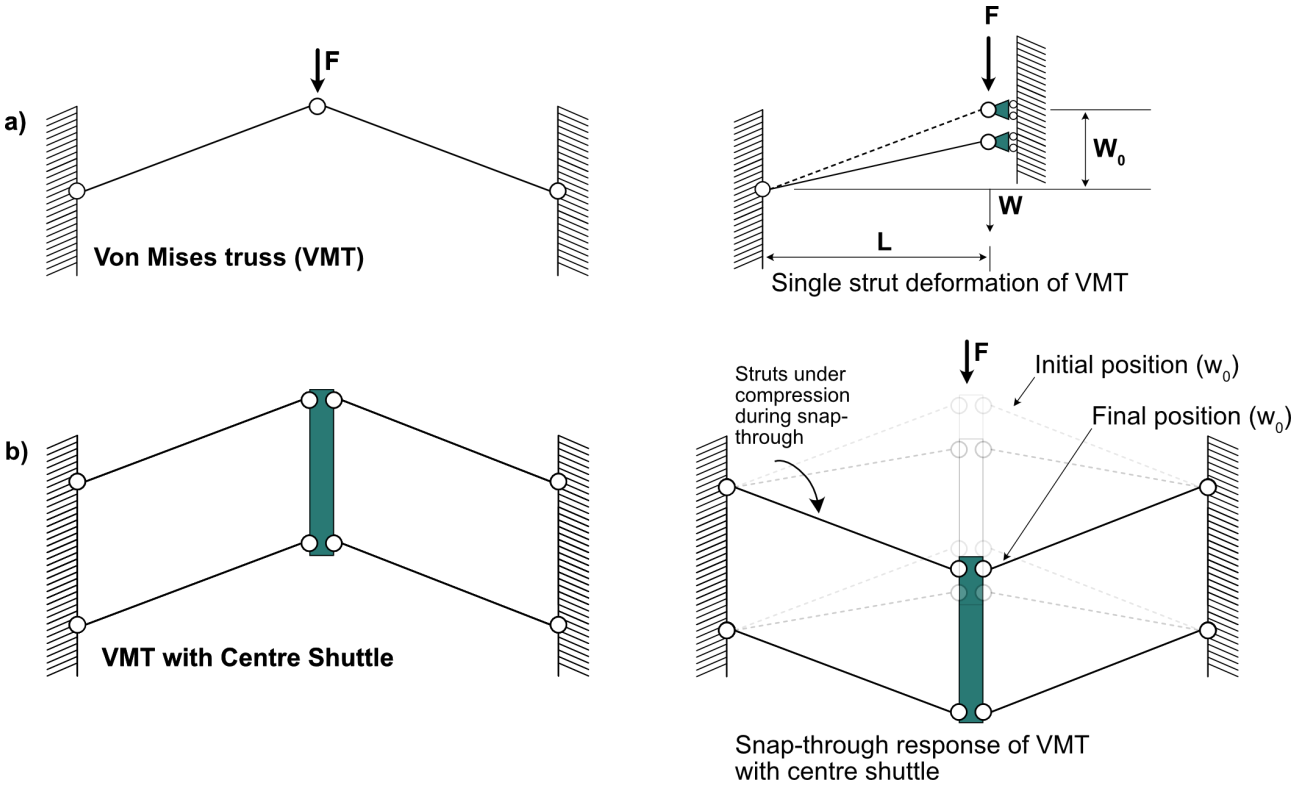


Figure 4.4: *a) Left - Schematic of a typical Von-Mises Truss, a two-bar structure of equal lengths are connected by a centre pin joint. Right - Deformation of a single strut with key parameters noted. b) Left - Pair of VMT structures are connected to a centre shuttle, to improve the stability of the system during a snap-through event. Right - Typical motion of the connected VMT structure from the initial to final position during a snap-through event. VMT schematic adapted from Schioler and Pellegrino [134].*

An alternative arrangement to a curved beam system is shown in Figure 4.4 [134], based on a Von-Mises Truss (VMT). A VMT structure typically comprises a two-bar structure of equal lengths, connected at the apex through pin joints. The beams of a VMT are often designed with large Euler buckling loads to ensure buckling of the beams does not occur. This ensures the beams remain linear-elastic and have a symmetric deformation pattern throughout an actuation event. Similar to Figure 4.3, a VMT structure is bistable. An increasing central force at the apex of the VMT will result in axial compression of the struts. As the force on the VMT reaches the threshold force, the system transitions to the second stable state.

The equation below highlights the relationship between the applied load (F) on a VMT and the corresponding motion of the system, defined by the rise of the apex (w) from the horizontal line [134].

$$F = -EA\left(\frac{1}{\sqrt{w^2 + L^2}} - \frac{1}{\sqrt{w_0^2 + L^2}}\right)w \tag{4.2}$$

where EA is the axial stiffness of the struts.

Although the VMT structure in Figure 4.4.a is designed to buckle in a symmetric pattern, the system is still susceptible to rotation during a snap-through event. The introduction of a centre shuttle and a double truss system, as shown in Figure 4.4.b, prevents rotation and significantly improves the stability of a snap-through event. This is also the case for a curved beam described by Qiu *et al.* [131]. If the side walls in the bistable system are not fixed, an inverse symmetric deformation pattern creates a push-pull effect of the sidewalls, and a rotational moment occurs. A connected double-curved system ensures these possible eccentricities (loads not acting through the centroid) formed by the moving side walls are minimised due to the symmetric deformation pattern during snap-through.

Although a VMT structure is easier to manufacture and the system response is easier to control, there are limitations to a classical VMT system. In particular, the apex w_0 must be kept low to ensure large strains in the system do not occur. Furthermore, as the struts are not designed to buckle or yield, they have a small axial stiffness compared to the force required for a snap-through [134]. An important parameter in a bistable system is the stroke length, as this dictates the potential output of the system. As w_0 is often shallow to ensure a snap-through event can occur, the stroke length of the system is restricted. However, concepts from MEMS designs have shown [135] rather than connect struts to revolute joints for a VMT system, utilising thin, slender joints that buckle elastically reduces the required snap-through load and increases the stroke length obtainable.

The proposed VMT in Figure 4.4 is a symmetric system with no implicit bias. As there is no favourable direction, if the effective length of the struts is increased, the system cannot be programmed in its current state to move in a particular direction. An alternative arrangement will look to replace the revolute joints shown with thin, slender joints that buckle elastically. Through this system, implicit bias can be added using the geometry of the elastic joints. Additionally, this will reduce the restriction of a shallow apex and increase the overall stroke length of the system.

4.3 Metamaterial Development

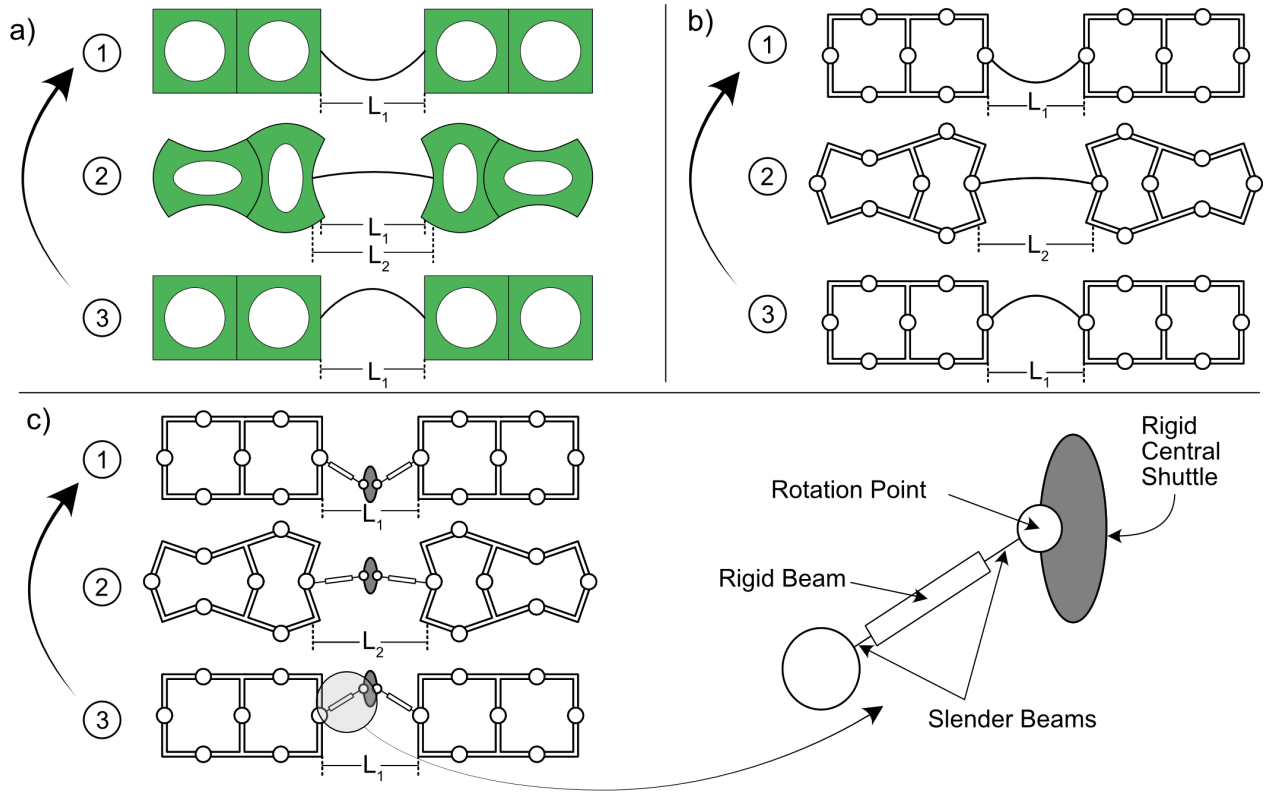


Figure 4.5: *Schematic of a) slender beam attached to 2D elastic unit cells (green squares), b) slender beam attached to 2D compliant unit cells, c) Central shuttle attached to 2D compliant unit cells. a-c) Step 1 - System is in a non-actuated energetic state (LOW), step 2 - system response during actuation and step 3 - system is in a bias state (HIGH).*

By combining slender beams with unit cells, the effective length of the beam can be controlled by the actuation of the unit cell. The schematic in Figure 4.5.a shows a slender beam connected to an elastic unit cell design, proposed by Bertoldi *et al.* [35] for a negative Poisson's MM. In step 1, the system is in a bistable *LOW* (logical 0) state. The system has an upward bias; thus, strain energy has been supplied to the system to place the beam in this position. By actuating the correct unit cells, the effective length of the beam is increased to L_2, releasing the potential energy in the beam as shown in step 2. In step 3, as the unit cells return to their undeformed shape, the effective length of the beam returns to L_1 and the beam transitions to a *HIGH* (logical 1) state.

During a snap-through event, the outward force at the ends of the beam can be significant, causing elastic unit cells such as the Bertoldi [35] design to warp. To make the system robust against inadvertent warping, combining rigid beams with elastic elements at the flexure points allows greater control over the snap-through response and improves the reliability of the MM. Figure 4.5.b shows in compliant mechanism notation the predicted functionality of the unit cell and bistable system. The metamaterial consists of two sets of connected unit cells (outer and inner cells). As shown in step 2,

the outer cell is actuated from the top and bottom; the sides deform into a convex pattern in response. This results in the pin joints of the inner unit cell moving towards the centre, creating a concave pattern. In response, the concave/convex shape of the inner unit cell determines if the effective length of the bistable system increases/decreases respectively. Due to the asymmetric energy profile of the beam system, increasing the effective beam length allows the shuttle to propagate to the lower potential equilibrium state.

The buckling of a slender beam can often take higher buckling modes if eccentric loads are present during actuation. Additionally, the asymmetric deformation of the beam during actuation is not ideal for systems where the beam ends are not completely fixed. The VMT shown in Figure 4.4 is used as the bistable actuator to improve the system's stability as it transitions between stable states. Figure 4.5.c shows the development of the bistable system in a compliant mechanism form. The central node at the apex of the struts is replaced with a rigid central shuttle. As the strain energy in the new system is primarily held in the slender beams, the actuation of the unit cells has a greater effect on the state of the MM. The slender beams minimise the risk of inadvertent buckling on the rigid members, and all the movement of the bistable system is implemented through the slender beam deformation. Furthermore, a central shuttle is most suitable for a double truss system, which is implemented to ensure a symmetric snap-through occurrence.

4.3.1 Multi-Material Development

Unit Cell Development

Material Jetting was selected as a suitable manufacturing process for the MM. Refer to the Material Jetting manufacturing process in Section 3.3 for detail on the printing process and settings used. In Figure 4.5, a 2D metamaterial example is shown, utilising the 2D auxetic structure purposed by Bertoldi [35]. The 2D unit cell constrains the system's design, as a desirable concave pattern of the inner unit cells is only obtainable through the actuation of the outer unit cells. By using 3D unit cells, additional control of the bistable system can be achieved. As shown in Figure 4.6.c & e, the 3D unit cell design is anisotropic; the system's response depends on the direction of mechanical actuation. For example, an actuating force along the y-axis results in a concave response along the x-axis and the expected convex response along the z-axis, otherwise described as a positive spin ($+\sigma_z$) of the unit cell. As a result, a single 3D unit cell system is suitable to replace a double 2D unit cell arrangement. The polarisation of a unit cell is determined by which axis the cross-section (outlined in red in Figure 4.6.c) intersects. For example, the unit cell highlighted in Figure 4.6.c is z-polarised as the cross-

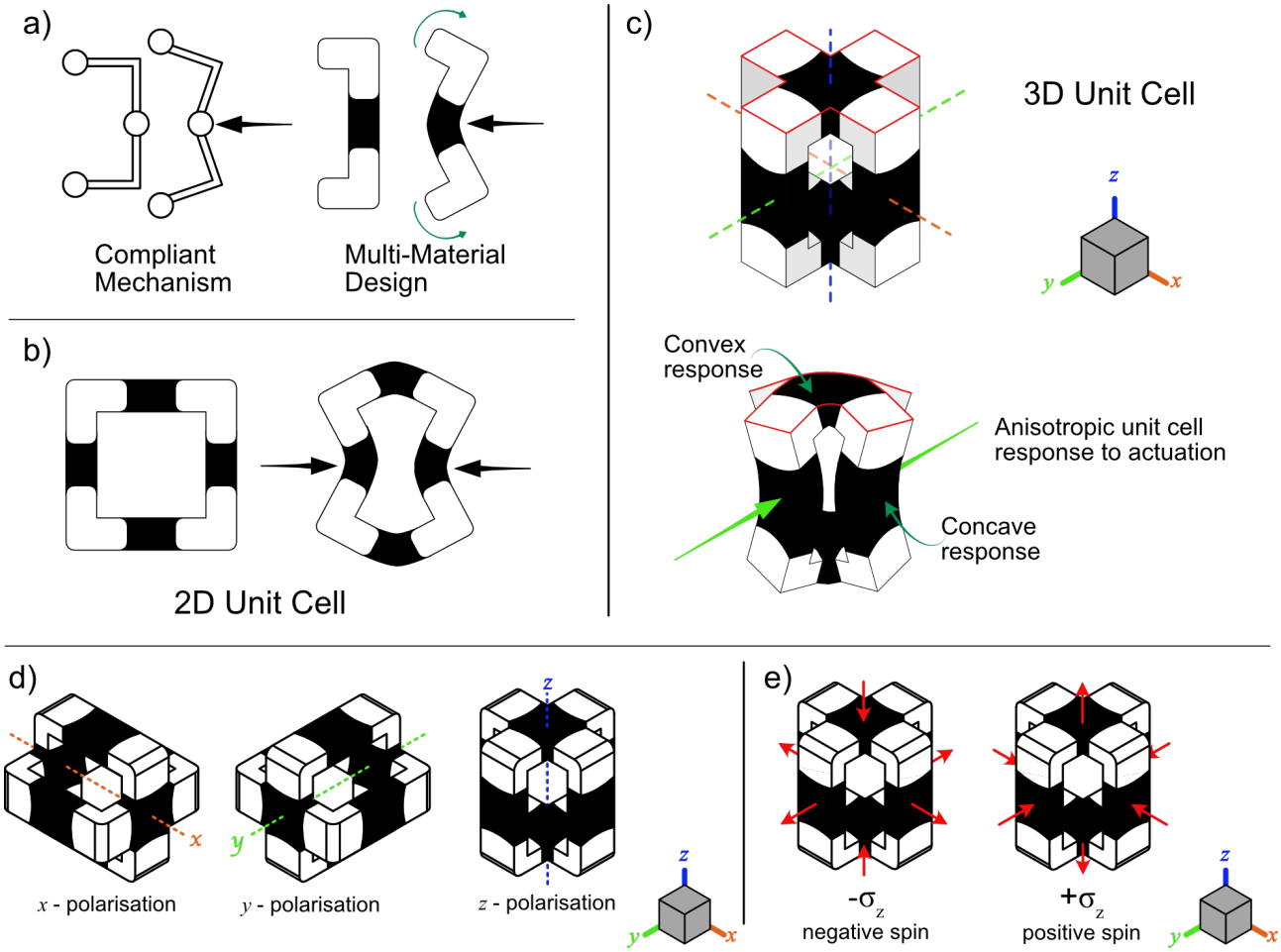


Figure 4.6: *a) Schematic of a compliant mechanism and multi-material flexure design (white segments are rigid, black segments are elastic). b) 2D unit cell design in its rest and actuated state. c) 3D unit cell shown in the rest and actuated states. 3D unit cell is shown in a z-polarised orientation, polarisation is determined by the axis the cross-section (red outline) intersects. d) x,y,z polarisation (unit cell orientation) with respect to axis. e) Actuation response and corresponding spin configuration of a z-polarised unit cell.*

section intersects the z-axis. As shown in Figure 4.6.d, the three different polarisation's possible are shown according to the axis the cross-section intersects.

Figure 4.7 shows six different 3D unit cell designs considered for the metamaterial and the testing strategy to determine the most suitable design. Each design utilises rigid elements with elastomeric joints to mimic the concave and convex response when the unit cells are actuated. One of the factors that limit the choice of design is the ability to combine multiple unit cells. When considering combinatorial design, specific unit cells dissipate mechanical forces further than others. The 3D renders show the rigid component (VeroWhite) in beige/white, the elastomeric material FLX9985 (%Agilus30 + %VeroClear) in grey, and FLX9950 in black. All unit cells were manufactured using the same PolyJet printer (Objet500). The change in design to incorporate rigid elements with elastomer flexure points results in the same deformation pattern as the Bertoldi [35] unit cell design. However, the updated design provides better resistance to warping from sidewall pressures.

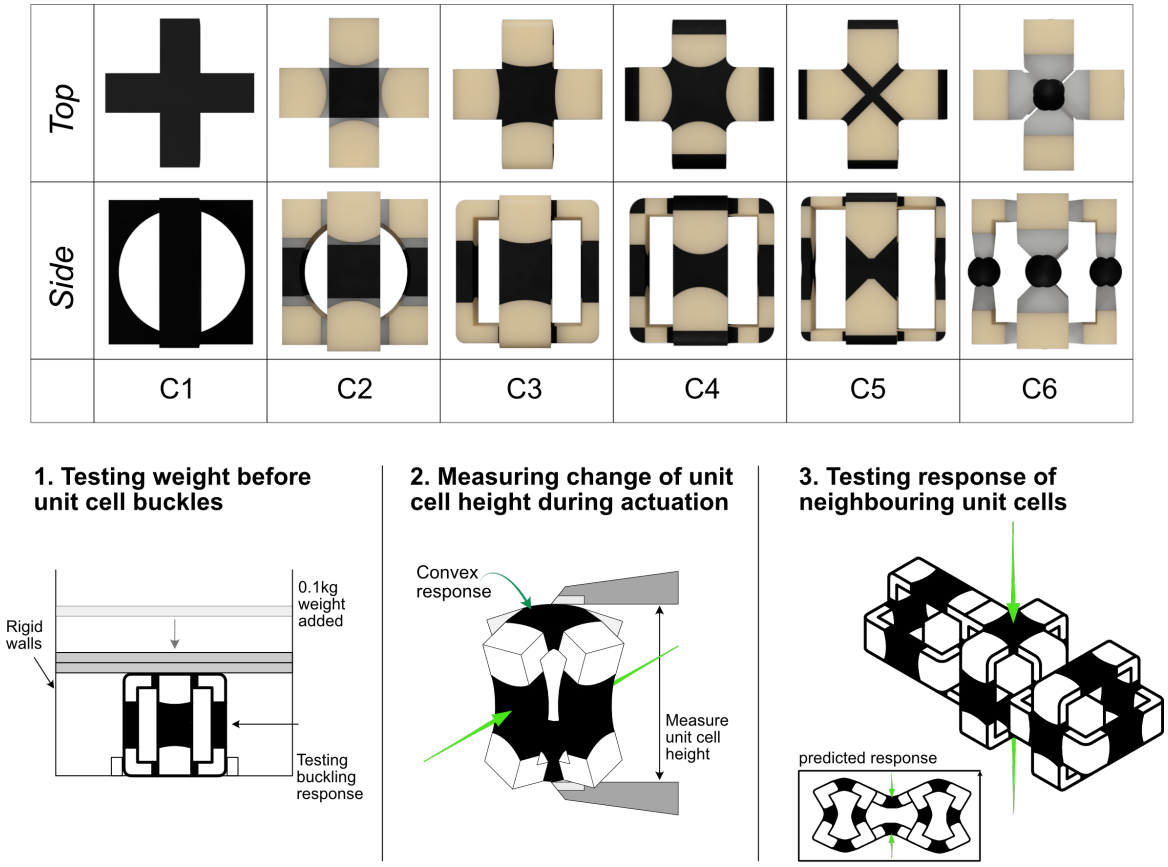


Figure 4.7: *Top and side view for 6 different 3D unit cell designs. Yellow sections indicate rigid polymer section. Black and grey sections indicate elastomer material, where black indicates a lower Shore hardness than grey. Below - a schematic of the testing strategy implemented to determine which unit cell design to further pursue.*

As shown in Figure 4.7, a three part testing strategy was used to determine a suitable unit cell design; this included a combination of qualitative and quantitative analysis. In the first test, the unit cell is placed in a rig designed to allow 100g weights to be gradually added on top of the cell. This test determines how much weight a single unit cell of dimensions $15mm$ x $15mm$ x $15mm$ can hold before buckling. Results are gathered five times and averaged, as any weight added at an angle created a rotational moment and caused the unit cell to buckle prematurely. The second test measures the increase in unit cell height when fully actuated. The convex response of the anisotropic unit cell is measured using a Vernier scale. The sidewalls of the unit cell are compressed until the walls touch. The extended length of the unit cell is measured to determine what design limits the response to actuation. The third test examines the dissipation of energy through the system. In a three unit cell combination, each with different orientations, a qualitative assessment is conducted on the connectivity of the unit cells. The centre unit cell is actuated, and an observation is made on the response of the two outer unit cells as to which design responds accordingly. The results of the three tests and the unit cell chosen for the MM are included in Table 4.1.

Table 4.1: *Unit cell testing results. 3 different tests were conducted on each unit cell C1-6, buckling mass, extension and 3×1 combination test. All unit cells successfully moved neighbouring cells when actuated. Error in extension measurements is* $\pm 0.1mm$*. Highlighted row indicates the chosen unit cell for the MM.*

Unit Cell	**Buckling Mass (kg)**	**Extension (mm)** ± 0.1
C1	0.1	18.4
C2	0.3	18.7
C3	0.5	19.0
C4	0.3	18.8
C5	0.2	19.8
C6	0.3	18.8

All unit cell designs successfully deformed neighbouring cells in the combination test. Evident from the results in Table 4.1, unit cell C3 provides the best overall results of buckling mass ($0.5kg$) and extension ($19mm \pm 0.1mm$). Although C5 has the most significant extension, the thinner flexure regions result in an unfavourable triangular deformation pattern and subsequent tearing along the hinges due to overextension. The use of rigid elements in C3 alongside thick elastomer flexures creates greater mechanical strength, as shown by its resistance to buckling. Additionally, the actuation response of unit cell C3 is repeatable and takes the concave/convex shape as expected. Designs C2 and C4 are very similar to C3, and the extension results show the minimal difference between the three. However, results from the buckling load test show, the rounded centre of C2 and the flexure points at the unit cell corners in C4 result in a lower buckling load. In comparison, the cubic features of C3 and the reduced flexure regions result in an increased capacity to resist buckling and, therefore, provide better resistance to sidewall pressures.

A schematic of the final unit cell design and dimensions are shown in Figure 4.8. The white segments indicate Stratasys VeroWhite material [136]; the rigid corners act as hinges, rotating in response to the flexible members. The VeroWhite sections are connected to thick flexible members; here, the digital material FLX9950 (VeroClear + Agilus30) with a Shore hardness of 35-40A is used. The hardness value was selected to maximise the concave and convex shape of the unit cell whilst still maintaining its structural rigidity to resist pre-buckling from the sidewall pressures created by the bistable system.

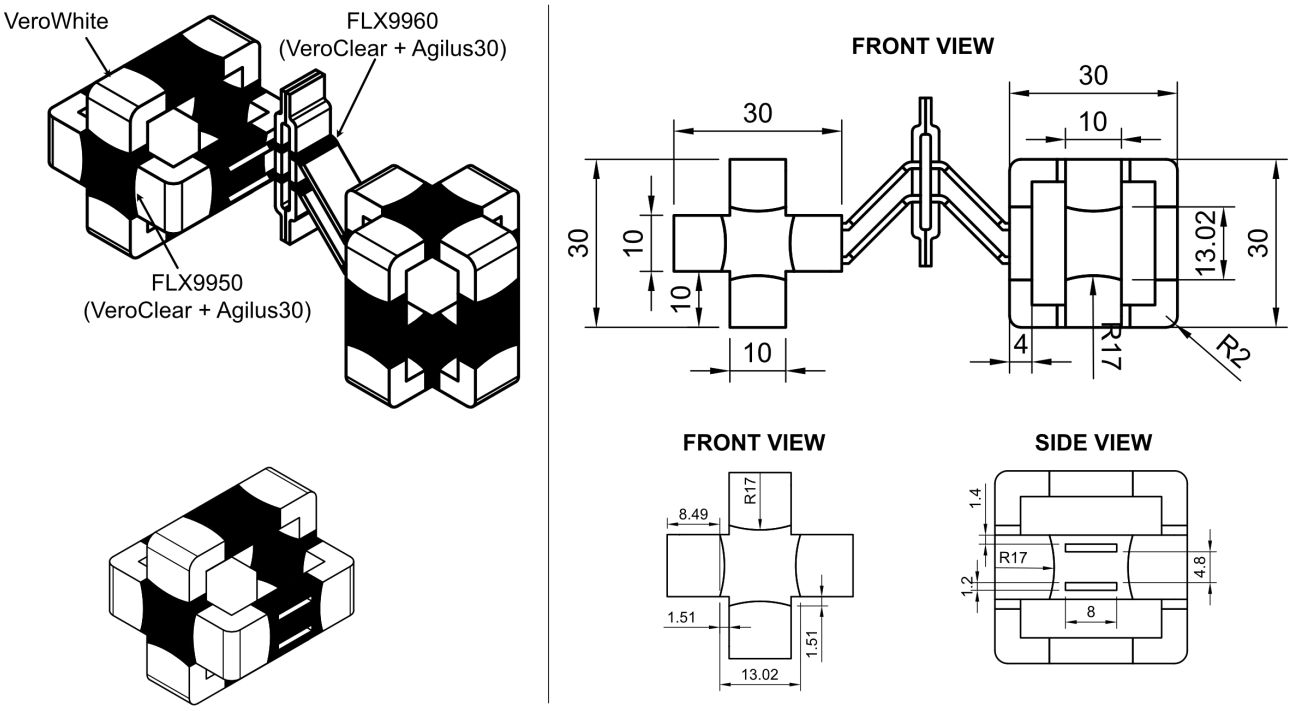


Figure 4.8: *Left - 3D render of MM in zy-configuration. Middle - 3D render of unit cell. Right - Technical drawing of unit cell. Units in mm, drawings not to scale.*

Bistable System Development

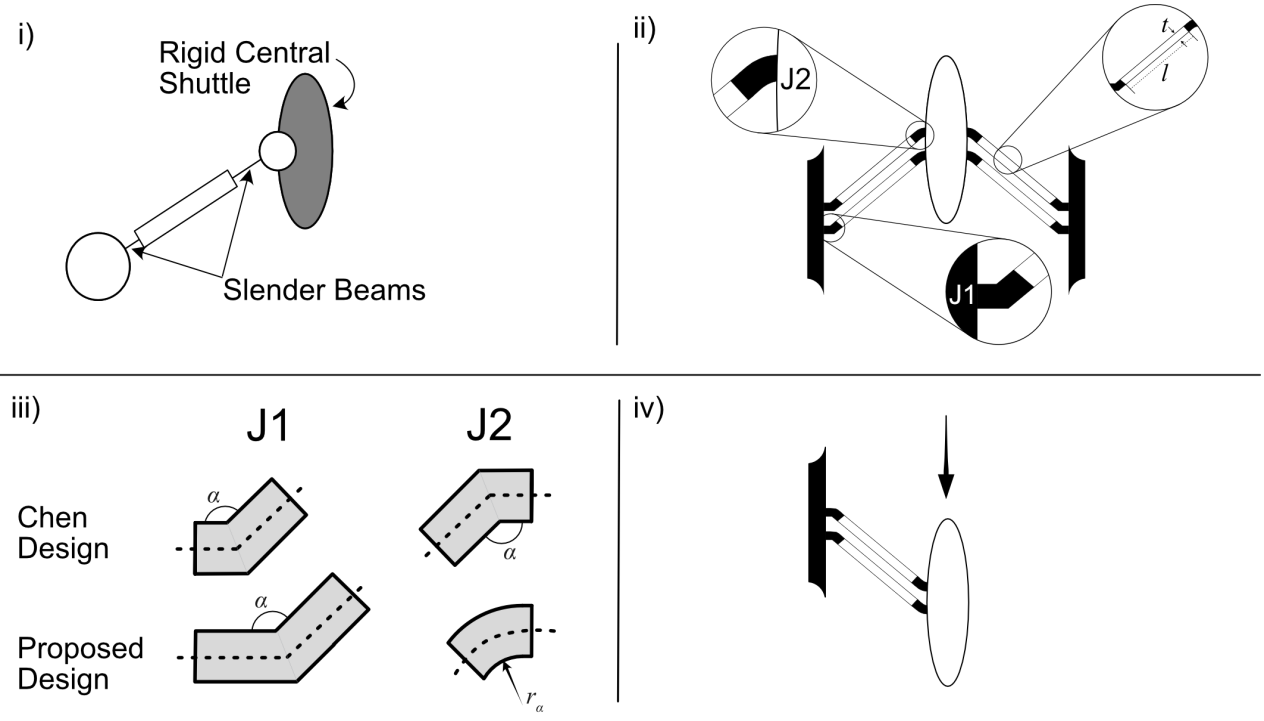


Figure 4.9: *Schematic of i) Compliant mechanism and multi-material flexure design (white segments are rigid, black segments are elastic), ii) 2D unit cell design in its rest and actuated state. Schematic of central shuttle as a i) compliant mechanism, ii) multi-material design and iii) in an energetic state against the biased printed orientation.*

The schematic in Figure 4.9 shows the development of the compliant bistable system into a design suitable for Material Jetting. As with the unit cells, the bistable system modelled from a VMT went through several testing and development stages. In particular, there are four variables to consider when designing the bistable system, the thickness (t), the strut length (l), the curvature of joint J1 & J2, and the hardness of the elastic material for the joints, highlighted in Figure 4.9.*ii*. The multi-material VMT design was first proposed by Chen *et al.* [45, 46] for a bistable unit actuator, connecting thin strut members to elastic joints. The initial dimensions of the bistable system were developed from the Chen actuator design [45, 46] along with the elastomer material properties, as the same Material Jetting technique is used. A study on the bistable properties for different hardness levels of the flexure mechanism has also been conducted by Chen [45, 46] informing the design changes of the proposed MM.

As the initial design is based on previous work using a similar process, an iterative design strategy is taken, qualitatively assessing how the snap-through response differs for different joint and strut designs. As shown in the schematic (Figure 4.9.*iii*), the joint designs J1 & J2 are compared between the original design ([45, 46]) and the proposed MM logic mechanism. These changes include increasing the length of the joint J1 to enhance the bias in the system. Joint J1 has a 135° gradient (α) for the bistable system to have a $+y$ bias. Additionally, the joint J2 is shortened and changed to a shallow curve to minimise the tearing of the elastic material. The slight curvature of J2 is designed to minimise any directional bias occurring from the shuttle. Joint J2 acts as a pivot, stabilising the movement of the shuttle. This ensures the system bias comes from J1, which is connected to the unit cell. Figure 4.9.*iv* shows the shape change of the joints when they are pushed against the printed biased state.

The schematics in Figure 4.10.a highlight the qualitative testing strategy. In the first test, the bistable system is connected in a 3x1 configuration to rigid walls fixed at a distance (d). As the separation distance remains the same, the different beam designs can be compared for their effectiveness at propagating mechanical signals. In the second test, the bistable system is connected to the unit cells, and the response to unit cell actuation is examined. By fixing the distance between unit cells to d, the different beam designs can be compared for their transition between stable states. Additionally, this helped determine the stresses involved during a snap-through event, the most promising joint design to minimise plastic deformation, and the elastomer properties that respond most effectively to unit cell actuation.

Several iterations of joint J2 were conducted, as shown in Figure 4.10.b. When stress testing the MM, joint design B1 continued to plastically deform and tear along the 135° (α) angle due to the

strain placed at the joint during a snap-through response. Joint design B3 takes a similar shape but uses a larger thickness to mitigate the tearing; however, this affected the system's responsiveness to unit cell actuation. Joint design B2 used a shallow curve; this was found to reduce any tearing during a snap-through event after several stress testing cycles.

Due to the nature of the Material Jetting process, a failure point of the VMT during testing was the connection between the elastomer and polymer sections. To mitigate this, J1 and J2 were extended through the shuttle and unit cell sections to increase the surface area between the different materials and improve adhesion. Figure 4.11 shows the final bistable system design and the corresponding dimensions as a technical drawing. The flexible hinges of the bistable system (J1 & J2) use the digital material FLX9960 (VeroClear + Agilus30). Although the material is tougher and has less elasticity than FLX9950, this adds a larger bias to the system to ensure a snap-through response is possible. Additionally, the tensile tear resistance is greater for FLX9960 (11-13Kg/cm). Due to the increased strain energy held at the ends of the VMT, excessive force and overextension of the MM often caused the joints to pull apart and fail. A failure point of using thin flexure elements is tearing along the joint, which is minimised when using FLX9960.

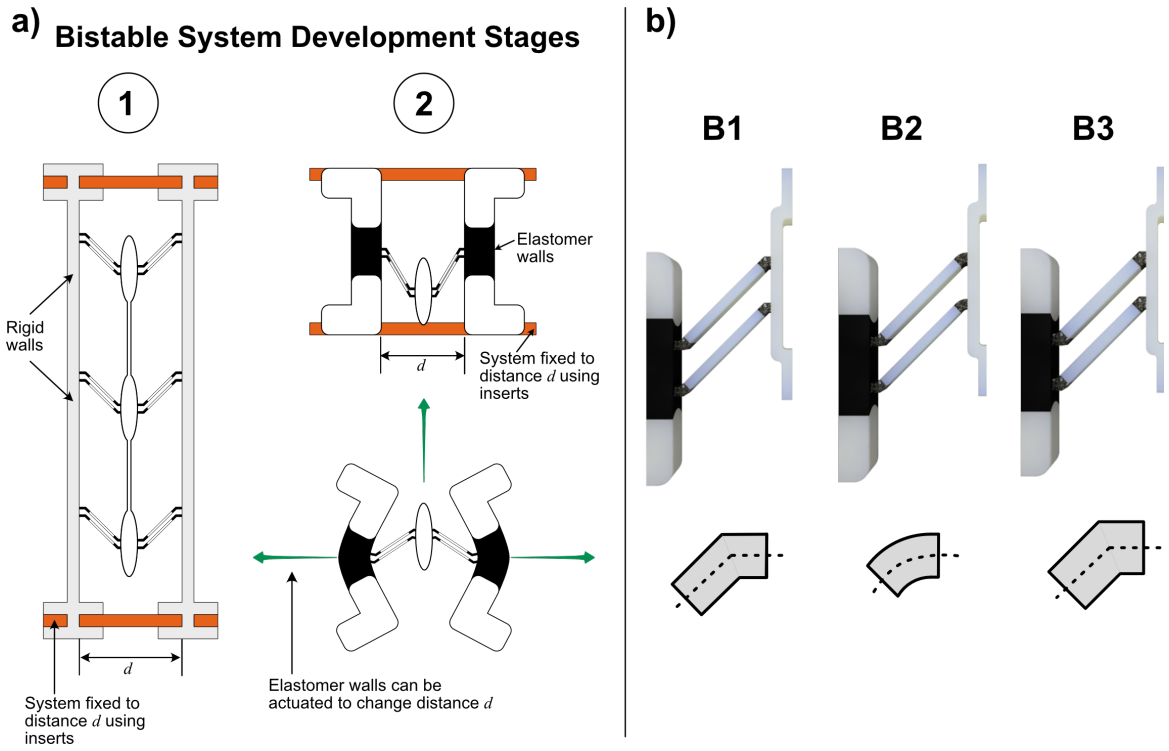


Figure 4.10: *a) 1 - 3×1 bistable system testing the propagation of a mechanical wave. 2 - testing the reponse of the bistable system to unit cell actuation at a fixed distance d. b) Three different beam and joint designs for the bistable system are shown. The schematic shows in closer detail the the J2 joint designs, which different in all three systems.*

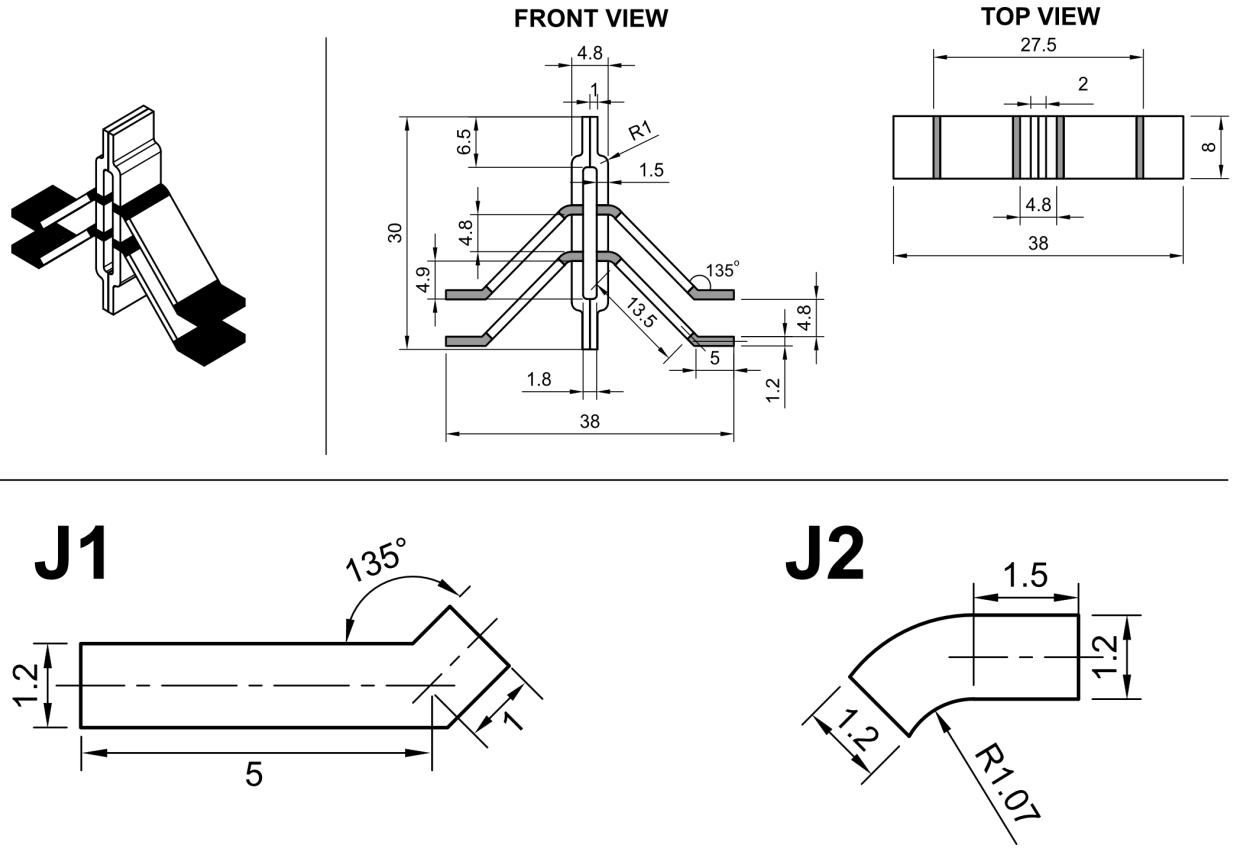


Figure 4.11: Left - 3D render of metamaterial in *zy*-configuration. Middle - 3D render of bistable system. Right - Technical drawing of bistable system. Units in *mm*, drawings not to scale.

4.4 Mechanical AND/OR Boolean Logic Gates

The purpose of developing the MM is to show that functional materials can perform mechanical logic, where the input and output are not unidirectional. In addition to the polarisation of the unit cells, the separation distance controls the effective length of the beam and determines the sequence of logic inputs necessary to allow the beam to move from a *LOW* (logical 0) to *HIGH* (logical 1) state. The schematic in Figure 4.12 shows how a 2D AND gate using this system functions. In step 1, the system is in its *LOW* state, as shown by the shuttle base positioned below the red line. As the unit cell on either side of the beam is actuated (step 2), the effective length of the beam increases. The potential energy in the beam is released at this stage, allowing it to propagate to a *HIGH* state (step 3), as shown by the shuttle apex above the green line. Due to the separation distance, both unit cells must be actuated simultaneously for the effective length to increase and the shuttle to move. Any other combination of inputs results in the shuttle remaining in a *LOW* state. The correct actuation sequence for an AND gate is shown in the printed example (Figure 4.12 - centre), the MM is inserted into a rig that maintains a separation distance of $31mm$ between the unit cells. The same MM can be inserted into a rig with a separation distance of $33mm$ to form an OR gate. In this case, only one unit cell

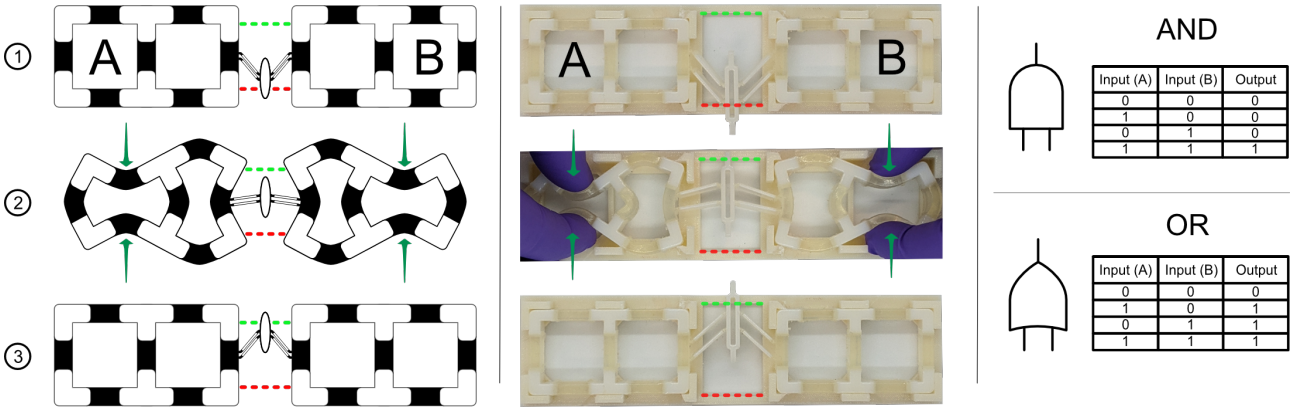


Figure 4.12: *Left - Schematic of a 2D mechanical AND gate. Centre - PolyJet printed 2D mechanical AND gate. Logic sequence of 2D mechanical AND gate - 1) LOW state (intersecting the bottom red line), 2) during actuation (unit cells A and B actuated simultaneously) and 3) HIGH state (intersecting the top green line). Right - AND\OR truth table.*

needs to be actuated for the shuttle to propagate. The subsequent investigation explores the change in logic conditions with changing separation distance for a 3D unit cell system.

As shown in this study, the use of anisotropic 3D unit cells offers significantly more control over the system's final state. Figure 4.13 shows the proposed PolyJet printed MM in a zy configuration for reference. The printed example has a z-polarised left unit cell and a y-polarised right unit cell, with respect to the defined axis. A *HIGH* input is defined as an actuation along the x, y or z-axis, and a *LOW* input denotes no actuation of the unit cell. The bistable system remains unchanged from the 2D example, moving along the y-axis. A *HIGH* output is in the $+y$ direction, and a *LOW* output remains in the $-y$ direction. The centre shuttle in Figure 4.13.a is currently in its printed state and therefore under a positive bias. The printed state is defined as the configuration in which the MM was manufactured on the PolyJet machine, in this state the shuttle has a positive bias facing along the $+y$-axis and the separation between the two unit cells is $30mm$.

In order to test the logic response as a function of separation distance between unit cells more robustly, a rig is designed to fix the unit cells (in any orientation) in place at a specific separation distance (d), and allows for mechanical actuation along the z-axis. As shown in Figure 4.13.b, the separation distance denoted d is the inner distance between the two unit cells. The proposed rig design shown in Figure 4.13 is printed in ABS (M30i) on a Fortus 400MC FDM printer. The rig comprises three main sections; the base holder, the fixed base, and the sliding base. The base holder lifts the MM to allow manual actuation along the z-axis and to hold the fixed and sliding base. The unit cells are inserted into an open base that holds them in place. The base can hold the unit cell in all three orientations, as shown in the schematic. The extruded section of the base holds the unit cell

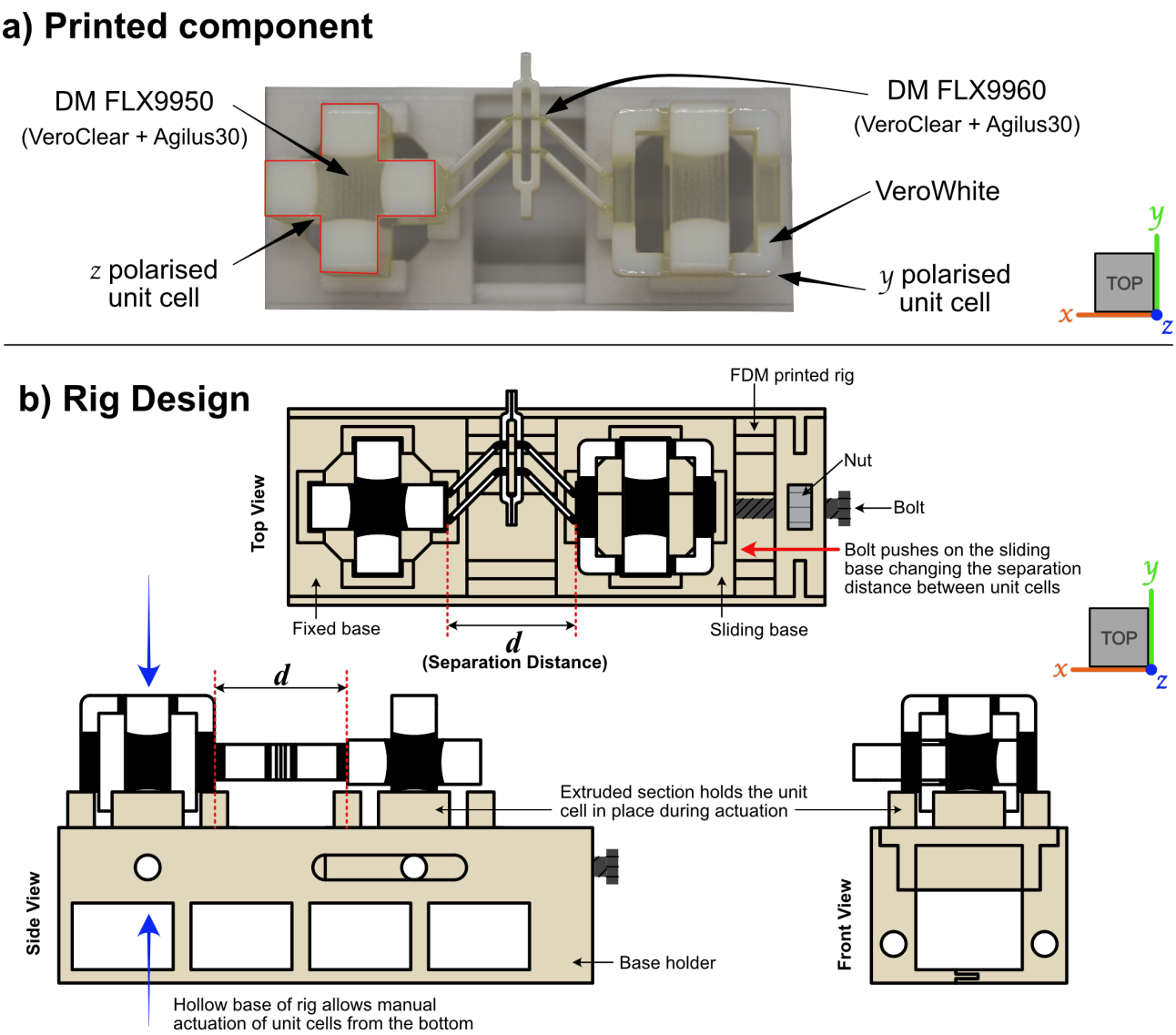


Figure 4.13: *a) 3D printed MM design held together in a variable distance rig. Printed mechanism is in a zy configuration. b) Top, side and front angles for the FDM printed variable distance rig.*

without impeding the concave/convex shape taken during manual actuation. Finally, the sliding base is free to move along the x-axis to change the separation distance d of the logic mechanism. The distance is changed using a bolt that pushes the sliding base in place. Once the distance is set, the sliding base is fixed in place using side bolts. The base holder and sliding bases limit the range of separation distances possible. Due to the design of the unit cell base holders, when the sliding bases are touching, a minimum distance of $d = 9mm$ between the two unit cells is achieved. When the sliding bases are extended towards the edge of the base holder, a maximum distance of $d = 39mm$ is achieved. $d = 39mm$ is also the physical maximum the VMT can be extended before stretching of the elastomeric joints takes place. At $d = 39mm$, the truss is horizontal, instead of the expected 45° angle when in the printed state. Although a Universal Testing Machine can accurately place the unit

cells in tension and compression, the multi-axis input approach poses several design challenges. The designed rig was purposely constructed as an open structure to allow manual actuation from all three axes whilst maintaining a fixed separation distance during testing.

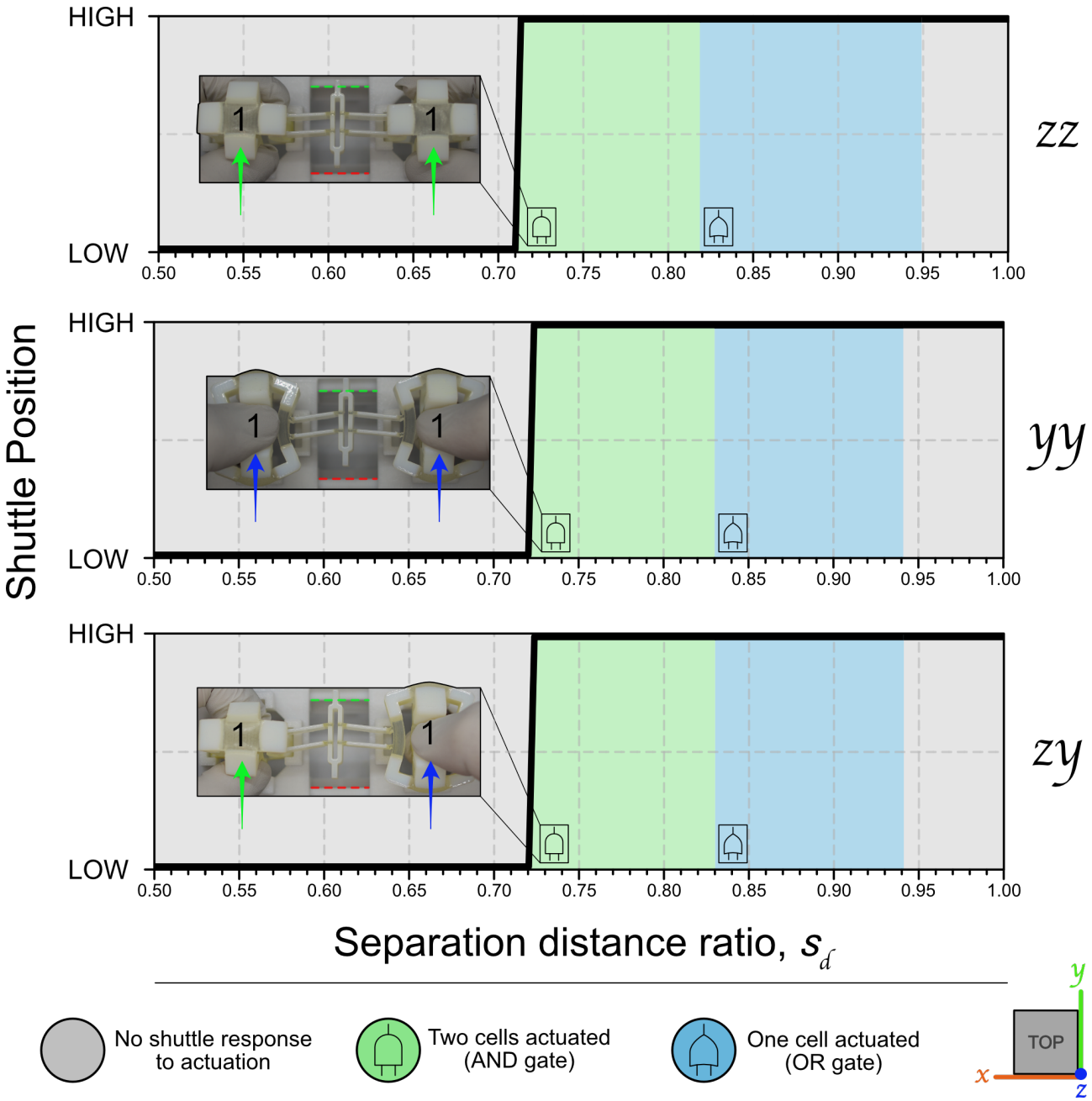


Figure 4.14: *Graphs show shuttle position against separation distance ratio (S_d) for three different logic gate configuration, zz, yy, zy. S_d is the separation between unit-cells (d) divided by the maximum length of the shuttle and slender beams (a) where a = 39mm. Coloured regions indicate the range of S_d values that result in a state change. Different colours indicate the number of unit cells to be actuated for a state change to occur, Green = 2 unit cells, Blue = 1 unit cell. Grey region indicates no system response to actuation, therefore remaining in a LOW or HIGH state. Inserts show the multi-planar MM AND gates during actuation, propagating from a LOW (red line) to HIGH (green line) state. Green/Blue arrows represent actuation in y/z directions respectively. [137]*

As shown by Song *et al.* [82], although planar mechanical logic systems can be 3D printed using two-photon stereolithography, the development to multi-planar systems has yet to be developed. The

printed logic MMs currently capture the mesoscale response of a mechanical system. However, the proposed functionality is independent of size and should function as predicted at the microscale. As a result, the following ratio is introduced,

$$S_d = \frac{d}{a} \tag{4.3}$$

where S_d is denoted the separation distance ratio, d is the current separation distance between unit cells and a is the maximum separation distance achievable for the mechanical system. The ratio S_d allows for comparison across multiple scales of mechanical systems and to aid in understanding the limitations in subsequent designs.

The graphs in Figure 4.14 show the response of the shuttle to unit cell actuation as a function of the separation ratio for three different configurations, zz, yy & zy. x-polarised unit cells have not been shown, as these require a combinatorial approach for the effective length of the bistable system to increase. The graphs show the ratio (S_d) required for the shuttle to propagate from a LOW to $HIGH$ state. The response of each MM for the different separation distances were tested five times. The results shown are the averages for the testing runs, the standard deviation and overall uncertainty in testing is discussed in later sections. The maximum length of the slender beams and shuttle is $a = 39mm$. The coloured regions of the graph show the number of unit cells that need to be actuated for the shuttle to propagate from a LOW to $HIGH$ state after two cells are actuated (green region) or one cell is actuated (blue region). When both unit cells require actuation for the shuttle to propagate, the MM behaves as an AND gate. When only one unit cell is required, the MM behaves as an OR gate, often at a larger separation distance. The grey region represents no shuttle response to actuation. When the system remains in a LOW state, this indicates the effective beam length cannot be increased by actuating the unit cells enough for the shuttle to propagate. When the system remains in a $HIGH$ state with no response to actuation, this is due to the lack of compression on the bistable system resulting in the elastic joints holding very little strain energy. At these separation distances, the system cannot be placed in a LOW state.

Actuation of the unit cells occurs through manually pressing the cells quasi-statically until the inner walls touch. Due to the viscoelastic properties of Agilus30, applying actuation quasi-statically is necessary to ensure consistency in gate inputs. The range of separation distances for each configuration differed, highlighting the effect polarisation and the direction of actuation have on the response of the shuttle system. Each MM is tested three times and the average result is shown in the graph. In the yy

& zy configurations, the MM behaved as an AND gate between separation ratios (S_d) $\sim 0.72-0.82$ (2 s.f.) and as an OR gate between $\sim 0.83-0.94$ (2 s.f.). In comparison, the zz configuration behaved as an AND gate between separation ratios $\sim 0.71-0.82$ (2 s.f.), and as an OR gate between $\sim 0.82-0.96$ (2 s.f.). Videos of the device behaving as an AND [1] [2] & OR [3] gate can be found using the footnote links. Measurements of separation distance were made using a Vernia scale. Due to orientation and the nature of the unit cell designs, the error in distance measurement is $\pm 0.1mm$, and the error in S_d is ± 0.005. The uncertainty in separation distance is an accumulation of the limiting error of the Vernia calipers used, error in printing dimensions from the 3D printing technology and measurement error in properly aligning the calipers to the rig. The uncertainty quoted takes into account error with the measurements and apparatus, but fails to capture the error in actuation (quasi-static loading by manual compression), the visco-elastic nature of the joint elements, and the ageing affects on the mechanical properties of polymers that will effect the long term repeatability of the mechanism. This is most evident at the limit regions for example, as the MM stops behaving as a mechanical buffer but transitions to a logical AND gate. The error taking into account the variability in testing gives an error in d of $\pm 0.2mm$ from the standard deviation, and the error in S_d is subsequently ± 0.01. A further study is required on the changes to the logic states over time, as the research has shown degradation and ageing affects of photopolymers over short and long periods [122, 138].

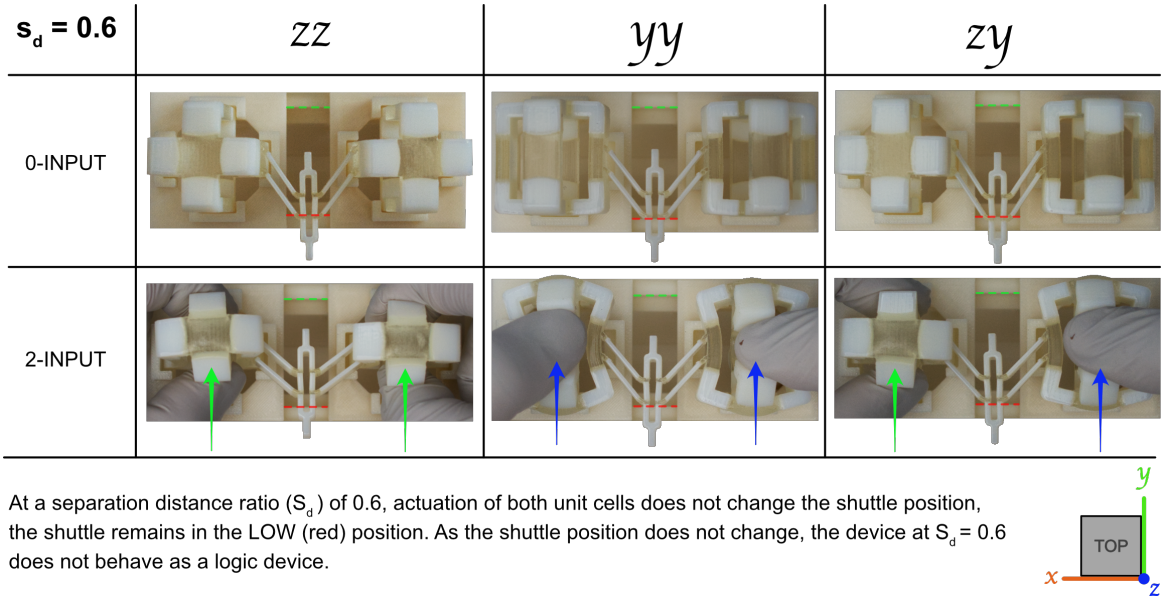


Figure 4.15: *Images capture the mechanical logic devices in three different configurations at a separation distance ratio of* $S_d = 0.6$.

[1] AND gate - `https://vimeo.com/532490204`
[2] zy AND gate - `https://vimeo.com/532491614`
[3] OR gate - `https://vimeo.com/532491022`

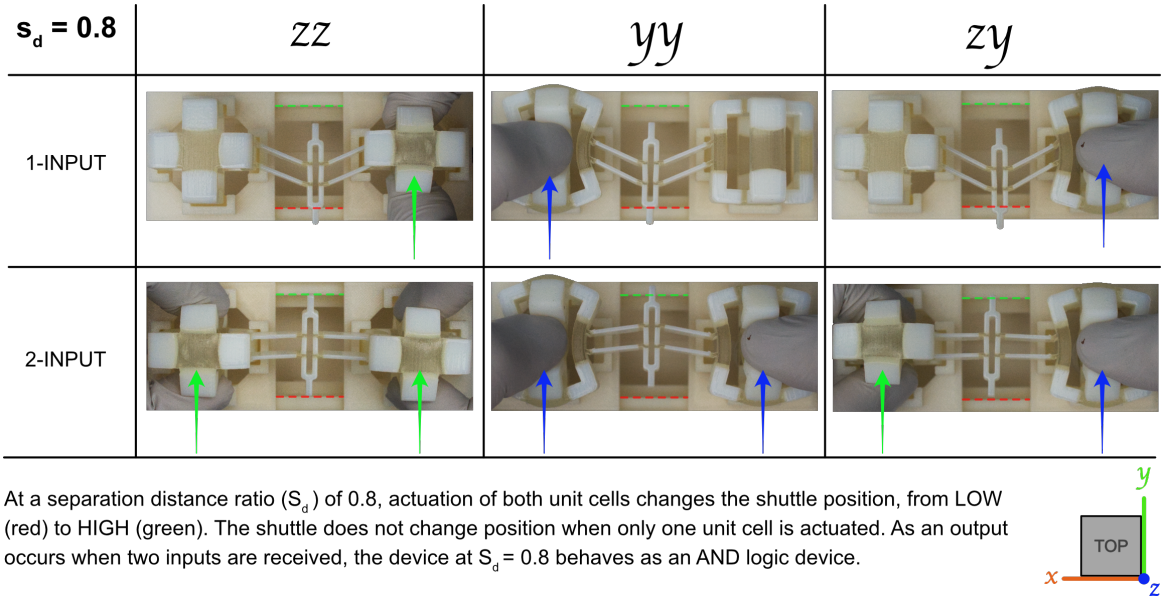


Figure 4.16: *Images capture the mechanical logic devices in three different configurations at a separation distance ratio of* $S_d = 0.8$.

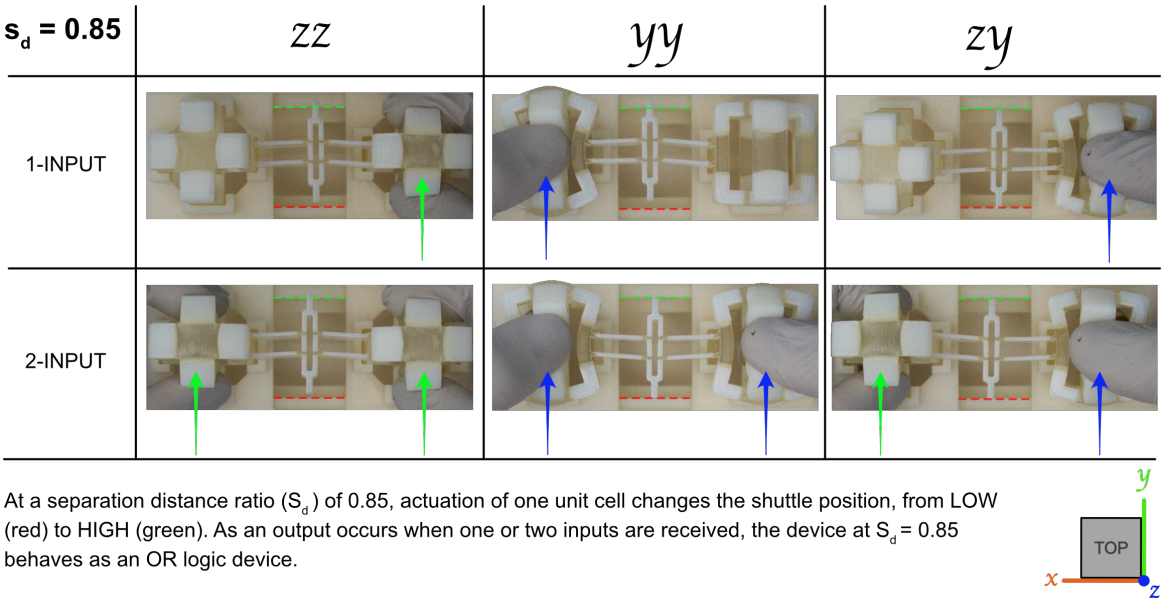


Figure 4.17: *Images capture the mechanical logic devices in three different configurations at a separation distance ratio of* $S_d = 0.85$.

The inserts in Figure 4.14 show the actuation and shuttle propagation for an AND gate for all three configurations. The blue and green arrows indicate the actuation of the unit cell from the z and y axis, respectively. The images capture the snap-through event during actuation as the shuttle system moves from a *LOW* (high strain) state to a *HIGH* (low strain) state. Further snapshots of the shuttle response during actuation for the four separate response regions $S_d = 0.6$ (grey), $S_d = 0.8$ (green), $S_d = 0.85$ (blue) and $S_d = 0.98$ (grey) are shown in detail in Figures 4.15, 4.16, 4.17 and 4.18 respectively.

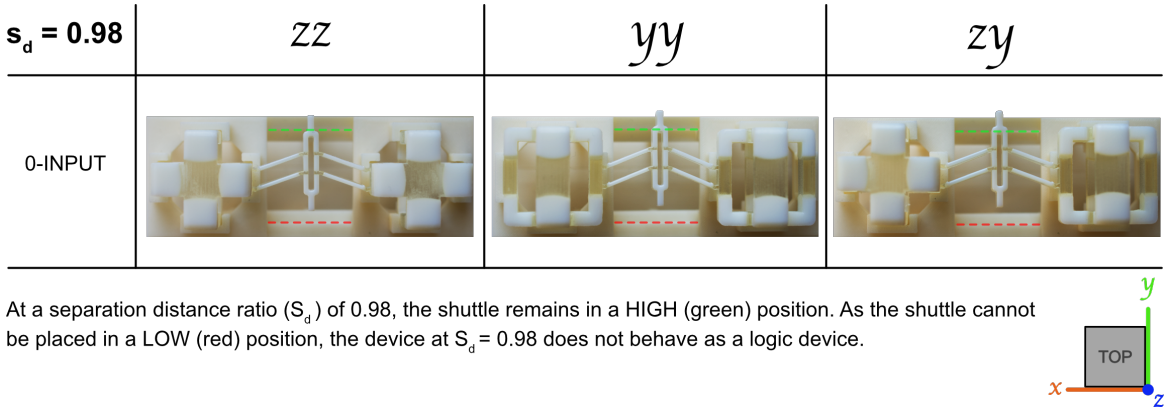


Figure 4.18: *Images capture the mechanical logic devices in three different configurations at a separation distance ratio of* $S_d = 0.98$.

At $S_d = 0.6$ (Figure 4.15), the separation distance between the unit cells is $23.4mm$. When both cells are actuated, the effective beam length cannot be increased far enough to allow the shuttle to propagate. The device at this separation distance does not perform mechanical logic.

When $S_d = 0.8$ (Figure 4.16), at this separation distance ($31.2mm$), all three configurations behave as an AND logic gate. The images shown are snapshots of the device during actuation. When one unit cell is actuated, the shuttle remains in a *LOW* position in all three configurations. When both unit cells are actuated, the effective beam length increases, allowing the shuttle to propagate from a *LOW* to *HIGH* state.

Figure 4.17 shows the device's response when $S_d = 0.85$, at this separation distance ($33.15mm$) all three configurations behave as an OR logic gate. As shown, the shuttle propagates from a *LOW* to *HIGH* state if either one or both unit cells are actuated.

When $S_d = 0.98$ (Figure 4.18), the central beam system is close to being fully extended. The figure shows that at a separation distance of $38.22mm$, all three configurations cannot be placed in the energetic *LOW* state. As a result, the actuation of the unit cells does not change the state of the system. The device at $S_d = 0.98$ does not perform mechanical logic.

4.4.1 X-Polarised Unit Cells

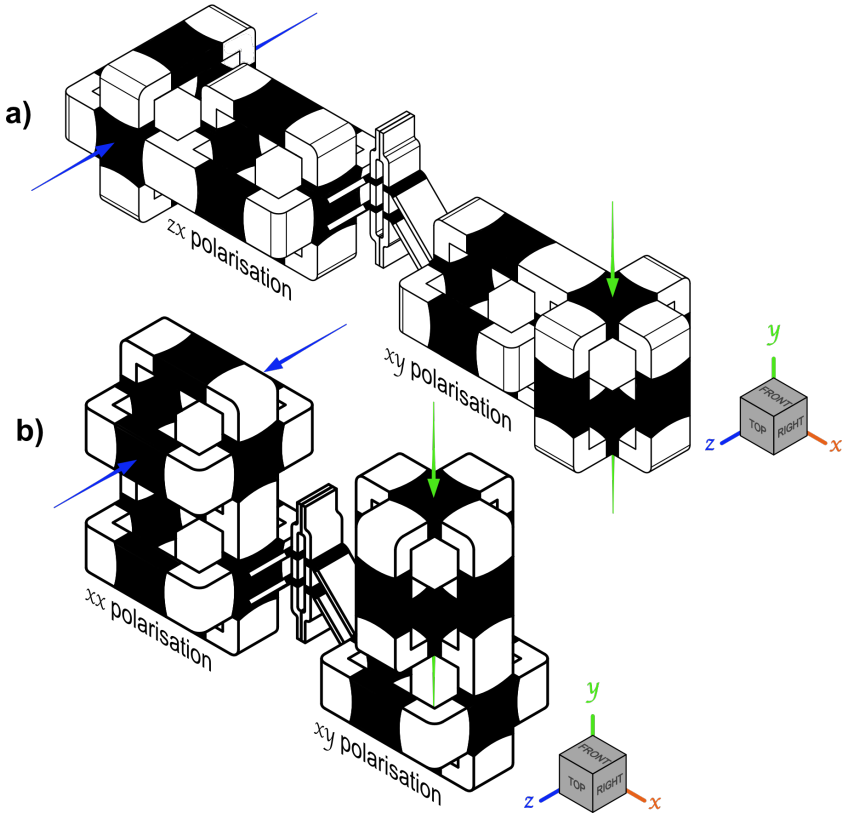


Figure 4.19: *Top - Schematic of a zx-xy polarised mechanical logic gate along the x-axis. Bottom - Schematic of a xx-xy polarised mechanical logic gate along the x-axis. Coloured arrows indicate the plane of actuation required to increase the effective beam length of the system.*

Figure 4.19 shows a schematic for a proposed AND/OR logic gate design using x-polarised unit cells. In single unit cell designs shown in Figure 4.14, the x-polarised unit cell has limited functionality; neither manual actuation (compression) from the y or z axis will cause the effective beam length to increase. This is unless the sides of the unit cell are pulled outwards (tension) instead of pushed inwards. As a result, a combinatorial approach is needed to create the desired concave shape for the x-polarised unit cell. The system's complexity increases; if the inner unit cells are x-polarised, there are nine different combinations for the outer unit cells.

The proposed zx-xy logic gate shown requires a z-axis actuation on the left-most unit cell and a y-axis actuation on the rightmost unit cell. This will cause the ends of the x-polarised unit cell to take a concave shape, increasing the effective beam length of the system. The number of configurations in a 4-unit cell device can be increased further by changing the connectivity axis between the unit cells. Figure 4.19 shows two logic gate designs, one in which the connectivity axis is along the x-axis and the other along the y-axis. The proposed xx-xy logic gate shown requires a z-axis actuation on the top left unit cell and a y-axis actuation on the top right unit cell. The two variations of the same logic

gate show the added programmability of using anisotropic unit cells, as input and output events in a single metamaterial device can occur in multiple planes.

There are, however, limitations to connecting unit cells for mechanical logic. As a result of the quasi-static loading on the unit cells, the energy loss during an actuating event from the elastic flexure elements results in a reduced transformation of the connecting unit cell. Moreover, as the inner x-polarised unit cells are connected to the bistable system, the tension in the combined system adds further resistance to deformation. This effect is minimised when the actuation is not quasi-static, as the momentum of compression improves the deformation of the connected unit cells. Also, taking a combinatorial approach and adding more than two unit cells on each side increases the deformation on the x-polarised connecting cell.

The two designs shown have been printed and successfully demonstrate Boolean AND/OR logic; however, as stated previously, the loss during quasi-static actuation results in an inconsistent response to actuation. Consequently, the results in Figure 4.14 focused on single unit cell designs to ensure results were repeatable and consistent.

4.5 Standard Logic Gates

In this section, different MMs to perform complex logic functions are developed. In particular, can universal logic gates be achieved? One strategy is to develop NAND and NOR gates, the complements of AND and OR, respectively. If NAND and NOR gates are achieved and gates can be cascaded, obtaining the standard logic gates (all Boolean functions) is theoretically possible. These include: AND, OR, NAND, NOR, NOT, Buffer, Exclusive-OR and Exclusive-NOR. This set of standard logic functions underpin modern computation today. As AND and OR gates have successfully been developed, the universal logic gates can be realised by developing an Inverter (NOT gate).

4.5.1 NOT Gate

Figure 4.20 shows a proposed Inverter. The design comprises a standard zz-polarised AND gate as shown in Section 4.4 and a flipped yy-polarised AND gate, the central shuttle of the two gates are connected. The schematic shows the systems state as printed and when inserted into a rig. As previously discussed, a *HIGH* state in the logic system is a low potential energy state of the MM.

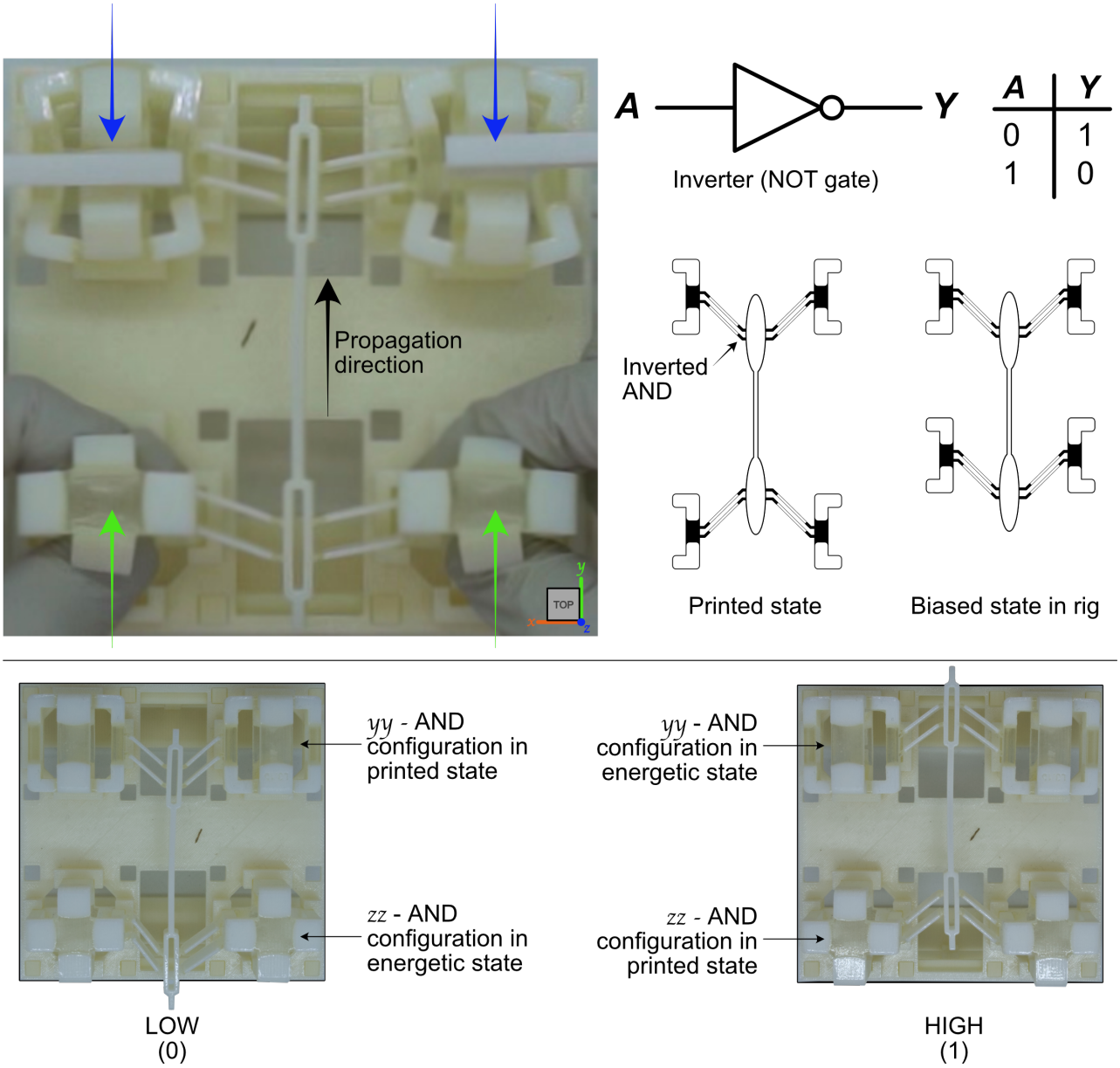


Figure 4.20: Proposed Inverter design. Top left - printed gate under actuation, arrows indicate the plane of input and the expected propagation direction of the system. Top right - NOT gate truth table and a schematic of the design in its printed state and once placed in a rig. Bottom - Images of the *LOW* and *HIGH* states of the NOT gate.

Conversely, a *LOW* state is a high potential energy state. The schematic of the MM placed in the rig shows the *zz* configuration in a *LOW* state and the upper flipped *yy* configuration in a *HIGH* state. It is predicted that as all unit cells are simultaneously actuated, the release of the potential energy in the *zz* system will force the opposing *yy* system into its energetic *LOW* state. As an entire logic system, this will result in an inversion of the output analogous to a NOT gate.

Figure 4.20 shows the printed gate design and the corresponding *LOW* and *HIGH* states of the NOT gate. The top left image shows a snapshot of an actuation event; the state is predicted to change

from *LOW* to *HIGH*. However, the printed MM does not invert the signal due to the losses that occur during actuation and snap-through. As the opposing shuttle is in its biased state, there is resistance against the propagating shuttle. Furthermore, the elastic flexure elements release energy; thus, the energy supplied into the system is not the same as the energy released during a snap-through event. This example shows the limitations of the mechanical systems, as the energy losses are significant barriers to cascading logic and obtaining the universal logic gates.

4.5.2 Connected Logic Gates

The previous section explored cascading logic gates and whether the output from one gate can influence the other. As shown, however, the current design using elastic flexure elements is a lossy mechanism that results in the snap-through event dissipating less energy. Although connecting the shuttle of two mechanisms in series has shown not to suit the current design, there are several different configurations of how logic gates can be connected. In this section, two connected AND gates sharing an input, and a four-input AND gate sharing an output are explored.

Connected AND gate

Figure 4.21 shows an example of two AND gates in series with a shared input. The double AND gates are in a yzz configuration, with two separate bistable systems sharing unit cell B. The top image shows the system's response to all three unit cells simultaneously actuated, resulting in a *HIGH* output for Y_1 and Y_2.

Figure 4.21.i, ii, & iii show the system's state in different input events. As shown in 4.21.i, the parallel set of AND gates can be actuated separately. If A and B are actuated, a *HIGH* output will occur at Y_1 as the system is currently in an AND configuration. As described earlier, an OR gate can be formed by increasing the separation distance between unit cells. If the system is changed to a double OR gate, actuation of unit cells A and B will result in a *HIGH* output at Y_1 and Y_2. The schematic in 4.21.ii shows the system's response when unit cells A and C are actuated. As this is an AND gate, both output Y_1 and Y_2 remain *LOW*. Example 4.21.iii shows the design freedom in a shared input system, as one system can be placed in a *HIGH* state whilst the other remains LOW. The propagation direction can also be flipped if unit cells A, B, and C are actuated simultaneously, Y_1 can propagate to a *LOW* position and Y_2 to a HIGH position.

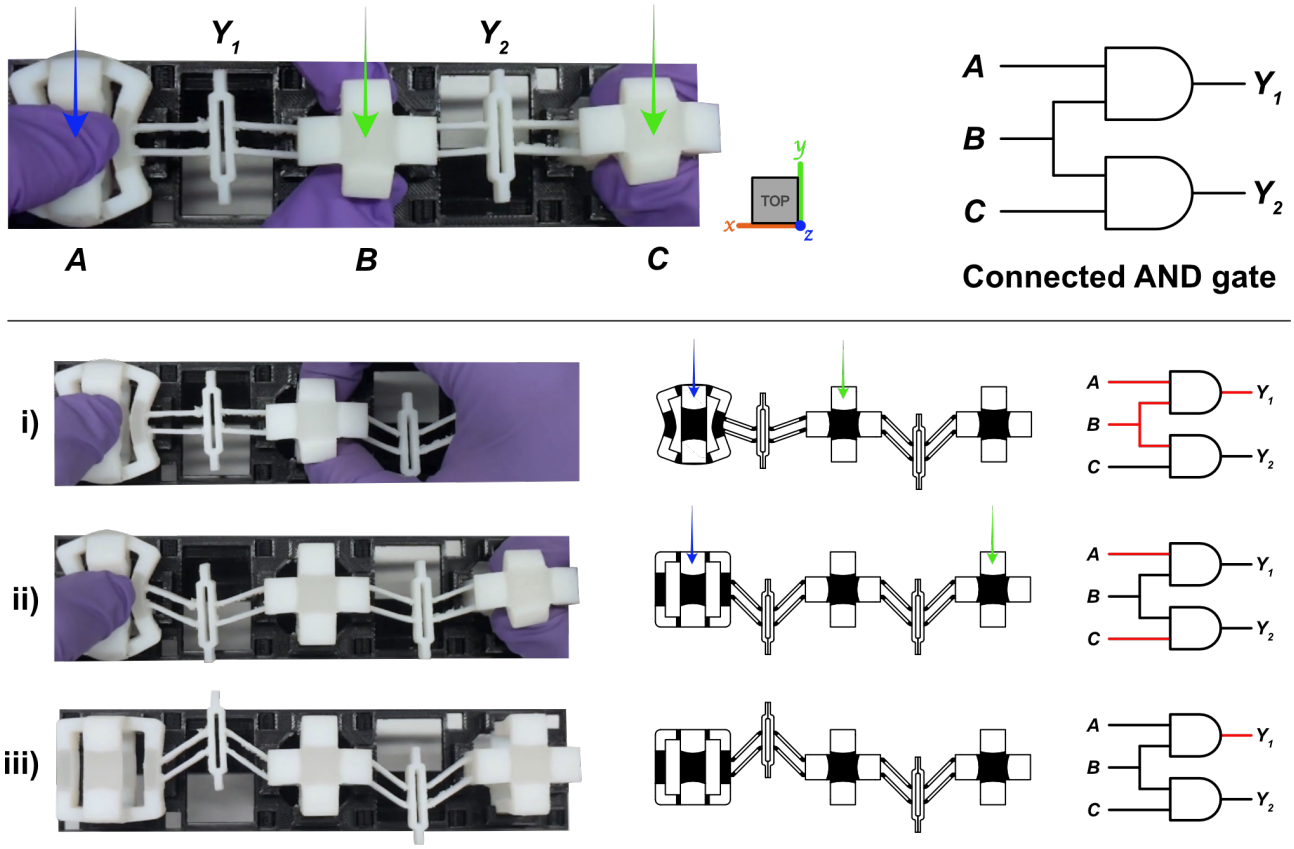


Figure 4.21: *Connected AND gate. Top - Snapshot of 2 AND gates with a shared input actuated simultaneously. Centre shuttles Y_1 and Y_2 transition from LOW to HIGH. i) Single angle is actuated, Y_1 becomes HIGH. ii) Outer unit cells are actuated, Y_1 and Y_2 remain LOW. iii) No actuation, Y_1 is HIGH and Y_2 is LOW.*

Four-input AND gate

Figure 4.22 shows a proposed four-input AND gate with separate inputs but a shared output. The system is a double AND gate with the central shuttle connecting the two logic MMs. Actuating unit cells A and C do not result in a change of state, as the beams connecting unit cells B and D are still in their LOW position resisting any upwards motion. To change the state of the system from LOW to $HIGH$, the four-unit cells $ABCD$ must be actuated simultaneously. The two images below in Figure 4.22 show the respective LOW and $HIGH$ states of the four-input AND gate. The system is robust; testing has shown that when three simultaneous inputs occur, the resistance from the single VMT in the LOW position resists a change of state. There are physical limitations of the current design compared to an interconnected input system. The central shuttle is a cuboid shape with each side joined to a VMT. This particular shuttle geometry is well suited for a four-input system. However, an input system larger than four will significantly change the central shuttle and VMT design. Moreover, additional unit cells are limited in their placement in the logic system without requiring unit cells to be combined.

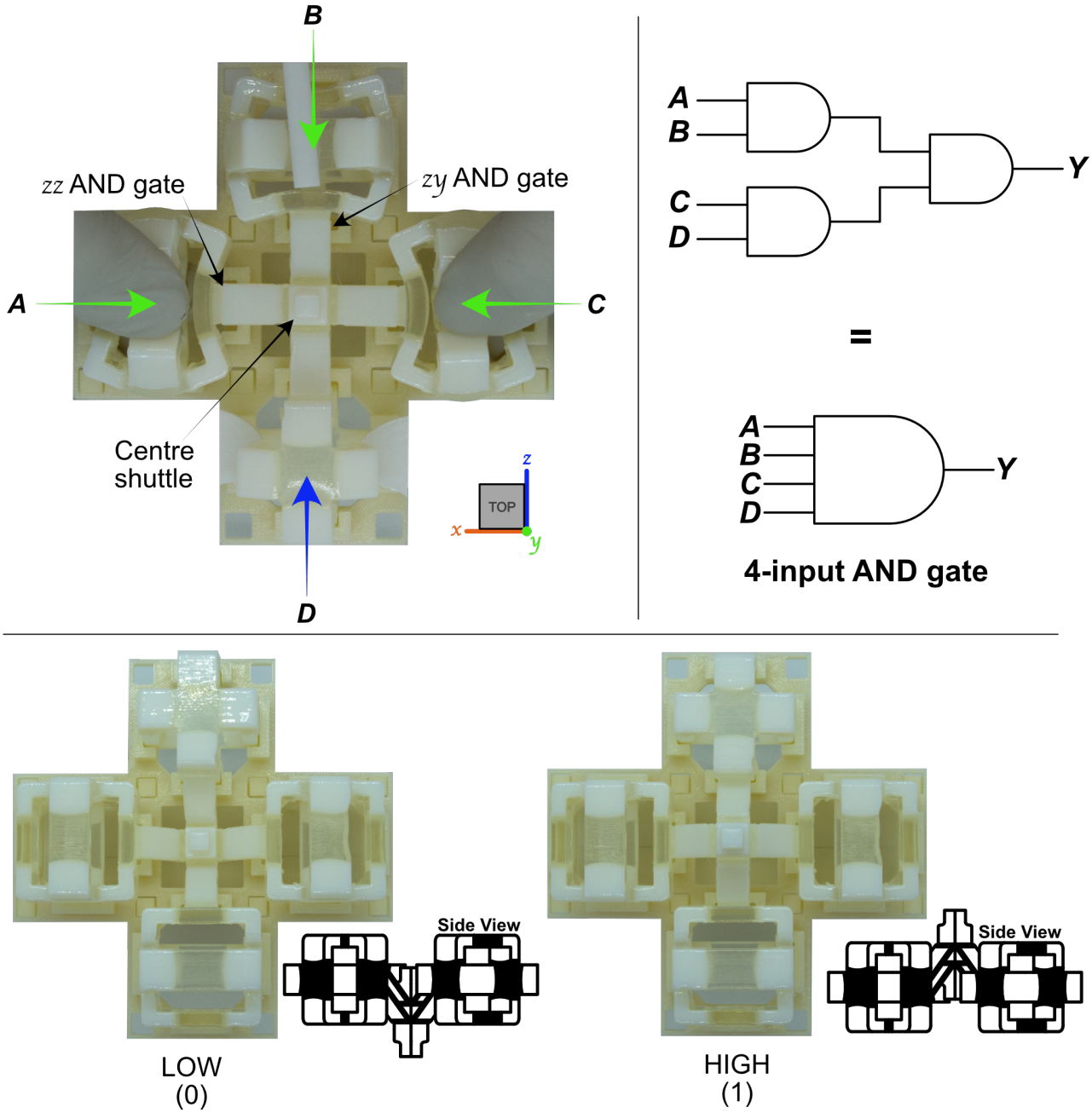


Figure 4.22: *Four-input AND gate. Top - Snapshot of Four-input AND gate with all unit cells correctly actuated, centre shuttle transitions from LOW to HIGH state. Below - Images of LOW and HIGH states for Four-input AND gate.*

4.6 Discussion

The logic gates in Figure 4.14 highlight the design freedom of 3D anisotropic unit cells. In previous examples [80, 81, 82, 126], the designs explored in the literature were unidirectional. This limited the number of responses possible for the MM design. Using anisotropic unit cells, the orientation of the cells provides a further layer of tunability to the FMM. Not only do the correct unit cells need to be actuated, but the direction of input must also be correct. This is shown in the *zy* AND gate; separate

inputs are required from the z and y directions for the shuttle to propagate. Due to the nature of the unit cell, incorrect input directions cause the separation distance and the effective beam length to reduce. Consequently, minimising the likelihood of a state transformation occurring as the potential energy barrier of the buckling system is increased.

The difference in separation distances for the three configurations highlights the importance of unit cell polarisation to the bistable system response. This is due to the beam joint (J1) orientation with the unit cell, most notable in the zz configuration as the joint extends in the z-axis, vertically across the unit cell. This results in the zz configuration having the most extensive range in separation distance from which the shuttle propagates. When fully actuated, the sides of the unit cell take a concave shape, reducing in width from $30mm$ to $22mm$. The width reduction remains the same when the unit cell is z or y-polarised. However, in a z-polarised unit cell, the joint passes through the centre of the elastic flexure element. As a result, when the cell is actuated, the maximum change in separation distance occurs. When in a y-polarisation, the joints do not pass through the centre of the unit cell; therefore, the shuttle system does not fully extend with the actuated unit cell.

Section 4.5 highlighted some of the shortfalls of using a biased VMT system for mechanical logic. A bistable system with asymmetric stable states limits the proposed logic gate design to single-use Boolean logic. When the state of the system changes from *LOW* to *HIGH*, significant losses are experienced as potential energy is released due to the nature of the elastic flexure elements. As a result, cascading logic gates where the output from one gate drives the input for the next becomes increasingly difficult, as evident in Section 4.5.1. The input energy required for the subsequent gate is higher than the output energy of the actuated gate. Furthermore, asymmetric states limit the different logic functions attainable. As the system always wants to return to a *HIGH* state, inverting an output by using NOT gates (4.5.1) cannot be achieved with the current design arrangement. Inverted gates such as NAND and NOR have yet to be demonstrated and remain a goal for multi-plane MM logic systems.

Previously mentioned by Merkle [78] for a reversible logic system, the implementation of mechanical computing redefines how logic is implemented. As shown in Sections 4.4.1 and 4.5.2, the use of anisotropic unit cells for logic manipulation introduces unique multi-plane configurations to be exploited. The use of MM for logic is not intended to replace current electronic systems and compete on efficiency. Instead, transforming direction dependant quasi-static inputs into distinct mechanical movements has advantages in many industries in which electronics are limited. The connected logic gates have shown as an early example; tunable materials can be built from controlling the

snap-through motion of nonlinear systems using anisotropic unit cells. It shows that complex logic systems are attainable, but a rethink of logic architecture is necessary to build FMMs.

In summary, this chapter aims to show the programmable and tunable nature of MM through the development of logic mechanisms that exhibit multi-plane behaviour; two of the questions to investigate for the research question. In conclusion, the manufactured MMs showed repeatably programmable and tunable behaviour in a multi-plane system that utilised different input and output directions to perform Boolean logic.

Chapter 5

Tunable Bistable Mechanical Metamaterial System

In this chapter, a novel MM control system is developed, combining compliant anisotropic unit cells to coupled slender beams. The separation distance between the fixed ends of a slender beam can be used to tune the MM between monostable and bistable states. The MM control system exhibits typical sense-decide-respond capabilities akin to a sensor and actuator system, subsequently allowing mechanical signals to pass only when the correct actuation pattern and force is applied. The FMM is shown to be inherently passive, as it returns to a monostable state after actuation. The FMM is printing using SLA technology and is experimentally validated using a Universal Testing Machine. The mechanism's bistable response is successfully programmed by changing the level of actuation on the unit cells. The proposed FMM has particular industrial applications as mechanical tunable accelerometers integrated into lattice systems.

5.1 Mechanical Control System

Active materials that respond to non-mechanical forms of energy have many applications in soft robotic systems, as a result of their ability to sense and adapt to environmental changes and subsequently actuate in response to system changes [75, 76, 77]. Light stimuli can inhibit a snap-through response of bistable arches [71], creating functional devices such as a light-driven Venus flytrap [65]. Hydrogels swell when exposed to water; this response is programmed to build complex three-dimensional morphologies [72, 73, 74] and have been shown to perform Boolean logic [66].

MM structures that respond to mechanical energy, such as the architected material with beam elements by Shan *et al.* [44], exhibit multistable capabilities suitable for trapping elastic strain energy. These energy-absorbing materials are beginning to be utilised in industry for personnel protective equipment and crash mitigation in automobiles. Structures such as the FRMM by Jackson *et al.* [63] presents tunable stiffness behaviour. This has been proposed for soft robotics and as rapidly adaptive helmets due to the significant changes in mechanical properties in response to a magnetic field. In addition to their energy-absorbing capabilities, auxetic structures are proposed as locomotion mechanisms in inchworm-type soft robots to crawl through small channels. Yang *et al.* [139] shows several actuator examples by developing a metamaterial that buckles under negative pressure. Finally, Chen *et al.* [46] has designed a propulsion mechanism for soft robots, tethering a shape memory polymer to actuate a bistable element that drives fins and propels a soft robot.

A common theme amongst many MMs is the utilisation of elastomeric structures to form adaptive complex mechanisms, due to large deformations and non-linear behaviour in response to stimuli. As shown in Chapter 4, these can be designed to have programmable and tunable behaviour. However, the previously proposed structures are limited to function only in specific well controlled environments. With the exemption of Origami and Kirigami deployable structures in the aerospace industry, MMs have seldom been explored for their control capabilities in applications that require mechanical *sense-decide-respond* control loops, to the complexity of microsystem devices used in harsh environments.

To create functional devices that can be utilised in mechanical systems such as accelerometers in automobiles and the aerospace industry, a level of compliance must be shown, that metamaterials can be manufactured using semi-rigid materials and withstand harsh environments whilst still maintaining functionality. Although the deformations possible will be limited, this chapter explores how compliance can be factored into a MM design to build functional mechanical systems.

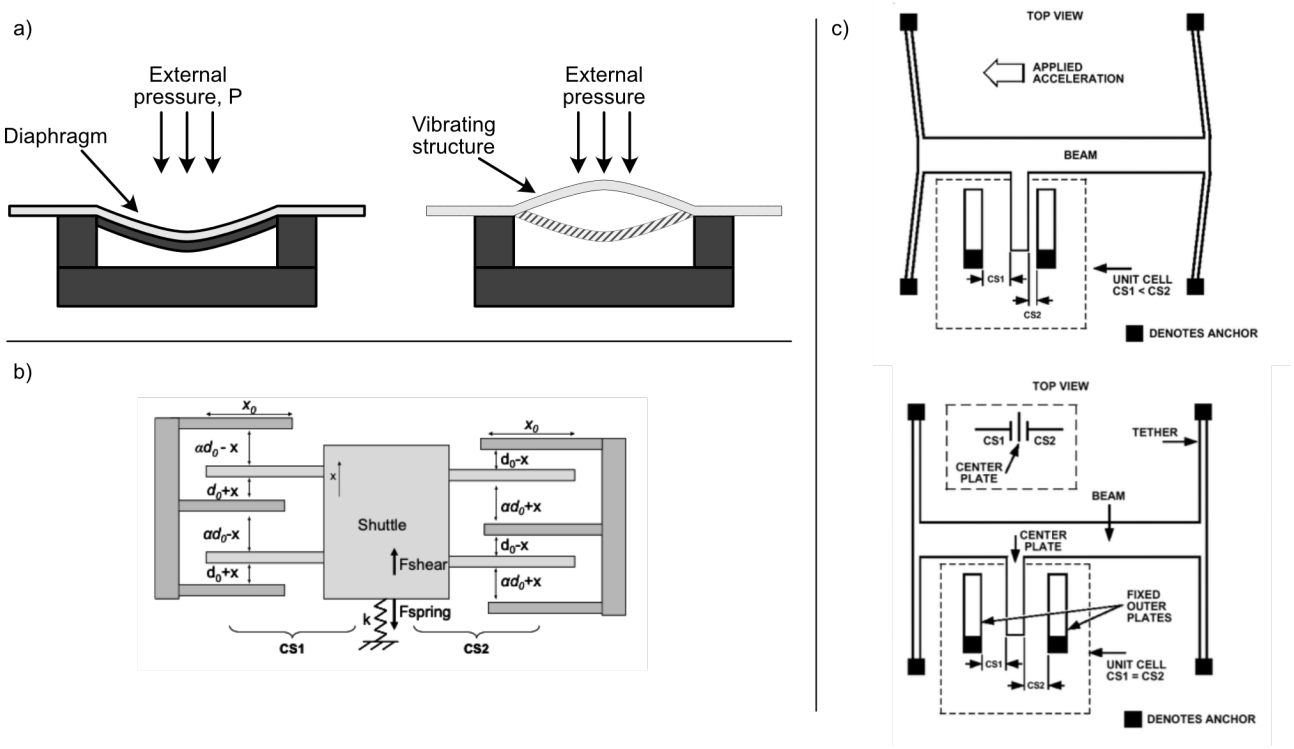


Figure 5.1: *Typical MEMS sensor designs used in industry. a) Force deflectors for elextronic pressure sensors. Left - Diaphragm based sensor. Right - Resonant based sensor [140]. b) Shear stress flow sensor for harsh environments measuring drag through differential capacitance [141]. c) Acceleration sensor, movable central plate deflects in response to changes in relative motion up to ±50g [142]. Schematics adapted from: (a) White and Kraft [140], (b) O'Grady et al. [141], and (c) Analog Devices, Inc. [142].*

To fully understand the role MM control systems can have in industry, it helps to understand current mechanical devices' uses and how similar design concepts are shared [143]. In particular, Micro Electro Mechanical Systems (MEMS) have several applications in industries such as automotive and aerospace [140]. MEMS refers to the process of combining mechanical and electrical components into an integrated device at the microscale. The mechanical functionality in MEMS devices is built on top of the integrated circuit technology; structures are formed using a multitude of techniques, including High Aspect Ratio Micromachining (HARM), a subtractive process, and Liga (lithography, electroplating and moulding), an additive and subtractive process that can manufacture multi-layered complex mechanical systems ontop of polysilicon wafers. MEMS has found significant uses as microsensors and microactuators due to their ability to be well integrated into the system's electronics. MEMS applications are vast, ranging from inkjet printer heads to data storage systems [140]. A widely used MEMS is the strain gauge, used for occupant sensing to ensure controlled airbag deployment is dependant on whether the passenger is a child or adult. Designs such as a diaphragm or resonant structure as shown in Figure 5.1.a are used to measure the external pressure on a car seat. In the automotive industry, designs such as the MEMS capacitive sensor

(Figure 5.1.c) are used as accelerometers for crash sensing systems, used within the electronic airbag control unit (ECU) [140]. ECU's monitor decelerations for frontal collisions in the order of 35 to 100g and accelerations for side impacts of up to 250g. MEMS systems are becoming an enabling technology in the aerospace industry due to their comparable size and weight reductions, their low power consumption, the efficiency of sensing capabilities, and the application in harsh environments. One such design is the shear stress sensor (a capacitive sensor) as shown in Figure 5.1.b [144, 141]. Here the shear force causes a displacement of a shuttle connected to a spring system. This displacement causes a change in the separation between fixed and moving electrodes resulting in a measurable capacitance change.

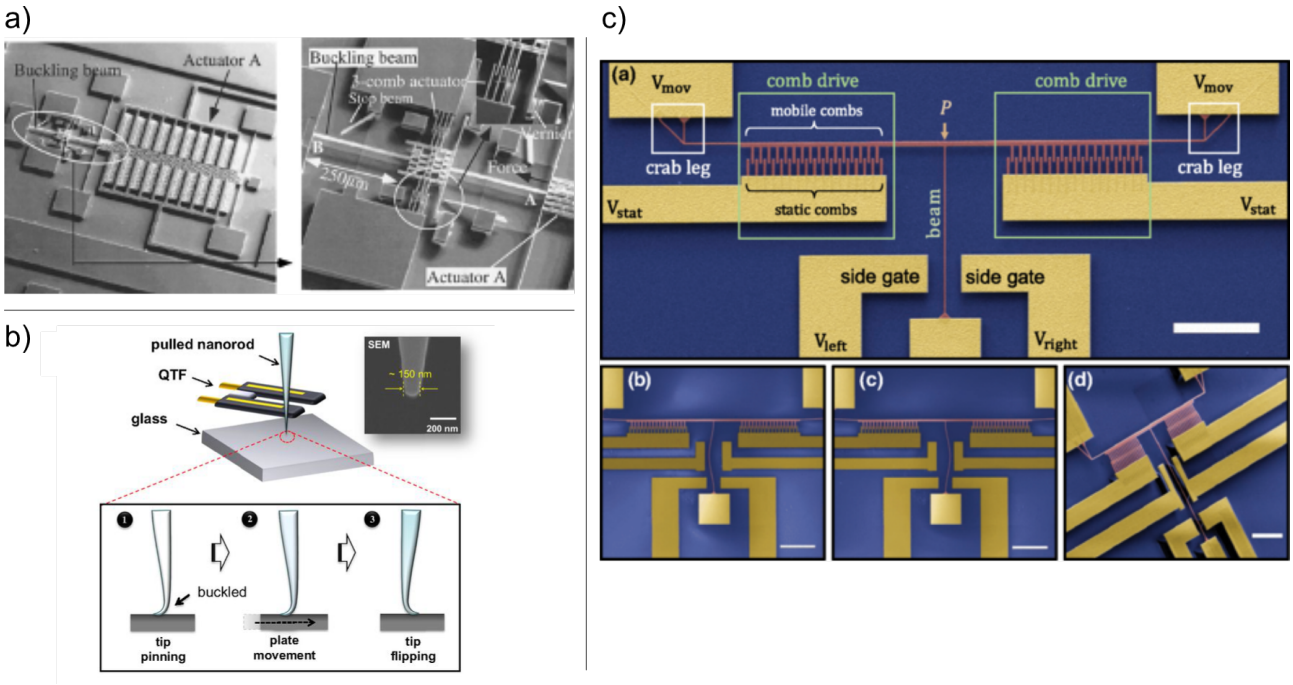


Figure 5.2: *MEMS examples utilising buckling instabilities. a) Three-comb actuator connected to a buckling beam creates a tunable buckling system for digital sensing of physical parameters [145]. b) Buckled cantilever beam for use as a mechanical force sensor [146]. c) Electrostatic control of buckling through mobile comb drives to tune the compressive force on a slender nanobeam [147]. Images adapted from: (a) Saif [145]. (b) An et al. [146], and (c) Erbil et al. [147].*

The advancements in manufacturability have significantly pushed the complexity of microsystems that are now adopted widely in everyday products. Of particular interest to functional material design using MM are microsystems that utilise buckling and snap-through phenomena for sensing and actuating capabilities. Bistable systems exhibit advanced sensing capabilities due to the large deflections possible when crossing a bifurcation point that is more apparent than tracking traditional dynamic behaviours, such as the system's natural frequency. As described in previous sections, MMs have been widely shown to utilise elastic instabilities but have yet to show a coherence with similar sensing and actuating applications developed in microsystems.

Designs such as a buckled cantilever beam (Figure 5.2.b) have been shown to function as highly sensitive force sensors capable of measuring precursor seismic events [146]. The pulled quartz nanorod cantilever design exhibits greater sensitivity, reproducibility and repeatability to conventional seismometers. A tunable mechanical relay is developed that utilises piezoelectric actuation. The piezoelectric films generate stress along the slender beam causing it to buckle [148]. Similarly, mechanical memory has been shown using a buckling beam. The beam buckles as a result of compressive stress through resistive heating [149]. The sensing and actuating capabilities introduced through bistable systems are numerous, including devices such as accelerometers, shock sensors, switches, thermal actuators, positioners, valves, relays and memory units [150].

The proposed metamaterial design in later sections explores tunable bistability first proposed by Saif [151, 145] and collaborators [152]. In addition to applications such as accelerometers, magnetic field sensors and tilt sensors, tunable bistable phenomena are practical for configurable optomechanical systems [153]. More recently, Erbil *et al.* [147] has shown the ability to tailor the response of a double-well system such as a buckled bistable beam. Bistable mechanisms have been shown to have far-reaching applications; for example, they are an active research initiative to implement qubits. The dynamic control of the compressive stress on a slender beam and the tuning of the potential energy landscape at will has not been fully explored and studied in great detail, particularly in purely mechanical systems [154]. It is desirable to show that a bistable system's tunable behaviour can be realised without the need for residual and thermal stresses in the system.

5.2 Proposed Tunable Bistable System

In this section, a novel mesoscale tunable bistable system is proposed. As AM technologies continue to develop and printing at the microscale becomes increasingly refined, programmable MM capabilities to perform functions over multiple axis is advantageous compared to typically planar microsystems. The proposed compliant MM transitions from monostable to bistable in response to a patterned actuation similar to the MM proposed by Coulais [58]. As a result, pattern-sensing coupled with a tunable bistable system opens up the capabilities for FMMs and their implementations into more complex systems.

Introduced in Section 4.2.1, Figure 5.3 shows the behaviour of a thin, slender beam under a compressive force above the critical buckling load (P_{cr}). As the force F, continues to increase above P_{cr}, the maximum deflection of the beam d begins to increase. This is registered in the potential

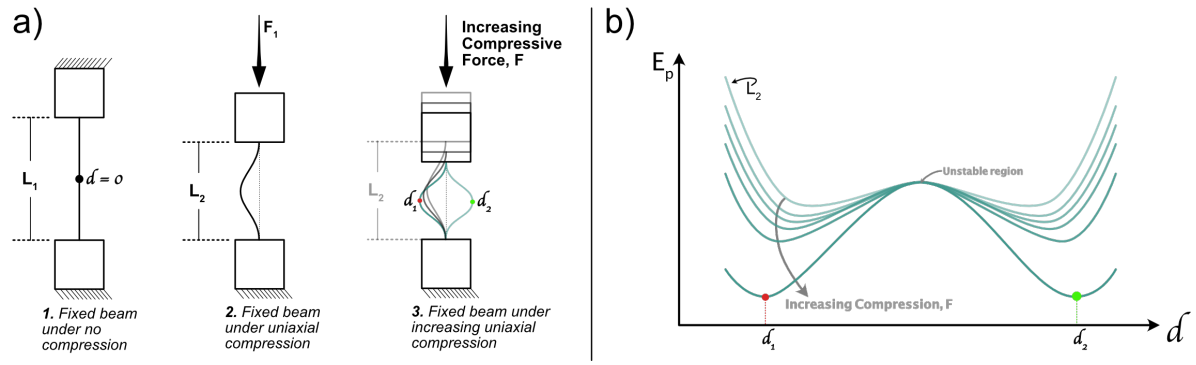


Figure 5.3: *a) Schematic of a fixed-fixed slender beam 1) under no compression, 2) under constant uniaxial compression and 3) under increasing uniaxial compression. b) Potential energy (E_p) vs displacement (d) graph for a beam under increasing compression. Potential barrier increases from initial buckled state L_2 as the uniaxial compressive force F is increased.*

energy vs displacement diagram, increasing the potential energy required to transition between states. As shown in previous examples [145, 147, 151, 152, 153], the ability to tune the critical snap-through load F_{th} by tuning the effective beam length can be used for sensing capabilities. Whereas the 'fine tuning' of the snap-through force in mechanical systems is often a result of the thermal or electrostatic response, the proposed mechanism explores an entirely mechanical system, combining anisotropic unit cells to a beam system. As shown in Chapter 2, MMs' unique properties result from the global response of units cells in a lattice structure. An entirely mechanical system that performs similar functionality allows for greater programmability of AM parts, introducing systems that respond to environmental changes coupled with actuation capabilities to dynamically respond.

Figure 5.4.a shows a simplified rigid body model of the tunable bistable system. Here, a linear spring is combined with a rigid beam and central shuttle restricted to vertical motion. When no force is applied, the system is in a monostable state. When a force is applied, this causes the shuttle to move either up or down. The shuttle position will remain stable in this position as long as the applied force remains constant. A second force on the shuttle can cause a transition between states. The linear springs are used to model the unit cell's expected deflection in response to an opposing force. In Figure 5.4.b & c, the proposed mechanism in compliant mechanism notation is shown. The central nodes indicate inflexion points, and the beams indicate rigid sections of the anisotropic unit cell. The schematic highlights the behaviour of the system during actuation. Figure 5.4.b shows the monostable state when no actuation is present. A probing force along the shuttle would cause a small oscillation along the $x = 0$ position until the equilibrium state is reached. When a correct actuation pattern and force above P_{cr} is reached, the system responds by causing the beams to buckle, as shown in Figure 5.4.c. The green nodes indicate the actuation position. Because the unit cells are combined,

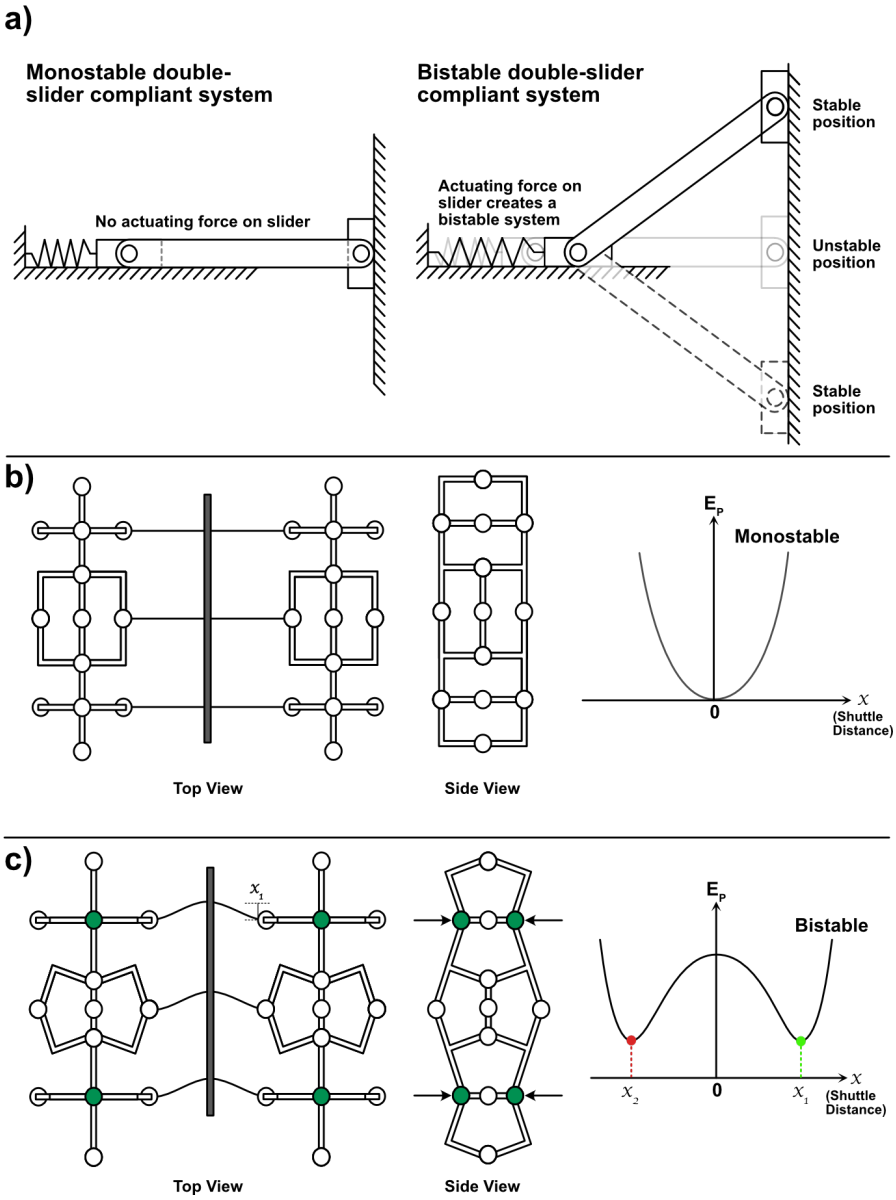


Figure 5.4: *a) A double-slider mechanism in a monostable and bistable configuration, dependent on the actuation force and sprint constant. Schematic adapted from Jensen and Howell [155]. b) Compliant mechanism design in a monostable state, unit cells connected to slender beams with no compressive actuation force. c) Compliant mechanism design in a bistable state, unit cells connected to slender beams with correct actuation force applied.*

the desired deformation occurs when the actuation is frustration-free, i.e. the load occurs on specific unit cells. A probing force on the central shuttle F_{th} will cause the beams to transition to their second stable state, defined as the snap-through event.

Although a single unit cell and beam system will show the same monostable to bistable phenomena in response to actuation, utilising frustration-free deformation of combined unit cells introduces additional capabilities of pattern sensing through textured input-output material response and holographic ordering first proposed by Coulais [58] for MMs. The proposed device is therefore

sensitive to the actuation force and its relative position, forming part of the *sense-decide-respond* control loop. Also, as first discussed by Vangbo [130], a single clamped-clamped beam can result in higher buckling modes under specific loading conditions and an asymmetric deformation pattern of the beam during a snap-through event. A coupled beam system is utilised to reduce the likelihood of higher buckling modes, ensuring the shuttle's linear movement. The bistable characteristics follow the same conditions as a fixed-fixed slender beam; however, no asymmetric modes can develop, therefore postponing the critical point of snap-through. This chapter limits the investigation to a three beam system; this simplifies the design for analysis and is shown in several research papers [156, 157, 158]. Although a smaller mechanical system (3x1) is investigated, the proposed unit cells can be combined into a larger architecture [58]. Furthermore, an array of bistable systems can be connected to allow propagation of mechanical waves [80], the proposed concept is scalable to larger or microscale metamaterial systems.

The proposed MM is a compliant mechanism to be manufactured using a semi-rigid polymer suitable for flexure mechanisms. SLA technology is better suited to printing flexure mechanisms than Material Jetting due to greater resistance against brittle fracture and isotropy. In Chapter 4, the PolyJet printed logic gates occupied a print bed area of $37cm^2$, with the unit cell size of $30mm$. Desktop SLA machines are limited in size; the Formlabs Form2 used to manufacture the MM has a print bed size of $210cm^2$. As a combinatorial MM design approach is taken, the proposed MM will have a 50% reduction in size, with a unit cell size of $15mm$. This allows the mechanism to still apply to mesoscale manufacturing techniques, but a 3x1 combined mechanism with a square area of $21cm^2$ can now be printed on a desktop SLA. As the MM is designed to behave as a tunable mechanical system, a smaller scale and compliant (single material) design better exemplify the functionality for industry applications.

5.3 Compliant Mechanism Design

There are several examples presented in the literature on compliant mechanism design of mechanical components. In particular, Compliant Mechanisms by Howell [143] provides a comprehensive introduction to mechanism design and explores in great detail bistable compliant systems. In most single material designs found in literature, the mechanical mechanisms are highly planar, rarely utilising added functionality from additional planes. The examples that propose multi-plane designs occur through out-of-plane compressive buckling of a 2D system [91]. The proposed MM design

poses several design challenges, as there has been little exploration of 3D printed compliant architectures. Furthermore, manufacturing 3D anisotropic unit cells with compliance poses challenges for repeatability and reproducibility.

5.3.1 Beam Design

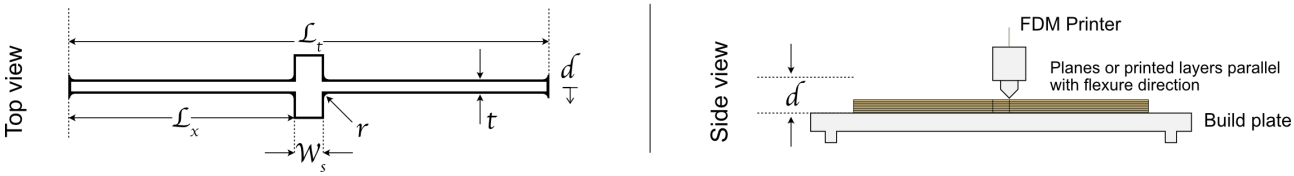


Figure 5.5: *Left - Schematic highlighting the key dimensions of the fixed-fixed slender beam including central shuttle connecting multiple beam systems. Right - Schematic showing the optimal layer build direction and printing orientation for improved flexural response of slender beam.*

Table 5.1: *Slender beam dimensions, variables refer to the schematic shown in Figure 5.5.*

L_t **(mm)**	L_x **(mm)**	W_s **(mm)**	t **(mm)**	S_r $(\frac{L_t}{t})$	d **(mm)**	**r (mm)**
21.88	10.31	1.25	0.6	36.46	2.50	0.15

In compliant systems constructed from semi-rigid materials, the slenderness ratio (thickness/length) strongly influences the mechanism's flexural response. This contrasts with the flexure mechanisms in Chapter 4 (VMT and unit cells). From utilising the multi-material printing capabilities, flexure was a result of the elastic joints connected to thicker rigid members. For the proposed compliant MM, a typical Euler-Bernoulli beam is used. The technical drawing in Figure 5.5.a shows the proposed beam design. Table 5.1 shows the respective beam dimensions.

A Euler-Bernoulli beam was also chosen due to the simplification in the manufacturing process. Whereas VMTs are best suited to PolyJet printing due to multi-material capabilities, printing compliant beams in a single material is possible using all technologies. As there is no curvature (pre-stress) to the slender beams, they can be manufactured in the optimal orientation to maximise the flexural response. This is by printing along the beams long axis, as shown in Figure 5.5.b using FDM as an example of the layer by layer AM process. Stepping can occur when gradients are introduced, as shown in Section 3.3; printing horizontal beams significantly improves the repeatability in the printing process and reduces any inconsistencies introduced when manufacturing in challenging orientations. Further discussion on the printing constraints of slender beams is described in Section 3.4.

In addition to the material properties and printing direction, the slenderness ratio defines the beam's buckling capabilities and snap-through properties. The slenderness ratio is limited to the printers resolution. Although the Formlabs Form2 printer has a laser spot size of $140\mu m$ and can print a beam of this thickness, testing has shown inconsistencies with such dimensions. Furthermore, due to likely defects during the printing process, printed slender beams are subject to breaking. As a result, a lower slenderness ratio was used (36.46). This was achieved by increasing the thickness of the beam to reduce the effect of any defects and maintaining the beam's length to ensure the overall mechanism size remains the same.

5.3.2 Unit Cell Design

The compliant mechanism unit cell design poses several challenges due to its 3D orientation. When printing horizontal with the print bed, the beam's properties are expected to be uniform, excluding any inconsistencies in the printing technology used. There are several orientations to consider in a 3D anisotropic unit cell and no favourable direction to maximise the entire unit cell's flexural response. The unit cell aims to transfer directional force to the beam ends, causing the beams to compress and buckle under the loading force or be in tension from the outward force created by the unit cell. The unit cell's actuation is direction-dependent, and the combination with neighbouring cells must be considered for frustration-free movement. As all three orientations can be used in the proposed mechanism (x, y, z-polarisation), the added flexural response gained from printing along the deformation direction is reduced. In addition to manufacturing 3D flexural components using AM processes, a compliant mechanism design and type of flexural response are challenges in 3D configurations. As shown in Chapter 4 for a 3D multi-material unit cell, the sections where the unit cell beams meet (often the thinnest section) is often the point of increased crack propagation and failure, due to restricted flexural response and point of increased stress during actuation. This is shown in Section 3.4 through design iteration and testing the anisotropic response of different flexure designs. As such, flexural designs must be considered that deform as expected in all three spatial directions, consider printing orientation and ensure no buckling occurs in response to the restoring force created from the beams outward side-wall pressure during snap-through.

The schematics in Figure 5.6 show the development of flexure hinge designs suitable for use in compliant mechanisms [159, 160]. As shown in Figure 5.6.a, a goal is to design a compliant unit cell design that replicates the elastic response of a biholar unit cell. In the 2D plane, this can be shown by using living hinges at the pivot points. Several single flexure designs are analysed in Figure 5.6.b,

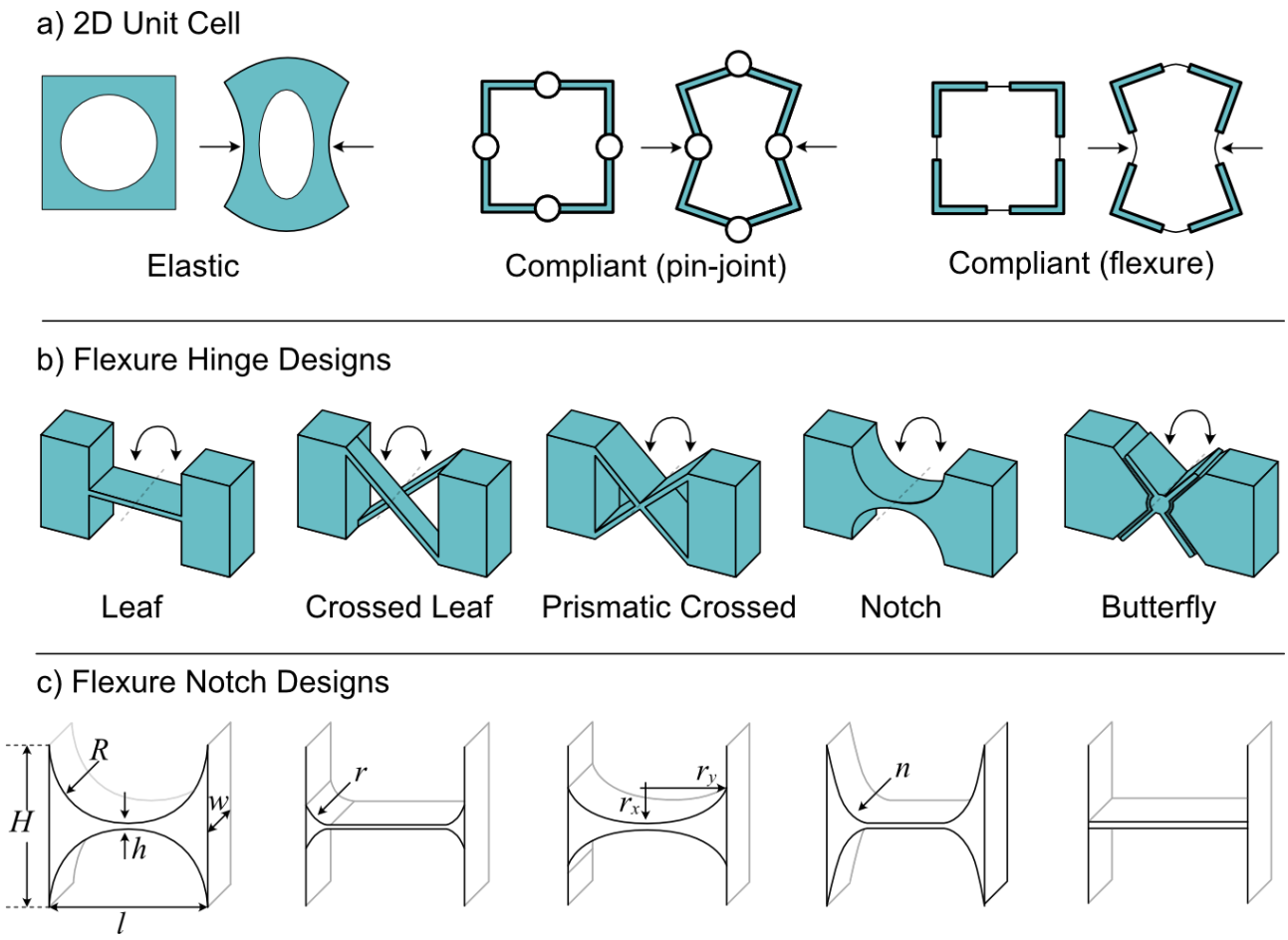


Figure 5.6: *a) 2D unit cell designs shown in elastic form, compliant form with pin joints at points of rotation and thin flexures (living hinges) at points of rotation. b) Types of flexure hinge designs - leaf, crossed leaf, prismatic crossed, notch and butterfly. Schematic adapted from Linß et al. [159]. c) Types of notch designs - circular contour, corner-filleted contour, semi-elliptical contour, power function-based contour and leaf spring contour. Schematic adapted from Henning et al. [160].*

as these are the building blocks to anisotropic unit cells. The crossed leaf, prismatic crossed, and butterfly designs are not suited for a 3D unit cell design, as two single-degree flexures cannot combine at their centres to create a three-degree of freedom system. Although the leaf design will produce the expected deformation pattern, the flexure's slender beam is likely to buckle under the restoring force from the compressed beam, in addition to a steeper gradient along the central point of rotation. If the connecting beam is along the flexure width, this does not pose a problem; however, a beam connected along the length restricts the hinging motion of the flexure.

A notch hinge is best suited for the intended unit cell deformation due to the gradual gradient at the hinge centre when deformed. Figure 5.6.c shows typical notch based designs for single-degree flexures, with the critical design parameters for each noted. Of the designs, an elliptical notch defined by r_x & r_y is best suited for the unit cell's intended deformation pattern, as the gradual gradient allows for a flat outward curvature along the points connected to the beam.

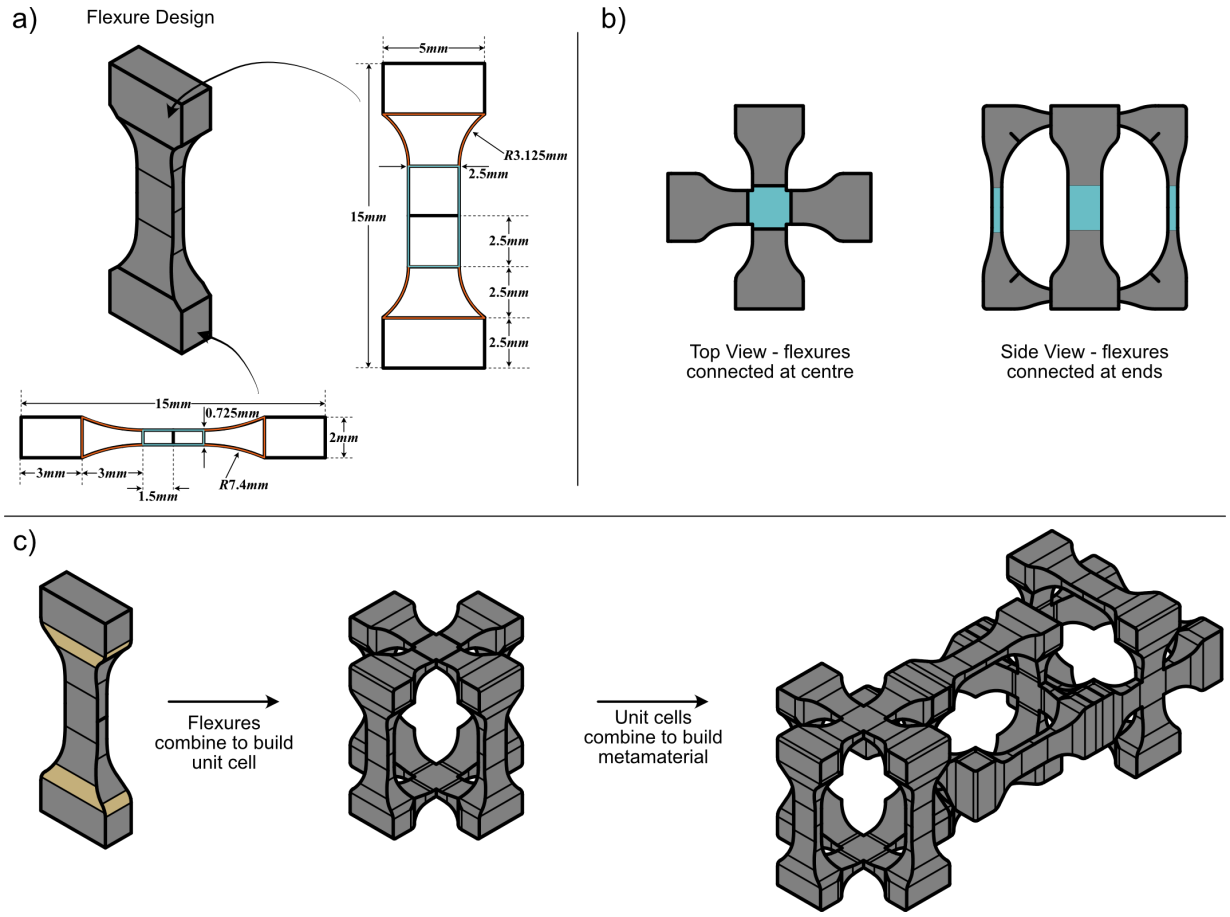


Figure 5.7: *Compliant unit cell development. a) CAD and accompanying technical drawing showing the elliptical based notch flexure design. b) Top and side view of unit cell, blue regions highlight connecting areas between unit cells. These sections are designed flat to allow unit cell combinations. c) Schematic showing the MM design process, designing a single flexure, combining to a 3D unit cell and subsequently into a functional combinatorial system.*

The schematic in Figure 5.7.a shows the final notch hinge design and respective dimensions. As the unit cell's overall size is constrained to $15mm$ x $15mm$ x $15mm$ in the x, y & z directions, respectively, the notch's length and thickness are limited by the printers minimum feature size. The design follows a similar shape to a semi-elliptical notch contour with dimensions $r_x = 0.625mm$ and $r_y = 4.5mm$. The semi-elliptical notch has a gradual curvature from the centre to the wider region; the shallow gradients allow for ease of printing and a deformation pattern that better resembles an elastic unit cell's deformation. The curvature radius is also suited for hinges that require less than 180° of flex. The region of interest that limits the flexure's curvature is highlighted in blue in Figure 5.7.b. These areas must be completely flat to ensure that unit cells in any of the three possible polarisation's can combine. Curvature in the connection regions would result in areas of overlap that differ depending on the unit cells' polarisation. The areas highlighted in orange are produced using an arc method to connect the cuboid central region to the flexure's non-deforming ends. Figure 5.7.c shows how a single-degree flexure is combined to build an anisotropic unit cell with three degrees of freedom

(through translational movement in 3 perpendicular axis) and how unit cells are combined to form MMs. The regions highlighted in brown indicate areas where fillets have been applied to the CAD model to reduce stepping. The schematic shows the flexures are combined in right angles to one another. When two squares are formed by combining the ends of the flexures, the flat centre regions are subsequently combined to form the anisotropic unit cells. For detail on the challenges of printing anisotropic unit cells, refer to Section 3.4.

5.3.3 MM Tunable System

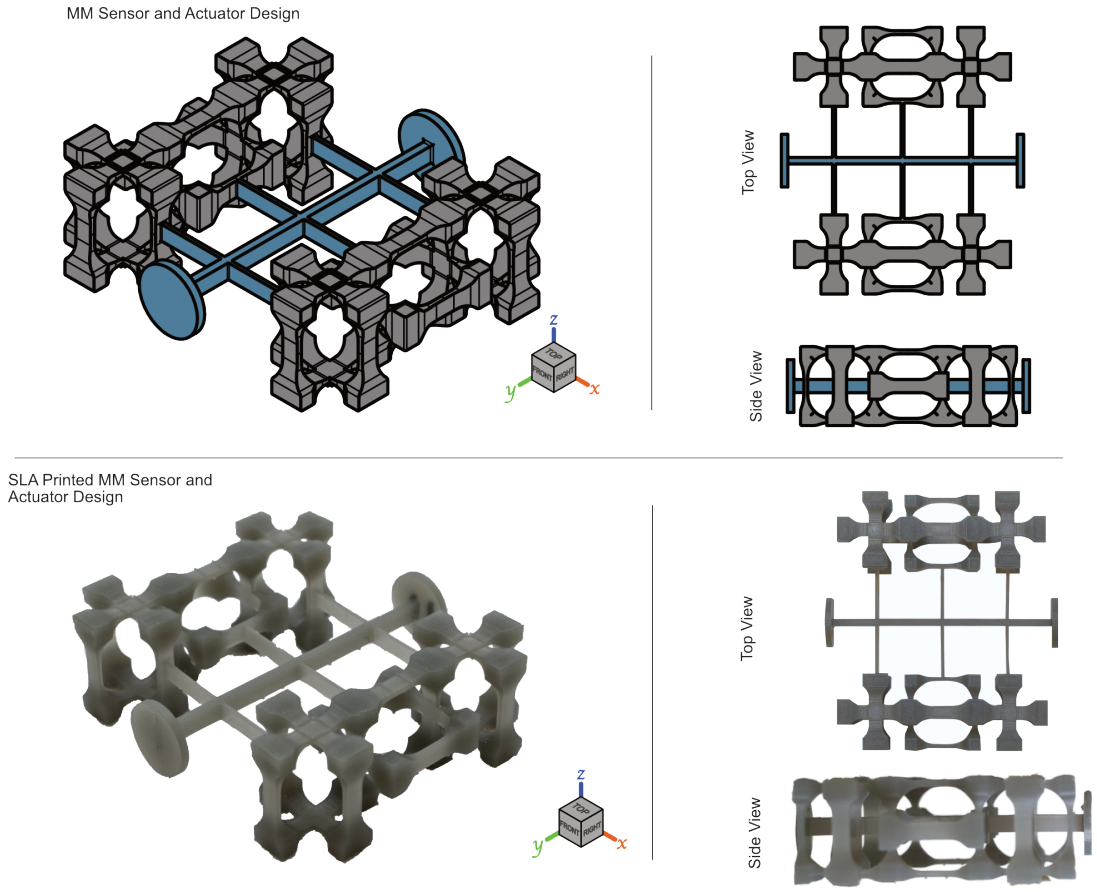


Figure 5.8: *Top - Schematic of the MM design in a zyz configuration. Bottom - SLA printed MM in a zyz configuration.*

Figure 5.8 shows the proposed MM tunable system in a zyz configuration. To simplify the analysis, the unit cells sharing a beam have the same orientation on either side of the connecting beam. For frustration-free deformation of the unit cells to occur and the beams to buckle, the unit cells in a z-polarisation must be actuated. If the y-polarised unit cell is actuated, the system is frustrated, leading to tension in one of the slender beams and a monostable system. The compliant MM is manufactured using a Formlabs Form2 SLA printer using Formlabs Tough1500 resin.

5.4 Analytical Model of a Compressed Coupled Bistable Buckled Beam

To better understand the tunable nature of the proposed MM, a relation between the beam dimensions, buckling, and the snap-through response due to an actuating force can be modelled. Several models on such systems have been presented in the literature [64, 130, 131, 145, 151, 156]. In particular the model proposed by Vangbo [130, 156] will be described in further detail. The model builds on the classical theory for 'slender beams' described by Euler for a fixed-fixed beam in the elastic regime. The classical text by Timoshenko provides further detail on Euler-Bernoulli buckling [129]. In particular, Vangbo's model provides a solution to the compressive behaviour working on the beam during a snap-through event as the beam is forced through the energy barrier.

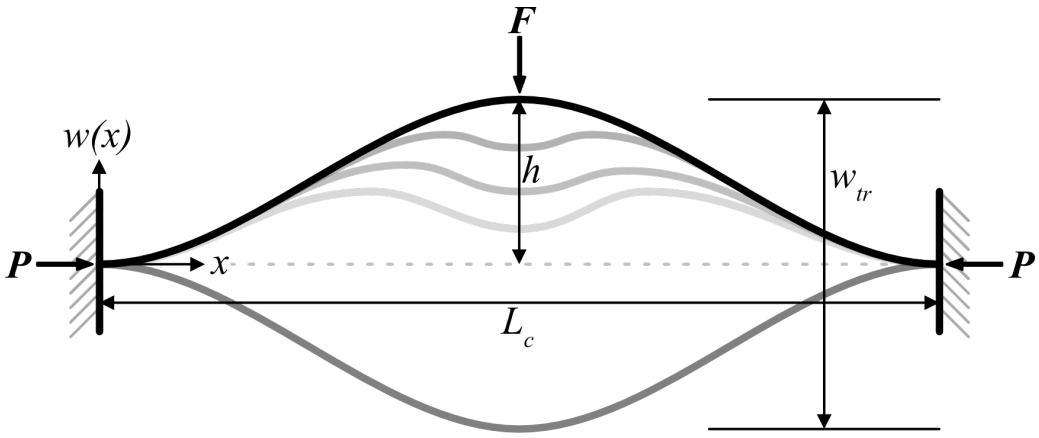


Figure 5.9: *Schematic of a buckled beam with fixed ends. Grey lines indicate the predicted beam deflection of a coupled system as it is pushed through to the second stable state. $w(x)$ denotes the deflection along the beam, F is the actuating force and P is the reactive side-wall pressure during a snap-through event.*

In Section 5.2, the MM was modelled as a spring system connected to a link and slider. In reality, however, once compression is placed on the unit cells and the slender beams buckle, the beams' boundaries can be assumed to be fixed in place. Figure 5.9 shows a double clamped single beam with fixed-fixed end conditions used in this model. The analysis of a coupled beam will be developed from the single beam analysis. The unit cells' reactive force causes the uncompressed beam of length L_t to be compressed a distance d_0 in the x-direction. This results in the beam L_t made to fit into a smaller length L_c. The beam thickness t and depth d can be found in Table 5.1. In Figure 5.9, F denotes the axial force on the beam in the central position $x = L_c/2$, P denotes the corresponding sidewall pressure, and w defines the centre point deflection of the beam.

For a double clamped beam under axial compression P, the Euler model predicts the behaviour

of the beam can be described by

$$\frac{d^4w}{dx^4} + n^2\frac{d^2w}{dx^2} = 0 \tag{5.1}$$

where

$$n^2 = \frac{P}{EI} \tag{5.2}$$

E is the Youngs Modulus and I is the beams moment of inertia. As a result of the double clamped boundary, the boundary conditions are $w(0) = w'(0) = w(L_c) = w'(L_c) = 0$. The eigenvalues n_iL_c of the homogeneous Sturm-Liouville problem are found to satisfy

$$1 - cos(n_iL_c) = \frac{1}{2}n_iL_csin(n_iL_c) \tag{5.3}$$

The eigenvalues result in non-trivial eigenfunctions that can be separated into even and odd solutions:

$$w_i(x) = \begin{cases} A_i[1-\cos(n_ix)] & \text{for } i = 0, 2, 4, \ldots, \\ & n_iL_c = 2\pi, 4\pi, 6\pi, \ldots \\ A_i[1-\cos(n_ix) - \frac{2}{n_iL_c}[n_ix - \sin(n_ix)]] & \text{for } i = 1, 3, 5, \ldots, \\ & n_iL_c = 2.86\pi, 4.92\pi, 6.94\pi, \ldots \end{cases} \tag{5.4}$$

where A_i are arbitrary constants. The ground state for a column with both ends fixed against rotation is an even solution with $i = 0$. Therefore,

$$P_0 = n_0^2EI = \frac{4\pi EI}{L_c^2} \tag{5.5}$$

is the compressive force on the boundary walls required for the slender beam to buckle into its first mode.

These equations describe the undisturbed case when $F = 0$. When applying a force $F > 0$, the system is described by the superposition $w(x)$ of the $w_i(x)$ that minimises the energy of the system. This is under the constraint of a given length $L+(d_0-d_p)$ where d_0 is the excess length when the beam is uncompressed, and d_p is the contraction from the sidewall pressure during actuation F. Therefore,

$$d_p = \frac{PL}{EA} \tag{5.6}$$

where A is the cross-section area of the beam. Solving for the length gives the constraint

$$g(\overline{A}) = (d_0 - d_p)L - \sum_{i=0}^{\infty} \frac{A_i^2 (n_i L)^2}{4} = 0 \tag{5.7}$$

As a result, the energy of the system can be written as

$$U(\overline{A}, F) = \frac{EI}{2L^3} \sum_{i=0}^{\infty} A_i^2 (n_i L)^4 + 2F \sum_{j=0}^{\infty} A_{4j} + \frac{P d_p}{2} \tag{5.8}$$

where the first term is the energy associated with beam bending, the second term is the energy from the load F at the centre of the beam and the third term is a result of lateral compression. A Lagrangian $\mathcal{L}$ is introduced to find the equilibrium state of a constant F,

$$\mathcal{L}(U, \lambda) = U(\overline{A}) + \lambda g(\overline{A}) \tag{5.9}$$

where

$$\frac{\delta \mathcal{L}}{\delta A_i} = 0 \text{ and } \frac{\delta \mathcal{L}}{\delta \lambda} = g(\overline{A}) = 0 \tag{5.10}$$

When $F \neq 0$, the A_i in the potential energy terms are

$$\begin{cases} A_i(F) = \frac{4FL^3}{EI(n_i L)^2((\eta L)^2 - (n_i L)^2)} & i = 0, 4, 8, \dots \\ A_i = 0 \quad \text{otherwise} \end{cases} \tag{5.11}$$

where

$$\eta^2 = \frac{P}{EI} \tag{5.12}$$

Inserting the respective A_i's into the boundary condition (Equation 5.7) and summation of the deflections ($w_i(x)$) of the different modes gives the centre point deflection of the beam as a function of force, on a parametric form.

$$F(\eta) = -\frac{4(\eta L)^2 EI}{L^3} \sqrt{(d_0 - d_p(\eta))L} \times \left[3 - \frac{3}{\eta L} \tan\left(\frac{\eta L}{4}\right) + \tan^2\left(\frac{\eta L}{4}\right) \right]^{-\frac{1}{2}} \tag{5.13}$$

$$w(\eta) = -\frac{L^3}{(\eta L)^2 EI} F(\eta) \left[\frac{1}{4} - \frac{1}{\eta L} \tan\left(\frac{\eta L}{4}\right) \right] \tag{5.14}$$

where $d_p(\eta) = (\eta L)^2 EI/LEA$.

In a coupled beam system, an asymmetric (odd) mode is prevented from forming. The per beam characteristics initially follow Equations 5.13 & 5.14, however, as no asymmetric modes can be developed, the critical snap-through point is postponed until $\eta = n_2$. The behaviour beyond the critical point is also evaluated by replacing n_1 with n_2 from Equation 5.14,

$$w(F) = -\frac{L^3}{(\eta_2 L)^2 EI} F \left[\frac{1}{4} - \frac{1}{n_2 L} \tan\left(\frac{n_2 L}{4}\right)\right] \tag{5.15}$$

5.5 Experimental Setup

An experimental method is established to measure the buckling response of the beam to unit cell compression and the subsequent snap-through response. Tests are conducted on the zyz configuration shown previously in Figure 5.8, as this allows testing in typical pattern-sensing conditions where the position of the actuating force is an additional factor that determines the state of the mechanical system.

5.5.1 Buckling Experimental Setup

Figure 5.10 shows the test set-up to measure the compliant MM's buckling properties. A Universal Testing Machine (1kN Instron - 5543) was used to apply a displacement controlled axial compressive force of 10mm/min on the unit cells to cause the beams to buckle. A custom fixture was developed to control the actuation position. The fixture was manufactured on a Stratasys Objet500 PolyJet printer in VeroClear. The schematics in Figure 5.10 show the top and side views of the custom fixture and the correct actuation pattern for the zyz configured MM. The unit cell compression was set to a maximum of 50% to minimise fracture risk and ensure measurements can be repeated on the same specimens. Three identical zyz mechanisms were tested five times for a total of fifteen tests. Repeated tests on the same component are vital for 3D printed components, as a bedding-in period to understand the wear and fatigue is necessary for repeatable results.

After each test, the mechanism was allowed to return to the unactuated rest state before repeating the measurement. The beam movement was captured on video using a Sony ILCE-7M3 with a 35mm prime lens to measure the beam's deflection in the y-direction. The recording was in 4K resolution (3840 x 2160 pixel) at 25fps. The Instron data was collected at 25Hz to match the compression test

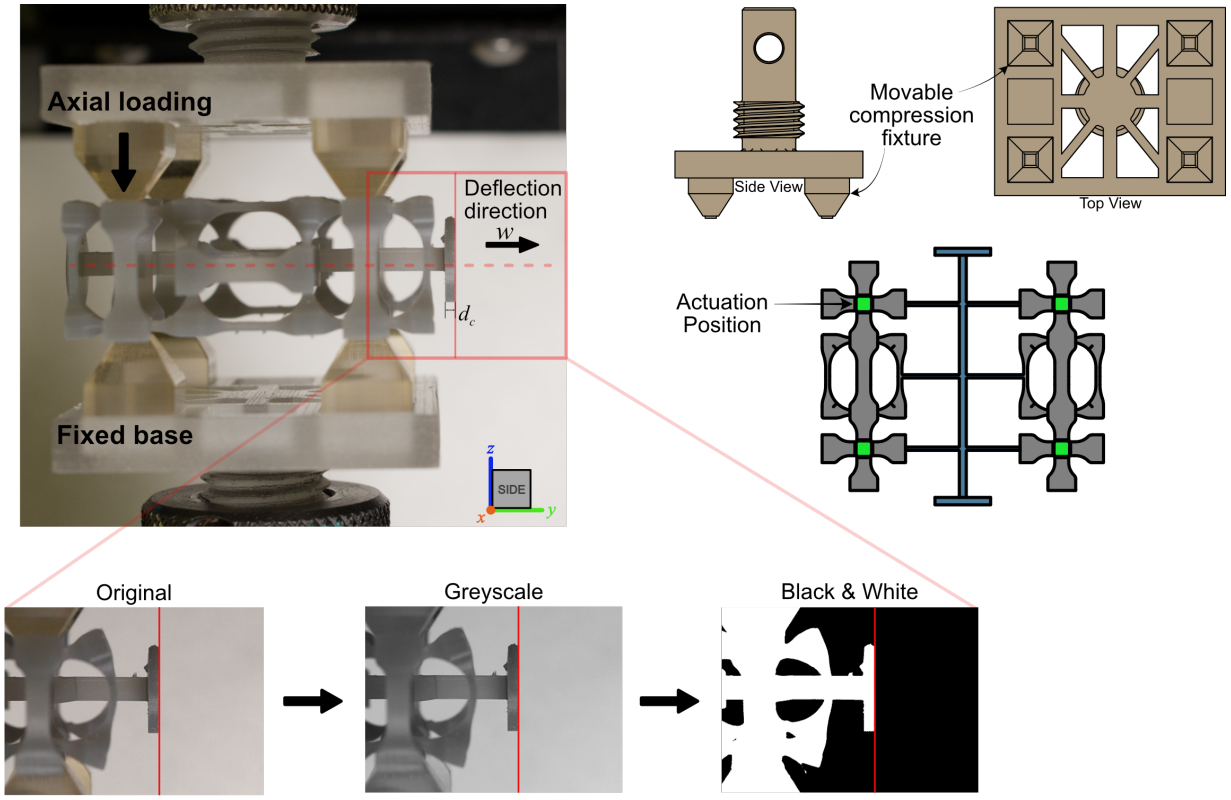


Figure 5.10: *Images show the buckling test set-up as viewed from the camera used to measure beam deflection. Custom fixtures are connected to the Instron machine to provide a patterned actuation. The images below show the image-processing workflow, converting each frame into greyscale and then black & white. The red line indicates the end of the beam, which is measured to determine beam deflection. The schematics show the top and side views of the custom fixture and the actuating position on the zyz configured MM.*

with the measured beam deflection. Using the '**imread**' function in MATLAB, each frame of the video was converted into a greyscale image and subsequently a binary image, as shown in Figure 5.10. The change in distance of the last white (binary 1) pixel between frames was used to measure the beam deflection (highlighted by the red vertical line). Each pixel's size was calculated using the thickness of the cylinders at the end of the beam shuttle, $d_c = 1.25mm$. The size of each pixel was calculated to be $0.0104mm \pm 0.0004mm$. The reference start and endpoints of the cylinder used to calculate the pixel size are manually selected; upper and lower bounds calculate the pixel size error by selecting incorrect reference points by a single pixel.

5.5.2 Bistable Experimental Setup

To test the bistable system's snap-through response, the MM is rotated 90° in order for the beam deflection w to be along the z-axis. As shown in Figure 5.11, a vice (Precision Tool Vice Type 2 - $90mm$ wide) with movable compression fixtures allows the MM to buckle under a correct compression pattern. The custom fixture is adapted from the buckling test to fit within the vice. The Instron has a

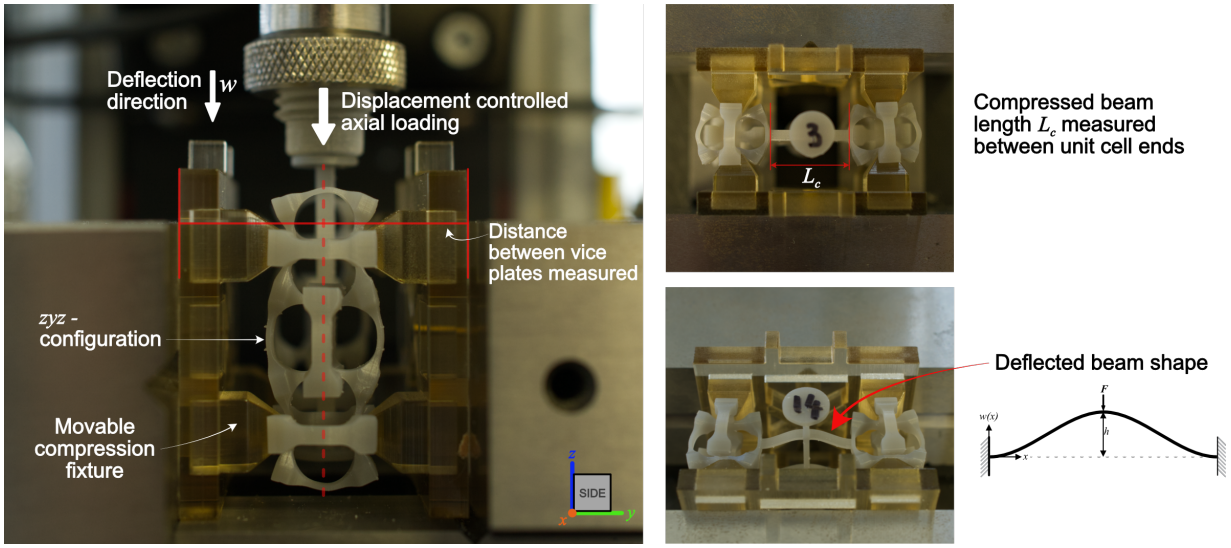


Figure 5.11: *Left - Image shows the bistable test set-up to measure the snap-through characteristics. zyz configured MM is compressed in the y-direction using a vice and custom fixture. An additional fixture is attached to the Instron to press directly on the shuttle and measure the beam deflection against force. Right - Image shows the unit cell deformation and beam buckling shape when compressed using the vice.*

custom attachment to push down on the cylindrical shuttle end. The two fixtures were manufactured on a Stratasys Objet500 PolyJet printer in VeroClear.

Displacement controlled loading at 10mm/min was performed until the beam transitioned to its second stable position. As the initial size and fixture lengths are known, the unit cells can be compressed to a defined percentage. Tests are performed at 15%, 20%, 25% and 35% compression of the unit cell from the undeflected length. This range allows the snap-through properties at different compression ratios to be tested whilst reducing beam fracture risk during testing. The beam length under compression L_c was measured manually at each compression using Vernier Calipers. Three *zyz* MMs were tested at each compression. In total, twelve specimens were printed in three printing runs; each print bed held four specimens. This ensures the three MMs tested at each compression are from separate printing runs to ensure batch variation. The snap-through response was tested several times for each MM, either until failure or until results became repeatable. The test gathers load and deflection data for the coupled bistable beams, this corresponds to a particular beam compression, and initial compressive force on the beam ends.

5.6 Results

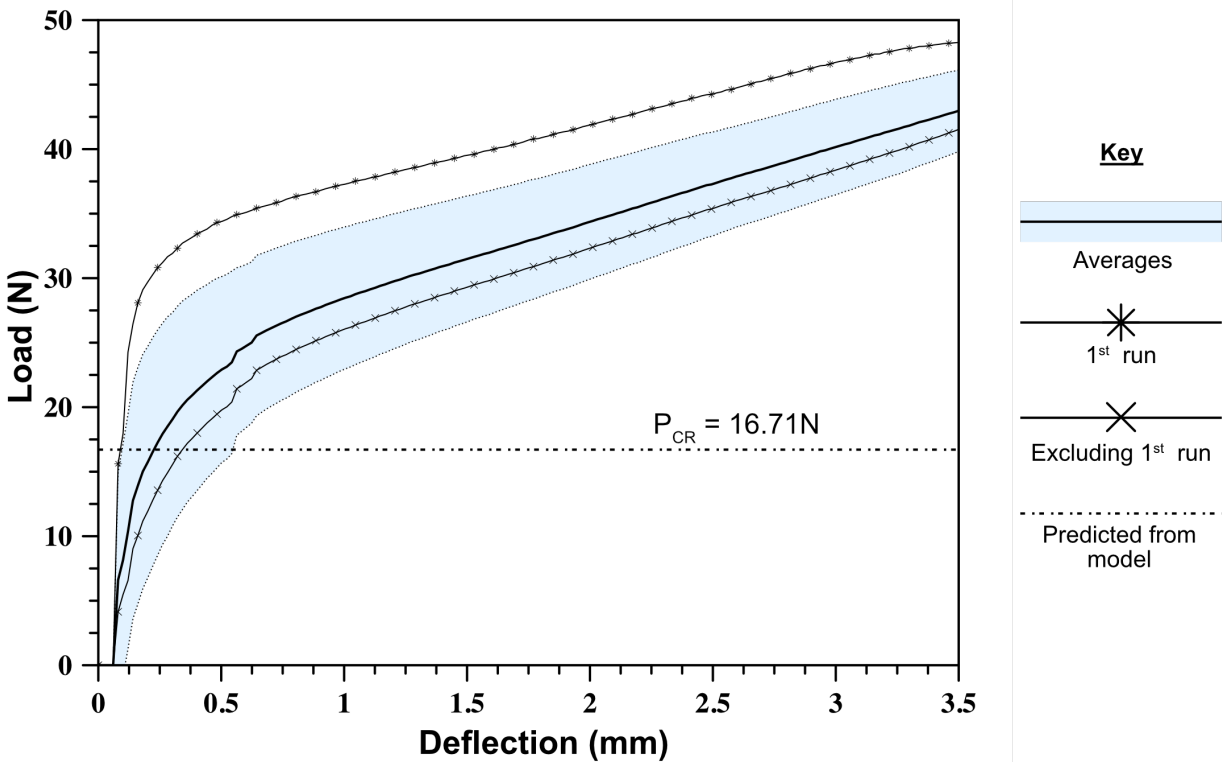


Figure 5.12: *Load (N) vs Deflection (mm) results for a zyz configured MM. Solid black line represents the averages of all measurements. Blue area highlights the error bounds in the experimental measurement, representing one standard deviation. Averages between the first run (*) and excluding the first run (x) are compared to show the changes when repeating measurements. P_{CR} line indicates the expected buckling load predicted from Equation 5.5.*

This section presents the results gathered from the two experiments and compares the predicted results from the analytical model. The buckling characteristics of the MM system are presented in Figure 5.12 from the Load vs Deflection observations. The graph shows three sets of results, the averages between all tests conducted (solid line), the averages between the first test for each MM (*), and the averages for all tests excluding the first run (x). The area in blue highlights the $\pm S_d$ (standard deviation) of the averaged results, showing the spread between multiple runs. Evident from the experimental results, the first run's buckling load is significantly higher than the results gathered in subsequent tests. Once buckling occurs, the change in deflection is also more abrupt, akin to typical changes in a buckled system. A material bedding process is observed for Tough1500 as measurements are repeated, showing a reduced critical buckling load.

The graph also indicates eccentricities are present due to the gradual change in deflection with increasing load. Eccentric axial loads are a result of the force not acting through the centroid of the slender beam. As a result, the applied load is equivalent to a centric load P and a coupled moment M_0 at the beam ends. As the axial force is initially applied, the beam begins to deflect from the onset. In

the proposed MM, the load is initially applied in the z-axis, translating to a compressive force in the x-axis. Printing inconsistencies, misalignment of force applied to the unit cell, and reactive forces on the slender elements of the unit cell by the beam explain why eccentric axial loads are present. The per beam buckling load of the system from Equation 5.5 is 5.57N. The horizontal line shows the expected buckling load of 16.71N of the coupled beam system, multiplying P_0 by three. The predicted P_{cr} is lower than the measured load. This is likely because the experiment measures the applied load on the z-polarised unit cell. This causes an outward force in the x and y directions, causing neighbouring unit cells to deform and the slender beam to buckle. As a result, the axial load directly on the beam is much lower than the load data presented in Figure 5.12.

Figure 5.13 shows the bistable characteristics of the MM at 15%, 20%, 25% & 35%. The data shows a clear difference between the $1^{st}/2^{nd}$ test results and the subsequent results once the Tough1500 material has bedded in. As a result, the data is separated into averages for the 1^{st} & 2^{nd} measurements (green) and the subsequent results (blue). The coloured regions indicate $\pm S_d$, indicating the spread of results. The number of tests conducted depended on the level of compression. At 15% compression, there was less likelihood of beam failure; on average, ten tests were conducted on each MM. For 20%, 25% & 35%, repeated tests resulted in beam fracture, often after eight tests were conducted. On average, the standard deviation represented by the blue region shows the spread of results over 18-24 tests. It is evident as the level of compression increases, the standard deviation in results reduces, showing repeatability once the MM has bedded in. Separating the initial runs was necessary to understand how the MM initially functions and how it behaves after several measurements.

In particular, there are two differences between the set of averages, the threshold force F_{th} and the beam travel w_{tr} during a snap-through event. This indicates the bedding in period changes not only the beam characteristics but also the unit cells. The initial test results per MM showed F_{th} (load required to cause snap-through) to be 2-3 times larger than the average once the material has bedded in. Furthermore, w_{tr} reduced after repeated measurements, indicated by the minima's position on the graphs. Between tests, the separation distance was measured and often remained in the range $\pm 0.05mm$; this minimal change in separation distance is not likely to be the cause, therefore. It is predicted the difference is from unit cell relaxation and reduced curvature of the beam due to fatigue. The bedding in process can also be deduced by the smoothing of results between the different averages shown. In the first measurements, characteristic 'kinks' in the data are observed (Figure 5.13 - green line). This is likely a result of the post-processing procedure; when removing support material, small nibs can be left behind, affecting the beam shape during actuation.

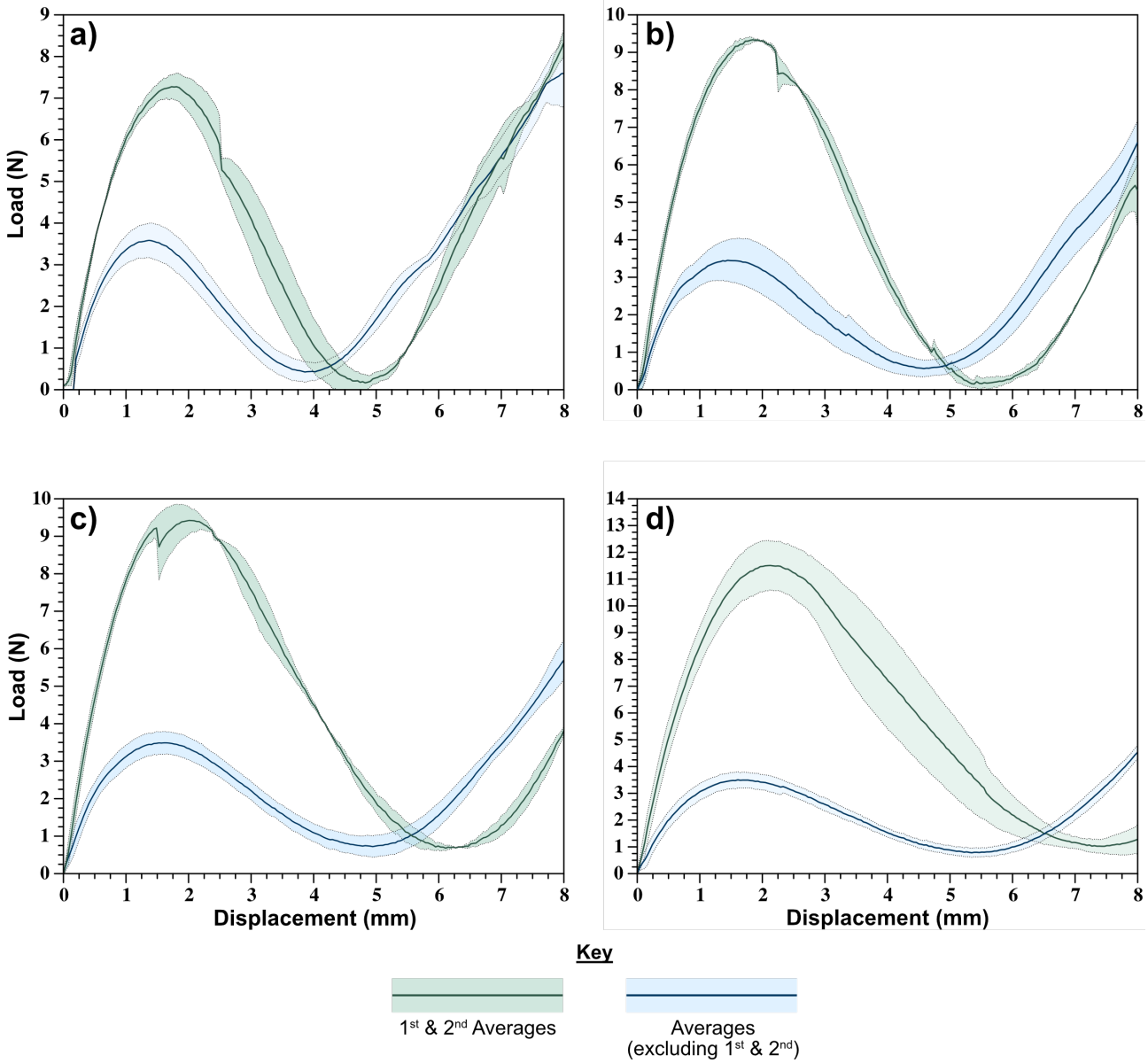


Figure 5.13: *Bistable (Load (N) vs Displacement (mm)) results for a zyz configured MM under a) 15%, b) 20%, c) 25% & d) 35% compression. Solid green line represents the averages between the 1^{st} and 2^{nd} measurements taken per specimen. Blue solid line represents averages excluding the 1^{st} and 2^{nd} measurements. Respective area highlights the error bounds in the experimental measurement, representing one standard deviation.*

Table 5.2: *Results showing the tunable threshold force F_{th} of the MM. For each compression, measured actuation force on the unit cells, and measured F_{th} are presented. This is compared to F_{th} from the analytical model.*

Compression %	**Load on unit cells (N)**	F_{th} **- 1^{st} & 2^{nd} test (N)**	F_{th} **- excluding 1^{st} & 2^{nd} tests (N)**	F_{th} **- Analytical model (N)**
15	36.53	7.27	3.59	39.89
20	43.80	9.34	3.45	49.46
25	47.48	9.42	3.49	61.23
35	49.65	11.51	4.03	68.41

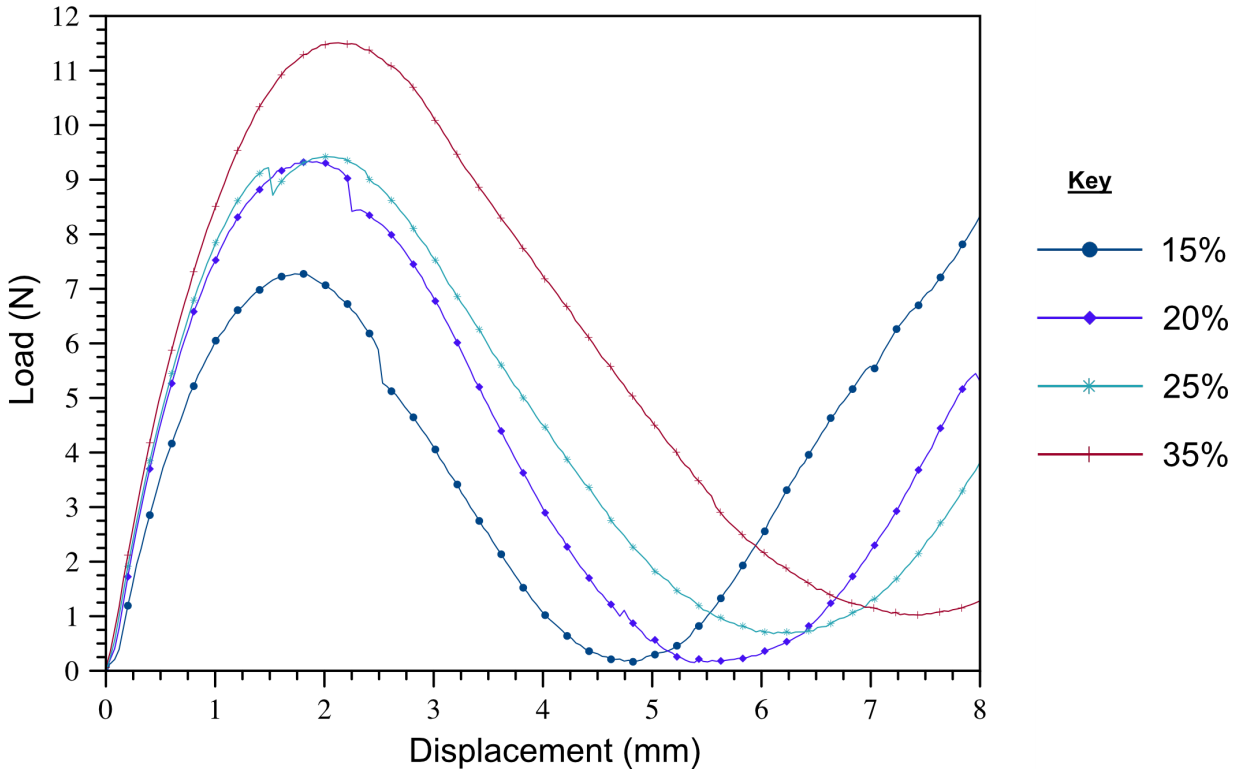


Figure 5.14: *Bistable (Load (N) vs Displacement (mm)) results for a zyz configured MM under 15% (●), 20% (♦), 25% (*) & 35% (+). Results are averages of the 1^{st} & 2^{nd} measurements for three tested specimens per compression.*

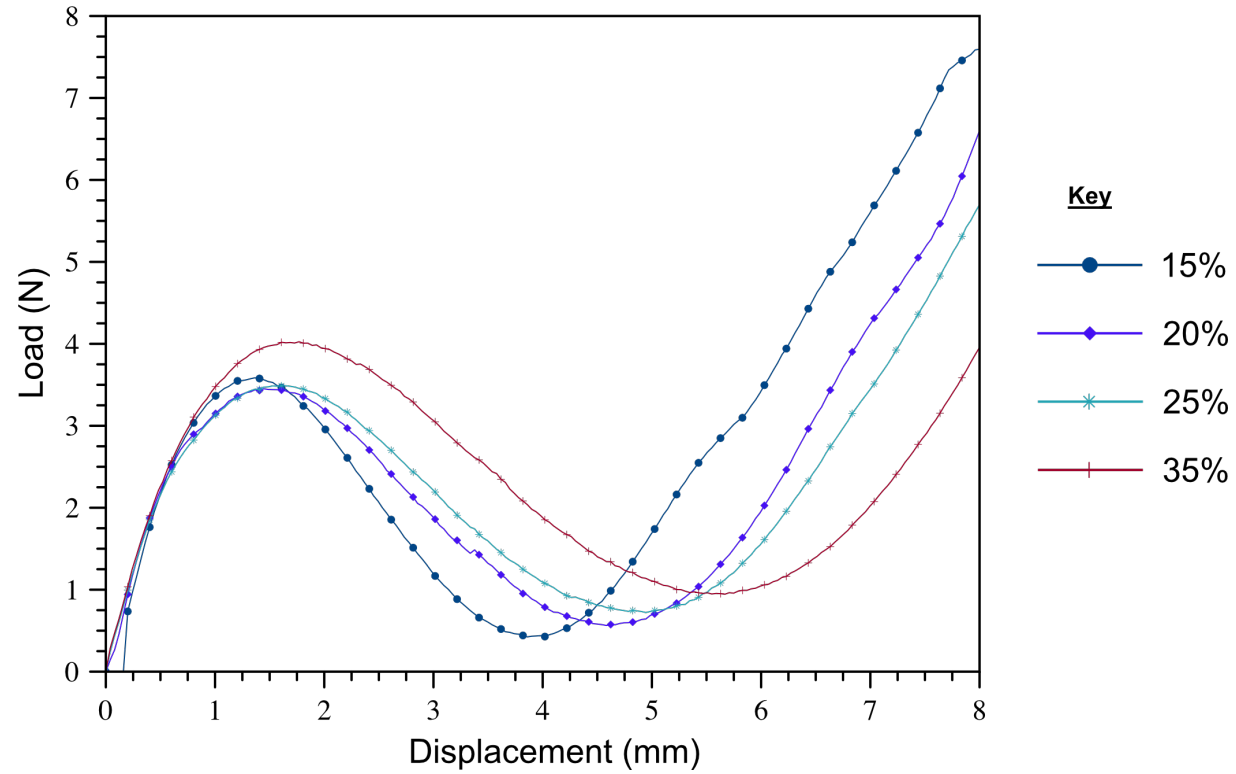


Figure 5.15: *Bistable (Load (N) vs Displacement (mm)) results for a zyz configured MM under 15% (●), 20% (♦), 25% (*) & 35% (+). Results are averages for three tested specimens per compression, excluding the 1^{st} & 2^{nd} measured results.*

Figure 5.14, 5.15 & Table 5.2 compare the snap-through characteristics at different compressions. This provides an understanding of the tunable nature of the proposed MM. It is evident from Figure 5.14 for the initial test results, there is an apparent increase in the threshold force F_{th} of the MM system and an increase in the beam travel during a snap through response. This is as expected with increasing compression of the unit cells. As the load on the unit cells increases, the beam's compressed length L_c reduces, resulting in a further deflected beam and a larger force required to transition to the second stable state.

In comparison, Figure 5.15 shows the MM results once the system showed a level of repeatability. There is a significant drop in threshold force for a snap through to occur and a change in the minima's displacement in the graph. Although the beam travel w_{tr} can still be distinguished between the different compressions, F_{th} shows no distinguishable difference between tests. Furthermore, there are significant differences between the measured threshold force F_{th} and the force predicted through the analytical model. The model predicts F_{th} to be 5-6 times larger than the measured results for the 1^{st} & 2^{nd} averages.

5.7 Discussion

Evident from the results (Figure 5.13), there are apparent discrepancies between the results when initially measured (1^{st} & 2^{nd} tests) and when subsequently collected (excluding 1^{st} & 2^{nd} tests). The likely explanation for the discrepancy in results is fatigue failure. The literature on fatigue's effects on SLA component failure and AM slender beams' failure mechanisms are limited.

Observation during the experiment showed most MM structures to adopt asymmetric snap-through patterns once fatigue and stress concentrations developed, evidently after the 1^{st} & 2^{nd} tests. This is mainly due to the displacement controlled test method developed. When manually testing the MM bistability, the snap-through transition is sudden, allowing for the rapid change in displacement. As the experiment measures the positive and negative stiffness regions in a displacement controlled experiment, the sudden transition between states is not observed. The quasi-static force and fatigue through multiple tests result in stress concentration along the beam, particularly in the $x = L_c/4$ and $x = 3L_c/4$ positions (see Figure 5.9 for corresponding beam schematic). With repeated testing, whitening areas appear, indicating stress concentration, increased material fatigue and possible plastic deformation. This subsequently results in buckling of the two halves of the beam and an asymmetric

snap-through pattern. In Figure 5.13, the concentration of stress on the slender beams results in a lower initial beam apex and beam travel; additionally, the pre-buckling results in a lower load required to transition between states.

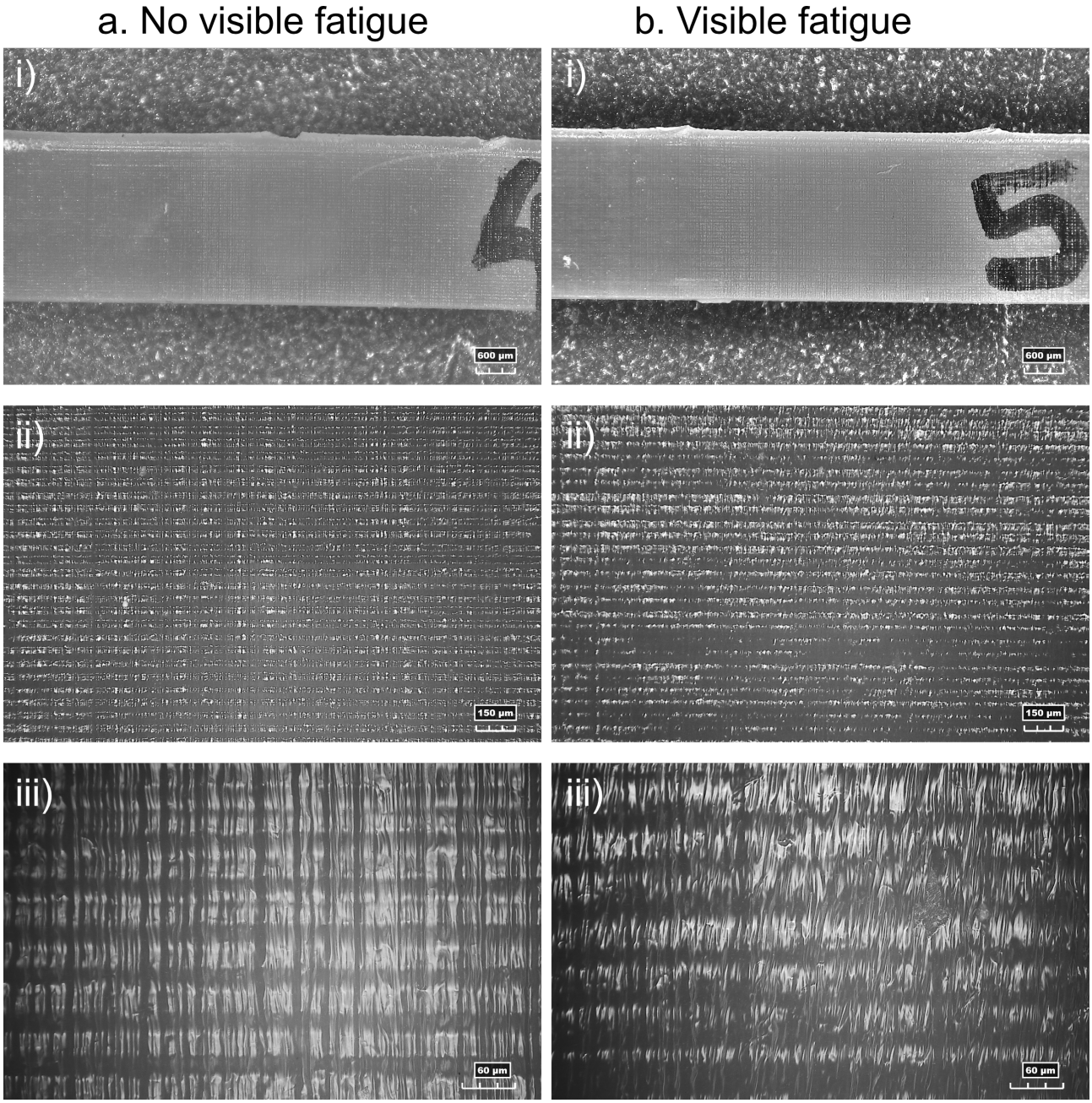


Figure 5.16: *Microscope images (in black and white) of Tough1500 beams after mechanical testing. a) Slender beam images from middle beam of a zyz MM, undergoing no visible fatigue during testing. b) Slender beam images from end beam of a zyz MM, undergoing visible fatigue (whitening areas) during testing. i) Low magnification (50x), ii) Medium magnification (200x) and iii) High magnification (500x).*

To better understand the changes occurring to the slender beams during snap-through, microscope images are analysed in Figure 5.16 for fatigue and plastic deformation effects. Images are taken from a Hirox 3D digital microscope (Hirox RH-2000 with MXB-2500 zoom lens) at three different

magnifications, i) low (50x), ii) medium (200x) and iii) high (500x). Two slender beams are compared from the same MM, Figure 5.16.a shows images of the left middle beam, no visible stress marks were observed and during testing, the middle beams did not pre-buckle as a result of fatigue. In comparison, Figure 5.16.b shows the left lower beam, which showed visible whitening indicating stress fatigue, pre-buckling was observed in this beam during testing. From the low magnification images, it is clear no conclusions can be made on the differences between the surfaces of the two beams. This is also the case for the medium magnification, which clearly shows the printed layers along the long axis of the slender beam, this is the ideal printing orientation to improve the flexural response of the system. The high magnification images, however, indicate a clear difference in the surface between the two. Figure 5.16.a.iii shows clear layer lines and a repeatable pattern throughout, indicating no changes to the slender beam. Conversely, Figure 5.16.b.iii shows a non-uniform rough pattern along the beam, indicating areas of fatigue. In particular, large vertical voids highlight areas in which plastic fatigue may have occurred, as this pattern is not present in any other section of the beam. Closer inspection also shows the surface to have several deformities against the repeatable printing pattern, highlighting failure points. The microscope images do not conclusively provide evidence on the failure mechanisms behind the difference in results between multiple snap-through transitions. It does, however, reaffirm the proposition fatigue and plastic deformation are the cause for the discrepancy in results, as Tough1500, although designed for compliant systems, is not ideal for large deformations under displacement controlled settings.

Although most data is collected when the MM is in the pre-buckled fatigued state (Figure 5.13 - blue line), this is not an accurate assessment of the MM bistable characteristics. The averages taken from the 1^{st} & 2^{nd} run, where a symmetric snap-through shape is observed, provides a correct assessment of the proposed MM's bistable properties.

Table 5.2 compares the measured threshold force F_{th} from the experiment and the predicted force from the analytical model. As described earlier, F_{th} is 5-6 times larger in the analytical model than the 1^{st} & 2^{nd} tests F_{th}. The model input parameters include the uncompressed length L_u, beam-width h, beam-depth b and Elastic modulus E. During the experiment, the compressed length L_c is measured to determine d_0, the compression on the beam. A sensitivity analysis shows with an inaccuracy of 10% on the printing dimensions of the MM (L_c, h, b), this cannot account for the 5x discrepancy between model and experiment. In order to obtain model results that match the experiment data, the Elastic Modulus (1.5 GPa) would have to be 20% (0.3 GPa) of the current value used in the model. Although the Elastic Modulus for Tough1500 was not measured manually to confirm the manufacturer's quoted

value, experiments on the anisotropy of SLA printed parts [120] confirm modulus values provided by Formlabs fall within an acceptable range of experimentally verified values. It is unlikely the modulus value used (1.5 GPa) is incorrect and the cause of the discrepancy between experiment and model.

Several SLA printing considerations could affect the measured F_{th} experimental results. S. Mansour [138, 122] describes the impact of short term ageing of SLA printed parts. In particular, with increasing age ∼28 days, parts become stiffer and more prone to brittle fracture. The age of the tested samples in the bistable experiment ranged from ∼10-30 days. Samples were stored at room temperature away from sunlight. Although age may cause brittle fracture of the beams after repeated use, this does not explain the discrepancy with the analytical model.

A further consideration is the effect of printing direction on the mechanical properties of SLA printed parts. The literature on this topic is very mixed, with further examination necessary to provide definitive answers. Most literature either concludes SLA parts are completely isotropic [120, 121] or transversely isotropic [122, 123]. Although some anisotropy may be present in SLA parts, it does not suffer the same failure points as FDM printed parts and unlikely to cause the 5x difference in predicted and measured results.

The discrepancy between the model and experimental data is due to assumptions on the MMs snap-through behaviour. The Vangbo model predicts the bistable behaviour of a fixed-fixed system. The beam ends in the MM system are assumed fixed when the unit cells are under compression. This assumption is not entirely correct. Evident in the buckling behaviour (Figure 5.12), eccentric loads are likely because of the unit cells' out of plane bending. Furthermore, as the slender beam is pushed in the transverse direction, this causes twisting of the unit cells, as the front and back of the MM are unbound. This effect is reduced in larger combinatorial systems, as shown in Section 7.3. Finally, the reactive sidewall forces (P) for the model are predicted for a fixed region. As the centre unit cell (y-polarised) of the MM is not directly actuated, they are not entirely fixed in place by the adjacent actuated unit cells. Reactive forces from the beams sidewall pressure may change the unit cells' shape and the overall bistable properties of the coupled system, resulting in a lower threshold force F_{th}. Although the analytical model captures the coupled bistable system's main dynamics, an FEA analysis will better capture the bistable system's complex nature with the combined unit cells. It should be noted very few studies have been conducted on the bistable nature of AM slender beams. As a result, further studies are required on whether AM slender beams' behaviour drastically differs from their subtractively manufactured polymer counterparts.

This research aims to show the tunable nature of MM, and how these can be developed into

functional mechanisms. Although there are several discrepancies with the analytical model, Figure 5.14 does show the tunable bistable nature of the proposed MM. The results confirm the position, and actuation load (compression) directly affects the threshold force F_{th}, and reaffirms the *sense-decide-respond* capabilities of the proposed FMM.

Chapter 6

Combinatorial Functional Mechanisms

In this chapter, by taking a combinatorial design approach, the multi-plane characteristics of MMs are explored. The multi-material MM in Chapter 4 and the compliant MM in Chapter 5 serve as the foundations for developing multi-plane FMMs (metadevices). Propagating mechanical signals in a multi-plane FMM is successfully demonstrated in both multi-material and compliant variations. The mechanical signals were transmitted in different directions and through different planes, showing significant actuator control in a multi-plane system. The design is expanded to a compliant rod-logic FMM; a gating system along the z-axis modulates mechanical signals passing through the x-y plane. Furthermore, multi-material FMMs are developed for use as integrated mechanical control systems. A fully integrated bistable system is successfully demonstrated, highlighting applications as an impact diagnostic feature in sports helmets. The FMMs demonstrate a high level of programmability and tunability over multiple planes and are early examples of morphological systems.

6.1 3D Mechanical Metamaterials

Mechanical metamaterials are defined as architected materials that exhibit properties superior to the constituent material. In the simplest of cases, this is observed as a change to the bulk mechanical properties of a material, such as a negative Poisson's ratio. However, as highlighted in the Literature Review in Chapter 2, MMs cover a broad array of mechanical phenomena which cannot easily be defined by a change to a single mechanical property. For example, the use of mechanical systems to exhibit Boolean logic is defined as a programmable MM, as further exhibited in Chapter 4. Frustration-free movement of anisotropic unit cells shows holographic ordering through a bulk architected material, highlighting the additional 'functional' capabilities which allow the structure to be defined as an MM. Similarly, the use of frustration creates different stress patterns, highlighting the tunability through design, allowing it to be defined as an MM. Finally, topological materials can be designed that maintain resilience against disorder and noise but can have soft compressive modes designed in. This is achieved through the careful design of the material architecture, allowing for the definition as an MM. A question to explore is whether the mechanical systems in Chapter 4 and Chapter 5 can be defined as mechanical metamaterials.

In Chapter 4, a VMT bistable system was developed and combined with anisotropic unit cells. A single-use logic gate system was successfully demonstrated, highlighting the capability to determine the 'output' of a mechanical system. This is reliant on the defined orientation of the connected unit cells and subsequently the order and direction of actuation. As the programmability of the system is determined by the orientation of the unit cells and the VMT, the proposed mechanical system can be defined as an MM, as it fits the same description of programmable control through design.

Similarly, in Chapter 5, a compliant system was developed to show the tunable bistable nature of MMs. Using a combinatorial approach first proposed by Coulais *et al.*[58], the mechanical system shows the control over the 'output' of the mechanical system is a consequence of the particular unit cell polarisations, how they are combined, the actuation pattern and the actuating force. The functionality of the said system is a result of the chosen polarisations and therefore shows programmable control through design. The two mechanical systems explored lay the foundation of how beams can be manipulated using anisotropic 3D unit cells. As a result, both systems are defined as MMs.

An objective of this chapter is to explore the functional capabilities of MMs. As such, the research proposal questions whether MMs can form part of larger morphological systems. Can the programmable MMs explored in previous chapters be implemented into the architecture of a larger

system? Where the functional capabilities of the MMs are the response to environmental changes to the bulk system. For example, accelerations/deceleration's in a shock-absorbing architected material. This chapter highlights the MM developments possible using designs from the two systems explored in previous chapters. Programmable behaviour through multiple planes and their functionality within larger architected systems are explored. Through a combinatorial design approach, multi-plane functional mechanical systems are achieved.

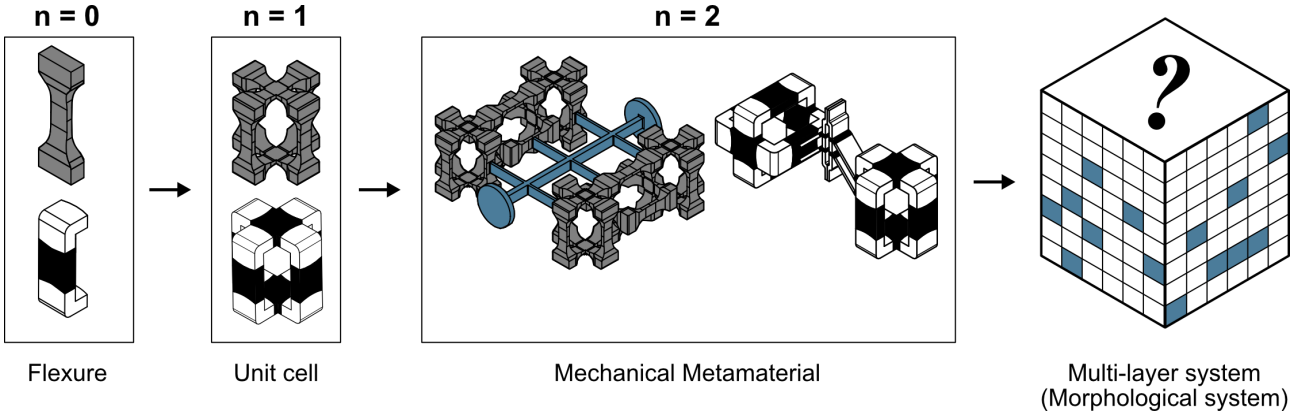


Figure 6.1: *Schematic shows the hierarchy of architected materials; the flexure component (n=0), the unit cell (n=1) and the combination of unit cells (n=2). The multi-layer system schematic highlights the next innovation stage, using the developed MMs to construct FMMs that function through multiple planes i.e. a morphological system.*

The field of MMs has yet to be fully explored, and the current design process is limited in most cases to a design iterative process as evident in the Literature Review (Section 2). A similar design iterative process was undertaken in designing the two systems in Chapters 4 & 5. Figure 6.1 describes the hierarchy of a MM system, from the flexure design (n=0), combining to build unit cells (n=1), and unit cells combining to construct a MM (n=2). A complete morphological system combines the programmable MMs (n=2) into a complete system fully integrated into the primary architecture. The general design principles for all MM designs largely follow the same architecture hierarchy described in Figure 6.1. For example, the bow-tie antenna design explored in Section 2.2.1 from a top-joint/sharp-tip flexure, which when combined forms a bow-tie unit cell. As the unit cells are combined into a periodic structure, auxetic mechanical properties can be realised. Often through the unit cell and the chosen periodicity, MMs are developed.

A research objective is to develop functional MMs that are programmable and tunable within a multi-plane morphological system. As a result, 3D MMs such as the Metacube example are explored in more detail for their programmable and holographic ordering capabilities. However, this system does not fully capture the intended functional and device like capabilities sought after in MM design. As a

result, the 3D anisotropic unit cells were adapted and combined with alternative tunable mechanical systems to develop FMMs that closely fit the specific problem to be addressed. This chapter highlights capabilities of the MM systems from Chapters 4 and 5 under a broader combinatorial approach. Multi-plane FMMs are to be developed; designed to be implemented into larger architected (morphological) systems.

6.2 Multi-Plane Bistable System

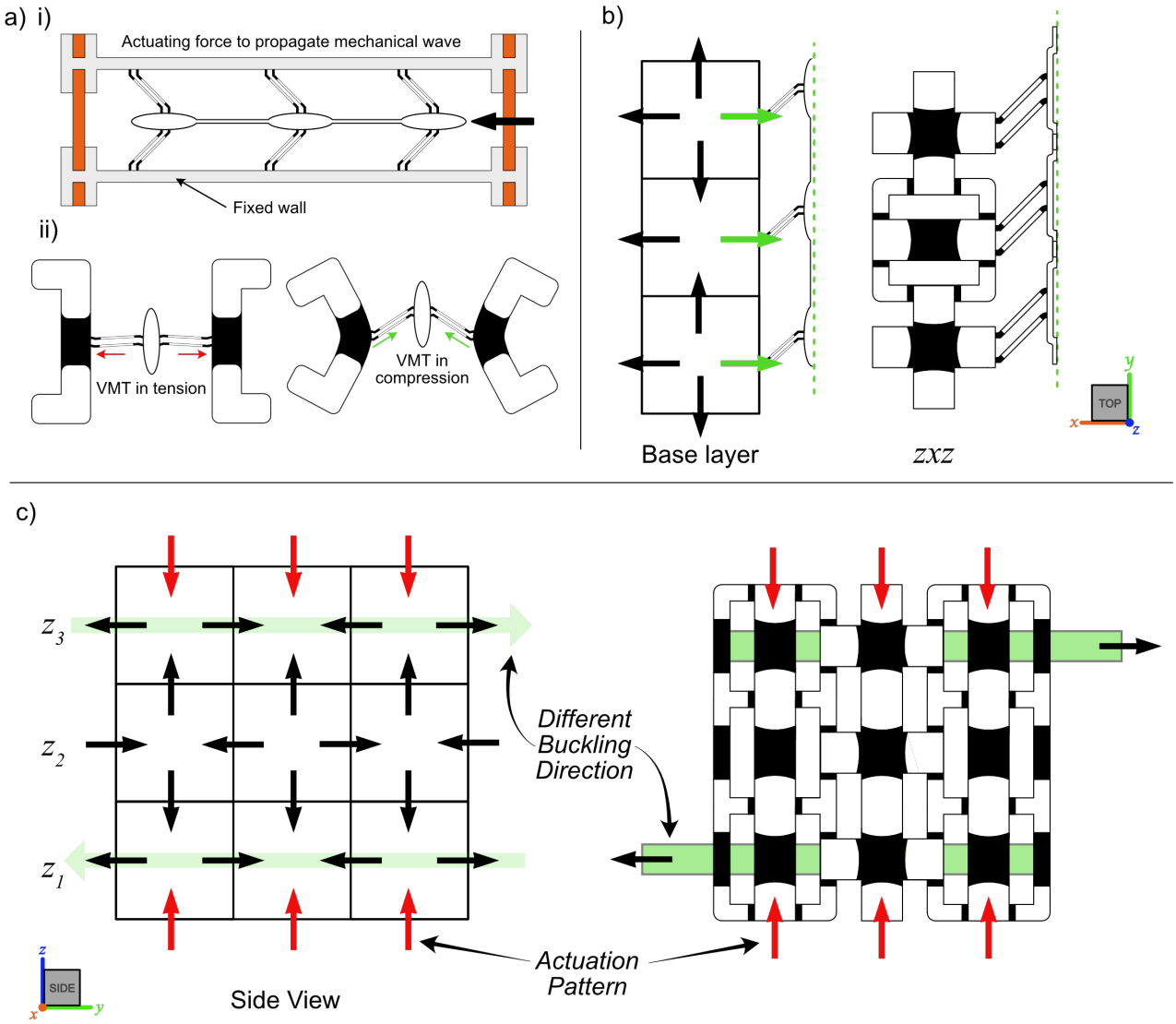


Figure 6.2: *a) i) Testing bistability in a coupled VMT system. ii) When connected to unit cells, the VTMs are in tension or compression representing monostable and bistable states respectively. b) Combinatorial design of unit cells connected to VMTs. Arrows indicate spins when correctly actuated, green arrows indicate the necessary spin for the MM to function correctly. Green dotted line indicates line of symmetry. c) Combining unit cells in a 3x3 arrangement, using the base layer design. Red arrows indicate the actuation pattern required for the FMM to correctly transition from monostable to bistable. As the VMTs are biased to one direction, they can be designed to buckle in different directions in the same connected system.*

In Chapter 4, a bistable system using VMTs was developed. Two methods of transitioning between stable states were explored, through a fixed separation distance as shown in Figure 6.2.a.i, or through expanding the beam separation distance subsequently used to perform mechanical logic. The compliant MM in Chapter 5 showed how slender beams connected to unit cells transition from monostable to bistable under the correct actuation sequence. The schematic in Figure 6.2 shows the multi-material MM design approach to perform the same function. By increasing the separation distance between the unit cells, the VMT system can be placed in tension resulting in a single equilibrium position (Figure 6.2.a). In response to the correct actuation sequence of the unit cell, the VMT transitions from monostable to bistable. The proposed FMM uses the same unit cell and VMT design proposed in Chapter 4; however, due to the larger combinatorial system, the scale is reduced by 50%. This results in a cubic unit cell of 15x15x15mm and VMT beam thickness of 0.6mm. The proposed FMM in Figure 6.2 shows how VMT systems connected throughout an architected structure allows multiple mechanical signals to pass in different directions, due to the asymmetry of the VMT. Compression of the MM in the z-axis will cause one VMT to buckle in the $+y$ direction and the other $-y$, whilst occupying different planes (z_3 and z_1 respectively) in the MM.

To combine such systems, the 'ice rule' must be utilised to ensure the spin configurations for a correct actuation pattern results in the sidewalls of the VMT compressing. As shown in Figure 6.2.b, the spins acting on the beams (green arrows) are first defined. The remaining arrows are subsequently determined to ensure spin parity is present between adjacent unit cells. The spin interactions in Figure 6.2 occupy a 2D plane. As all three unit cells can be defined by spin configurations on a 2D plane, once the orientation of one cell is defined, the parity conditions discussed in Section 2.2.5 can be used to construct the remaining structure. In Figure 6.2.b, the spin configurations of the connecting unit cells in the z_1 plane are first determined. This results in the final multi-plane design (Figure 6.2.c) shown with the input sequence (red arrows) established for a bistable response. The proposed MM has a zxz configuration in all three planes z_1, z_2 & z_3.

Figure 6.3 shows the response to actuation for two printed multi-plane FMMs. A video showing the functionality of the two multi-plane MMs propagating mechanical signals [1] can be found using the footnote link. Figure 6.3.a is a multi-material design manufactured by PolyJet (Section 3.3). Figure 6.3.b is a compliant design manufactured by SLA (Section 3.4). The compliant FMM has identical dimensions to the system explored in Chapter 5. Both multi-plane bistable systems are in a zxz configuration in all three planes. As shown, when the FMM is under no actuation (i), it is

[1] Multi-Plane FMMs - `https://vimeo.com/541450698`

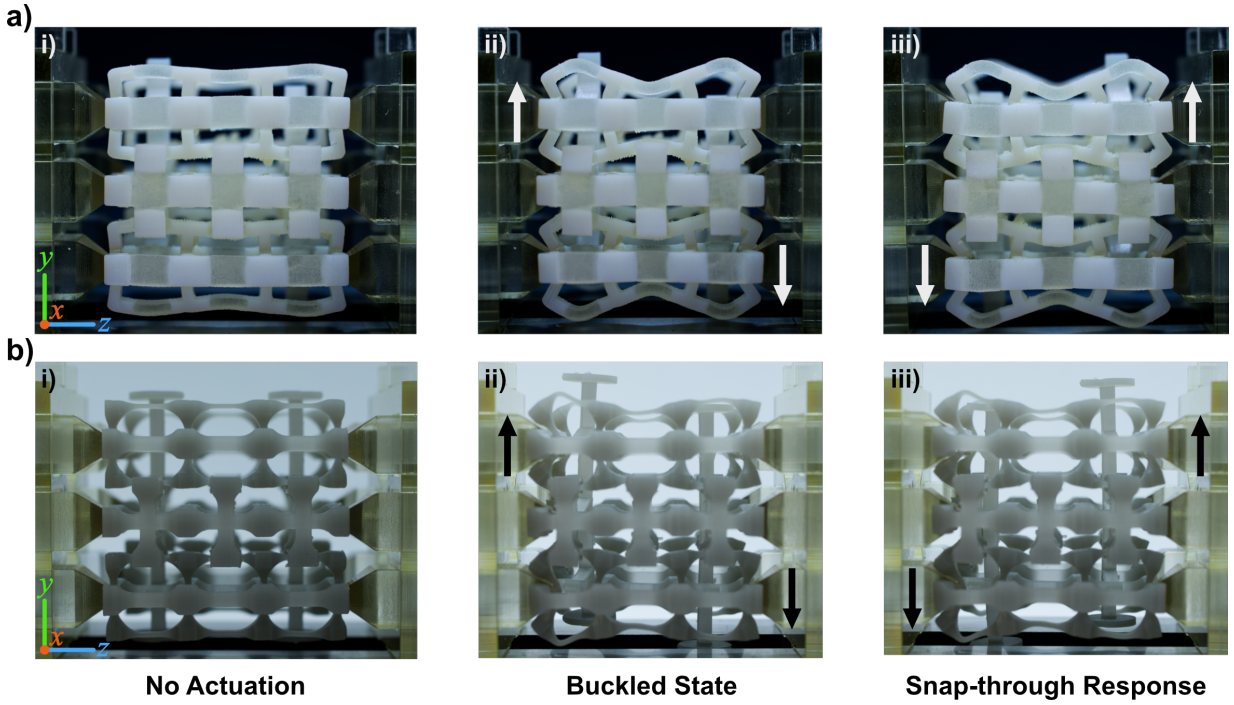


Figure 6.3: *Experimental validation of multi-plane bistable system. FMMs are compressed along the z-axis by a vice patterned compression fixture. a) Multi-material VMT FMM. b) Compliant FMM. i) FMM under no actuation. ii) FMM in the buckled state, left and right shuttle in $+y$ and $-y$ directions respectively. iii) Opposing force in the $-y$ (left) and $+y$ (right) direction above the threshold force cause a snap-through response (wave propagation through material).*

in a monostable state. For the multi-material design, this is a result of tension on the VMTs. The compliant system is in its printed state with the slender beam straight. As the correct actuation is received (ii), both systems buckle along the y-axis. The joint angle determines the buckling direction for the VMT in (a) and through a single-sided chamfer (acting as a defect) of the slender beam connected to the unit cell in (b). An actuation opposing the buckling direction caused a snap-through response of the three-beam system (iii). Thus the two FMMs experimentally verify the ability to propagate mechanical waves in multiple directions in an architected (morphological) system.

6.3 Rod-Logic Mechanical Metamaterial

The capability to propagate mechanical signals in multiple directions through a lattice structure presents opportunities for morphological computation. The Boolean logic gates explored in Section 2.3.2 utilised similar design configurations of bistability, defects and blocking elements such as rods. A common theme between many designs is the planar nature of the logic devices; input and output signals occur in the same plane. The proposed MM in Chapter 4 showed that input and output signals could differ in direction due to unit cell polarisation. Complex multi-plane behaviour can be exhibited by combining multiple unit cells. One particular concept explored by Merkle [78] and Ion [81] is

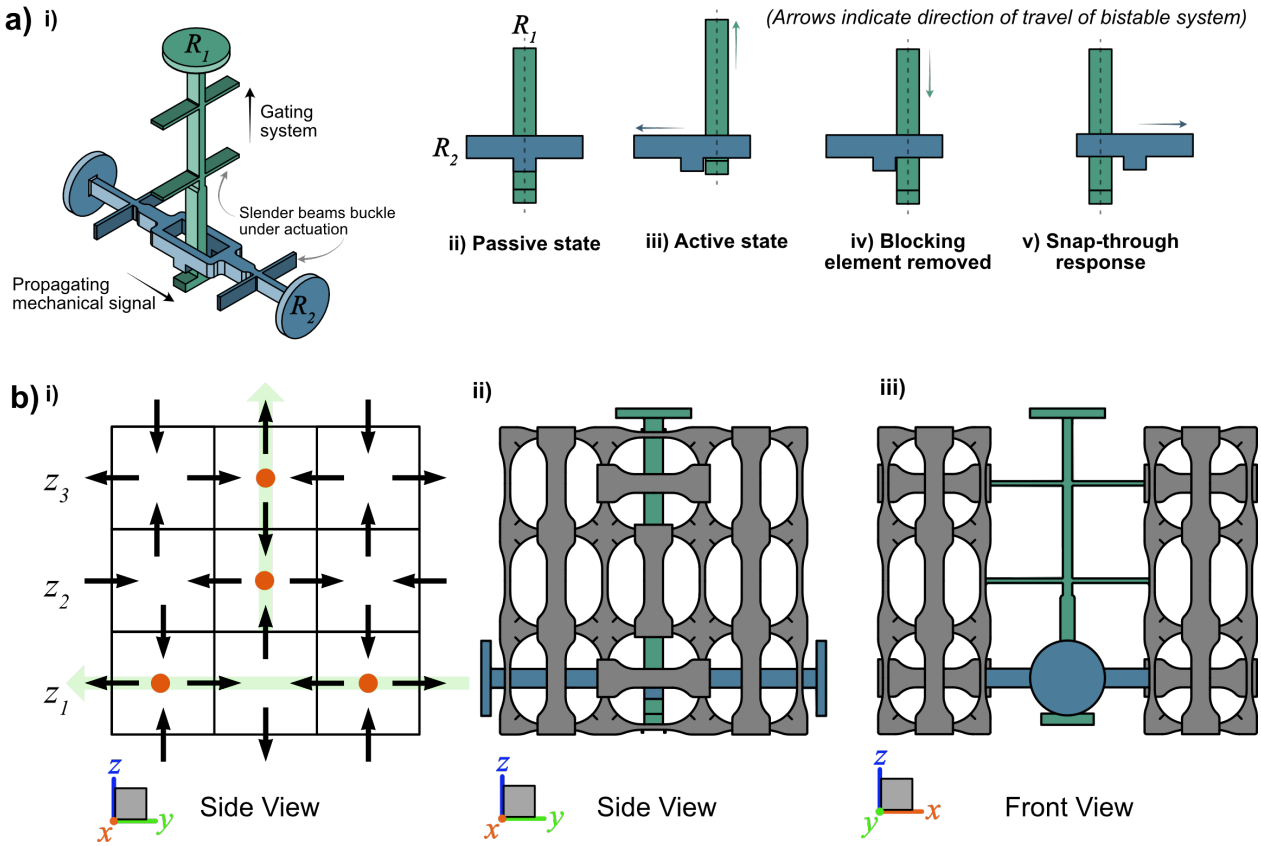


Figure 6.4: *a) Schematic showing the working principle of rod-logic. i) Two separate bistable systems are connected to the same architected material. ii) Passive state - No actuation of FMM. iii) Active state - Actuation of FMM. iv) Blocking element removed - bistable gating system actuated. v) Snap-through response - horizontal bistable system actuated. b) Schematic showing the combinatorial unit cell design. i) Orange dots show the out of plane deformation necessary for the FMM to function correctly. Green arrows indicate buckling direction of bistable systems. Side view (ii) and front view (iii) of rod-logic FMM.*

rod-logic for computation. In principle, rod-logic describes conditional statements, for example, *if* a beam in the z-plane is actuated, *then* a signal can pass through the y-plane, *else* the system remains frustrated. This is the basis of Boolean conditions.

The proposed rod-logic design is shown in Figure 6.4. The schematic shows the development of a compliant FMM with a bistable rod latching system. As elucidated in previous chapters, the mechanism is monostable and passive when under no actuation—the latching system functions when the FMM is actuated correctly. Deformation of the unit cells will cause the connected beams to buckle in the $+z$ (R_1) and $-y$ (R_2) directions, respectively. As the beams occupy different planes, this causes the two systems to interfere with one another, restricting the propagation of mechanical signals along the z_1 plane. The design has sequential ordering; the blocking rod elements (R_1) must first be actuated for the bistable system (R_2) in the z_1-plane to propagate. Figure 6.4.b shows the schematic of the proposed rod-logic system and the corresponding unit cell arrangement.

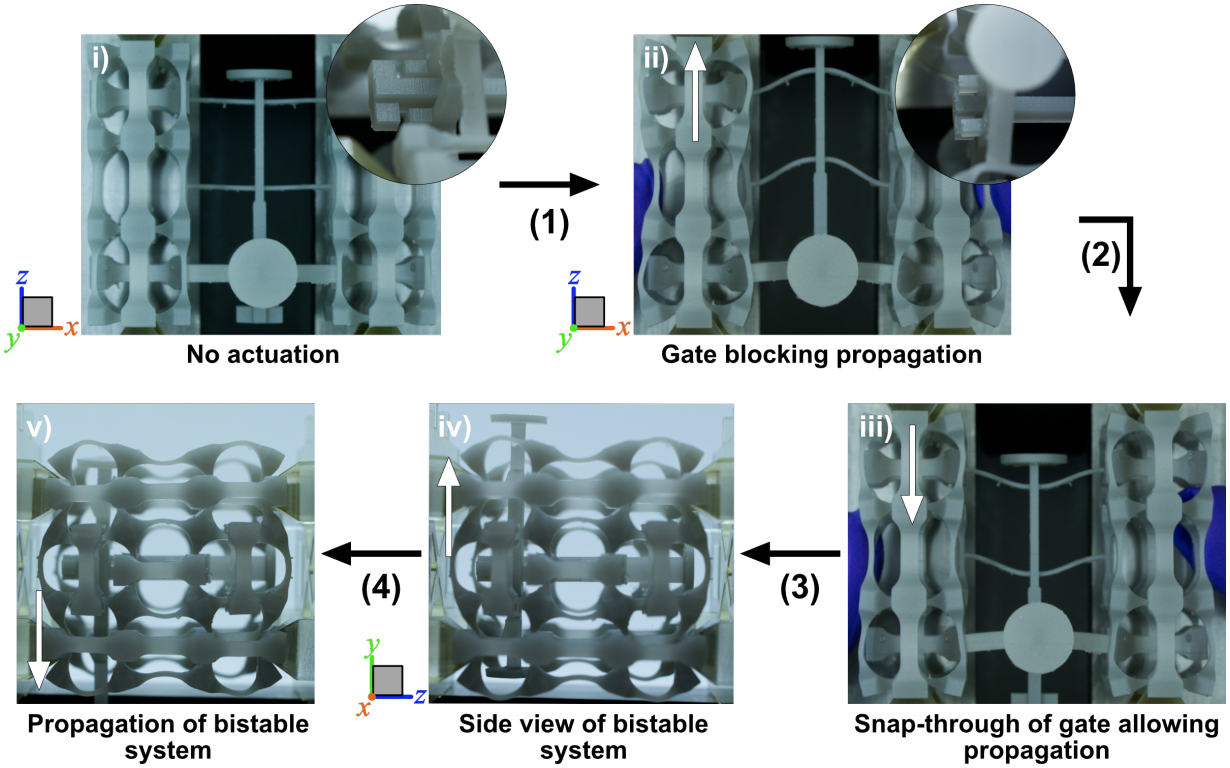


Figure 6.5: *Experimental validation of rod-logic FMM. i) System under no actuation, blocking elements are apart. ii) Actuation of unit cells cause both beam systems to buckle, blocking elements are in contact. iii) Actuation in $-z$ direction causes R_1 to transition to second stable state, blocking elements move apart. iv) Side view of FMM, after R_1 transition. v) Actuation along $+y$ direction on R_2 causes mechanical signal to propagate along z_1 plane.*

Figure 6.5 shows the experimental validation of the rod logic system. Under a correct actuation sequence, the two-beam systems buckle in the $+z$ (R_1) and $-y$ (R_2) directions respectively. This causes the two blocking elements to be aligned. In this 'active' configuration, mechanical signals across the z_1 plane are blocked from propagating. Actuation at position R_1 will cause a snap through response and displacement of the blocking element. This allows signal propagation along the z_1 plane by actuating R_2. A video of the proposed compliant rod-logic FMM [2] can be found using the footnote link.

There are several novel attributes to the rod-logic FMM. The two bistable systems are integrated with the broader metamaterial. AM allows moving sections to be interwoven with one another, as shown in Figure 6.4.a.i. The proposed system is *passive*, and the *active* state only occurs under a correct force and position. In the *active* state, mechanical signals can pass through the metamaterial as long as the gating function (R_1) is released. The system forms the basis for larger complex systems, where mechanical signals can be transmitted in multiple directions through an architected material, and the gating function controls which signals are allowed to propagate and when. The experimental validation shows greater complexity and functionality in multi-plane FMMs.

[2]Compliant Rod-Logic FMM - `https://vimeo.com/541446770`

6.4 Mechanical Metamaterial Safety System

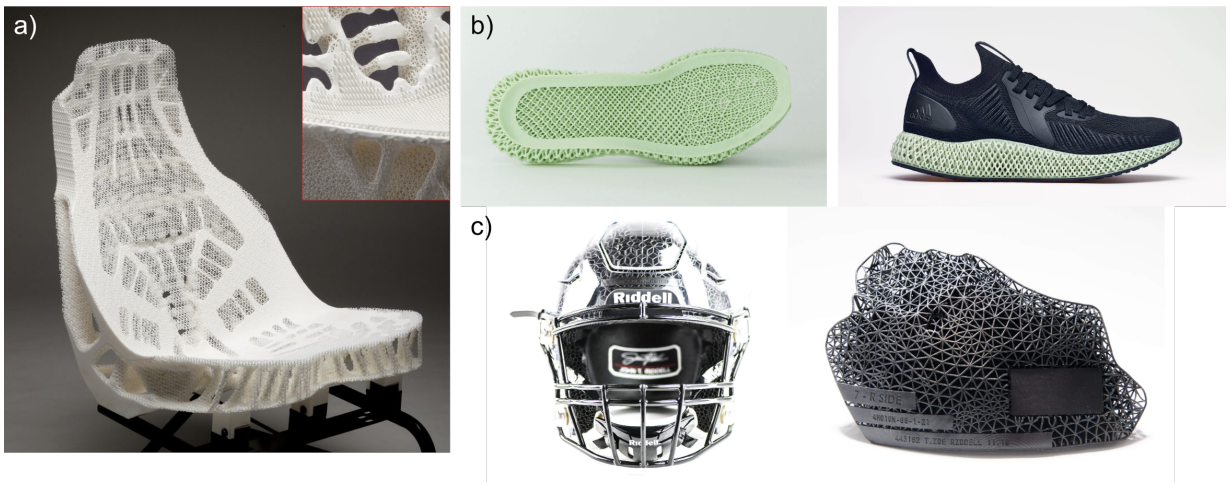


Figure 6.6: *a) Materialise car seat design for Toyota [161]. 72% volume reduction was achieved through topology optimisation and a new unit cell structure. b) Adidas Futurecraft 4D, manufactured by Carbon using Digital Light Synthesis [88]. Designed for comfort and superior impact absorption. c) Riddell Speedflex Diamond Helmet, manufactured by Carbon using Digital Light Synthesis [162]. High damping elastomer used as a American Football helmet liner for improved impact absorption.*

Multi-plane systems can also function as mechanical safety systems through impact diagnostics. The growing capabilities of AM and industry adoption were discussed in Chapters 2 and 3. One avenue where AM and lattice-based design are increasingly popular is energy harvesters and shock absorption. As shown in Figure 6.6, this has resulted in commercial products such as 3D printed lattice insoles for performance (b) [88], car seats for comfort and weight reduction (a) [161] and helmets for safety (c) [162]. The objective of FMMs is to add additional functionality in architected materials. In addition to their multistable energy absorbing capabilities, can a metamaterial system be used to perform an additional simultaneous function? The proposed FMMs utilise the asymmetric bistable properties of VMTs for mechanical pattern sensing and control capabilities. As a particular force and position are necessary to increase the effective length, the system can be programmed to propagate a mechanical signal in response to lattice deformation.

The schematic in Figure 6.7.a shows the proposed integrated VMT design. By designing the VMT to fit within a unit cell, frustration free deformation and hence actuating forces can deform the bulk lattice, and cause an outward programmed response of the VMTs. It is achieved by adopting the VMT design used in Chapter 4. However, the rigid truss length is reduced from $6.75mm$ to $3.5mm$. By reducing the size of the VMT, the same logic described in Chapter 4 can be integrated within a combinatorial structure. This is shown in Figure 6.7.b for a proposed multi-plane mechanical system

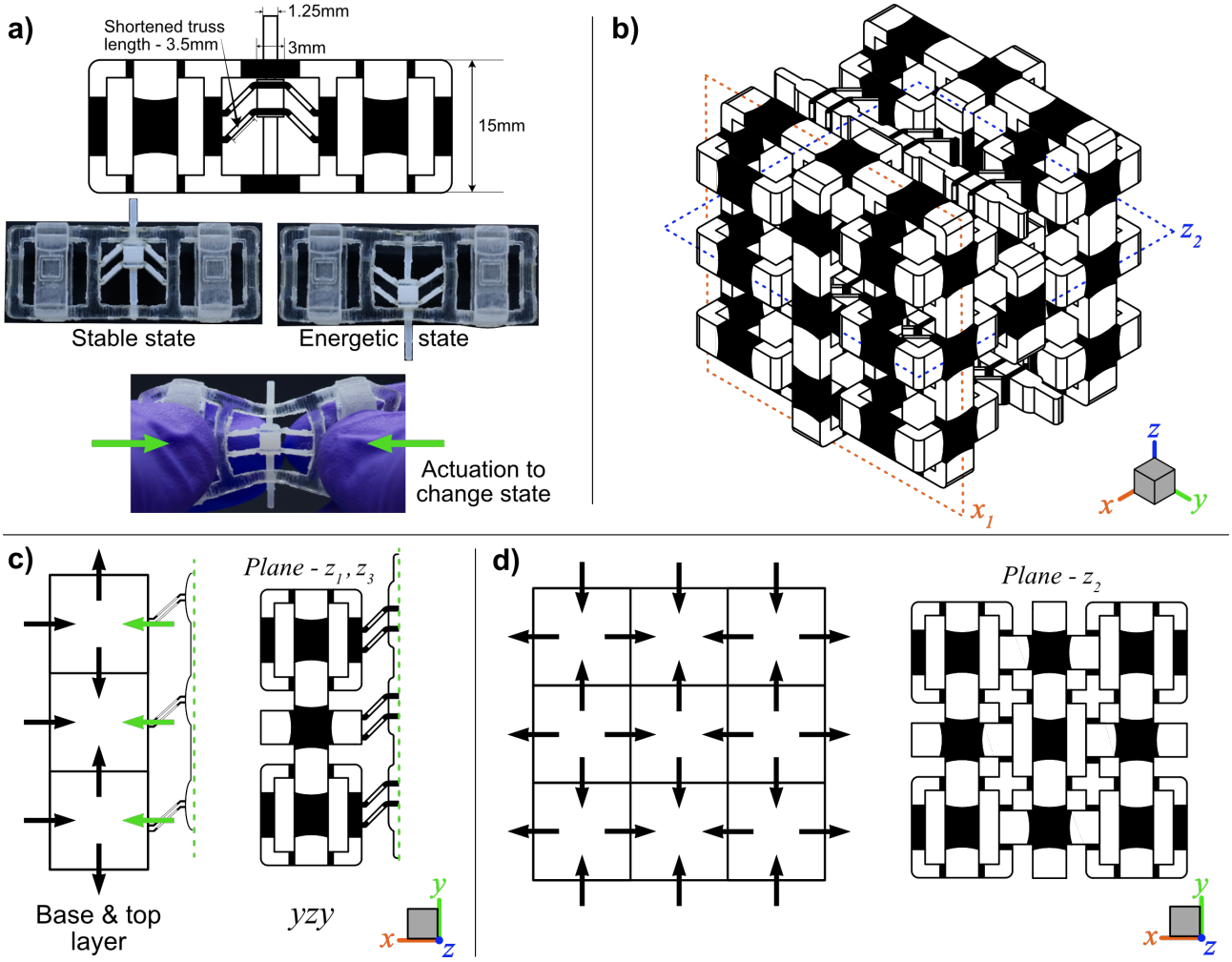


Figure 6.7: *a) Updated VMT design, rigid truss (VeroWhite) shortened from 6.75mm to 3.5mm to fit within unit cell. Images show the VMT in a stable state (printed state), energetic state (against the bias) and during actuation as it transitions between states. b) Proposed 3x3 FMM. Row $x_2 - z_1$ and $x_2 - z_3$ has a 3× coupled VMT system for signal propagation. Row $x_2 - z_2$ has a zyz unit cell combination. c) Green arrows indicate initial constraints for FMM to correct sense and propagate mechanical signal. d) Correct spin configuration for z_2 plane unit cells.*

that propagates mechanical signals. Although there are similarities to the FMM in Figure 6.3, the proposed mechanical system allows for complete integration into an architected material. This is evident from the unit cells in the x_2 plane. The spin configurations of the proposed design are shown in Figure 6.7.c. The green arrows indicate initial constraints, where the unit cell must move inwards $(-\sigma)$ in response to actuation for the MM to function. Once the polarisations of the unit cells in z_1 are defined, the remaining unit cells are defined using the ice rule.

The experimental validation is shown in Figure 6.8. A video of the multi-material FMM propagating signals under the correct actuation can be found using the footnote link[3]. The images in Figure 6.8 show the rigid sections of the unit cell are printed in VeroClear; this allows a better view

[3]FMM Propagating Sensor - `https://vimeo.com/541449016`

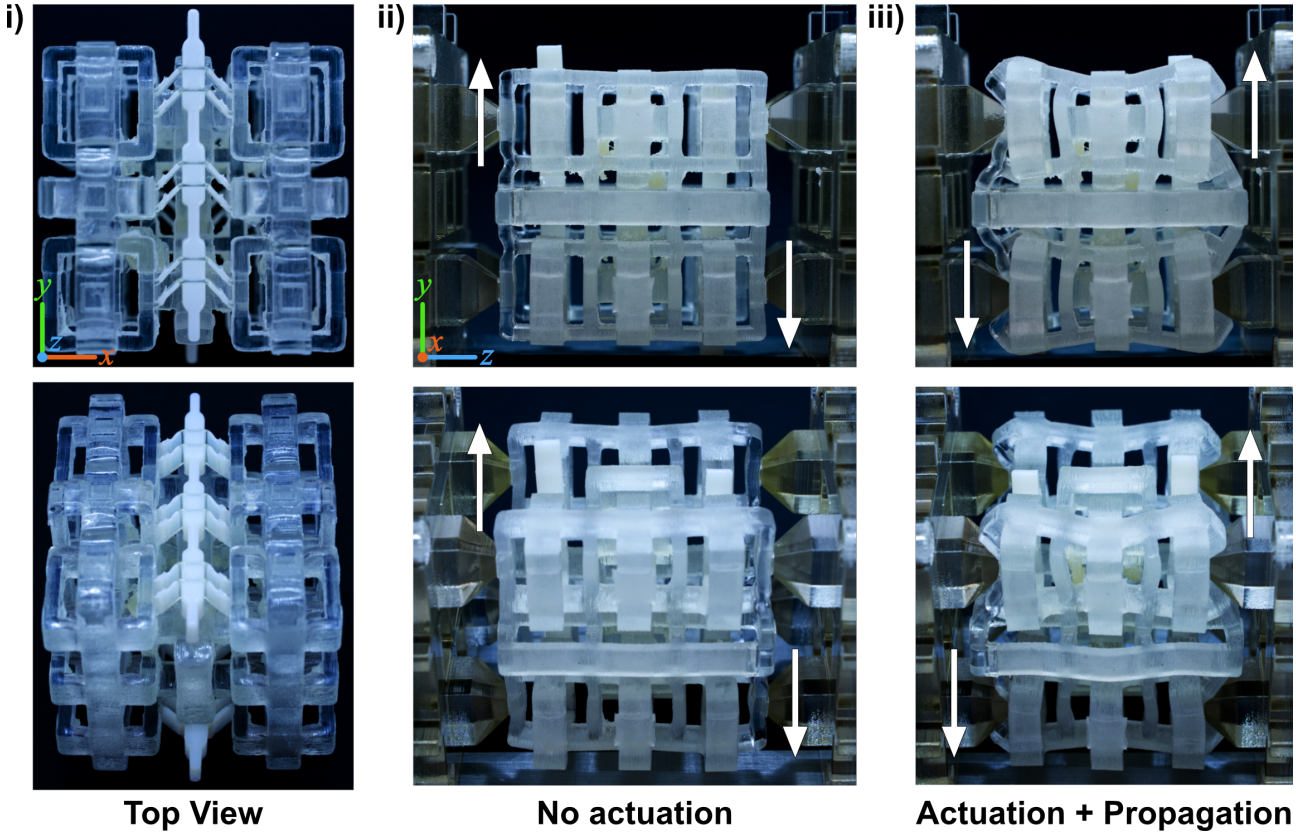


Figure 6.8: *Images show the PolyJet printed FMM sensor design for propagating signals. The rigid sections of the unit cell are printed in VeroClear to allow a better view of the VMT system. i) Top view of FMM - VMT is in a energetic state (against the bias). ii) Side view of FMM in vice under no actuation. Arrows indicate direction of VMTs in $+y$ (left) and $-y$ (right) respectively. iii) Under a patterned actuation from the vice, potential energy is released and signals propagate through system. Arrows indicate direction of propagation $-y$ (left) and $+y$ (right) respectively.*

of the functioning bistable system. According to Section 3.3, the mechanical properties of VeroWhite and VeroClear are almost identical. Therefore, the two materials are interchangeable in the FMM design without affecting functionality. The bistable system is first placed in an energetic state (against the bias) (i & ii). The correct actuation sequence causes the frustration-free deformation of the combinatorial system. This causes the unit cells connected to the VMT to take a concave shape ($-\sigma$), resulting in the release of stored energy in the bistable system and propagating the mechanical waves in the $+x$ and $-x$ directions simultaneously (iii). The propagation only occurs under the correct actuation pattern and force, functioning as connected AND gates. As the VMT is the size of the unit cell, a more extensive combinatorial system can be realised with mechanical signals passing through the system in $\pm x, \pm y$ and $\pm z$ directions.

As first highlighted by Raney *et al.* [80] for a series of connected bistable arches, stable propagation of mechanical signals with controllable velocity and high fidelity can be achieved. This is also validated in the VMT system under the correct actuation sequence, as each VMT releases its own stored energy in addition to the actuating force from the connected VMT, causing stable

mechanical signals to propagate, that are repeatable and propagate only under the correct input conditions. In this system, the size of the proposed MM is not limited to a 3x3 configuration, which has been chosen due to manufacturing and testing constraints. The proposed FMM highlights the additional functional capabilities by combining a 'response' system to a combinatorial unit cell system. Raney *et al.* [80] proposes propagating mechanical signals in soft media can be used for a new class of tunable and responsive systems and devices such as soft robotics, microfluidics and adaptive optics. The proposed FMM shows the additional programmable features that can be achieved, furthering the field of morphological computing paradigms using soft media.

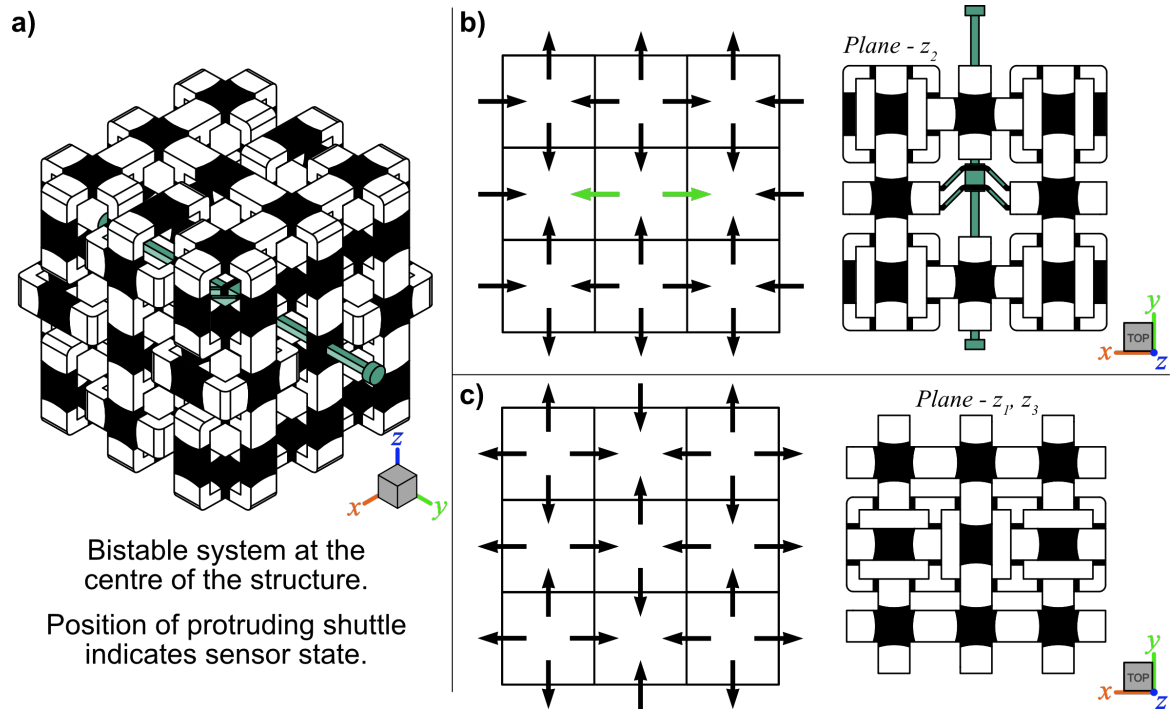


Figure 6.9: *a) Schematic shows the proposed 3x3 FMM integrated sensor. The VMT is fully enclosed in the centre unit cell, moving along the y-axis. b) Spin configuration for the z_2 plane, centre unit cell requires a $+\sigma$ deformation the extended the effective length of the VMT and cause a transition from LOW (energetic - against bias) to HIGH (printed state). c) Spin configurations for the z_1 and z_3 planes to correctly actuate centre unit cell holding the sensor.*

A further implementation of a mechanical safety system is to have the bistable VMT fully enclosed in the unit cell as shown in Figure 6.7.a. The schematic in Figure 6.9.a shows the proposed FMM integrated system. The MMs functionality is to determine a correct actuation pattern and load, releasing elastically stored energy and transitioning to its low energy printed state. As the VMT is enclosed within the combinatorial system, the shuttle is extended to protrude through multiple unit cells (shown in green). This allows the current state of the FMM to be determined by the shuttle's position along the y-axis. The spin configurations of the z_2 plane enclosing the VMT are shown in Figure 6.9.b. The green arrows indicate the spin constraints for the VMT to propagate from a correct

actuation, i.e. $+\sigma$ of the centre unit cell. In a 3x3 system, the number of possible configurations increases significantly. Figure 6.9.c shows the spin and unit cell configurations for planes z_1 & z_3, which are identical in this instance.

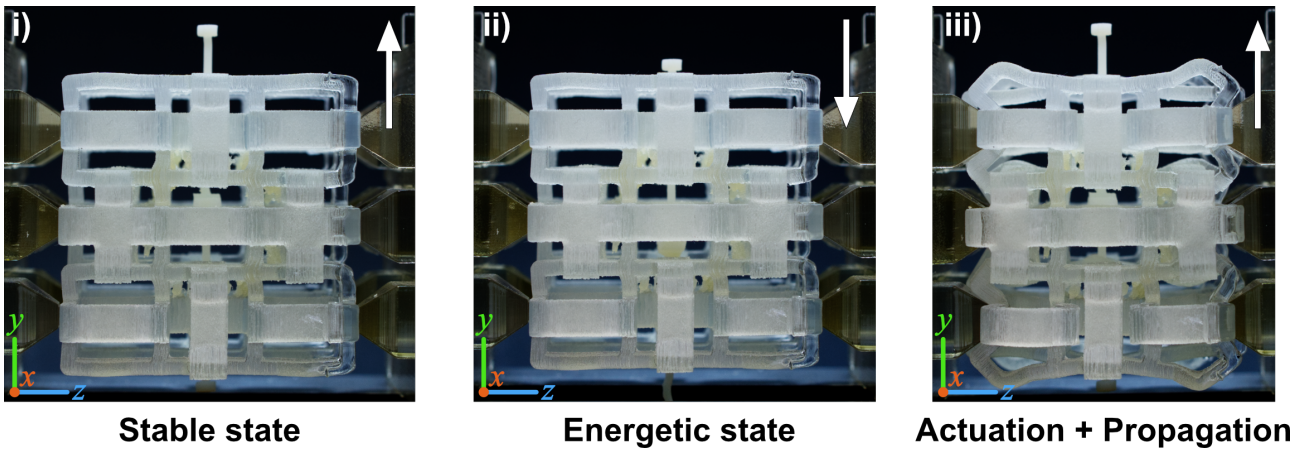


Figure 6.10: *Images show the PolyJet printed FMM integrated sensor in vice and patterned actuation. The rigid sections of the unit cell are printed in VeroClear to allow a better view of the enclosed sensor. i) FMM in stable (HIGH, $+y$) printed state under no actuation - unable to sense load. ii) FMM placed in energetic state (LOW, $-y$) against the bias. iii) FMM under actuation, transitioning from LOW to HIGH state.*

The experimental validation of the proposed FMM is shown in Figure 6.10. The images show the system when under no actuation (i), the VMT in its energetic (LOW) state, against the printed bias (ii), and in response to actuation, the bias ($HIGH$) printed state (iii). The arrows indicate the position of the VMT system. Under a correct actuation pattern and a specific minimum load, the effective length of the integrated VMT is increased, releasing the stored potential energy. In contrast, an incorrect actuation pattern results in frustration, and $-\sigma$ of the centre unit cell, pushing the VMT ends together. The behaviour of the FMM is highly tunable, as changes to the Shore hardness of the elastic flexures and changes in the combinatorial design affect the minimum required load for the VMT to propagate. Furthermore, the truss and joint length all factor into the effective length of the VMT and the required separation distance to allow a VMT to change state. This allows multiple mechanical systems to be integrated into an morphological system, with the ability to sense pattern and load specific events.

Although an extended shuttle is shown for visual purposes, this is not necessary for the functionality of the FMM. The bistable system can be placed in any orientation and in any unit cell to function as a mechanical programmable system. The proposed FMM is disruptive to several industries in which passive systems can be advantageous for diagnostic reading. As previously stated and shown in Figure 6.6, the availability of AM technologies has allowed significant advances to manufacturing capabilities,

often allowing for lightweight structures and improved mechanical properties that are tuned to the specific use-case.

The proposed FMM highlights the potential capabilities of integrated programmable materials within a bulk architected system. For example, this system can be used as a passive diagnostic tool in accident scenarios. In particular, for the sporting industry, reducing the likelihood and faster responses to concussion events is of huge importance to safety in sports. As a result, lattice-based helmets through 3D printing have been an area of particular interest due to their controllable mechanical properties. The proposed FMM is designed to function within a larger structure such as a helmet (Figure 6.6.c) [162]. A large impact on the helmet will typically cause the lattice structure to deform. Integrated bistable VMTs introduce a passive programmable aspect to the helmet design, allowing information to be gathered on the range of forces and the stress concentration observed near the VMT, as asymmetric unit cells programmed as AND gates require actuation from both sides. In its simplest of cases, this mechanical system can be termed a passive mechanical sensor that sits within a structure and can be used to provide basic information on the current state of the structure. In a potential concussion event, the helmet can be inspected; the VMT state provides information on the location and minimum force experienced in a collision which a physician can then use to properly diagnose a condition. Furthermore, the tunability of the system opens the space for additional sensitivity, allowing for an easily produced, passive system that indicates the current integrity of the architected system. The proposed FMM has its limitations as a complete sensor due to the lack of electronic input/output information that can accurately be provided. However, the ease in manufacturing the passive safety systems during the AM printing process is a cost-effective, minimally invasive programmable feature that fits within the architecture without changing the bulk properties.

6.5 Discussion

The FMMs tested in this chapter were developed to investigate whether multi-plane programmable behaviour can be achieved, and whether the proposed MMs form part of larger morphological systems. The FMMs are developed from the basic multi-material and compliant MMs explored in previous chapters. The previous designs were single plane systems, although the input and output directions differed. An objective of the multi-plane systems developed is to show that multiple outputs can occur in an architected system whilst still sharing the same input conditions. This was shown for a VMT and compliant system in Figure 6.3. The buckling direction was defined by the angle of the elastic joints in the VMT (135°) and the single-sided chamfer ($0.4mm$) on the slender compliant beam connected to the unit cells. Through compression, both FMMs buckled as intended and transitioned to their second stable state under actuation. The system is validated experimentally through a textured input using a vice and manual actuation through the bifurcation point to the second stable state.

Although the system was experimentally validated, the printed mechanisms did pose several problems in repeatability after frequent use, as highlighted for the MMs developed in Chapter 5. Particularly for the SLA printed compliant FMM, the mechanism was prone to brittle fracture. This is likely due to an increase in areas of stress concentration and the effect of defects. Shrinkage occurs during the curing process for SLA components, this introduces areas of residual stress particularly in larger multi-plane systems that can lead to fractures. Furthermore, defects such as inconsistent thickness, notches and nibs left on during post-processing affected the functionality of the printed mechanism. The defects are pronounced in comparison to previous MM prints due to the particular challenges of printing larger structures; for example, more internal support was required and difficult to reach areas for support removal.

The rod-logic FMM highlighted several problems when printing multi-plane systems using SLA technology, that was lesser realised during the design phase and testing of the 3x1 MMs. In an idealised frustration-free system, the actuation of the top and bottom layers would cause the unit cells of the MM to deform equally. In the MM investigated in Section 6.3, the unit cell at the centre of the MM is influenced the least, resulting in less compression of the middle slender beams and a reduced buckling height compared to the beam at plane z_3 from Figure 6.4. The effect was mitigated by compressing from the outer unit cell faces, as a means of simulating the MM response if it formed part of a larger morphological system. In general, for compliant systems, the influence of an actuated unit cell is less pronounced in neighbouring unit cells due to the tension present in printed semi-flexible plastics

constructed into a lattice. 3x1 systems do not show the same failure points of restricted unit cell deformation due to the shared middle unit cell that is deformed by both neighbouring unit cells in a *zyz* configuration. In compliant systems, functionality is limited unless the input sequence actuates at least every other unit cell. In contrast, the influence on neighbouring unit cells is significantly more pronounced in fully elastic systems.

In addition, the gating system of the proposed MM was shown not be to as robust as anticipated. In the active state, gate R1 interacts with the propagating system R2, restricting propagation. However, as the end of the gating system is free-hanging, the threshold force on R2 is significant enough to move R1 and allow propagation. The FMMs investigated have been limited to 3x3 systems due to print bed size and post-processing constraints. In a more extensive MM system, the rod section of R1 would be connected to additional bistable beams. As a result, the end will not be free-hanging, and the gate will provide enough resistance to restrict propagation.

The proposed rod-logic FMM has several implications for morphological computation and programmable MMs. In particular, the use of multi-plane, multi-directional mechanical systems that respond to inputs and outputs according to the event sequence show the basis for complex computational logic. Although a simple configuration is studied, previous research [14, 80, 81] in MM logic have described the ambition to achieve complexity to this scale. FMMs such as the rod-logic example are highlighted as disruptive to several industries such as robotics and have wider implications for the development of mechanical logic systems. The rod-logic example in Figures 6.4 and 6.5 highlight several aspects sought after to achieve programmable mechanical structures. The combination of a bistable system within a lattice highlights the ability to propagate mechanical signals through an architecture. Furthermore, the anisotropic nature of the unit cells adds programmable capabilities to the system. Finally, with the use of AM, greater complexity can be achieved in integrating complex systems. Bistable systems that propagate in multiple directions and function as blocking elements can be designed in, introducing decision tree mechanical logic.

Testing the rod-logic system highlighted additional development work required on the AM process for the system to be considered robust for future uses. Bedding in the unit cells for a compliant MM was necessary to reduce flexural stiffness. However, consequently, the slender beams had limited usage and risked fracturing as a result of repeated actuation. This is currently a constraint of the Tough1500 and SLA printing of functional structures, and highlights one of the main limitations of a compliant functional architected material, where a large flexural response is required in all three principal axes. As the structures explored require large deformations and exhibit anisotropic behaviour, semi-rigid

systems currently limit the propagation of signals to only the neighbouring unit cell. As a result, the functionality of the proposed FMM in a complete morphological system is currently limited. However, the rod-logic FMM highlights the scope of complex programmable materials within larger domains that can be envisaged.

The MMs proposed in Section 6.4 show the potential of functional materials integrated into larger lattice systems. AM is increasingly being explored for improved safety, reduction in weight and superior performance. The proposed MMs show programmable functionality (akin to mechanical fuses), that can easily be embedded into architected systems during the printing process. There are, however, design constraints in multi-plane systems to consider. As mentioned for the restriction in movement of neighbouring unit cells in compliant systems, this is also present in multi-material MMs. Particularly in unit cell combinations, i.e. xx, xy, & xz, the actuation of either unit cell does not fully actuate the neighbouring cell. This effect is less pronounced in larger connected systems; however, it is still evident on the outer face of unit cells not directly actuated. As shown in Figure 6.8, for MM configurations where the pattern is repeated in the z_1, z_2 & z_3 plane, this effect is minimised. However, in configurations such as Figure 6.10, the multiple orientations reduce the dissipation of force throughout the structure. Testing different configurations showed less influence on the centre unit cell holding the bistable unit than favourable configurations such as the MM proposed in Figure 6.3 and 6.8.

Inspection throughout a lattice structure remains a challenge. Although support is dissolvable and the majority is removed during the PolyJet post-processing, harder to reach areas can leave residual layers of support material that affect longer-term functionality. Additionally, although the MMs were stored at room temperature and enclosed away from light, polymers do have an ageing effect which factors into the flexural response. Further development of MMs would require a detailed materials study from completely elastic systems to semi-rigid compliant systems and the design of a new photopolymer resin that best suits the intended design outcomes.

The MMs in this chapter highlight the capabilities of functional mechanical systems over multiple planes. For example, greater complexity in mechanical logic systems, gating signal pathways and integrated mechanical fuses for use as a diagnostic tool is proposed. This results from the anisotropic 3D unit cell allowing for different frustration-free configurations and bistable systems that combine in multiple orientations to add *respond* functionality to the system. Additional control can be implemented by altering the beam characteristics, for example, a change to the beam thickness. This results in a change to the effective length of the beam and a resulting tuning of the buckling and

snap-through properties. The change in beam parameters results in a tunable bistable system with different levels of sensitivity to opposing forces within one multi-plane morphological system. For example, these can be implemented as single-use 'passive fuses' in car seats, functioning as fully mechanical accelerometers, where snap-through motion from deceleration can be programmed independently for the x, y & z axis. The proposed iteration of such a mechanism would be to explore multi-axis printable electronics, integrating the tunable FMM into an electron safety unit.

What is particularly novel of all FMM systems explored is their passive nature; systems are only *activated* under the right conditions, for example, sitting down and applying a steady force on a car seat. In the compliant mechanical systems, the beam system transitions from monostable to bistable only after the correct actuation pattern and load is applied, transitioning from a *passive* state to an *active* state, where the mechanical system can respond to changes as long as the patterned load is constantly applied. Snap-through only occurs when an opposing load reaches the threshold force. This system highlights the multiple environmental conditions that need to be met for the functionality of an FMM to be *activated*.

The multi-plane combinatorial FMMs have highlighted programmable and tunable behaviour in several examples. In particular, the systems explored all MM features for answering the research question. The FMM propagating mechanical wave system in Figure 6.8 and integrated safety system in Figure 6.10 utilise a mechanical AND gate in a multi-plane configuration. Furthermore, a combinatorial approach is taken, leading to FMM functionality in larger morphological systems. Additionally, the bistable FMMs in Figure 6.3 and the rod-logic system in Figure 6.5 highlight MMs' tunable and programmable capabilities that can function through multiple planes and be integrated into broader lattice systems.

Chapter 7

Case Study - Nuclear Safety Mechanism

In this chapter, the applicability of MMs for use in nuclear safety mechanisms is examined. Discriminating mechanisms are mechanical safety devices critical to detonation safety in nuclear deterrents. Traditional discriminator designs such as Pin-in-Maze and Counter-Meshing-Gears are safety mechanisms because of their effectiveness at differentiating signals and rendering the device incompatible. However, the designs are often planar, challenging to manufacture without specialist techniques, reliant on multiple moving parts, and the discriminating pattern can easily be determined. The compliant MM in Chapter 5 is extended to a 6×1 *system to show a 6-bit implementation of a unique signal. Three different combinatorial systems are successfully demonstrated. Under the correct 'input signal' (actuation pattern), the FMM becomes bistable, allowing mechanical signals to propagate. An incorrect input results in frustration in the FMM, the resulting tension along the slender beams places the safety mechanism in a monostable state (incompatibility). Frustration in some cases can lead to a fracture in the compliant system and irreparable damage to the safety system (inoperability).*

7.1 Nuclear Safety Principles

This chapter explores the potential safety benefits of using a combinatorial MM as a safety device for the nuclear industry. As with many of the examples explored in the Literature Review (Section 2.3), the MMs described are seldom used for engineering purposes in industries such as aerospace and nuclear. The compliant mechanical system explored in Chapter 5 highlights MMs' programmable and tunable behaviour. In addition, Chapter 6 highlighted the functional capabilities and developed passive mechanical systems akin to passive safety system design. The following discussion provides a case study on the development of mechanical safety mechanisms employed in the nuclear industry and the potential safety implications of adopting MMs. In particular, the multi-plane input/output MM design and the implementation of broader lattice systems are examined for their suitability in next-generation safety design.

When developing a novel safety mechanism for the nuclear industry, it is necessary to understand the importance of safety themes that have influenced past designs. Major accidents involving nuclear deterrents, such as the events in Thule and Palomares [163], thrust nuclear deterrents' safety as a primary cause for concern. Greater surety was required on the response of devices in nuclear deterrents when subject to accident environments. As a result, 'the principle of enhanced nuclear detonation safety' (ENDS) was developed. The principle sought to bring structure to safety design, embedding critical features into integral parts of the weapon system. Known as safety-critical subsystems and components, these are designed to protect the detonation critical system, a configuration of which is shown in Figure 7.1. Four safety themes were introduced as the most fundamental characteristics to ensure nuclear detonation safety: isolation, incompatibility, inoperability and independence [164, 165, 166, 167, 168].

7.1.1 Isolation

The principle of isolation is shown in Figure 7.1 as the energy (structural) barrier surrounding the detonation system. This creates an exclusion region between the detonation system and the outside environment, a region that remains free from all energies deemed compatible with the system. The energy barrier must be robust and designed to last, protecting the detonation system from all potential risks; this includes extreme events such as lightning and power surges. Due to implementing a structural barrier protecting key components, an energy gateway is required, allowing signals to pass through the exclusion region to the detonation system. Stronglink devices

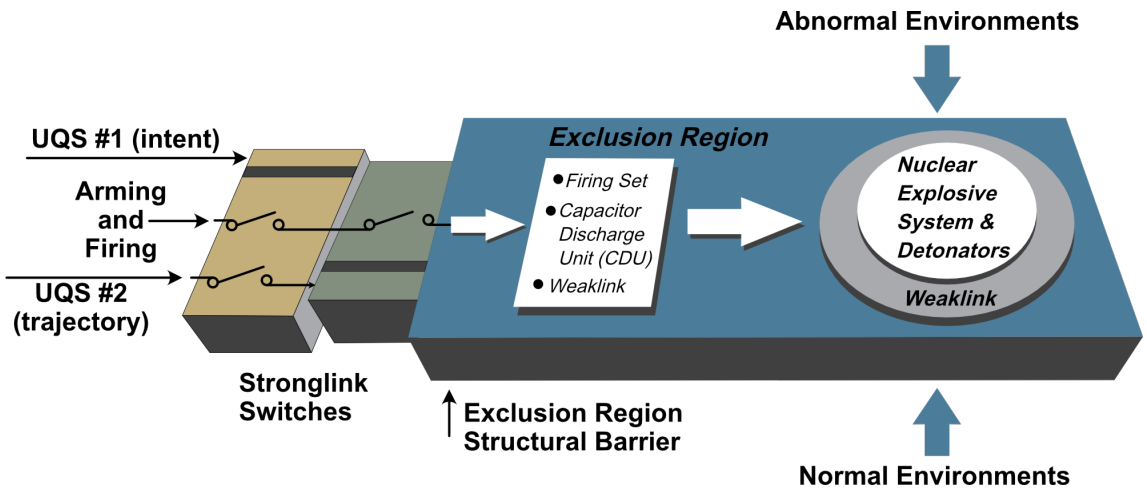


Figure 7.1: *Schematic from the US DoD on the current implementation of the ENDS principles employed around detonation critical components [169].*

ensure a safe pathway for signals to reach the critical components in response to correct authorisation. When a stronglink is in an engaged state, correct energies (signals) can reach the critical components. In its disengaged state, the stronglink forms part of the energy barrier blocking/diverting any signals. Isolation is key to the success of a stronglink device due to its role as a fundamental component of the energy barrier.

7.1.2 Incompatibility

The principle of incompatibility is integral to nuclear deterrent safety, as a stronglink device needs to distinguish between signals that can/cannot pass through the exclusion region. The discriminating mechanism within a stronglink device determines this logic, responding to signals passing through the stronglink. At each input event, the discriminator determines if the signal is correct. Incorrect signals result in the device locking in place and protecting the system from any outer energies. A correct input allows the energy gateway to be engaged and signals to pass through the exclusion region [170, 171].

The two main purposes of incorporating incompatibility through the use of discriminating mechanisms are:

- To prevent accidental loss of isolation through the stronglink.
- To complete the detonation pathway when given unambiguous intent.

Discriminating mechanisms are designed to respond to Unique Signals (UQS). These signals comprise 24 bi-valued input events; at each input event, the discriminator must determine correctness. Although, at a basic level, a discriminating mechanism functions very similar to a

combination lock, these mechanisms are engineered to respond only to UQS signals and ensure isolation in all other cases. A UQS discriminator is of little help if the energy barrier can easily be circumvented. Likewise, a discriminator easily bypassed by non-unique signals negates the isolation function of the energy barrier.

7.1.3 Inoperability

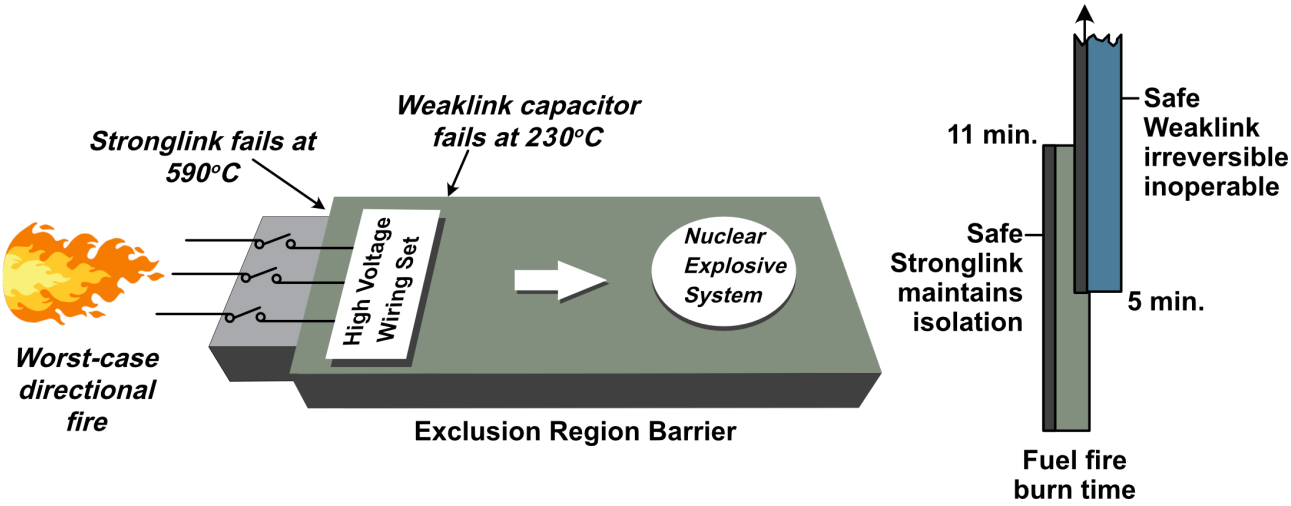


Figure 7.2: *Schematic from the US DoD showing how stronglinks and weaklinks are expected to respond in abnormal environments, such as a worst-case directional fire [169].*

To ensure deterrent safety is upheld in all environmental situations, the principle of inoperability is implemented through weaklinks. These are detonation critical components designed to irreversibly fail when a deterrent is exposed to an environment outside the defined stockpile-to-target sequence. By incorporating environmental vulnerability into weaklinks, an additional safety barrier is introduced. Weaklinks are designed to become inoperable before the barriers in place from the stronglink and exclusion region are at their limits of failure. The schematic in Figure 7.2 shows the deterrent safety systems response to a worst-case directional fire. A common weaklink used in deterrents are capacitors in detonators. The materials used in the capacitors have a lower melting point than other critical components in deterrents [172]. The capacitors melt and become irreversibly inoperable well before the isolation from the stronglink is at risk. As a result, the risk of accidental detonation and a nuclear yield occurring is significantly reduced. Co-location of the weaklink mechanism is also necessary, as the energy barrier, stronglink, and weaklink should experience the same environmental conditions.

7.1.4 Independence

The principle of independence is introduced to a deterrent safety design to ensure multiple barriers are in place in device failure. Although designed to be robust and only respond to a correct UQS, maintaining two independent stronglinks which require different UQS sequences, actuation methods, and different methods of discriminating the signal; increases the redundancies in the safety system. A stronglink system within nuclear deterrents comprises two separate and independent devices, the intent stronglink and the trajectory stronglink. The intent stronglink is engaged before the deterrent takes its trajectory; this is often a manual insertion of the UQS. The trajectory stronglink is engaged during the stockpile-to-target sequence of the deterrent. As the correct trajectory is followed, a UQS is sent to the stronglink to engage the system. This ensures there are multiple barriers in place to protect against accidental detonation.

7.1.5 Unique Signals

The 'Walske Letter' of 1968 stated that 'the probability of a premature detonation shall not exceed 1 in 10^6 per exposure or accident' [171]. Maintaining this level of safety in nuclear deterrent systems in abnormal environments gave rise to the ENDS principles and UQS. A UQS sequence comprises 24 individual bi-valued events used to navigate a discriminating mechanism. The safety provided by a UQS such as *AAABBAABBBAAABBBAABABBAB* [173] is given by the pattern design choices made.

The report 'Mathematical Aspects of Unique Signal Assessment' by J. Cooper [171] provides an in-depth analysis of the UQS sequence. In this section, a brief overview of the UQS is discussed. The UQS pattern is designed to ensure the correct sequence to navigate a discriminating mechanism that cannot be randomly generated in abnormal environments, maintaining a safety level per stronglink of 1 in 10^3 per exposure or accident. A UQS pattern provides resistance to inadvertent independent threats through event type balancing. The pattern *AAABBAABBBAAABBBAABABBAB* has 12 A events and 12 B events satisfying this condition. Further resistance is also provided by ensuring the pattern follows transition balancing rules. A first-order transition evaluates input pairs, for example, *BA*. The optimum resistance, considering a statistical bias towards one transition pair over another, is achieved using the same number of transition pairs for a pattern. For example, the UQS shown above has the following: *6AAs, 6ABs, 5BAs, 6BBs.* In addition, UQS patterns also balance second-order transitions i.e. *ABA*.

The dependencies in the system primarily drive the pattern design of a UQS. Particularly as

these signals are sent to mechanical components, dependencies may be present due to design and environmental factors. Adjacent dependencies are the 'inadvertent generation of an event, conditional on the previous event or events being generated'. The probability for first and second-order dependence is calculated using the equations below:

First Order dependence equation

$$P(E_i \cap E_{i+1}) = P(E_i) \times P(E_{i+1} \mid E_i) \tag{7.1}$$

Second Order dependence equation

$$P(E_i \cap E_{i+1} \cap E_{i+2}) = P(E_i) \times P(E_{i+1} \mid E_i) \times P(E_{i+2} \mid E_{i+1}) = P(E_i \cap E_{i+1}) \times P(E_{i+2} \mid [E_i \cap E_{i+1}]) \tag{7.2}$$

Table 7.1: *Table showing UQS patterns for bi-valued, tri-valued and quad-valued event types. Adapted from Cooper [171].*

Number of Event Types	**UQS Pattern**
2	A,B,A,A,A,B,B,A,A,A,B,B,B,B,A,B,A,A,B,A,B,B,B,A
3	A,B,A,A,C,B,B,A,C,C,B,C,A,B,C,C
4	B,C,A,D,C,C,B,A,B,D,D,A

Where E_i denotes the event number, $\cap$ represents logical "AND" and $\mid$ represents "conditional on". As previously stated, to increase resistance to threats, the UQS pattern should be designed so that the conditions of balanced events and balanced first and second-order transition events are met. Table 7.1 shows what a potential pattern may look like if these conditions are met for 2, 3 and 4 event types. By combining the following patterns with our adjacent dependence equations, we can obtain the overall dependence of our pattern.

The graph in Figure 7.3 shows the effect signal dependence has on UQS threat. As the dependence order increases, the resistance of the pattern to threat significantly reduces as the number of event types change from bi-valued to quad-valued. When each event is truly independent of one another, the threat protection is comparable in all three cases. However, as environmental factors may present potential dependencies between events, greater threat resistance is exhibited by bi-valued events. When defining an abnormal environment, it is conceivable that not all biases in a system are known and, more practically, cannot be determined. These are often defined as unknown and unknowable biases. The design choices behind a 24 bi-valued UQS, using the specific set of rules in generating

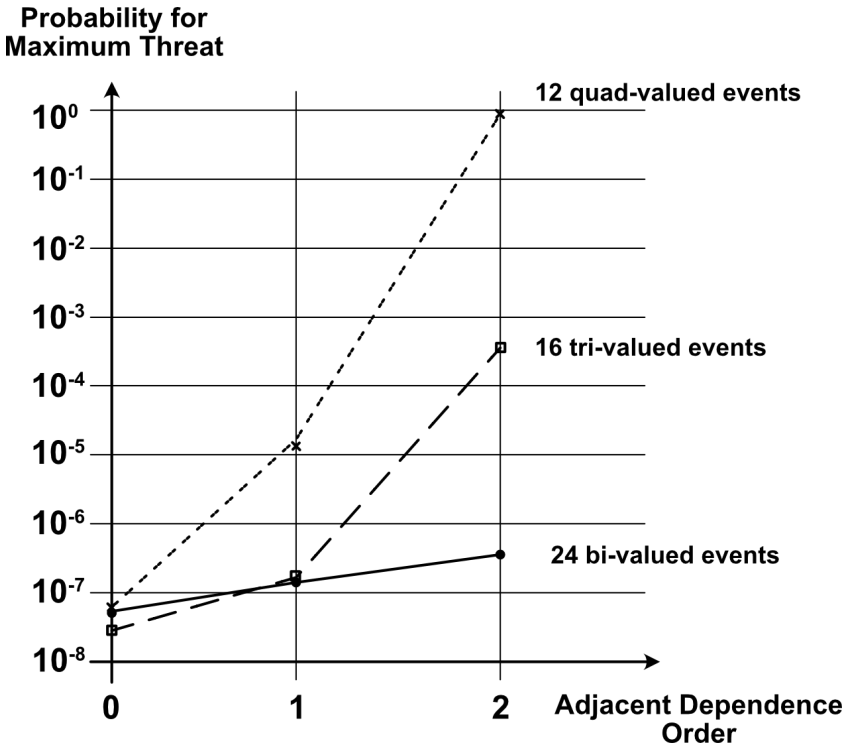


Figure 7.3: *Graph showing how the probability of threat to the UQS changes, depending on the type of signal pattern generated and the adjacent dependence order between signals. Graph adapted from Cooper [171].*

the pattern, limit the susceptibility to any potential abnormal environments that may create system biases. Within a stronglink mechanism, bi-valued events are often well suited due to the mechanical switch like configurations most notable in current designs. However, there is scope to explore how the discriminating mechanism design and the UQS pattern affect the susceptibility to different biases, for example, exploring the adjacent dependence of a system if inputs are in three separate plane directions instead of one. This is of particular importance in considering the added design space introduced through multi-plane FMMs.

7.2 Discriminating Mechanisms

In this section, a detailed study is conducted on how the ENDS principles are implemented in the design of discriminating mechanisms [166, 174, 175, 176]. The paper 'A Primer on Unique Signal Stronglinks' by D. W. Plummer *et al.* [165] describes the 'Anatomy of a Stronglink', comprising of a Prime Mover, Discriminator and Energy-Coupling element. Table 7.2 provides detail on the anatomy for standard stronglink devices used in the nuclear industry. The discriminator is the main component of a stronglink, holding the UQS pattern and guaranteeing incompatibility is ensured if incorrect signals are received. The prime mover describes the motors used to move the discriminating

mechanism as a UQS is received. When a correct 24-bit sequence is received, the coupling scheme defines the mechanism to allow a specific type of energy through the exclusion region.

Table 7.2: *Anatomy of a Stronglink, showing the fundamental components and design considerations in a stronglink device. Adapted from Plummer et al. [165].*

Discriminator	**Prime Mover**	**Coupling Scheme**	**Energy**
MC2969	Rotary Solenoids	Coupling Contacts	Electrical
MC2935	Rotary Solenoids	Coupling Contacts	Electrical
C Mod	Rotary Solenoids	Interrupted Transformer	Magnetic
D Mod	Rotary Solenoids	Interrupted Transformer	Magnetic
MSAD	Linear Solenoids	Explosive Pellet	Kinetic
DSSL	Rotary Solenoids	Explosive Pellet	Kinetic
Pin in Maze	Stepper Motor	Prism Alignment	Optical
Leaf Spring	Stepper Motor	Paste Explosive Valves	Chemical

The MC2935 trajectory stronglink [176] was an early stronglink design that utilised rotary solenoids and electrical coupling contacts to perform safety functions. The MC2935 discriminator shown in Figure 7.4 consists of a double-radii wheel, a locking pawl and a wand arm check wheel in a cylindrical arrangement. The locking pawl has a protruding pin caught by a hook on the wand arm check wheel if the locking pawl follows the outer radii edge of one of the two discriminator wheels. This occurs if the two solenoids with different patterned double radii wheels are pulsed out of sequence when receiving a UQS. A correct UQS signal will allow the patterned wheels to rotate and engage the electrical contacts. An incorrect input will result in the wand arm catching the locking pawl pin; this stops any further rotations in the device from occurring. The MC2935 discriminator design uses several components to determine the correctness of a UQS. In particular, the signal interrogation system uses a spring to ensure it hooks onto the lock pawl pin if an incorrect input occurs, a potential failure point of the mechanism. Furthermore, the UQS signal is easily determined by observing the double radii wheel. This makes the discriminator easy to manoeuvre by pulsing the solenoid for the corresponding wheel that follows the inner radii.

The MC2935 was initiated in 1979, as shown in Table 7.2, several discriminating mechanism designs have been developed since. Current discriminating mechanisms used in the nuclear industry are developed from two key design concepts, Pin-in-Maze (PIM) mechanisms and Counter Meshing Gears (CMG). Sections 7.2.1 and 7.2.2 take a closer look at the discriminating mechanism concepts and how they successfully incorporate the ENDS principles.

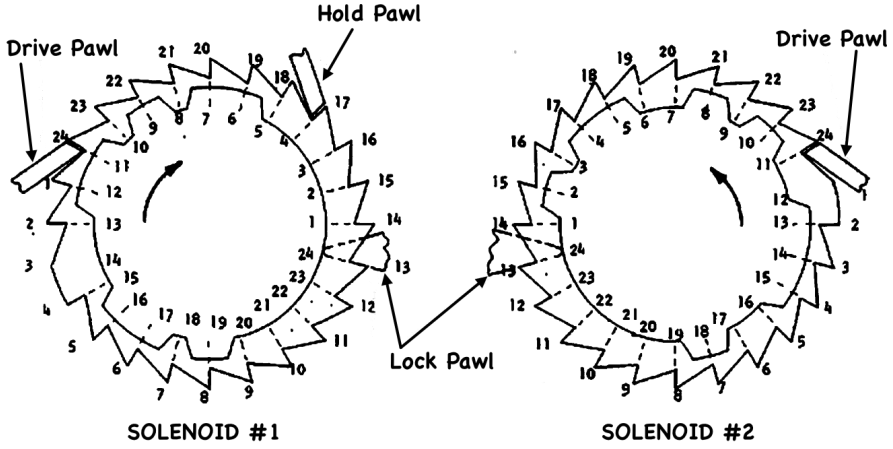


Figure 7.4: *MC2935 discriminator design. a. UQS double radii patterned wheel with ratchet wheel. b. Wand arm mechanism showing how the pin is caught and locks the system. Schematic adapted from Carnicom and Schreiner [176].*

7.2.1 Pin-in-Maze

The rotary PIM design by Benavides is shown in Figure 7.5. A contact pin **16** which protrudes into maze **18** must navigate the entire maze before allowing signals through the exclusion region. In this arrangement, the pin-wheel **12** rotates either clockwise or anticlockwise under actuation from a binary signal, defining an A or B event. The maze wheel **14** only rotates clockwise and is restricted in rotating in the anticlockwise direction due to ratchet **109** and hold pawl **108**. The UQS input directs the pin-wheel to move in either of the directions. A correct signal will follow maze **18** in the defined path. An incorrect input will result in the pin becoming trapped in a dead-end section of the maze. Due to the rotation of maze wheel **14** the pin is no longer able to rotate in either direction, and there is no possibility of the pin backtracking to rectify the incorrect input [177]. Upon completing the unique signal, the pin exits through the exit path **19**. As stated in Table 7.2, the coupling scheme for a pin in maze design is through prism alignment, allowing optical signals to pass through the exclusion region.

The PIM design has been a successful concept for discriminating mechanisms in the nuclear

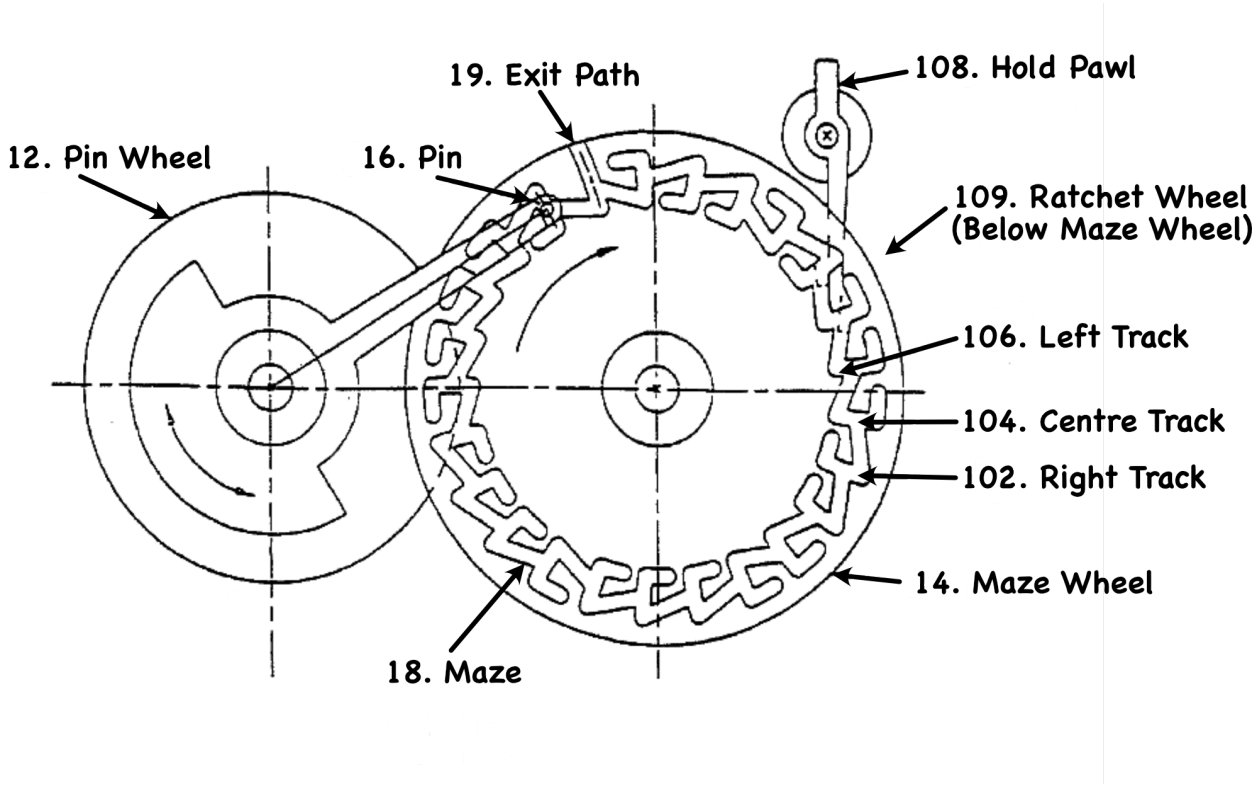


Figure 7.5: *Benavides - rotary pin in maze design. Patent provided by Sandia National Laboratories, patent number - 5,626,040. Top view of maze wheel and pin configuration. Schematic adapted from Benavides [173].*

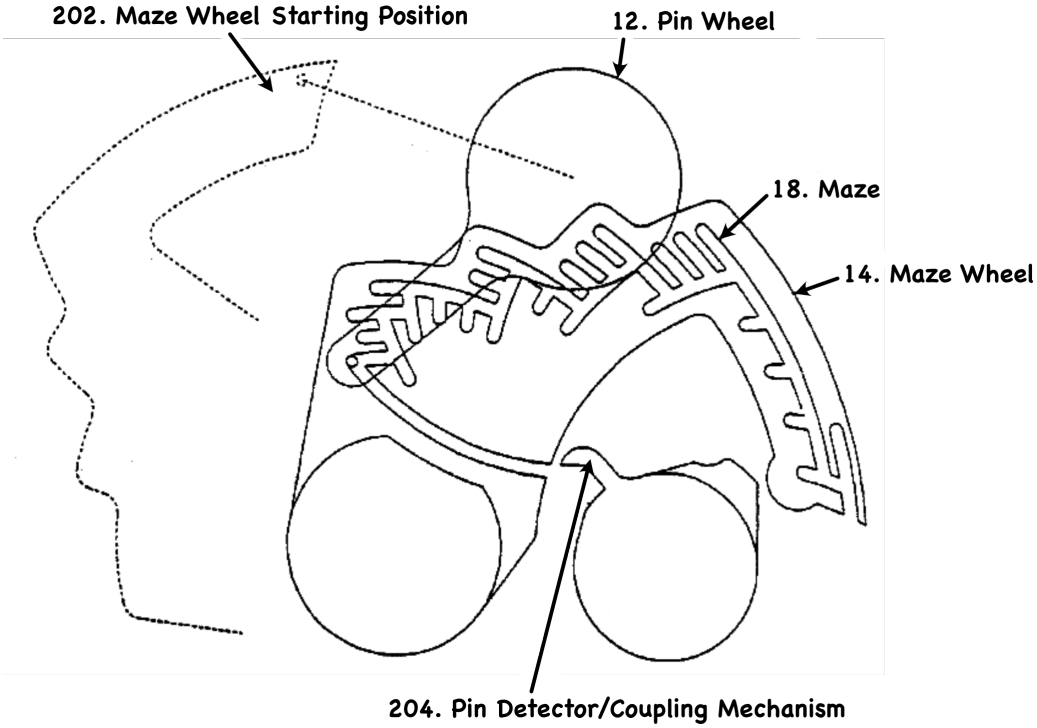


Figure 7.6: *Benavides - rotary pin in maze design. Patent provided by Sandia National Laboratories, patent number - 5,626,040. Alternative configuration in which only the pin or maze is required to move at each event sequence. Schematic adapted from Benavides [173].*

industry because of the effectiveness of implementing inoperability. The locking feature is reliable due to the physical entrapment of the pin if it is navigated down an incorrect pathway. An input event is completed once the pin-wheel and maze-wheel have rotated. As each event requires the rotation of both wheels, the dependencies between input events are reduced. A limiting factor of the design in Figure 7.5 is the reliance on the hold pawl to ensure the maze wheel cannot rotate in the anticlockwise direction. The ratchet wheel becomes redundant if the hold pawl is compromised and does not work as intended, opening the possibility for the discriminator to be taken out of a locked state.

Considering part reconciliation in the design of discriminating mechanisms is essential in improving system safety. By reducing the number of parts in a device, maintaining the ENDS principles no longer relies on multiple components. It can be argued that this reduces the safety redundancies in the device as there is an increased reliance on a small number of components. However, as observed in the PIM design in Figure 7.5, the failure of one component affects the safety of the entire system as incompatibility cannot be assured. The single-action PIM mechanism in Figure 7.6 is an example of part reconciliation. Only the pin-wheel or the maze-wheel needs to rotate to complete an input event, compared to Figure 7.5 where both wheels must rotate. There are two distinct advantages of the single-action design, the speed at which the UQS is implemented and the use of one actuator, which is bi-directional.

In general, there are three limitations to PIM concepts. Using a maze wheel restricts the length and complexity of the pattern and the movement the pin can take. Furthermore, the pattern of a PIM is easy to determine. Although the primary role is to ensure incompatibility from environmental stimuli, a degree of secrecy on the 24-bit sequence is necessary; this is not provided by the ease in determining the correct UQS. Finally, the designs are highly planar as the maze-wheel and pin-wheel always rotate in the same plane. As a result, the PIM device has less resistance to cascading events, in which multiple events can occur from a single stimulus.

7.2.2 Counter Meshing Gears

The CMG design by Polosky is shown in Figure 7.7. There are three polysilicon layers on each gear (**12** & **14**), with variable spacing between protruding teeth **18** for each layer. The teeth arrangement on the gears makes up the UQS pattern, as shown by the Scanning Electron Microscope (SEM) image (Figure 7.8). On a single gear, there can be a maximum of two teeth per section. A UQS input actuates one of the two drive pinions (**16** or **17**). Actuation of pinion **16** causes anticlockwise rotation

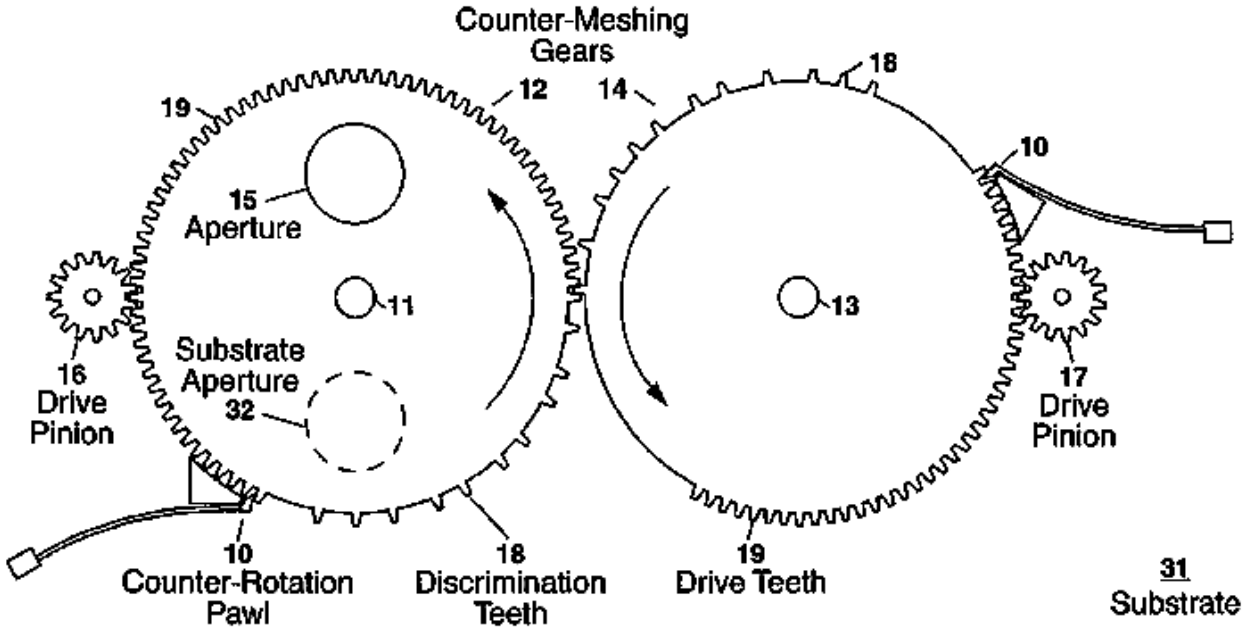


Figure 7.7: *Polosky - Surface micro-machined counter-meshing gears discriminating device. MEMS device, gears* ***12*** *&* ***14*** *comprise of three layers with discrimination teeth* ***18*** *placed according to the UQS code. Patent provided by Sandia National Laboratories, patent number - 6,158,297. Schematic adapted from Polosky et al. [178].*

of the left gear, whilst actuation of pinion **17** causes clockwise rotation of the right gear. Correct inputs will result in the precise order of rotation of the two gears, resulting in no obstruction between the gear teeth. An incorrect input will result in the teeth from both gears impeding one another, leaving the gears in a locked position, unable to complete the rotation. Counter rotation pawls **10** are also implemented on both gears to ensure inputs cannot be reversed [177]. Upon correct completion of the UQS, the left gear will have rotated by 180°, aligning an aperture to allow optical signals to pass through the exclusion region.

The CMG concept has proven popular in the nuclear industry, widely used as a discriminating mechanism. Several different CMG configurations have been developed at a range of length scales. The CMG design by Polosky proposed a Micro-Electromechanical System (MEMS) discriminator device. Four separate layers of polysilicon deposited onto a silicon substrate [178, 179] are used to create the device. Although the concept of CMG devices is widely used, the utilisation of MEMS technology for discriminators is still debated among designers. D'Antonio and Caldwell argue MEMS devices are too small to provide an effective barrier against abnormal environments [5, 180]. In particular, they conclude that MEMS devices do not "*respond in a predictable way to energy management*" because of their "*sensitivity to a large number of potential environmental threats*" [180]. On the contrary, reports by the Naval Surface Warfare Centre have tested MEMS devices and have shown that they

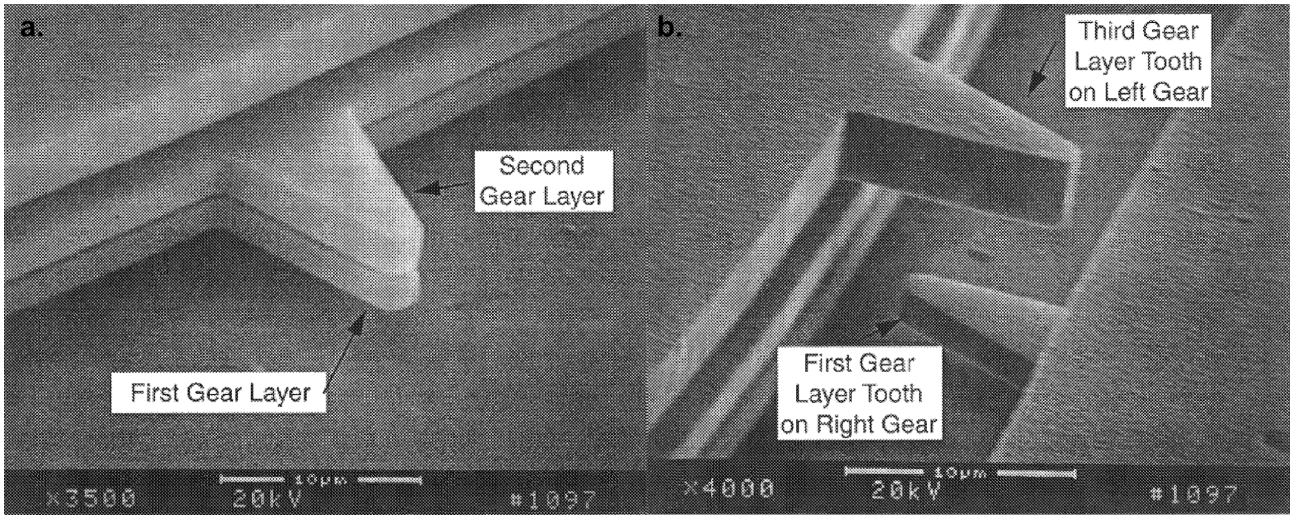


Figure 7.8: *SEM images of a MEMS CMG discriminating mechanism. a) Gear shown with protruding teeth on first and second gear layers. b) Two CMG gears shown that are free to rotate, as the protruding teeth do not obstruct one another. Patent provided by Sandia National Laboratories, patent number - 6,158,297. Images adapted from Polosky et al. [178].*

can operate in multiple environments, having passed a sea and explosive test [181].

Similar to PIM concepts, CMG designs have several favourable features that uphold the ENDS principles. The multi-layered approach of a CMG mechanism makes it difficult to predict the UQS pattern, as the sequence differs in each layer. Without reversing the rotation of the gears, there is no possible method of aligning the aperture without receiving a correct UQS. Incompatibility is ensured if an incorrect signal is received, as the teeth of the gears will impede one another and leave the system in a frustrated state. As with PIM devices, a limitation to CMG designs is the use of counter-rotation pawls. Failure of these components presents the opportunity to circumvent the UQS pattern entirely. Furthermore, although a multi-layered approach is taken, the gear rotation is always in the same plane, providing less resistance to cascading events.

7.2.3 Discriminator Summary

In Section 7.2.1 and 7.2.2, mechanical discriminators that meet the ENDS principles were evaluated. The PIM and CMG designs are used widely in the nuclear safety industry due to their reliable locking features and predictable movements in normal and accident scenarios. Although the mechanisms are widely used in industry, the designs are highly planar, and the UQS pattern is easily recognisable. Also, the discriminators are mechanical devices with reliance on critical components to ensure safety principles are upheld. This requires the system to be designed with additional redundancies. Furthermore, mechanical components are designed with specialist techniques. Mechanical systems are combined with actuators and motors for functionality, and respond to a

UQS to physically align and couple the energy barrier to allow signals into the exclusion region. The discriminator itself and the focus of the 'safety' features come from the mechanical design aspect, where the physical barrier between coupling schemes ensures safety. In the two systems, this is a result of a trapped pin or obstructing gear systems. Advanced manufacturing methods have not influenced designs. As such, concepts that are not possible using traditional manufacturing processes may open innovations in discriminator design, such as the MM designs explored in previous chapters.

In this section, we have evaluated legacy discriminator design used within stronglinks. There are a number of common themes between all designs that must be highlighted as potential routes of improvement for discriminating mechanisms, and avenues to exploit when considering additive manufacturing techniques. In particular, four areas of improvement are highlighted as focal points for improvement in design:

- **Planar Design** - Most discriminating mechanisms utilise a single plane of motion. Excessive forces in the same plane as the discriminator may cause cascaded events to occur, in which several input events transpire before the mechanism locks. Utilising multiple planes to navigate a discriminating mechanism protects the system from cascaded events. This will improve the resilience against abnormal environments as there will be no favourable directions of motion.

- **Manufacturing Difficulty** - A nuclear discriminator is a precise and compact mechanism produced under the tightest of tolerances. All the components of a stronglink, such as the MC2935, were compacted into a $116mm$ x $24mm$ x $24mm$ body that weighed 280g. The traditional manufacturing techniques limited the design of discriminators, often resulting in planar shapes that exposed the UQS pattern. Advanced manufacturing techniques expand the design scope, allowing highly compliant components that are still manufactured to tolerances required in the nuclear industry.

- **UQS Pattern Recognition** - Discriminating mechanisms in stronglink devices are fundamentally safety components, not security components. As a result, the discriminator designs often leave the UQS pattern exposed. It can be argued that the safety of a nuclear component is improved if the UQS pattern cannot be readily determined. By understanding how a single PIM mechanism behaves, all PIM discriminators become easier to circumvent. In contrast, if the method of discriminating a signal cannot easily be determined, all discriminators of the particular design will be more robust against safety and security infringements.

- **Component Reliance** - Nuclear discriminators are designed to remain dormant for extended periods and function in extreme environments. By reducing the number of moving parts and surfaces in contact with one another, the failure points in the mechanism can be reduced. Mechanical devices that require multiple components to function as designed increase the points of failure of a device. Besides, reliance on particular components to ensure the device is locked and maintained in an incompatible state places the device in a vulnerable position if the component fails. By increasing the compliance of a mechanism, the reliance on particular components reduces. Failure of one part directly affects the entire mechanism from responding to external stimuli.

7.2.4 Recent Developments

The design of discriminating mechanisms and stronglink devices are continuously under review to maintain a credible level of safety for nuclear deterrents. Outside of the national defence laboratories of P5 nuclear countries, the literature on the developments of discriminating mechanisms for nuclear safety is limited. Many institutions choose not to release information on discriminator designs to maintain deterrent safety. In particular, UQS patterns must not be revealed to ensure a discriminator cannot be unlocked without the proper chain of authorisation. Shanghai Jiaotong University (SJU) and Sandia National Laboratories (SNL) are two institutions focusing on the innovation of discriminator design.

Researchers at SJU have developed a CMG device (Figure 7.9) for high consequence systems based on MEMS CMG designs. Proposed CMG mechanisms such as the Polosky design in Section 7.2.2 have been criticised for the complex device configuration, sliding friction, and dynamic problems that ultimately affect the performance of the device [182, 183]. The group designs a CMG discriminator directly driven by axial flux permanent magnetic micromotors to simplify and further compact the design. Furthermore, the gears are formed from a five-layer Ni metal structure fabricated by a LiGA-like process to add mechanical strength. The Polosky CMG design used multi-layered polysilicon film to create the CMG gears; this was found to lack the necessary mechanical strength required for a high consequence system.

Research from SNL explores different discriminator designs using AM processes [184]. It is recognised that advanced manufacturing techniques widen the design space of novel discriminating mechanisms. The Wedge discriminator concept shown in Figure 7.10 utilises AM to build stacked plates that rotate by compliant springs on a set axis. The plates must be positioned in one of two

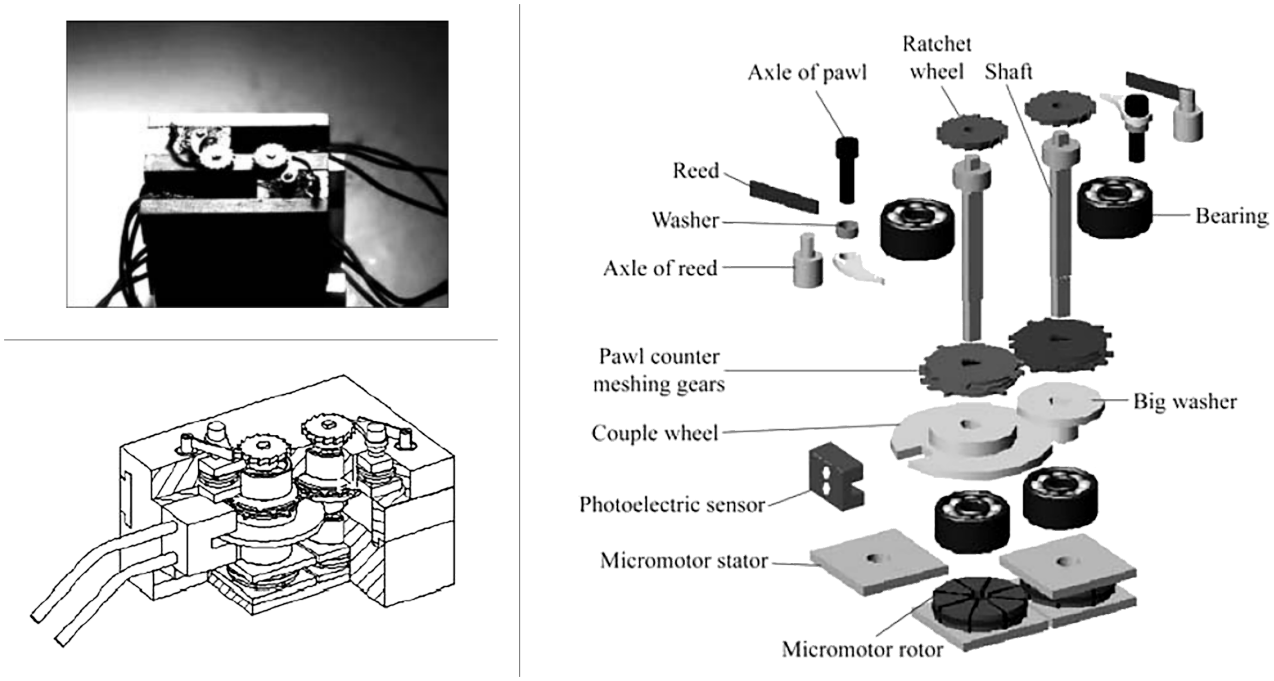


Figure 7.9: *Li et al. CMG stronglink design with multi-try functionality. Device has dimensions of; length 24mm, width 18mm and height of 13mm. Schematics adapted from Li et al. [182, 183].*

positions to align optical holes. A successful UQS sequence will result in all-optical holes aligning and signals passing through the exclusion region. An incorrect input will result in the optical holes misaligning, blocking optical signals from passing through the discriminator. Inputs are registered by rotating a plate and moving a rod through one of two position holes that register and store an A or B UQS input.

The discriminator concept addresses previous concerns over planar designs. In this design, the plates rotate in one plane, and the rod moves in an alternative plane, incorporating multiple axes of movement. The plates rotate in one of two directions; as a result, excessive force in one direction could align multiple plates causing a cascading event sequence to occur. The discriminating mechanism is also reliant on the rod to store the position of the plates. Rod failure makes it possible to circumvent the discriminator entirely. The rod is a limiting feature of the design, as it is used to store the plate position for every event. This restricts the speed of the discriminating mechanism. Size is also a constraint for this concept, 24 individual plates for a UQS sequence will result in a considerably high stack, although significant improvements are being made in AM printing at the microscale.

The Knot discriminator (Figure 7.11) by SNL is an additional concept that explores the expanded design space introduced by AM. It is a multi-component design that utilises various degrees of freedom to create an interlocked discriminator. AM is particularly well suited for this concept, as the components are designed into the Knot configuration that would be impossible using

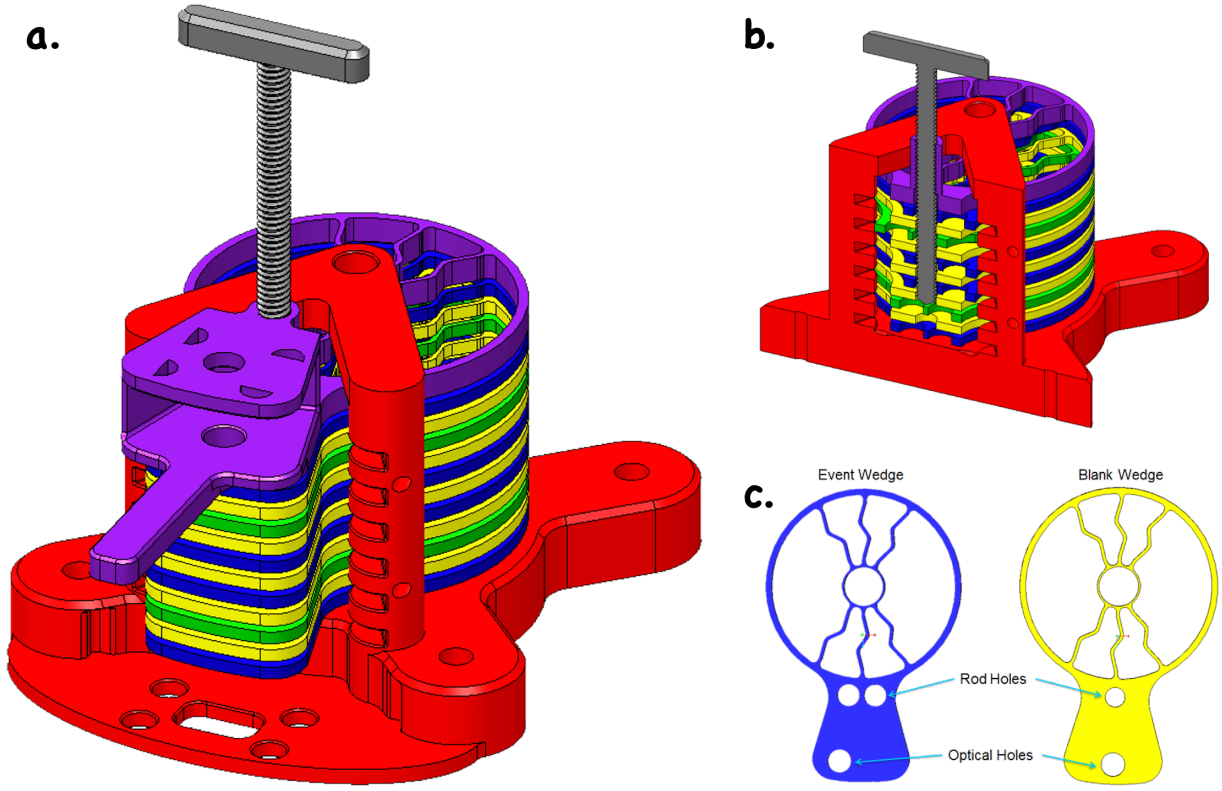


Figure 7.10: *Design concept from Miller et al. looking at stronglink design through additive manufacturing. a) Complete view of proposed design. b) Slice through system showing wedge position after several inputs have been made. c) Different types of wedges used and their corresponding optical hole and rod hole placements. Schematic adapted from Miller and Moore [184].*

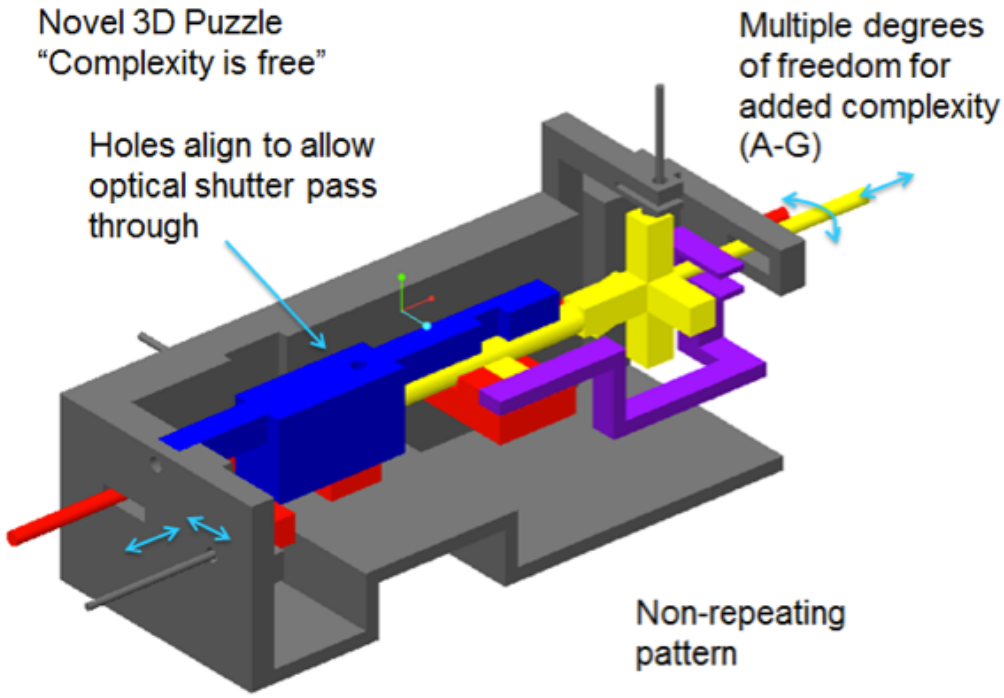


Figure 7.11: *Knot stronglink design proposed by Miller et al. highlighting the non-repeating pattern and multiple degrees of freedom discriminator concept. Schematic adapted from Miller and Moore [184].*

traditional manufacturing techniques. A discriminating sequence is complete when apertures in each component align to allow optical signals through the exclusion region. The design explores several new features for discriminating mechanisms. Although bi-valued event inputs are employed, multiple planes of motion are utilised. Components are designed to rotate or translate in multiple axes.

The added complexity makes this concept highly robust against cascading events; any forced input in one direction creates frustrated states in other components, causing the discriminator to lock. As the components are 'woven', once an incorrect event occurs and the holes are misaligned, the system remains in a 'tangled' lock state until a reset sequence is implemented. Discrimination is inherent in the design itself; locking is instantaneous and effective against a diverse set of signals that can cause inadvertent actuation. The UQS sequence is well hidden in the Knot discriminator, as the interlinked features add significant complexity in determining the correct sequence of movement. The Knot design still has limitations in meeting the ENDS principles, as 24 separate components are required to implement a 24-bit UQS successfully. This significantly increases the size of the device. Furthermore, a large number of components and driving motors introduces several points of failure in the device. Although incompatibility will still be achieved if a component fails, discriminators must be reliable when called upon.

In this section, legacy and current developments in discriminating mechanisms have been explored. PIM and CMG designs used in the nuclear industry successfully implement the ENDS principles. Areas of improvement have been determined; planar design, manufacturing difficulty, UQS pattern recognition and component reliance. Discriminators that utilise AM technologies such as the Knot and Wedge design introduce novel methods to discriminate a signal. The designs utilise the geometric freedom of AM to design discriminators that are interlocked and challenging to build using traditional manufacturing techniques. Very few of the designs analysed have shown innovations beyond the common principles of mechanical devices first set out in the nuclear industry. The AM designs did not fully utilise the integrated capabilities of AM in its design, and heavily relied on actuators for complete functionality. Although the knot design is viable and merits many similarities to concepts such as rod-logic mechanisms in Figure 6.4, it is not achievable in the current design state due to the number of additional actuators required. The key innovations desired in discriminators aligns with the research objectives of this project, of multi-plane functionality with significant programmable and tunable control for functional mechanical capabilities. The lack of progress in developing novel mechanical discriminators further clarifies the need for innovation by exploring advanced technologies and manufacturing techniques, and the principles developed in MM design.

7.3 MM for Discriminating Mechanisms

The compliant MM developed in Chapter 5 provides a novel design approach to nuclear discriminating mechanisms. Due to the requirement for a discriminator to withstand harsh environments, a compliant flexure approach is most suited for this case study, as a single material was used in the tunable bistable mechanism study in Chapter 5. The Knot stronglink design proposed by Sandia functions similarly to combinatorial MMs as it uses frustration to maintain incompatibility. An incorrect input results in frustration as knot 'puzzle pieces' obstruct one another, resulting in no subsequent movement. Because of a designed ratchet system, inoperability is maintained as the knot system is fixed in place in the incorrect configuration. Similar properties are shared with the compliant MM explored in Chapter 5. Due to a combinatorial design, the correct patterned actuation is necessary for frustration-free deformation. This subsequently results in the bistability of the beam system. Incorrect inputs result in frustration and tension along the beam as it remains in a monostable state, this is otherwise termed the systems incompatible state. Figure 7.12 shows the three potential states of the proposed MM, the no actuation state (A - passive), the incorrectly actuated state (B - active - frustrated) and the correctly actuated state (C - active - frustration-free). Highlighted in the schematic, frustration between the unit cells creates tension (pulling the ends of the slender beams) which results in a monostable incompatible state. Conversely, the correct sequence applies the characteristic sidewall pressure and buckling response studied in Chapter 5. In this section, the compliant MM is studied in further detail for its use as a mechanical discriminating mechanism.

Figure 7.13 shows the proposed compliant MM in a configuration suited to function using a truncated UQS. As previously stated, correctness within the system is judged by the buckling of the beam system in response to the unit cells. The buckled state is termed the *active* state, as a load is constantly applied to maintain the current state of the system. For buckling to occur, the beam from both ends must be equally compressed, functioning as an AND gate. The proposed system maintains the same dimensions and orientation as the MM explored in Chapter 5 where the beam system is along the y-axis. To simplify further for testing and analysis, actuation can only occur along the z-axis. For a single beam system (unit cells are not combined with neighbouring cells), to apply the correct sidewall pressure on the beam for buckling to occur, unit cells must be either orientated in the x or z polarisation. The corresponding $+\sigma$ or $-\sigma$ response respectively of the unit cells, applies a force on the slender beam causing it to buckle above its critical buckling load. In a combinatorial system, however, there is significantly more control over input sequences, as neighbouring unit cells

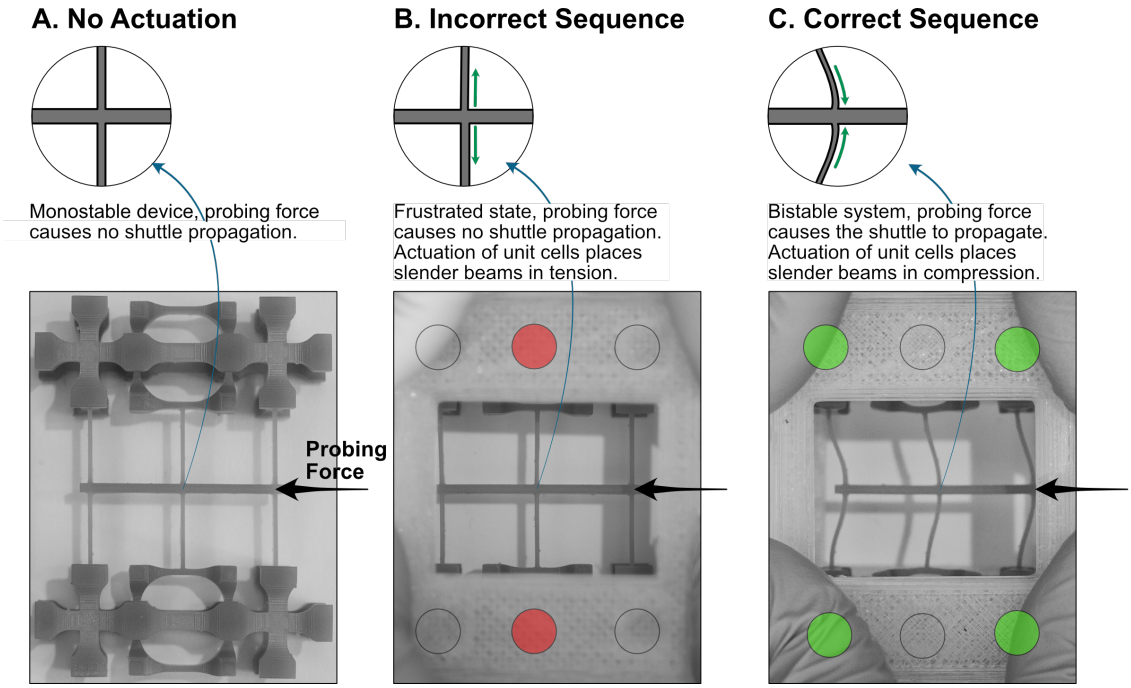


Figure 7.12: *SLA printed compliant MM in three different states as a result of the actuation sequence. Coloured circles indicate applied load above and below unit cell. A) No actuation - monostable passive state, MM has no deformation as a result of no actuating forces. Beams return back to original position after an applied probing force. B) Incorrect sequence - monostable active state, MM unit cells are deformed due to applied load. However, incorrect sequence leads to frustration and areas of tension along slender beam. Active state because a constant load is applied to the unit cell. C) Correct sequence - bistable active state, MM unit cells are deformed correctly in response to actuation pattern. Probing force against the curvature and above the threshold force results in a snap-through transition.*

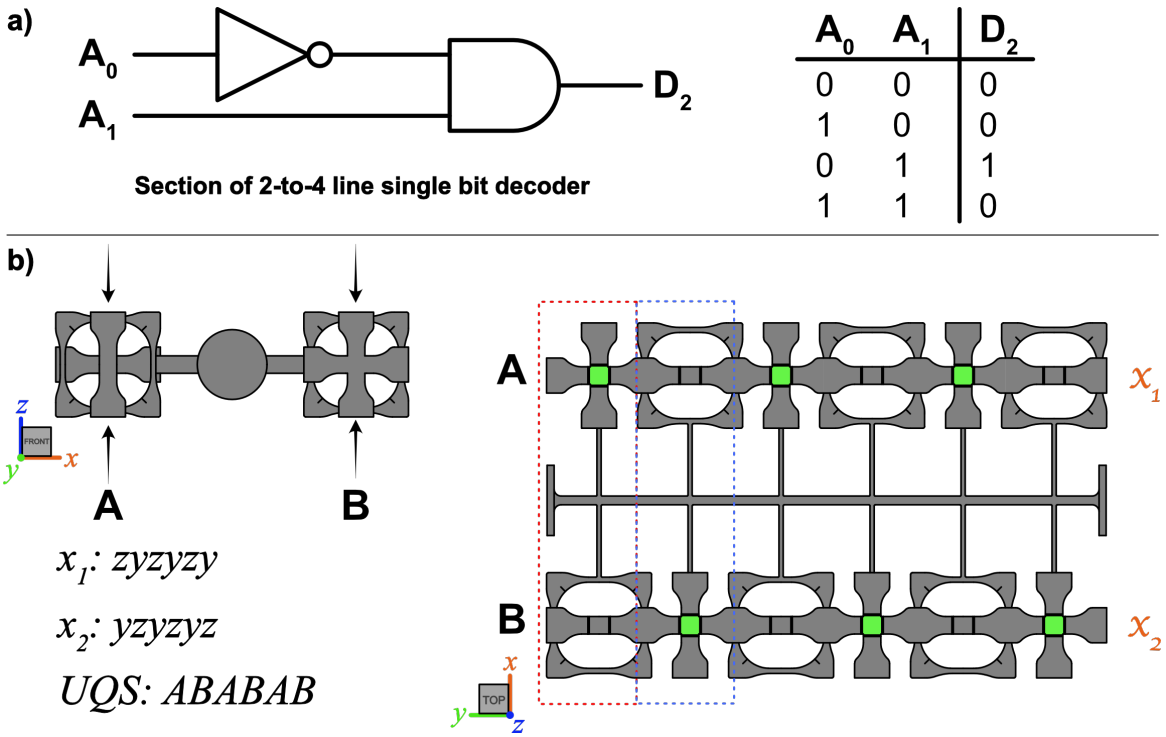


Figure 7.13: *a) Diagram showing sections of a 2-to-4 line single bit decoder and the corresponding truth table [185]. b) Proposed 6-bit MM Discriminator (UQS-ABABAB). A and B inputs occur through actuation along the z-axis (above and below unit cell) on the x_1 and x_2 rows respectively. Green indicators show the correct input pattern for bistability and propagation. Applied load (actuation) occurs on the top and bottom surfaces of the unit cell in the z-axis within the green coloured region.*

influence the state of the previous and next events. As a result, bi-valued event sequences can be implemented by utilising y and z polarisations as shown in Figure 7.13.b. The MM can be designed to input either the left x_1 or the right unit x_2 cell, representing an A or B input, respectively. This functionality can be defined by the logic system shown in Figure 7.13.a, where $A_1 = A$ and $A_0 = B$ for the system highlighted inside the orange box (Figure 7.13.b). The logic arrangement forms part of a larger 2-to-4 line single bit decoder. The system is similar to an OR gate; however, only one '1, 0' or '0, 1' input statement results in a '1' output. This is dependent on which input signal is inverted. For the second logic step highlighted by the blue box (Figure 7.13.b), the inverter is in the A_1 pathway. This is possible in a combinatorial MM, as frustration-free deformation is necessary for functionality. The first input influences the subsequent inputs and vice versa. Therefore, for the beam highlighted in the orange box to buckle, a B input is required in the highlighted blue box, affecting the state of the first beam. The UQS for the proposed discriminator in Figure 7.13.b is ABABAB, indicated by the green actuation markers.

Figure 7.14.a shows an alternative discriminator arrangement where an A input event represents both unit cells actuated, and a B input event represents one input per logic step. In this system, each correct input event is represented by an AND gate or a 2-to-4 bit decoder (Figure 7.13.a). The discriminator in Figure 7.14.b has UQS-$BABABA$. In this system, however, the B inputs occur only along the x_1 plane. In comparison, the discriminator in Figure 7.14.c with UQS-$BABBAB$ does not place this restriction. This is also represented in the non-alternating A and B UQS pattern.

Figure 7.15 shows the experimental validation of the three proposed discriminator designs printed in Tough1500 using SLA. The proposed MM discriminators were printed horizontally along the print bed in line with the previous manufacturing procedure as detailed in Section 3.4. The discriminators are shown in their passive state with no actuation (i) and their active state under the correct actuation sequence and compression (ii). The MM discriminators were compressed using a vice with a custom fixture that allowed a patterned actuation by changing the location of the ridges. The ridges of the custom fixture fit within the central region of the unit cells which are designed with a rim to ensure repeatable alignment during testing. Testing was conducted as proof of concept, highlighting the capability of actuating multiple unit cells and allowing a mechanical signal to propagate through six slender beam systems parallel to one another. As a result, compression of the unit cells was conducted by manually closing the vice until the beams buckled and the shuttle edge was in line with the edge of the vice. The discriminators successfully transmitted mechanical signals, transitioning to a second stable state due to an actuating force on the shuttle. Videos of the three proposed MM discriminators

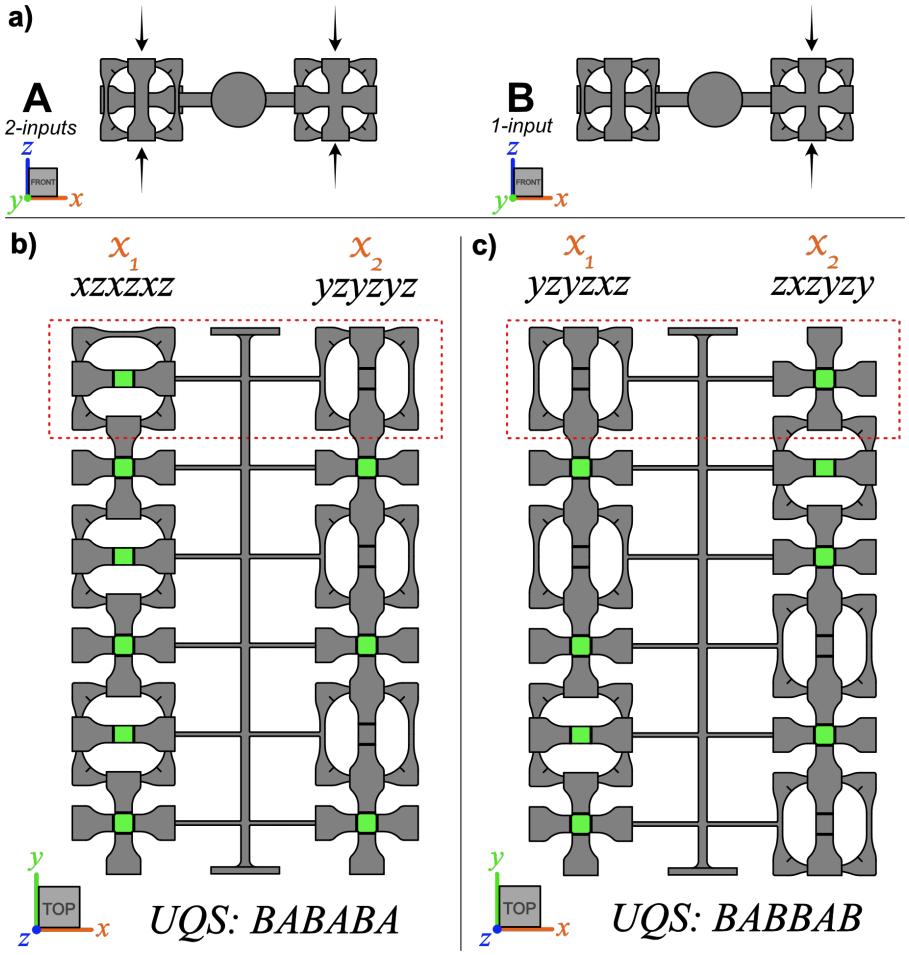


Figure 7.14: *a) Discriminator mechanism where an A input event represents actuation of both unit cells and a B input event represents actuation of one unit cell. Schematic shows MM discriminators with UQS b) BABABA and c) BABBAB. Applied load (actuation) occurs on the top and bottom surfaces of the unit cell in the z-axis within the green coloured region.*

propagating mechanical signals under the correct actuation pattern[1] can be found using the footnote link.

The key functionality of a discriminating mechanism is to determine with unambiguous intent the correct UQS and to protect the nuclear system from external energies. Although the MM highlights the capabilities of reading and assessing a UQS, we have yet to highlight how the system forms part of the energy barrier and maintains isolation in all cases except when the correct UQS is applied. The current printed configuration of the MM is limited in its implementation as a discriminator, due to the lack of coupling mechanisms and signal pathways. A key development to realise MMs as viable options for such systems is the integration with electronic components whilst still maintaining the mechanical safety aspect of the design. The proposed implementation is shown in Figure 7.16, the MM has a copper channel running through the entire shuttle system, allowing electrical signals to pass. One end

[1]MM Discriminators - `https://vimeo.com/541445483`

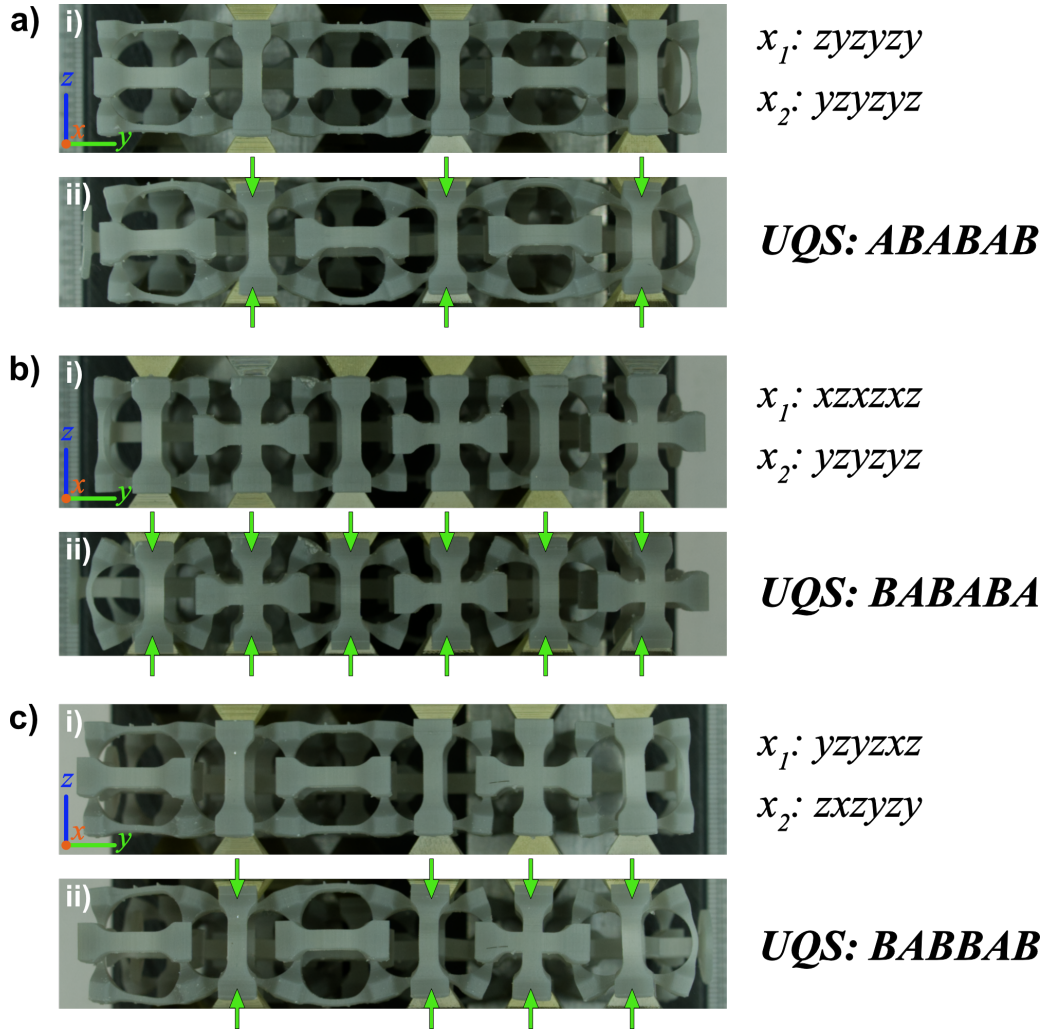


Figure 7.15: *Printed MM Discriminators for three different configurations: a) UQS-ABABAB b) UQS-BABABA and c) UQS-BABBAB. Images show x_1 row for MM in i) Passive state (no actuation) and ii) Active state (correct actuation sequence - green arrows, along the z-axis).*

of the shuttle and wire system connects to the nuclear system through the exclusion barrier. The open end of the shuttle is separated by a well-defined distance from the arming and firing (A&F) system. A connection is required between the two to pass signals to the nuclear system. If the MM can be assumed to be fixed in place so that movement of the shuttle only occurs through external forces or from deformation of the unit cells, isolation is implemented by the physical separation between the A&F unit and the shuttle end.

In its passive state, the parallel set of beams are monostable, external forces can cause movement of the beams but with a significant energy penalty for large deformations. This is further compounded by the unit cells that restrict movement, and depending on the orientation, create a pulling effect in response to external environmental forces. The likelihood of the isolation barrier being broken by external factors is therefore low. The second main function of a discriminating mechanism is to

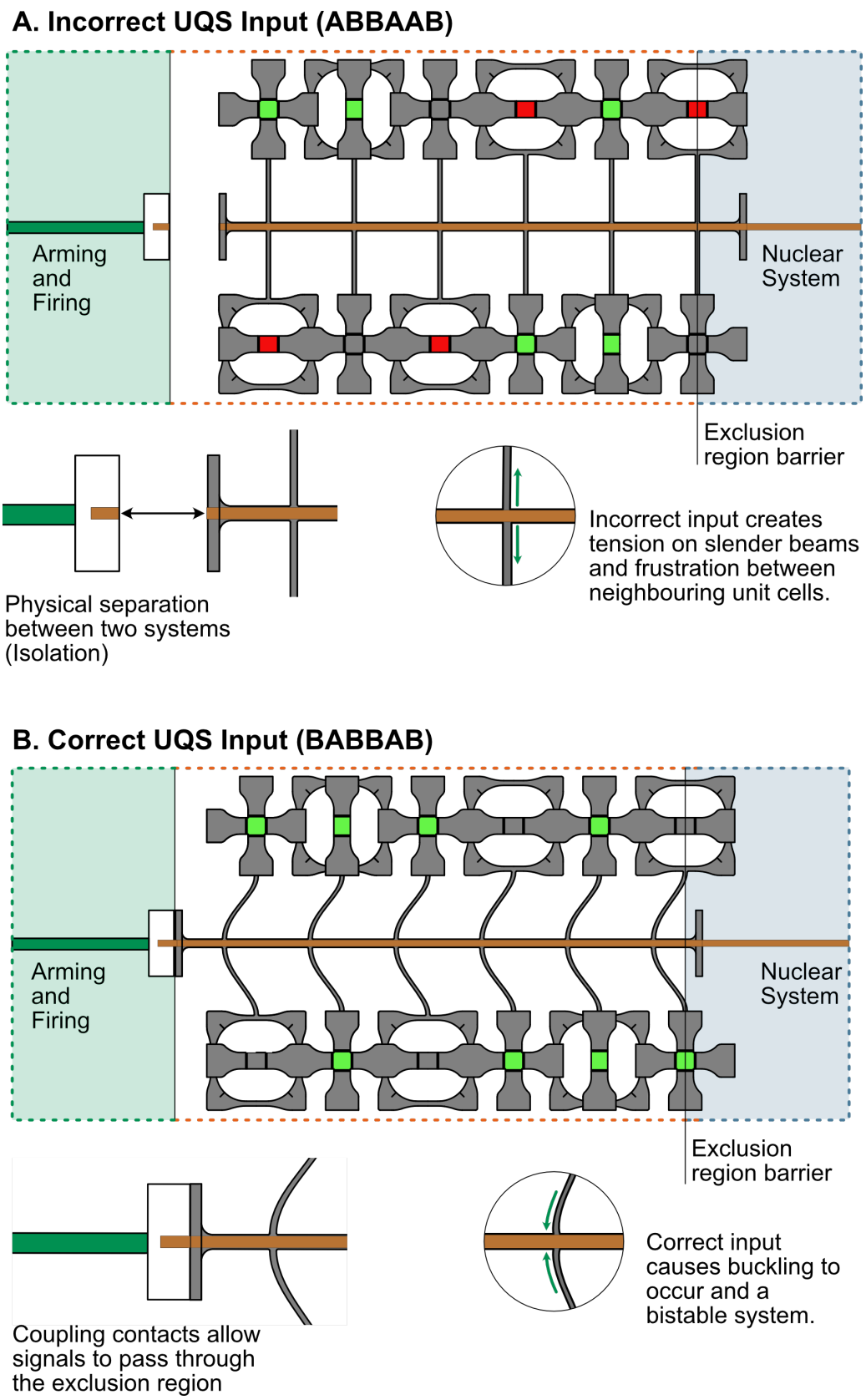


Figure 7.16: *Schematic showing the functionality of the MM in a stronglink safety system. Physical separation ensures isolation of the nuclear system, forming part of the exclusion region barrier. A) Incorrect UQS creates tension along slender beams and frustration between unit cells. This results in restricted movement of the beams ensuring isolation is maintained. B) Correct UQS input causes the beams to buckle, creating a contact point between the arming and firing units and the nuclear system. Applied load (actuation) occurs on the top and bottom surfaces of the unit cell within the coloured (red and green) region.*

ensure incompatibility. The MM explored in Figure 7.16 is the same MM tested in Figure 7.14.c. Here, an A input is defined as both unit cells actuated, and a B input is defined as only one unit cell actuated. The active state (when the unit cells are actuated) is shown for two cases, when an incorrect (incompatible) UQS is received and when a correct UQS is received. As highlighted previously, an incorrect actuation pattern on the MM results in tension along the slender beams and frustration between the unit cells. Because of the integrated mechanical system that is an MM, these effects compound one another, the parallel beams under tension result in an overall monostable static system. Furthermore, the frustration limits the deformation of correctly actuated unit cells, points of stress will lead to inoperable failure due to fracture. Increasing loads in an accident scenario in which an incorrect UQS is applied increases stress between unit cells, this leads to subsequent failure through buckling of the unit cells and increased likelihood of fracture of the flexural elements resulting in inoperability. An incorrect UQS input such as ABBAAB, therefore, results in incompatibility as the MM remains in a monostable frustrated state, and the physical separation between the two systems is upheld. Conversely, a correct UQS sequence (BABBAB) results in beam buckling and travel of the shuttle. This creates the necessary contact between the shuttle and A&F unit to allow signals to pass through to the nuclear system, due to the connection of the electrical systems.

The connection is also robust because of the potential well of the bistable system ensuring the most stable position of the shuttle is at the contact point with the A&F unit. An alternative arrangement can be developed that results in buckling in the opposite direction. Once the UQS is implemented, the active MM discriminator is in a 'ready' state with separation still maintained. The connection can then be implemented by the propagation of the mechanical wave and transition to the second stable state. The proposed discriminator shows how the principles of enhanced nuclear detonation safety (isolation, incompatibility, inoperability and independence) can effectively be implemented into the suggested MM.

7.4 Discussion

The proposed use of MM's for nuclear discriminating mechanisms is a novel concept previously unexplored. Although a typical bi-valued UQS system is successfully demonstrated in Figure 7.15, the proposed MMs only showed discriminating capabilities on a single plane. This is due to manufacturing limitations and testing capabilities. The number of combinatorial configurations was limited as a result; an input on a y-polarised unit cell results in tension along the beam. An effective discriminator such as the PIM and CMG designs had complete flexibility on the UQS signal that could be implemented. A further limitation of the single-plane design is the possible length when implementing a 24-bit UQS. Similar to the Sandia Wedge discriminator design issues, the single-plane MM will be much longer and require a significant amount of force to actuate 24 coupled parallel bistable beams.

The limitations of the proposed MM discriminator can be mitigated by implementing a multi-plane design. Like the FMMs explored in Chapter 6, multi-plane MMs significantly expand the design control and allow any UQS to be implemented. There are several different implementations possible, for example, the multi-plane bistable system in Section 6.2. Multiple beam systems can be stacked on planes with different propagation directions rather than a linear 24 coupled beam system. Multiple output directions add a further layer of safety to discriminators, as it ensures an unambiguous output signal is a result of a correct UQS and activation signal, and not external environmental factors, i.e. acceleration or deceleration in one direction. For example, as shown in the schematics in Figure 7.16, a correct UQS closes the physical separation between the two systems and allows for signals to pass. This can be expanded to a multi-plane system, where multiple contact points are added to connect to several shuttle systems. This implementation is akin to a pin-contact energy coupling system, for example, in a CMG discriminator. In a different implementation to the CMG shown in Figure 7.7, the correct rotation of the gear in receipt of the UQS causes contact pins to rotate and align with the A&F unit allowing the circuits to be engaged.

Furthermore, designs such as the rod-logic FMM share similarities to the Sandia Knot discriminator design. Instead of multiple moving parts, the connected unit cell and rod system behave in a coupled 'knotted' system. The combinatorial design of unit cells ensures frustration-free deformation only when the correct UQS is received. Consequently, frustration in the system results in tension along the slender beams, leading to brittle fracture and inoperability. The addition of the rod elements adds a further layer of safety, the gating rod feature blocks any mechanical propagation, rendering the

discriminator incompatible unless the correct UQS creates the desired deformation pattern on the unit cells and moves the blocking elements. With the MM discriminator explored in Figure 7.16, potential concerns arise on the surety that physical separation is maintained by the monostable system in an accident scenario. A rod-logic configuration offers an additional barrier of protection, as it requires a sequential ordering in triggering the bistable units to take place. In the passive and frustration-active states, the blocking element effectively 'locks' the shuttle from movement. Once the blocking element is moved out of position, the shuttle can engage with the A&F unit.

Multi-plane MMs offer a novel design approach for implementation in trajectory stronglinks to be explored. In traditional trajectory stronglinks, as the deterrent follows the defined stockpile-to-target sequence, the UQS is released navigating the discriminating mechanism. However, as shown in the tunable compliant system in Chapter 5, the actuation pattern and force can be used to tune the bistable properties of a slender beam, functioning similar to an accelerometer. As a multi-plane MM allows propagation of mechanical waves along multiple axes; when a deterrent follows a set trajectory, axis specific sequential buckling from deterrent acceleration/deceleration is proposed. Combining with rod-logic design principles, the sequence of buckling can be designed to move gated rod elements in and out of propagating mechanical signals. Although only a basic rod-logic FMM was demonstrated in Section 6.3, morphological systems offer a promising avenue to explore discriminating mechanisms in trajectory stronglinks.

A multi-plane MM discriminator offers several safety innovations to be considered for future use in surety mechanisms. However, the mechanism and design changes suggested struggle to fit into the current definition of a discriminator and the particular rules for nuclear safety set in place. The mechanisms in Figure 7.15 were selected due to their clear implementation of a bi-valued UQS. A and B inputs can easily be differentiated and both are events that change the state of the system. A larger multi-plane 'morphological' system struggles to fit within this definition, as input events can occur all along the outer surface of the MM; simplifying to bi-valued events restricts the design space. A key factor for the nuclear industry is the capability to test the state of the system at every event sequence. In the proposed MMs, the correctness of the UQS is judged in the end when all events are defined and an actuation against the shuttle defines the final state of the system. Although each set of unit cells can be actuated as separate events from one another, the 'correctness' cannot be determined until the end because all sections of an MM are connected. An additional rule in the current discriminator design is for each event to be independent of the next. Metamaterials behave oppositely, as all inputs change the system, subsequently influencing all input events to come after.

Although there are significant differences in designs, there are also similarities between the proposed MMs and current discriminating mechanisms. For example, the rod-logic MM in Section 6.3 can be expanded into a larger system to receive and implement a 24-bit UQS. The MM transitions from a passive state to an active state (actuated compression) to receive the UQS. The rod-blocking beams move either out of the way or block the bistable system from propagating, depending on the location of the blocking element and the input. As a result, the activation signal that propagates and connects the shuttle to the A&F system only functions when all blocking elements are moved away from the shuttle system. In this example bi-valued events are easier to configure. Incompatibility is achieved from the rod-blocking element interfering with the movement of the larger shuttle system. Likewise, incompatibility is implemented in a CMG discriminator by the gears interfering with one another. However, unlike the CMG discriminator, a rod-logic system does not provide sufficient information on the state of the system after every input, as correctness is still judged at the end through a final evaluation signal (propagation of shuttle to a second stable state).

In Figure 7.15, the MM discriminator designs were chosen to fit the design rules defined by the ENDS principles and the standard bi-valued event inputs used in previous discriminators. However, morphological systems such as multi-plane MMs offer a novel approach to discriminating mechanisms that reduce the dependence on bi-valued UQS inputs. In typical discriminating systems, each event sequence must be independent of the next. In contrast, every input influences the entire material in MMs, which is an advantage in safety for MM discriminators; frustrated systems and stress concentration from a single input influence the functionality of the entire device. Restricting to A and B inputs becomes redundant in such a system due to the multiple dependencies between input events. This does not, however, indicate a loss of safety. The MM discriminators explored prompt further discussion within the nuclear safety industry on an update to the ENDS principles, as advanced manufacturing techniques such as AM allow for geometric and design freedom.

It should be noted the concept of MM for nuclear safety is a disruptive design idea, and the proposed designs stand as proof of concepts on potential development routes for future innovations of discriminating mechanisms. Stronglinks have for many years adopted the same PIM and CMG discriminating methods that utilise specialist manufacturing techniques however, as shown previously, suffer design flaws such a planar design, manufacturing difficulty, UQS pattern recognition and component reliance. The introduction of programmable and tunable MMs offers a novel approach to safety, as unambiguous intent and surety can still be achieved in a multi-plane system using advanced manufacturing techniques. However, there are several shortfalls when

considering the proposed MMs as ready to use safety systems. For example, the actuators have not been considered in the MMs discussed, which would require additional components to ensure each unit cell is correctly actuated in the specific event sequence. Furthermore, although only suggested, an effective coupling method must be considered that fits within current nuclear deterrent safety systems. Finally, the materials and manufacturing method used is currently highly restrictive. Nuclear safety systems must be robust, repeatable and be able to withstand temperatures up to 590°C before failure. Although compliance in MMs is explored, significant developments are required in the material choice and manufacturing method to ensure robustness to the requirement of current nuclear safety systems.

This chapter has shown the potential of MMs in nuclear safety systems. The MM presents passive safety when not in use (under no actuation). The compliant mechanical design ensures safety in abnormal environments. Furthermore, multi-plane systems open an expansive design library of potential discriminator designs for intent and trajectory stronglinks. Although several aspects of the current MM are not suited for nuclear safety systems, the concepts introduced on the use of MM for safety are novel and have been examined to meet all ENDS principles of isolation, incompatibility, inoperability and independence.

Chapter 8

Conclusion and Future Work

8.1 Conclusion

The research question proposed in Chapter 1 stated **"Can functional devices be developed using 3D mechanical metamaterials that exhibit programmable and tunable behaviour in response to mechanical actuation?"**. As shown in the Literature Review (Chapter 2), research on novel mechanical phenomena from MMs is an active and expanding research field. Several researchers have also studied the tunable and programmable behaviour of metamaterials, exhibiting Boolean logic [80, 81, 82, 126]. In many of the MMs explored, there lacked a focus on the 'functional' nature of such systems. Furthermore, designs typically operated in a single plane, restricting the size and complexity of FMMs. As a result, from investigating and answering the research question, it is hoped that 3D MMs can be conclusively shown to exhibit programmable and tunable behaviour to mechanical actuation. Successful implementation of programmable and tunable MMs have novel and far-reaching applications from soft robotic systems to morphological safety systems. Videos of the proposed Functional Mechanical Metamaterials explored throughout this research can be found using the footnote link[1].

In Chapter 4, Boolean logic in MMs was successfully demonstrated, by combining multi-material anisotropic unit cells to a biased VMT bistable system. The Boolean functions (AND/OR) were defined by the particular separation distance between the unit cells of the MM. Actuation of the unit cells would increase the effective length of the beam and result in the release of the elastic potential energy of the VMT, transitioning from one stable state to the other. The multi-material MM was manufactured using PolyJet technology. Due to the 3D nature of the unit cells, the polarisation defined

[1]Functional Mechanical Metamaterials - `https://vimeo.com/showcase/8400741`

the corresponding logic sequence and results in increased complexity of the MM logic gates, as inputs must be order and orientation specific. AND and OR logic gates are successfully demonstrated in zz, yy and zy-polarisation.

Bistable mechanical logic systems have previously been explored in several research papers. However, the novelty of the proposed MMs is the multi-plane nature of the design. In previously explored mechanical logic MMs, the input and output were in the same plane. This limited the design scope and complexity of the systems, as additional cascading logic sequences would have to be on the same plane of motion. In comparison, the direction and location of actuation form part of the logic sequence in the proposed metadevices, this provides a significant leap forward in morphological and adaptive systems. The AND and OR logic devices showed multi-plane capabilities through the different planes of motion in which the MM received inputs and actuated in response. However, the novel development of MMs is through the combinatorial approach that can be taken, for example, stacking multiple AND gates atop one another. There were, however, several limitations of the current multi-material single gate devices that restricted their uses for mechanical Boolean systems. Most notably, an asymmetric bistable design choice was made, meaning elastic potential energy was stored in the system when the VMT was placed against the bias state. Actuation of the VMT into the second stable state resulted in significant energy losses and a one time use of the system. Consequently, although the MM poses several advantages for single-use mechanical *fuses*, the current implementations are still restrictive for cascading logic systems with greater programmable complexity.

In further exploring the capabilities of multi-material MMs, a combinatorial design approach was taken. The design scope was increased to multi-plane systems, to examine the functionality of MMs as part of larger morphological systems. The particular combinatorial design takes inspiration from the Metacube example [58], utilising similar anisotropic 3D unit cells. However, the bistable VMT adds a further dimension of programmability to the mechanism. Chapter 6 highlights the potential applications of multi-plane combinatorial systems and examines specific use-cases for designs. By combining multiple unit cells and connecting VMTs in parallel, a multi-plane bistable system was successfully demonstrated. A propagating bistable system shows the direction of mechanical signals can be controlled through an architected material. This highlights the programmable and tunable capabilities of multi-plane MMs.

Furthermore, with the increasing use of AM lattices in safety items such as helmets, the proposed FMM can be utilised as a passive mechanical control system for diagnostic purposes in accident

scenarios. The multi-plane combinatorial MMs are morphological systems, which adapt to surrounding deformations as part of the programmable control loop. The orientation of each unit cell is defined to interact with neighbouring cells in a programmed manner. The fully integrated VMT ensures the systems can *sense, decide* & *respond* to mechanical actuation. The multi-material MM is a multi-plane 3D system with programmable and tunable behaviour in response to mechanical actuation. The integrated VMT functions similar to a mechanical fuse within a larger lattice and provides realistic diagnostic information on the state of the system. Although the complexity of the system is limited without additional sensing components, the passive nature of the proposed MM and the ease in manufacturing are notable innovations in the field of flexible mechanical metamaterials.

To show usability in semi-rigid structures, a compliant MM was developed by combining anisotropic unit cells with slender beams. Actuation of unit cells transitions the slender beams from monostable to bistable through an axial force that causes the beams to buckle. It is experimentally shown that the actuation on the unit cells can tune the bistable characteristics of the slender beam system. The MM was manufactured in Formlabs Tough1500 material using SLA technology. A compliant unit cell using living hinges was developed to ensure a correct deflection in semi-rigid polymers in response to actuation occurred (Chapter 5). Although tunable bistability in MMs was successfully demonstrated, akin to tunable MEMS devices, the printed MMs posed several issues in repeatability during testing due to fatigue. Slender beams were often plastically deformed and fractured during testing due to fatigue of the flexural components.

The compliant FMM in Chapter 6 successfully demonstrated multi-plane programmable capabilities, showing coupled beam systems can transition from monostable to bistable under a correct actuation pattern, as a function of *pattern sensing* in semi-rigid structures. As a result, mechanical signals could propagate throughout the architected system along multiple planes via the coupled parallel bistable beams. The use of semi-rigid polymers and the compliant design shows the potential of MMs in applications such as accelerometers in the automotive industry and as safety systems for the nuclear industry. For example, tunable bistability in compliant MMs allows the relative compression of the unit cells to tune the threshold force of the slender beams. This allows threshold accelerations/decelerations to be determined through a mechanical passive mechanism.

A specific use-case is explored for compliant MMs to function as a nuclear safety device (a discriminating mechanism). The monostable to bistable transition is favourable in safety systems, as the FMM is inherently passive and only allows propagation under the correct actuating force and position. A 6x1 compliant MM is explored and experimentally demonstrated for the ability to

distinguish unique signals (UQS) and determine correctness, maintaining isolation against all incorrect signals. The principles and design ideas explored, highlight the additional safety features of mechanical systems that feature a *passive* safety attribute. The adaptive features of the design and additional complexity when considering multi-plane safety systems introduce additional safety benefits of adopting mechanisms with MM design principles. Although the potential upside to safety systems of adopting MMs could be disruptive to the nuclear industry, the manufacturing capabilities, materials selected and integration with electronics are all factors that require significantly more research to conclusively decide on the suitability as a nuclear safety system.

The development of multi-plane compliant MMs also demonstrated the capabilities of sequential logic and conditional statements. A rod-logic FMM was successfully demonstrated, showing the potential for mechanical signals to propagate along multiple axes with sequential ordering in an architected system. The FMM shows how signals passing through a lattice can be modulated by a gating system, highlighting logical processes throughout the MM and the potential application for morphological computation. The rod-logic highlights additional complexity achievable in MMs and combined several design principles. The proposed rod-logic FMM achieved many of the research objectives intended in answering the research question. The FMM is multi-plane, programmable and tunable. In addition, the MM functions in multiple axes, allowing mechanical signals to propagate through the entire structure. Programmable logic such as AND is inherent in the design to translate from a monostable to a bistable system. Finally, the combinatorial approach highlights its usability in larger morphological systems.

The two proposed MMs and their multi-plane systems highlight the functional capabilities of metadevices. The examples show a high degree of programmability and tunability in response to mechanical actuation. Furthermore, the design freedom in multi-plane systems has shown FMMs can be realised that utilise the entire architecture of the material. This provides a solid grounding for further development into morphological systems, and the exploration of functional materials and lattice-based design into a wide range of engineering applications.

8.2 Future Work

The scope of the research question was to show that using experimentation and a design iterative process, 3D MMs can be programmed and tuned to respond to mechanical actuation. This has been shown through several unit cell/bistable system configurations. However, the research has highlighted several avenues of future work required to reaffirm arguments made within the research, to better understand the systems at hand, or the requirement to further develop the system for future applications.

In Section 5.4, an analytical model was used to describe the behaviour of the MM under an actuation sequence. The model and experimental results showed a significant discrepancy (5-6)x, highlighting the need to develop a model that considers the coupling of the unit cell to the slender beam. This is most suitable for FEA analysis, which will help explain where the stress is most concentrated during a snap-through event and how this affects the overall bistable characteristics of the system. Also, it will help explain the pre-buckling behaviour observed after repeated testing. As the unit cell and bistable system combination are fundamental to the larger multi-plane MMs, an FEA analysis would aid in the design of functional MMs and the energy distribution in larger systems, which also posed an issue during testing.

The study focused on two AM technologies, Material Jetting and Stereolithography. Although FMMs were successfully demonstrated, both printing technologies had limitations if the proposed MMs are to be used in industry. Fatigue was a limiting factor in both technologies; after several cycles, the Agilus30 and VeroWhite boundary of the VMT would break away in PolyJet printed MMs. In the SLA printed MMs, brittle fracture would occur on the slender beam after repeated snap-through motion. In addition, SLA technology limits the complexity of the functional MM, as dissolvable support cannot be utilised. The two technologies are limited to printing polymer materials. This can be suitable in specific industries such as safety helmets and footwear, or soft robotics, where flexible mechanical metamaterials are often used. However, the material limitations restrict FMMs use for automotive and aerospace applications, where it is believed the passive nature of the devices, and the manufacturing techniques, can be advantageous and disruptive for future technology systems. Furthermore, for the proposed use as a discriminating mechanism, MMs must be printed in materials required to withstand temperatures up to 590°C before failing. To better understand the capabilities of the designed FMMs in industrial applications, printing using SLS technology should be explored. SLS adds additional design freedom and allows for printing in metal, which will help in understanding

the useability of the proposed FMMs in harsh environments.

The specific use-case of a MM safety system opens several questions on the applicability of compliant MMs in harsh environments and for engineering applications. Additionally, although the compliant MM in Chapter 5 highlighted the tunable and programmable capabilities, there also lacked the detailed sensor capabilities that could fully compare the system to the MEMS tunable bistable system studied. As a result, exploring 3D electronics and designing a MM compatible with electronic systems will significantly increase its usability in applications such as soft robotics and as potential accelerometers in the automotive industry.

Throughout the study, the same cubic anisotropic unit cell is studied, with changes made for the particular printing technology used. Future work from this study would be to expand the library of unit cells investigated for use as FMMs. The use of different 3D unit cells is proposed to introduce novel *sense, decide* and *respond* functionality to MMs, and further expand the functional capabilities of MMs in industry.

Bibliography

[1] T. Toffoli and N. Margolus, "Programmable matter: Concepts and realization", *Physica D: Nonlinear Phenomena*, vol. 47, pp. 263–272, 1991. DOI: 10.1016/0167-2789(91)90296-L.

[2] Y. Fang, V. V. Yashin, S. P. Levitan, and A. C. Balazs, "Pattern recognition with "materials that compute"", *Science Advances*, vol. 2, 2016. DOI: 10.1126/sciadv.1601114.

[3] M. A. McEvoy and N. Correll, "Materials that couple sensing, actuation, computation, and communication", *Science*, vol. 347, 2015. DOI: 10.1126/science.1261689.

[4] M. R. Werner and W. R. Fahrner, "Review on materials, microsensors, systems and devices for high-temperature and harsh-environment applications", *IEEE Transactions on Industrial Electronics*, vol. 48, pp. 249–257, 2001. DOI: 10.1109/41.915402.

[5] M. Caldwell and P. E. D'Antonio, "A study of using electronics for nuclear weapon detonation safety", *American Institute of Aeronautics and Astronautics*, 1998. DOI: 10.2514/6.1998-3465.

[6] D. Isbell, "High Consequence Operations Safety Symposium II", in *HCOSSII*, ser. SAND98-1557, Sandia National Laboratories, 1997.

[7] I. Peralta, V. D. Fachinotti, and J. C. Álvarez Hostos, "A brief review on thermal metamaterials for cloaking and heat flux manipulation", *Advanced Engineering Materials*, vol. 22, p. 1 901 034, 2020. DOI: 10.1002/adem.201901034.

[8] N. I. Zheludev and Y. S. Kivshar, "From metamaterials to metadevices", *Nature Materials*, vol. 11, pp. 917–924, 2012. DOI: 10.1038/nmat3431.

[9] G. Memoli, M. Caleap, M. Asakawa, D. R. Sahoo, B. W. Drinkwater, and S. Subramanian, "Metamaterial bricks and quantization of meta-surfaces", *Nature Communications*, vol. 8, p. 14 608, 2017. DOI: 10.1038/ncomms14608.

[10] R. Lakes, "Foam structures with a negative poisson's ratio", *Science*, vol. 235, pp. 1038–1040, 1987. DOI: 10.1126/science.235.4792.1038.

[11] G. W. Milton and A. V. Cherkaev, "Which Elasticity Tensors are Realizable?", *Journal of Engineering Materials and Technology*, vol. 117, pp. 483–493, Oct. 1995. DOI: 10.1115/1.2804743.

[12] K. Bertoldi, V. Vitelli, J. Christensen, and M. van Hecke, "Flexible mechanical metamaterials", *Nature Reviews Materials*, vol. 2, p. 17066, 2017. DOI: 10.1038/natrevmats.2017.66.

[13] M. van Hecke, "Jamming of soft particles: Geometry, mechanics, scaling and isostaticity", *Journal of Physics: Condensed Matter*, vol. 22, p. 033101, Dec. 2009. DOI: 10.1088/0953-8984/22/3/033101.

[14] M. F. Berwind, A. Kamas, and C. Eberl, "A Hierarchical Programmable Mechanical Metamaterial Unit Cell Showing Metastable Shape Memory", *Advanced Engineering Materials*, vol. 20, p. 1800771, Nov. 2018. DOI: 10.1002/adem.201800771.

[15] M. Kadic, G. W. Milton, M. van Hecke, and M. Wegener, "3D metamaterials", *Nature Reviews Physics*, vol. 1, pp. 198–210, 2019. DOI: 10.1038/s42254-018-0018-y.

[16] J. U. Surjadi, L. Gao, H. Du, X. Li, X. Xiong, N. X. Fang, and Y. Lu, "Mechanical Metamaterials and Their Engineering Applications", *Advanced Engineering Materials*, vol. 21, p. 1800864, Mar. 2019. DOI: 10.1002/adem.201800864.

[17] H. M. A. Kolken and A. A. Zadpoor, "Auxetic mechanical metamaterials", *RSC Advances*, vol. 7, pp. 5111–5129, 2017. DOI: 10.1039/C6RA27333E.

[18] S. Babaee, J. Shim, J. C. Weaver, E. R. Chen, N. Patel, and K. Bertoldi, "3d soft metamaterials with negative poisson's ratio", *Advanced Materials*, vol. 25, pp. 5044–5049, 2013. DOI: 10.1002/adma.201301986.

[19] K. K. Saxena, R. Das, and E. P. Calius, "Three decades of auxetics research - materials with negative poisson's ratio: A review", *Advanced Engineering Materials*, vol. 18, pp. 1847–1870, 2016. DOI: 10.1002/adem.201600053.

[20] T. Mullin, S. Deschanel, K. Bertoldi, and M. C. Boyce, "Pattern transformation triggered by deformation", *Phys. Rev. Lett.*, vol. 99, p. 084301, Aug. 2007. DOI: 10.1103/PhysRevLett.99.084301.

[21] J. B. Choi and R. S. Lakes, "Fracture toughness of re-entrant foam materials with a negative Poisson's ratio: experiment and analysis", *International Journal of Fracture*, vol. 80, pp. 73–83, 1996. DOI: 10.1007/BF00036481.

[22] K. E. Evans and A. Alderson, "Auxetic materials: Functional materials and structures from lateral thinking!", *Advanced Materials*, vol. 12, pp. 617–628, 2000. DOI: 10.1002/(SICI)1521-4095(200005)12:9<617::AID-ADMA617>3.0.CO;2-3.

[23] I. Fernandez-Corbaton, C. Rockstuhl, P. Ziemke, P. Gumbsch, A. Albiez, R. Schwaiger, T. Frenzel, M. Kadic, and M. Wegener, "New twists of 3d chiral metamaterials", *Advanced Materials*, vol. 31, p. 1 807 742, 2019. DOI: 10.1002/adma.201807742.

[24] T. Frenzel, M. Kadic, and M. Wegener, "Three-dimensional mechanical metamaterials with a twist", *Science*, vol. 358, pp. 1072–1074, 2017. DOI: 10.1126/science.aao4640.

[25] J. N. Grima, R. Gatt, A. Alderson, and K. E. Evans, "On the auxetic properties of 'rotating rectangles' with different connectivity", *Journal of the Physical Society of Japan*, vol. 74, pp. 2866–2867, 2005. DOI: 10.1143/JPSJ.74.2866.

[26] Z. Wang and H. Hu, "Auxetic materials and their potential applications in textiles", *Textile Research Journal*, vol. 84, pp. 1600–1611, 2014. DOI: 10.1177/0040517512449051.

[27] W. Wu, W. Hu, G. Qian, H. Liao, X. Xu, and F. Berto, "Mechanical design and multifunctional applications of chiral mechanical metamaterials: A review", *Materials & Design*, vol. 180, p. 107 950, 2019. DOI: 10.1016/j.matdes.2019.107950.

[28] B. Haghpanah, L. Salari-Sharif, P. Pourrajab, J. Hopkins, and L. Valdevit, "Multistable shape-reconfigurable architected materials", *Advanced Materials*, vol. 28, pp. 7915–7920, 2016. DOI: 10.1002/adma.201601650.

[29] Y. Bar-Sinai, G. Librandi, K. Bertoldi, and M. Moshe, "Geometric charges and nonlinear elasticity of two-dimensional elastic metamaterials", *Proceedings of the National Academy of Sciences*, vol. 117, pp. 10 195–10 202, 2020. DOI: 10.1073/pnas.1920237117.

[30] J. T. Overvelde and K. Bertoldi, "Relating pore shape to the non-linear response of periodic elastomeric structures", *Journal of the Mechanics and Physics of Solids*, vol. 64, pp. 351–366, 2014. DOI: 10.1016/j.jmps.2013.11.014.

[31] B. Florijn, C. Coulais, and M. Van Hecke, "Programmable mechanical metamaterials", *Physical Review Letters*, vol. 113, pp. 1–5, 2014. DOI: 10.1103/PhysRevLett.113.175503. arXiv: 1407.4273.

[32] J. Shim, S. Shan, A. Košmrlj, S. H. Kang, E. R. Chen, J. C. Weaver, and K. Bertoldi, "Harnessing instabilities for design of soft reconfigurable auxetic/chiral materials", *Soft Matter*, vol. 9, pp. 8198–8202, 34 2013. DOI: 10.1039/C3SM51148K.

[33] J. T. B. Overvelde, S. Shan, and K. Bertoldi, "Compaction through buckling in 2d periodic, soft and porous structures: Effect of pore shape", *Advanced Materials*, vol. 24, pp. 2337–2342, 2012. DOI: 10.1002/adma.201104395.

[34] K. Bertoldi and M. C. Boyce, "Mechanically triggered transformations of phononic band gaps in periodic elastomeric structures", *Phys. Rev. B*, vol. 77, p. 052 105, Feb. 2008. DOI: 10.1103/PhysRevB.77.052105.

[35] K. Bertoldi, P. M. Reis, S. Willshaw, and T. Mullin, "Negative poisson's ratio behavior induced by an elastic instability", *Advanced Materials*, vol. 22, pp. 361–366, 2010. DOI: 10.1002/adma.200901956.

[36] M. Johnson, Y. Chen, S. Hovet, S. Xu, B. Wood, H. Ren, J. Tokuda, and Z. T. H. Tse, "Fabricating biomedical origami: a state-of-the-art review", *International Journal of Computer Assisted Radiology and Surgery*, vol. 12, pp. 2023–2032, 2017. DOI: 10.1007/s11548-017-1545-1.

[37] S. Kamrava, D. Mousanezhad, S. M. Felton, and A. Vaziri, "Programmable origami strings", *Advanced Materials Technologies*, vol. 3, p. 1 700 276, 2018. DOI: 10.1002/admt.201700276.

[38] J. L. Silverberg, J.-H. Na, A. A. Evans, B. Liu, T. C. Hull, C. D. Santangelo, R. J. Lang, R. C. Hayward, and I. Cohen, "Origami structures with a critical transition to bistability arising from hidden degrees of freedom", *Nature Materials*, vol. 14, pp. 389–393, 2015. DOI: 10.1038/nmat4232.

[39] J. L. Silverberg, A. A. Evans, L. McLeod, R. C. Hayward, T. Hull, C. D. Santangelo, and I. Cohen, "Using origami design principles to fold reprogrammable mechanical metamaterials", *Science*, vol. 345, pp. 647–650, 2014. DOI: 10.1126/science.1252876.

[40] Y. Tang, G. Lin, S. Yang, Y. K. Yi, R. D. Kamien, and J. Yin, "Programmable kiri-kirigami metamaterials", *Advanced Materials*, vol. 29, p. 1 604 262, 2017. DOI: 10.1002/adma.201604262.

[41] K. Miura, *Method of Packaging and Deployment of Large Membranes in Space*, ser. Institute of Space and Astronautical Science report No. 618. Institute of Space and Astronautical Sciences, 1985.

[42] A. Rafsanjani, K. Bertoldi, and A. R. Studart, "Programming soft robots with flexible mechanical metamaterials", *Science Robotics*, vol. 4, Apr. 2019. DOI: 10.1126/scirobotics.aav7874.

[43] S. Sengupta and S. Li, "Harnessing the anisotropic multistability of stacked-origami mechanical metamaterials for effective modulus programming", *Journal of Intelligent Material Systems and Structures*, vol. 29, pp. 2933–2945, 2018. DOI: 10.1177/1045389X18781040.

[44] S. Shan, S. H. Kang, J. R. Raney, P. Wang, L. Fang, F. Candido, J. A. Lewis, and K. Bertoldi, "Multistable architected materials for trapping elastic strain energy", *Advanced Materials*, vol. 27, pp. 4296–4301, 2015. DOI: 10.1002/adma.201501708.

[45] T. Chen, J. Mueller, and K. Shea, "Integrated Design and Simulation of Tunable, Multi-State Structures Fabricated Monolithically with Multi-Material 3D Printing", *Scientific Reports*, vol. 7, 2017. DOI: 10.1038/srep45671.

[46] T. Chen, O. R. Bilal, K. Shea, and C. Daraio, "Harnessing bistability for directional propulsion of soft, untethered robots", *Proceedings of the National Academy of Sciences*, vol. 115, pp. 5698–5702, 2018. DOI: 10.1073/pnas.1800386115.

[47] D. M. Correa, T. Klatt, S. Cortés, M. Haberman, D. Kovar, and C. Seepersad, "Negative stiffness honeycombs for recoverable shock isolation", *Rapid Prototyping Journal*, vol. 21, pp. 193–200, 2015. DOI: 10.1108/RPJ-12-2014-0182.

[48] J. Paulose, B. G.-g. Chen, and V. Vitelli, "Topological modes bound to dislocations in mechanical metamaterials", *Nature Physics*, vol. 11, pp. 153–156, 2015. DOI: 10.1038/nphys3185.

[49] J. Paulose, A. S. Meeussen, and V. Vitelli, "Selective buckling via states of self-stress in topological metamaterials", *Proceedings of the National Academy of Sciences*, vol. 112, pp. 7639–7644, 2015. DOI: 10.1073/pnas.1502939112.

[50] D. Z. Rocklin, S. Zhou, K. Sun, and X. Mao, "Transformable topological mechanical metamaterials", *Nature Communications*, vol. 8, 2017. DOI: 10.1038/ncomms14201.

[51] M. Thorpe, "Bulk and surface floppy modes", *Journal of Non-Crystalline Solids*, vol. 182, pp. 135–142, 1995. DOI: 10.1016/0022-3093(94)00545-1.

[52] C. L. Kane and T. C. Lubensky, "Topological boundary modes in isostatic lattices", *Nature Physics*, vol. 10, pp. 39–45, 2014. DOI: 10.1038/nphys2835.

[53] S. H. Kang, S. Shan, Ko šmrlj, W. L. Noorduin, S. Shian, J. C. Weaver, D. R. Clarke, and K. Bertoldi, "Complex ordered patterns in mechanical instability induced geometrically frustrated triangular cellular structures", *Phys. Rev. Lett.*, vol. 112, Mar. 2014. DOI: 10.1103/PhysRevLett.112.098701.

[54] C. Merrigan, C. Nisoli, and Y. Shokef, *Topologically protected steady cycles in an ice-like mechanical metamaterial*, 2021. arXiv: 2010.05227 [cond-mat.soft].

[55] A. S. Meeussen, E. C. Oğuz, Y. Shokef, and M. van Hecke, "Topological defects produce exotic mechanics in complex metamaterials", *Nature Physics*, vol. 16, pp. 307–311, 2020. DOI: 10.1038/s41567-019-0763-6.

[56] B. Pisanty, E. C. Oguz, C. Nisoli, and Y. Shokef, "Putting a spin on metamaterials: Mechanical incompatibility as magnetic frustration", *SciPost Phys.*, vol. 10, p. 136, 6 2021. DOI: 10.21468/SciPostPhys.10.6.136.

[57] A. Bossart, D. M. J. Dykstra, J. van der Laan, and C. Coulais, "Oligomodal metamaterials with multifunctional mechanics", *Proceedings of the National Academy of Sciences*, vol. 118, no. 21, 2021, ISSN: 0027-8424. DOI: 10.1073/pnas.2018610118.

[58] C. Coulais, E. Teomy, K. De Reus, Y. Shokef, and M. Van Hecke, "Combinatorial design of textured mechanical metamaterials", *Nature*, vol. 535, pp. 529–532, 2016. DOI: 10.1038/nature18960.

[59] J. Ou, Z. Ma, J. Peters, S. Dai, N. Vlavianos, and H. Ishii, "Kinetix - designing auxetic-inspired deformable material structures", *Computers & Graphics*, vol. 75, pp. 72–81, 2018. DOI: 10.1016/j.cag.2018.06.003.

[60] C. Coulais, A. Sabbadini, F. Vink, and M. van Hecke, "Multi-step self-guided pathways for shape-changing metamaterials", *Nature*, vol. 561, pp. 512–515, 2018. DOI: 10.1038/s41586-018-0541-0.

[61] S. T. Bramwell and M. J. P. Gingras, "Spin ice state in frustrated magnetic pyrochlore materials", *Science*, vol. 294, pp. 1495–1501, 2001. DOI: 10.1126/science.1064761.

[62] C. Nisoli, R. Moessner, and P. Schiffer, "Colloquium: Artificial spin ice: Designing and imaging magnetic frustration", *Rev. Mod. Phys.*, vol. 85, pp. 1473–1490, Oct. 2013. DOI: 10.1103/RevModPhys.85.1473.

[63] J. A. Jackson, M. C. Messner, N. A. Dudukovic, W. L. Smith, L. Bekker, B. Moran, A. M. Golobic, A. J. Pascall, E. B. Duoss, K. J. Loh, and C. M. Spadaccini, "Field responsive mechanical metamaterials", *Science Advances*, vol. 4, 2018. DOI: 10.1126/sciadv.aau6419.

[64] C. Yang, M. Boorugu, A. Dopp, J. Ren, R. Martin, D. Han, W. Choi, and H. Lee, "4d printing reconfigurable, deployable and mechanically tunable metamaterials", *Mater. Horiz.*, vol. 6, pp. 1244–1250, 2019. DOI: 10.1039/C9MH00302A.

[65] O. M. Wani, H. Zeng, and A. Priimagi, "A light-driven artificial flytrap", *Nature Communications*, vol. 8, 2017. DOI: 10.1038/ncomms15546.

[66] Y. Jiang, L. M. Korpas, and J. R. Raney, "Bifurcation-based embodied logic and autonomous actuation", *Nature Communications*, vol. 10, 2019. DOI: 10.1038/s41467-018-08055-3.

[67] M. A. C. Stuart, W. T. S. Huck, J. Genzer, M. Müller, C. Ober, M. Stamm, G. B. Sukhorukov, I. Szleifer, V. V. Tsukruk, M. Urban, F. Winnik, S. Zauscher, I. Luzinov, and S. Minko, "Emerging applications of stimuli-responsive polymer materials", *Nature Materials*, vol. 9, pp. 101–113, 2010. DOI: 10.1038/nmat2614.

[68] Q. Ge, H. J. Qi, and M. L. Dunn, "Active materials by four-dimension printing", *Applied Physics Letters*, vol. 103, 2013. DOI: 10.1063/1.4819837.

[69] B. Jin, H. Song, R. Jiang, J. Song, Q. Zhao, and T. Xie, "Programming a crystalline shape memory polymer network with thermo- and photo-reversible bonds toward a single-component soft robot", *Science Advances*, vol. 4, 2018. DOI: 10.1126/sciadv.aao3865.

[70] T. G. Leong, C. L. Randall, B. R. Benson, N. Bassik, G. M. Stern, and D. H. Gracias, "Tetherless thermobiochemically actuated microgrippers", *Proceedings of the National Academy of Sciences*, vol. 106, pp. 703–708, 2009. DOI: 10.1073/pnas.0807698106.

[71] M. R. Shankar, M. L. Smith, V. P. Tondiglia, K. M. Lee, M. E. McConney, D. H. Wang, L.-S. Tan, and T. J. White, "Contactless, photoinitiated snap-through in azobenzene-functionalized polymers", *Proceedings of the National Academy of Sciences*, vol. 110, pp. 18 792–18 797, 2013. DOI: 10.1073/pnas.1313195110.

[72] A. Sydney Gladman, E. A. Matsumoto, R. G. Nuzzo, L. Mahadevan, and J. A. Lewis, "Biomimetic 4D printing", *Nature Materials*, vol. 15, pp. 413–418, 2016. DOI: 10.1038/nmat4544.

[73] I. Burgert and P. Fratzl, "Actuation systems in plants as prototypes for bioinspired devices", *Philosophical Transactions of the Royal Society A: Mathematical, Physical and Engineering Sciences*, vol. 367, pp. 1541–1557, 2009. DOI: 10.1098/rsta.2009.0003.

[74] G. Stoychev, L. Guiducci, S. Turcaud, J. W. C. Dunlop, and L. Ionov, "Hole-programmed superfast multistep folding of hydrogel bilayers", *Advanced Functional Materials*, vol. 26, pp. 7733–7739, 2016. DOI: 10.1002/adfm.201602394.

[75] L. Hines, K. Petersen, G. Z. Lum, and M. Sitti, "Soft actuators for small-scale robotics", *Advanced Materials*, vol. 29, 2017. DOI: 10.1002/adma.201603483.

[76] A. Rafsanjani, K. Bertoldi, and A. R. Studart, "Programming soft robots with flexible mechanical metamaterials", *Science Robotics*, vol. 4, 2019. DOI: 10.1126/scirobotics.aav7874.

[77] M. Wehner, R. L. Truby, D. J. Fitzgerald, B. Mosadegh, G. M. Whitesides, J. A. Lewis, and R. J. Wood, "An integrated design and fabrication strategy for entirely soft, autonomous robots", *Nature*, vol. 536, pp. 451–455, 2016. DOI: 10.1038/nature19100.

[78] R. C. Merkle, "Two Types of Mechanical Reversible Logic", *Nanotechnology*, vol. 4, pp. 114–131, 1993. DOI: 10.1088/0957-4484/4/2/007.

[79] "International Technology Roadmap for Semiconductors 2.0 - Beyond CMOS", Semiconductors Industry Association, Tech. Rep., 2015. [Online]. Available: http://www.itrs2.net.

[80] J. R. Raney, N. Nadkarni, C. Daraio, D. M. Kochmann, J. A. Lewis, and K. Bertoldi, "Stable propagation of mechanical signals in soft media using stored elastic energy", *Proceedings of the National Academy of Sciences*, vol. 113, pp. 9722–9727, Aug. 2016. DOI: 10.1073/PNAS.1604838113.

[81] A. Ion, L. Wall, R. Kovacs, and P. Baudisch, "Digital Mechanical Metamaterials", in *CHI*, ACM, 2017, pp. 977–988. DOI: 10.1145/3025453.3025624.

[82] Y. Song, R. M. Panas, S. Chizari, L. A. Shaw, J. A. Jackson, J. B. Hopkins, and A. J. Pascall, "Additively manufacturable micro-mechanical logic gates", *Nature Communications*, vol. 10, 2019. DOI: 10.1038/s41467-019-08678-0.

[83] P. Kuppens, M. Bessa, J. Herder, and J. Hopkins, "Monolithic binary stiffness building blocks for mechanical digital machines", *Extreme Mechanics Letters*, vol. 42, 2021. DOI: 10.1016/j.eml.2020.101120.

[84] D. J. Preston, P. Rothemund, H. J. Jiang, M. P. Nemitz, J. Rawson, Z. Suo, and G. M. Whitesides, "Digital logic for soft devices", *Proceedings of the National Academy of Sciences*, vol. 116, pp. 7750–7759, 2019. DOI: 10.1073/pnas.1820672116.

[85] B. Treml, A. Gillman, P. Buskohl, and R. Vaia, "Origami mechanologic", *Proceedings of the National Academy of Sciences*, vol. 115, pp. 6916–6921, 2018. DOI: 10.1073/pnas.1805122115.

[86] Z. Meng, W. Chen, T. Mei, Y. Lai, Y. Li, and C. Chen, "Bistability-based foldable origami mechanical logic gates", *Extreme Mechanics Letters*, vol. 43, p. 101 180, 2021. DOI: 10.1016/j.eml.2021.101180.

[87] E. T. Filipov, T. Tachi, and G. H. Paulino, "Origami tubes assembled into stiff, yet reconfigurable structures and metamaterials", *Proceedings of the National Academy of Sciences*, vol. 112, pp. 12 321–12 326, 2015. DOI: 10.1073/pnas.1509465112.

[88] Carbon, *The perfect fit: Carbon + adidas collaborate to upend athletic footwear*, Carbon, Nov. 2020. [Online]. Available: https://www.carbon3d.com/resources/adidas/.

[89] T. Ravenscroft, *Nike reveals hands-free go flyease trainer*, dezeen, Feb. 2021. [Online]. Available: https://www.dezeen.com/2021/02/01/nike-go-flyease-trainer-hands-free/.

[90] P. Bettini, A. Airoldi, G. Sala, L. D. Landro, M. Ruzzene, and A. Spadoni, "Composite chiral structures for morphing airfoils: Numerical analyses and development of a manufacturing process", *Composites Part B: Engineering*, vol. 41, pp. 133–147, 2010. DOI: 10.1016/j.compositesb.2009.10.005.

[91] S. Xu, Z. Yan, K.-I. Jang, W. Huang, H. Fu, J. Kim, Z. Wei, M. Flavin, J. McCracken, R. Wang, A. Badea, Y. Liu, D. Xiao, G. Zhou, J. Lee, H. U. Chung, H. Cheng, W. Ren, A. Banks, X. Li, U. Paik, R. G. Nuzzo, Y. Huang, Y. Zhang, and J. A. Rogers, "Assembly of micro/nanomaterials into complex, three-dimensional architectures by compressive buckling", *Science*, vol. 347, pp. 154–159, 2015. DOI: 10.1126/science.1260960.

[92] H. M. A. Kolken, S. Janbaz, S. M. A. Leeflang, K. Lietaert, H. H. Weinans, and A. A. Zadpoor, "Rationally designed meta-implants: A combination of auxetic and conventional meta-biomaterials", *Mater. Horiz.*, vol. 5, pp. 28–35, 1 2018. DOI: 10.1039/C7MH00699C.

[93] A. G. Mark, S. Palagi, T. Qiu, and P. Fischer, "Auxetic metamaterial simplifies soft robot design", in *2016 IEEE International Conference on Robotics and Automation (ICRA)*, 2016, pp. 4951–4956. DOI: 10.1109/ICRA.2016.7487701.

[94] A. Rafsanjani, Y. Zhang, B. Liu, S. M. Rubinstein, and K. Bertoldi, "Kirigami skins make a simple soft actuator crawl", *Science Robotics*, vol. 3, 2018. DOI: 10.1126/scirobotics.aar7555.

[95] A. Maziz, A. Concas, A. Khaldi, J. Stålhand, N.-K. Persson, and E. W. H. Jager, "Knitting and weaving artificial muscles", *Science Advances*, vol. 3, 2017. DOI: 10.1126/sciadv.1600327.

[96] T. Chen, M. Pauly, and P. M. Reis, "A reprogrammable mechanical metamaterial with stable memory", *Nature*, vol. 589, pp. 386–390, 2021. DOI: 10.1038/s41586-020-03123-5.

[97] X. Ning, X. Wang, Y. Zhang, X. Yu, D. Choi, N. Zheng, D. S. Kim, Y. Huang, Y. Zhang, and J. A. Rogers, "Assembly of advanced materials into 3d functional structures by methods inspired by origami and kirigami: A review", *Advanced Materials Interfaces*, vol. 5, 2018. DOI: 10.1002/admi.201800284.

[98] X. Ning, X. Yu, H. Wang, R. Sun, R. E. Corman, H. Li, C. M. Lee, Y. Xue, A. Chempakasseril, Y. Yao, Z. Zhang, H. Luan, Z. Wang, W. Xia, X. Feng, R. H. Ewoldt, Y. Huang, Y. Zhang, and J. A. Rogers, "Mechanically active materials in three-dimensional mesostructures", *Science Advances*, vol. 4, 2018. DOI: 10.1126/sciadv.aat8313.

[99] A. Maggi, H. Li, and J. R. Greer, "Three-dimensional nano-architected scaffolds with tunable stiffness for efficient bone tissue growth", *Acta Biomaterialia*, vol. 63, pp. 294–305, 2017. DOI: 10.1016/j.actbio.2017.09.007.

[100] R. Gatt, L. Mizzi, J. I. Azzopardi, K. M. Azzopardi, D. Attard, A. Casha, J. Briffa, and J. N. Grima, "Hierarchical Auxetic Mechanical Metamaterials", *Scientific Reports*, vol. 5, 2015. DOI: 10.1038/srep08395.

[101] D. Rakwal, S. Heamawatanachai, P. Tathireddy, F. Solzbacher, and E. Bamberg, "Fabrication of compliant high aspect ratio silicon microelectrode arrays using micro-wire electrical discharge machining", *Microsystem Technologies*, vol. 15, pp. 789–797, 2009. DOI: 10.1007/s00542-009-0792-7.

[102] J. Li, C. Myant, and B. Wu, "The current landscape for additive manufacturing research", Imperial College London, Tech. Rep., 2016.

[103] T. D. Ngo, A. Kashani, G. Imbalzano, K. T. Nguyen, and D. Hui, "Additive manufacturing (3d printing): A review of materials, methods, applications and challenges", *Composites Part B: Engineering*, vol. 143, pp. 172–196, 2018. DOI: 10.1016/j.compositesb.2018.02.012.

[104] T. Greicius, *Nasa's perseverance rover bringing 3d-printed metal parts to mars*, NASA, Oct. 2020. [Online]. Available: https://www.nasa.gov/feature/jpl/nasas-perseverance-rover-bringing-3d-printed-metal-parts-to-mars.

[105] 3DHubs, *3d printing - the definitive guide*, 3D Hubs, Nov. 2020. [Online]. Available: https://www.3dhubs.com/guides/3d-printing/.

[106] F. S. Ben Redwood and B. Garret, *The 3D Printing Handbook - Technologies, design and applications*. 3D Hubs, 2017, ISBN: 978-90-827485-0-5.

[107] Stratasys, *Vero Material Data Sheet - MDS PJ Vero 1020a*, 2020. [Online]. Available: https://www.stratasys.com/-/media/files/material-spec-sheets/mds_pj_vero_1020a.pdf.

[108] ——, *VeroClear Material Data Sheet - MDS PJ VeroClear 0320a*, 2020. [Online]. Available: https://www.stratasys.com/-/media/files/material-spec-sheets/mds_pj_veroclear_0320a.pdf.

[109] MatWeb, *Arkema Plexiglas V825 Acrylic*. [Online]. Available: http://www.matweb.com/search/DataSheet.aspx?MatGUID=bdfa9a3b599f4df6941c181dba5f7324&ckck=1.

[110] Stratasys, *Agilus30 Material Data Sheet - MDS PJ Agilus30 1020a*, 2020. [Online]. Available: https://www.stratasys.com/-/media/files/material-spec-sheets/mds_pj_agilus30_1020a.pdf.

[111] ——, *MSS PJ DigitalMaterialsDatasheet 0617a*, 2017. [Online]. Available: https://www.stratasys.com/-/media/files/material-spec-sheets/mss_pj_digitalmaterialsdatasheet_0617a.pdf.

[112] MatWeb, *Precision Polymer Engineering R50D Natural Rubber*. [Online]. Available: http://www.matweb.com/search/DataSheet.aspx?MatGUID=66e0de70fe5c44c1a62501d753df06cc.

[113] Y. L. Yap, C. Wang, S. L. Sing, V. Dikshit, W. Y. Yeong, and J. Wei, "Material jetting additive manufacturing: An experimental study using designed metrological benchmarks", *Precision engineering*, vol. 50, pp. 275–285, 2017. DOI: 10.1016/j.precisioneng.2017.05.015..

[114] T. S. Lumpe, J. Mueller, and K. Shea, "Tensile properties of multi-material interfaces in 3d printed parts", *Materials & Design*, vol. 162, pp. 1–9, 2019.

[115] J. Mueller, K. Shea, and C. Daraio, "Mechanical properties of parts fabricated with inkjet 3d printing through efficient experimental design", *Materials & Design*, vol. 86, pp. 902–912, 2015. DOI: 10.1016/j.matdes.2015.07.129.

[116] Formlabs, *Guide to stereolithography (sla) 3d printing*, Formlabs, Nov. 2020. [Online]. Available: https://formlabs.com/uk/blog/ultimate-guide-to-stereolithography-sla-3d-printing/.

[117] ——, *Durable Material Data Sheet*, 2018. [Online]. Available: https://formlabs-media.formlabs.com/datasheets/1801084-TDS-ENUS-0P.pdf.

[118] ——, *Tough 1500 Material Data Sheet*, 2020. [Online]. Available: https://formlabs-media.formlabs.com/datasheets/Tough_1500_TDS_EN.pdf.

[119] MatWeb, *Mitsubishi Chemical Advanced Materials Proteus PP*. [Online]. Available: http://www.matweb.com/search/DataSheet.aspx?MatGUID=d936b5dd8d514f64a984e68b645532c6&ckck=1.

[120] F. Cosmi and A. Dal Maso, "A mechanical characterization of sla 3d-printed specimens for low-budget applications", *Materials Today: Proceedings*, vol. 32, pp. 194–201, 2020, DAS2019. DOI: 10.1016/j.matpr.2020.04.602.

[121] S. Aravind Shanmugasundaram, J. Razmi, M. J. Mian, and L. Ladani, "Mechanical anisotropy and surface roughness in additively manufactured parts fabricated by stereolithography (sla) using statistical analysis", *Materials*, vol. 13, 2020. DOI: 10.3390/ma13112496.

[122] J. R. C. Dizon, A. H. Espera, Q. Chen, and R. C. Advincula, "Mechanical characterization of 3d-printed polymers", *Additive Manufacturing*, vol. 20, pp. 44–67, 2018. DOI: 10.1016/j.addma.2017.12.002.

[123] S. Wang, Y. Ma, Z. Deng, K. Zhang, and S. Dai, "Implementation of an elastoplastic constitutive model for 3d-printed materials fabricated by stereolithography", *Additive Manufacturing*, vol. 33, 2020. DOI: 10.1016/j.addma.2020.101104.

[124] A. G. Bromley, "Charles Babbage's Analytical Engine, 1838", *IEEE Ann. Hist. Comput.*, vol. 20, pp. 29–45, Oct. 1998. DOI: 10.1109/85.728228.

[125] R. C. Merkle, R. A. Freitas , Jr, T. Hogg, T. E. Moore, M. S. Moses, and J. Ryley, "Mechanical Computing Systems Using Only Links and Rotary Joints", *Journal of Mechanisms and Robotics*, vol. 10, Sep. 2018. DOI: 10.1115/1.4041209.

[126] M. Zanaty, H. Schneegans, I. Vardi, and S. Henein, "Reconfigurable Logic Gates Based on Programable Multistable Mechanisms", *Journal of Mechanisms and Robotics*, vol. 12, Feb. 2020. DOI: 10.1115/1.4045970.

[127] N. Hu and R. Burgueño, "Buckling-induced smart applications: Recent advances and trends", *Smart Materials and Structures*, vol. 24, May 2015. DOI: 10.1088/0964-1726/24/6/063001.

[128] D. J. Gere and B. J. Goodno, *Mechanics of Materials, SI Edition*, 8th ed. Stamford: Cengage Learning, 2013, ISBN: 978-1-111-57774-2.

[129] S. P. Timoshenko and J. M. Gere, *Theory of elastic stability*. Courier Corporation, 2009, ISBN: 978-0-486-47207-2.

[130] M. Vangbo, "An analytical analysis of a compressed bistable buckled beam", *Sensors and Actuators A: Physical*, vol. 69, pp. 212–216, 1998. DOI: 10.1016/S0924-4247(98)00097-1.

[131] Jin Qiu, J. H. Lang, and A. H. Slocum, "A curved-beam bistable mechanism", *Journal of Microelectromechanical Systems*, vol. 13, pp. 137–146, 2004. DOI: 10.1109/JMEMS.2004.825308.

[132] Z. Zhang, S. Pusateri, B. Xie, and N. Hu, "Tunable energy trapping through contact-induced snap-through buckling in strips with programmable imperfections", *Extreme Mechanics Letters*, vol. 37, 2020. DOI: 10.1016/j.eml.2020.100732.

[133] Y. Chandra, I. Stanciulescu, T. Eason, and M. Spottswood, "Numerical pathologies in snap-through simulations", *Engineering Structures*, vol. 34, pp. 495–504, 2012. DOI: 10.1016/j.engstruct.2011.10.013.

[134] T. Schioler and S. Pellegrino, "Space frames with multiple stable configurations", *AIAA Journal*, vol. 45, pp. 1740–1747, 2007. DOI: 10.2514/1.16825.

[135] J. Qiu, J. H. Lang, and A. H. Slocum, "A centrally-clamped parallel-beam bistable mems mechanism", in *Technical Digest. MEMS 2001. 14th IEEE International Conference on Micro Electro Mechanical Systems (Cat. No.01CH37090)*, 2001, pp. 353–356.

[136] Stratasys, *PolyJet Digital Materials Data Sheet*. [Online]. Available: https://www.stratasys.com/materials/search/agilus30 (visited on 04/06/2020).

[137] U. Waheed, C. Myant, and S. Dobson, "Boolean and/or mechanical logic using multi-plane mechanical metamaterials", *Extreme Mechanics Letters*, vol. 40, 2020. DOI: 10.1016/j.eml.2020.100865.

[138] S. Mansour, M. Gilbert, and R. Hague, "A study of the impact of short-term ageing on the mechanical properties of a stereolithography resin", *Materials Science and Engineering: A*, vol. 447, pp. 277–284, 2007. DOI: 10.1016/j.msea.2006.10.007.

[139] D. Yang, B. Mosadegh, A. Ainla, B. Lee, F. Khashai, Z. Suo, K. Bertoldi, and G. M. Whitesides, "Buckling of elastomeric beams enables actuation of soft machines", *Advanced Materials*, vol. 27, pp. 6323–6327, 2015. DOI: 10.1002/adma.201503188.

[140] N. M. White and M. Kraft, *MEMS for automotive and aerospace applications*. Woodhead Publishing, 2013, ISBN: 978-0-85709-118-5.

[141] A. O'Grady, R. Larger, N. Tiliakos, G. Papadopoulos, V. Modi, and L. G. Frechette, "A mems sensor for mean shear stress measurements in high-speed turbulent flows with backside interconnects", in *TRANSDUCERS 2009 - 2009 International Solid-State Sensors, Actuators and Microsystems Conference*, 2009, pp. 272–275. DOI: 10.1109/SENSOR.2009.5285510.

[142] "Monolithic accelerometer with signal conditioning - adxl50", Analog Devices, Tech. Rep., 1996.

[143] L. L. Howell, *Compliant mechanisms*. John Wiley & Sons, 2002, ISBN: 0-471-38478-X.

[144] *A MEMS-Based Shear Stress Sensor for High Temperature Applications*, vol. Volume 2: Fora, Parts A and B, Fluids Engineering Division Summer Meeting, Jul. 2007, pp. 1477–1478. DOI: 10.1115/FEDSM2007-37700.

[145] M. T. A. Saif, "On a tunable bistable mems-theory and experiment", *Journal of Microelectromechanical Systems*, vol. 9, pp. 157–170, 2000. DOI: 10.1109/84.846696.

[146] S. An, B. Kim, S. Kwon, G. Moon, M. Lee, and W. Jhe, "Bifurcation-enhanced ultrahigh sensitivity of a buckled cantilever", *Proceedings of the National Academy of Sciences*, vol. 115, pp. 2884–2889, 2018. DOI: 10.1073/pnas.1716067115.

[147] S. O. Erbil, U. Hatipoglu, C. Yanik, M. Ghavami, A. B. Ari, M. Yuksel, and M. S. Hanay, "Full electrostatic control of nanomechanical buckling", *Phys. Rev. Lett.*, vol. 124, Jan. 2020. DOI: 10.1103/PhysRevLett.124.046101.

[148] U. Zaghloul and G. Piazza, "Highly scalable nems relays with stress-tuned switching voltage using piezoelectric buckling actuators", *IEEE Transactions on Electron Devices*, vol. 61, pp. 3520–3528, 2014. DOI: 10.1109/TED.2014.2331914.

[149] D. Roodenburg, J. W. Spronck, H. S. J. van der Zant, and W. J. Venstra, "Buckling beam micromechanical memory with on-chip readout", *Applied Physics Letters*, vol. 94, 2009. DOI: 10.1063/1.3129195.

[150] R. L. Harne and K. W. Wang, *Harnessing bistable structural dynamics: for vibration control, energy harvesting and sensing*. Wiley Blackwell, 2017, ISBN: 978-1-119-12804-5.

[151] M. T. A. Saif and N. C. MacDonald, "Measurement of forces and spring constants of microinstruments", *Review of Scientific Instruments*, vol. 69, pp. 1410–1422, 1998. DOI: 10.1063/1.1148809.

[152] M. Sulfridge, T. Saif, N. Miller, and M. Meinhart, "Nonlinear dynamic study of a bistable mems: Model and experiment", *Journal of Microelectromechanical Systems*, vol. 13, pp. 725–731, 2004. DOI: 10.1109/JMEMS.2004.835766.

[153] M. Sulfridge, T. Saif, N. Miller, and K. O'Hara, "Optical actuation of a bistable mems", *Journal of Microelectromechanical Systems*, vol. 11, pp. 574–583, 2002. DOI: 10.1109/JMEMS.2002.803417.

[154] S. Abu-Salih and D. Elata, "Experimental validation of electromechanical buckling", *Journal of Microelectromechanical Systems*, vol. 15, pp. 1656–1662, 2006. DOI: 10.1109/JMEMS.2006.886015.

[155] B. D. Jensen and L. L. Howell, "Bistable configurations of compliant mechanisms modeled using four links and translational joints", *ASME. J. Mech. Des.*, vol. 126, pp. 657–666, 2004. DOI: 10.1115/1.1760776.

[156] M. Vangbo and Y. Bäcklund, "A lateral symmetrically bistable buckled beam", *Journal of Micromechanics and Microengineering*, vol. 8, pp. 29–32, Mar. 1998. DOI: 10.1088/0960-1317/8/1/005.

[157] Ü. Sönmez and C. C. Tutum, "A compliant bistable mechanism design incorporating elastica buckling beam theory and pseudo-rigid-body model", *ASME. J. Mech. Des.*, vol. 130, 2008. DOI: 10.1115/1.2839009.

[158] G. H. T. G. L. Holst and B. D. Jensen, "Modeling and experiments of buckling modes and deflection of fixed-guided beams in compliant mechanisms", *ASME. J. Mech. Des.*, vol. 133, p. 051 002, 2011. DOI: 10.1115/1.4003922.

[159] S. Linß, S. Henning, and L. Zentner, "Modeling and design of flexure hinge-based compliant mechanisms", in *Kinematics*, J. Mizrahi, Ed., Rijeka: IntechOpen, 2019, ch. 3. DOI: 10.5772/intechopen.85224.

[160] S. Henning, S. Linß, P. Gräser, R. Theska, and L. Zentner, "Non-linear analytical modeling of planar compliant mechanisms", *Mechanism and Machine Theory*, vol. 155, 2021. DOI: 10.1016/j.mechmachtheory.2020.104067.

[161] Materialise, *Materialise slicing technology enables toyota's lightweight car seat*, Materialise, Jan. 2021. [Online]. Available: https://www.materialise.com/en/cases/materialise-slicing-technology-enables-toyota%E2%80%99s-lightweight-car-seat.

[162] Carbon, *Rethinking foam - the carbon lattice innovation*, Carbon, Jan. 2021. [Online]. Available: https://www.carbon3d.com/resources/whitepaper/rethinking-foam-carbons-lattice-innovation/.

[163] DOD, "Narrative summaries of accidents involving U.S. nuclear weapons 1950-1980", Department of Defense, Tech. Rep., 1981.

[164] J. Covan and J. Cooper, "Predictable safety in the control of high consequence systems", in *Proceedings Third IEEE International High-Assurance Systems Engineering Symposium (Cat. No.98EX231)*, 1998, pp. 200–204. DOI: 10.1109/HASE.1998.731612.

[165] D. W. Plummer and W. H. Greenwood, "A Primer on Unique Signal Stronglinks", Sandia National Laboratories, Tech. Rep. SAND93-0951, 1993.

[166] R. H. Hansen, "Nuclear Safety Themes for Earth Penetrating Weapons, Issue C", Sandia National Laboratories, Tech. Rep. 97-13(14)H, 1993.

[167] S. D. Spray and J. A. Cooper, "Passive safety concepts applied to critical functions", Sandia National Laboratories, Tech. Rep. SAN095-0347C, 1995.

[168] P. D'Antonio, "Surety Principles Developedment and Integration for Nuclear Weapons", in *High Consequence Operations Safety Symposium II*, 1998.

[169] "Nuclear Matters Handbook 2020", The Office of the Deputy Assistant Secretary of Defense for Nuclear Matters (ODASDM(NM)), Tech. Rep., 2020.

[170] "The Unique Signal Concept for Detonation Safety In Nuclear Weapons", Sandia National Laboratories, Tech. Rep. SAND91-1269, 1992.

[171] J. A. Cooper, "Mathematical Aspects of Unique Signal Assessment", Sandia National Laboratories, Tech. Rep. SAND2002-1306, 2002.

[172] D. W. Plummer and W. H. Greenwood, "The history of nuclear weapon safety devices", *American Institute of Aeronautics and Astronautics*, 1998.

[173] G. L. Benavides, "Rotary Pin-in maze discriminator", United States Patent, US5626040A, 1997.

[174] R. B. Wolfgang, "The Enhanced Nuclear Detonation Safety Theme - An Introduction", Sandia National Laboratories, Tech. Rep. SAND2012-0793C, 2012.

[175] "Approach for Achieving Nuclear Weapon Electrical System Safety In Abnormal Environments", Sandia National Laboratories, Tech. Rep. SC-DR-72 0492, 1998.

[176] D. E. Carnicom and E. T. Schreiner, "Characteristics and development report for the mc2935 trajectory strong link switch (314965)", Sandia National Laboratories, Tech. Rep. SAND78-1925, 1979.

[177] N. Sclater and N. Chironis, *Mechanisms and Mechanical Devices Sourcebook, Third Edition*. Mcgraw-hill, 2006, ISBN: 978-0071361699.

[178] M. A. Polosky, E. J. Garcia, and J. J. Allen, "Surface micromachined counter-meshing gears discrimination device", United States Patent, US6158297, 2000.

[179] M. Rodgers, J. Sniegowski, S. Miller, and P. McWhorter, "Method for fabricating five-level microelectromechanical structures and microelectromechanical transmission formed", United States Patent, US6082208, 2000.

[180] M. Caldwell, J. A. Cooper, J. M. Covan, P. D'Antonio, and S. Spray, "Potential disadvantages of microtechnology for future high consequence safety applications", Sandia National Laboratories, Tech. Rep. SAND98- 2829C, 1998.

[181] P. J. Smith, "MEMS Based Fuzing/Safety and Arming Systems", Naval surface warfare center, Tech. Rep. RTO-EN-AVT-105, 2004.

[182] S. Li, W. Chen, W. Zhang, Q. Xiao, S. Tan, and M. Feng, "Structure mechanism of MEMS security stronglink with multi-try function", in *International Conference on Smart Materials and Nanotechnology in Engineering*, vol. 6423, SPIE, 2007. DOI: 10.1117/12.780095.

[183] S. Y. Li, W. Y. Chen, W. P. Zhang, Q. J. Xiao, S. Y. Tan, and M. H. Feng, "Counter-meshing gears stronglink with multi-try function based on MEMS technology", *Journal of Shanghai University*, vol. 12, pp. 249–254, 2008. DOI: 10.1007/s11741-008-0311-1.

[184] S. E. Miller and B. J. Moore, "2015 Summer Design Challenge: Team A&E (2241) Additively Manufactured Discriminator", Sandia National Laboratories, Tech. Rep. SAND2016-11284.

[185] P. Horowitz and W. Hill, *The Art of Electronics*. Cambridge University Press, 2015, ISBN: 978-0-521-80926-9.